36420

National Library of Canada
Bibliothèque nationale du Canada

CANADIAN THESES ON MICROFICHE

THÈSES CANADIENNES SUR MICROFICHE

NAME OF AUTHOR/*NOM DE L'AUTEUR* CHONG-LIEK LIU

TITLE OF THESIS/*TITRE DE LA THÈSE* ON THE MECHANISM AND KINETICS OF THE H_2S/SO_2 REACTION

UNIVERSITY/*UNIVERSITÉ* UNIVERSITY OF ALBERTA

DEGREE FOR WHICH THESIS WAS PRESENTED/ *GRADE POUR LEQUEL CETTE THÈSE FUT PRÉSENTÉE* Ph.D

YEAR THIS DEGREE CONFERRED/*ANNÉE D'OBTENTION DE CE GRADE* 1978

NAME OF SUPERVISOR/*NOM DU DIRECTEUR DE THÈSE* Dr. I. G. Dalla Lana

Permission is hereby granted to the NATIONAL LIBRARY OF CANADA to microfilm this thesis and to lend or sell copies of the film.

The author reserves other publication rights, and neither the thesis nor extensive extracts from it may be printed or otherwise reproduced without the author's written permission.

L'autorisation est, par la présente, accordée à la BIBLIOTHÈQUE NATIONALE DU CANADA de microfilmer cette thèse et de prêter ou de vendre des exemplaires du film.

L'auteur se réserve les autres droits de publication; ni la thèse ni de longs extraits de celle-ci ne doivent être imprimés ou autrement reproduits sans l'autorisation écrite de l'auteur.

DATED/*DATÉ* April 20/1978 SIGNED/*SIGNÉ*

PERMANENT ADDRESS/*RÉSIDENCE FIXÉ*
15104 - 67 STREET
EDMONTON T5C 0E1
ALBERTA.

NL-91 (3-74)

National Library of Canada

Cataloguing Branch
Canadian Theses Division

Ottawa, Canada
K1A 0N4

Bibliothèque nationale du Canada

Direction du catalogage
Division des thèses canadiennes

NOTICE

The quality of this microfiche is heavily dependent upon the quality of the original thesis submitted for microfilming. Every effort has been made to ensure the highest quality of reproduction possible.

If pages are missing, contact the university which granted the degree.

Some pages may have indistinct print especially if the original pages were typed with a poor typewriter ribbon or if the university sent us a poor photocopy.

Previously copyrighted materials (journal articles, published tests, etc.) are not filmed.

Reproduction in full or in part of this film is governed by the Canadian Copyright Act, R.S.C. 1970, c. C-30. Please read the authorization forms which accompany this thesis.

THIS DISSERTATION
HAS BEEN MICROFILMED
EXACTLY AS RECEIVED

AVIS

La qualité de cette microfiche dépend grandement de la qualité de la thèse soumise au microfilmage. Nous avons tout fait pour assurer une qualité supérieure de reproduction.

S'il manque des pages, veuillez communiquer avec l'université qui a conféré le grade.

La qualité d'impression de certaines pages peut laisser à désirer, surtout si les pages originales ont été dactylographiées à l'aide d'un ruban usé ou si l'université nous a fait parvenir une photocopie de mauvaise qualité.

Les documents qui font déjà l'objet d'un droit d'auteur (articles de revue, examens publiés, etc.) ne sont pas microfilmés.

La reproduction, même partielle, de ce microfilm est soumise à la Loi canadienne sur le droit d'auteur, SRC 1970, c. C-30. Veuillez prendre connaissance des formules d'autorisation qui accompagnent cette thèse.

LA THÈSE A ÉTÉ
MICROFILMÉE TELLE QUE
NOUS L'AVONS REÇUE

NL-339 (3/77)

THE UNIVERSITY OF ALBERTA

ON THE MECHANISM AND KINETICS OF THE H_2S/SO_2 REACTION

BY

Ⓒ CHONG-LIEK LIU

A THESIS
SUBMITTED TO THE FACULTY OF GRADUATE STUDIES
IN PARTIAL FULFILMENT OF THE REQUIREMENTS FOR THE DEGREE
OF DOCTOR OF PHILOSOPHY

DEPARTMENT OF CHEMICAL ENGINEERING

EDMONTON, ALBERTA
SPRING 1978

THE UNIVERSITY OF ALBERTA

FACULTY OF GRADUATE STUDIES AND RESEARCH

The undersigned certify that they have read, and recommend to the Faculty of Graduate Studies and Research, for acceptance, a thesis entitled . . . . ON THE MECHANISM AND KINETICS OF THE H_2S/SO_2 REACTION

submitted by . . . Chong-Liek Liu . . . .

in partial fulfilment of the requirements for the degree of

Doctor of Philosophy

in Chemical Engineering.

. . IG Dalla Lana . . . .
Supervisor

. . Sieghard Wanke . .

. . Donald Quon . . . .

. . Ronald G Cavell . .

. . James B Hyne . . . .
External Examiner

Date. March 31, 1978 . . . .

ABSTRACT

An experimental investigation of the reaction between H_2S and SO_2 was conducted over a γ-alumina catalyst (Alon) in a stainless steel recycle reactor. The steady-state conversions as a function of temperature and space velocity were measured "in situ" using infrared spectroscopy. A total of 118 experiments at 6 different temperatures between 200 and 323°C and at varying partial pressures of H_2S, SO_2 and H_2O were performed to provide kinetic data. By introducing only the reaction products over the catalyst and by the subsequent failure to detect either reactants, the reverse reaction was found to be negligible under the experimental conditions adopted. Water exerted a retarding effect on the reaction rate as indicated by the decrease in the reaction conversion with increased amounts of water in the feed stream.

Infrared spectroscopic results indicated that both H_2S and SO_2 adsorbed on the Lewis-acid sites of the catalyst. Above 100°C, the spectral bands representing the adsorbed H_2S and SO_2 were undetectable. Adsorption models for H_2S and SO_2 on γ-alumina were proposed based upon this evidence and lattice and atomic dimensions. It was also observed that a finite amount of oxygen on the catalyst (whose state is still unknown) was capable of oxidizing H_2S or CS_2 to sulfur at room temperature. This oxidizing capability could be removed by pretreating the catalyst with H . Although the oxide-ion sites of the catalyst are not believed to be directly involved as adsorption sites for either H_2S or SO_2, their presence was found to be vital for catalyzing the H_2S/SO_2

reaction. Possible catalyst poisoning from sulfate formation on the catalyst surface has also been investigated. No sulfate formation could be detected by contacting SO_2 with the catalyst. The presence of SO_3 or O_2 together with SO_2, was necessary for the formation of sulfate. The analysis of a catalyst wafer which was exposed for a period of experimental conditions longer than any wafer employed in the kinetic runs failed to reveal the presence of sulfate.

These observations on the surface chemistry of the catalyst and the nature of the reaction were used to construct various reaction mechanisms and their corresponding kinetic models. The statistical model discrimination method developed by Singh [130] was employed to select the kinetic model which best correlated the measured reaction rates. The best rate function was found to be in the form

$$(-r_{SO_2}) = b_{10} \exp(-E_{10}/RT)\, P_{H_2S}\, P_{SO_2}{}^{1/2} / [1 + b_{20} \exp(-E_{20}/RT)\, P_{H_2O}]^2\, p^{1/2x}$$

where,

$b_{10} = (9.72 \pm 4.37)\ 10^{-5}$

$E_{10/R} = 3509 \pm 254$

$b_{20} = (1.15 \pm 2.18)\ 10^{-5}$

$E_{20/R} = 3158 \pm 1049$

The model on which the rate function is based is in near agreement with an earlier model proposed from McGregor's [84] studies using a bauxite catalyst and or different experimental reaction.

ACKNOWLEDGEMENTS

The author wishes to express his thanks to various individuals who have assisted in different ways in his research and in particular to convey his sincere appreciation to Dr. I.G. Dalla Lana for his advice and guidance during the course of this study and slso for his valuable criticism and help in the period of preparation of this thesis.

Thanks are also due to Dr. H. Singh for his assistance in kinetic model discrimination and Mr. H. Ramstead for his help in computer application.

The author's greatest personal debt is to his wife, Kim-Ping, whose encouragement and patience were very important for the completion of this work.

The financial support of the Shell Canada Ltd. Fellowship and the University of Alberta is gratefully acknowledged.

TABLE OF CONTENTS

Page

CHAPTER I INTRODUCTION

1.1 Background 1

1.2 Objectives of This Work 2

CHAPTER II LITERATURE SURVEY

2.1 Methods of Recovering Sulfur from H_2S - Containing Gases 4

2.1.1 Wet-Bed Processes 4

2.1.2 Dry-Bed Processes 6

2.2 Review of Heterogeneous Catalytic Reaction of H_2S and SO_2 8

2.2.1 General Review 8

2.2.2 Mechanistic Studies 10

2.2.3 Kinetic Studies 14

2.3 Surface Properties of γ-Alumina 21

2.3.1 The Crystalline Structure of γ-Alumina 22

2.3.2 The Surface of γ-Alumina 25

2.3.3 The Adsorption Properties and Surface Chemistry of γ-Alumina 32

CHAPTER III REAGENTS AND CATALYST

3.1 Reagents 51

3.1.1 Reagents Used for Kinetic Studies 51

3.1.2 Reagents Used for Studying Adsorption and Surface Reaction on γ-Alumina 52

3.1.3 Reagents Used for Studying Sulfate Formation on γ-Alumina 53

3.2 Alumina Catalysts 54

TABLE OF CONTENTS (continued)

Page

CHAPTER IV ADSORPTION AND SURFACE REACTION OF γ-ALUMINA

4.1 Experimental Equipment 60
  4.1.1 Infrared Cell 60
  4.1.2 Vacuum System 64
4.2 Preparation and Pretreatment of Catalyst Wafer 64
4.3 Experimental Procedure 65
  4.3.1 Recording Infrared Spectrum 66
  4.3.2 Adsorption - Desorption Studies 69
  4.3.3 Surface Reaction of γ-Alumina 70

CHAPTER V STUDIES ON KINETICS AND MECHANISM

5.1 Experimental Equipment 72
  5.1.1 Feed System 74
  5.1.2 Recirculation Pump 77
  5.1.3 Infrared Cell-Reactor and Catalyst Holder 80
5.2 Process Measurements 88
  5.2.1 Reactor Temperature 88
  5.2.2 Reactor Pressure 89
  5.2.3 Process Flow Rate 90
5.3 Operation of Equipment and Experimental Procedure 91
  5.3.1 Start-up and Catalyst Pretreatment 91
  5.3.2 Steady-State 96
  5.3.3 Shutdown 99

TABLE OF CONTENTS (continued)

Page

5.4 Analysis and Data Evaluation 101

5.4.1 Analysis 101

5.4.2 Data Evaluation 111

CHAPTER VI RESULTS AND DISCUSSION

6.1 Oxidizing Property of γ-Alumina 116

6.1.1 Oxidizing Property Demonstrated by H_2S Adsorption 118

6.1.2 Oxidizing Property Demonstrated by CS_2 Adsorption 120

6.1.3 The Postulated Forms of "Oxygen" on γ-Alumina 122

6.2 Adsorption of H_2S on γ-Alumina 124

6.2.1 Selective Adsorption Method to Evaluate Sites of Adsorption 125

6.2.2 Adsorption Model Concluded from the Present Work 140

6.2.3 The Effect of Temperature on H_2S Adsorption 142

6.3 Adsorption of SO_2 on γ-Alumina 143

6.3.1 Selective Adsorption Method to Evaluate Sites of Adsorption 146

6.3.2 Adsorption Model Concluded from the Present Work 150

6.3.3 The Effect of Temperature on SO_2 Adsorption 151

6.4 The Relative Importance of Various Types of Sites for Reaction 153

6.5 Sulfate Formation on γ-Alumina 157

TABLE OF CONTENTS (continued)

Page

6.5.1 Sulfate Formation from SO_2 158

6.5.2 Sulfate Formation from SO_2 and O_2 159

6.5.3 Sulfate Formation from SO_3 160

6.5.4 Sulfate Formation in the Presence of Water Vapor 162

6.6 Preliminary Kinetic Experiments 163

6.6.1 Blank Run 164

6.6.2 The Reversibility of the Reaction 165

6.6.3 Mass Transfer Consideration 172

6.6.4 Stability of the Catalyst Activity 181

6.7 Infrared Spectra of γ-Alumina Under Reaction Condition 186

6.8 Kinetics and Mechanism 186

6.8.1 General Methods for Developing and Testing Kinetic Models 188

6.8.2 Development of Kinetic Models 192

6.9 Model Discrimination 211

6.9.1 Statistical Model Discrimination Technique 211

6.9.2 Some Published Models on Claus Reaction 218

6.9.3 Correlation of Modified McGregor's Model 225

6.9.4 Discrimination Among Models Derived in the Present Work 228

6.9.5 Kinetic Models with Temperature Dependency 234

TABLE OF CONTENTS (continued)

Page

CHAPTER VII CONCLUSIONS AND RECOMMENDATIONS

7.1 Conclusions 236

7.1.1 Adsorption of H_2S and SO_2 on γ-Alumina 236

7.1.2 The Catalytic Role Played by γ-Alumina in Claus Reaction 237

7.1.3 Kinetics and Mechanism of Claus Reaction 238

7.2 Recommendations 240

7.2.1 Equipment 240

7.2.2 Studies on Equilibrium Conversion 242

7.2.3 Kinetics and Mechanism 243

BIBLIOGRAPHY 246

NOMENCLATURE 256

APPENDIX A CALIBRATION OF GAS CHROMATOGRAPH A-1

APPENDIX B COMPUTER PROGRAMS FOR MODEL DISCRIMINATION B-1

APPENDIX C CALIBRATION OF LIQUID SYRINGE FEEDER C-1

APPENDIX D INFRARED SPECTROSCOPIC CALIBRATION OF SO_2 D-1

APPENDIX E CALIBRATION OF SULFUR FEED SYSTEM E-1

APPENDIX F MASS TRANSFER LIMITATIONS F-1

APPENDIX G PUMP PERFORMANCE AND CHARACTERISTIC CHECK G-1

APPENDIX H SAMPLE DERIVATIONS FOR RATE EQUATIONS H-1

APPENDIX I DATA REDUCTION I-1

LIST OF FIGURES

Figure — Page

2-1 The Oxygen Lattice Arrangement of Aluminas 24

2-2 Peri's Model on arrangement of OH Groups of γ-Alumina 27

3-1 Adsorption Isotherm of γ-Alumina (Alon) 57

3-2 Pore Size Distribution for γ-Alumina (Alon) 58

4-1 Infrared Cell for Adsorption Studies 61

5-1 Schematic Diagram of Experimental Equipment for Kinetic Study 73

5-2 Infrared Cell-Reactor 81

5-3 Catalyst Wafer Holder in Infrared Cell-Reactor 87

5-4 Infrared Spectrum of Gaseous SO_2 97

5-5 Sketch of Recirculation Reactor Loop for Calculation of Reaction Conversion 112

6-1 Infrared Spectra of (a) Oxidized γ-Alumina (b) Reduced γ-Alumina (c) H_2S Adsorbed on Oxidized γ-Alumina (d) H_2S Adsorbed on Reduced γ-Alumina 117

6-2 Infrared Spectra of (a) CS_2 Adsorbed on Oxidized γ-Alumina (b) CS_2 Adsorbed on Reduced γ-Alumina (c) COS Adsorbed on Reduced γ-Alumina 121

6-3 Infrared Spectra of OH Groups of γ-Alumina Evacuated at (a) Room Temperature (b) 100°C (c) 200°C (d) 300°C (e) 400°C (f) 500°C 127

LIST OF FIGURES (continued)

Figure		Page
6-4	Infrared Spectra of Some Acidic and Basic Gases Adsorbed on γ-Alumina (a) Baseline (b) Ammonia (c) Pyridine (d) Hydrochloric Acid (e) Acetic Acid (f) Boron Trifluoride	129
6-5	Effect of Preadsorption of Some Acidic or Basic Gases Upon H_2S Adsorption on γ-Alumina	132
6-6	Adsorption of H_2S on γ-Alumina at Various Temperatures	144
6-7	Effect of Preadsorption of Some Acidic or Basic Gases Upon SO_2 Adsorption on γ-Alumina	147
6-8	Adsorption of SO_2 on γ-Alumina at Various Temperatures	152
6-9	Effect of Changing Acidity or Basicity of γ-Alumina Upon Its Catalytic Activity	156
6-10	Infrared Spectra of Sulfate Formation on γ-Alumina	161
6-11	Equipment Used for Reaction Equilibrium Study	167
6-12	Infrared Spectra for Reaction Equilibrium Study	170
6-13	Evaluation of Pore Diffusion	182
6-14	Examination of Stability of the Catalyst Activity	184
6-15	Infrared Spectra of γ-Alumina under Reaction Conditions	187
6-16	Displacement of H_2S and SO_2 by H_2O on γ-alumina	232
A-1	Apparatus for GC Calibration	A-2
A-2	GC Calibration Curve for H_2S	A-9

LIST OF FIGURES (continued)

Figure		Page
A-3	GC Calibration Curve for SO_2	A-11
C-1	Calibration Curve for Syringe Feeder at Low Speed Range	C-3
C-2	Calibration Curve for Syringe Feeder at High Speed Range	C-5
D-1	Apparatus for IR Calibration of SO_2	D-2
D-2	IR Calibration Curve for SO_2 at 1369 cm^{-1} using Beer's Law	D-5
D-3	IR Calibration Curve for SO_2 at 1357.8 cm^{-1} using Beer's Law	D-7
D-4	IR Calibration Curve for SO_2 at 1339 cm^{-1} using Beer's Law	D-9
D-5	IR Calibration Curve for SO_2 at 2500 cm^{-1} using Beer's Law	D-11
D-6	IR Calibration Curve for SO_2 at 2506 cm^{-1} using Beer's Law	D-13
D-7	IR Calibration Curve for SO_2 at 2485 cm^{-1} using Beer's Law	D-15
D-8	IR Calibration Curve for SO_2 at 1162 cm^{-1} using Beer's Law	D-17
D-9	IR Calibration Curve for SO_2 at 1132 cm^{-1} using Beer's Law	D-19

LIST OF FIGURES (continued)

Figure		Page
E-1	Apparatus for Calibration of Sulfur Feed System	E-2
E-2	Calibration Curve for Sulfur Feed System	E-4
G-1	Apparatus for testing Pump Performance	G-2
G-2	Performance Curves for Recirculation Pump	G-3

LIST OF TABLES

Table		Page
2-1	Peri's IR Spectrums of Hydroxyl Groups on Alumina	26
2-2	Infrared Bands of H_2S Adsorbed on γ-Alumina Observed by Deo et al.	34
2-3	H_2S Adsorption on γ-Alumina Measured by Volumetric Method	38
2-4	Infrared Bands of SO_2 Adsorbed on γ-Alumina Observed by Deo et al.	39
2-5	Infrared Bands of Some of the Inorganic Sulfites, Sulfates and Bisulfates	41
2-6	SO_2 Adsorption on γ-Alumina and Silica-Gel Measured by Volumetric Method	44
3-1	Reagents used for Kinetic Studies	51
3-2	Reagents used for Adsorption and Surface Reaction on γ-Alumina	52
3-3	Reagents used for Studying Sulfate Formation on γ-Alumina	54
3-4	Typical Properties of Alon (from Cabot)	56
3-5	Pore Size Distribution for the Alumina Catalyst	59
5-1	Operating Conditions of Gas Chromatograph	102
5-2	Frequencies and Pressure Range Employed for Quantitative Analysis of SO_2	109

LIST OF TABLES (continued)

Table | | Page
6-1 Infrared Band Frequencies for H_2S and D_2S Adsorbed on γ-Alumina at Room Temperature 125
6-2 Infrared Band Frequencies for SO_2 Adsorbed on γ-Alumina at Room Temperature 145
6-3 Behavior of Various Kinetic Parameters in Each Domain of Control 173
6-4 Reaction Conditions used for Examining Gas-Film Diffusion 176
6-5 Experimental Conditions used for Examining the Stability of the Catalyst Activity 185
6-6 Partial Pressure Range of the Components in Kinetic Runs 188
6-7 Kinetic Models Derived from Reaction Mechanism Involving Dissociation of Adsorbed H_2S into Hydroxyl Groups 202
6-8 Kinetic Models Derived from Reaction Mechanism Involving Adsorbed H_2S Reacting with Surface "Oxygen" and Hydroxyl Groups 205
6-9 Kinetic Models Derived from Reaction Mechanism Involving Dissociation of Adsorbed H_2S by the Sulfur on Catalyst Surface But Without the Participation of Hydroxyl Groups in Reaction 209

LIST OF TABLES (continued)

Table | | Page
6-10 Kinetic Models Derived from Reaction Mechanism Involving Dissociation of Adsorbed H_2S by the Sulfur on Catalyst Surface but with the Participation of Hydroxyl Groups in Reaction 212
6-11 Correlation of Some Published Kinetic Models with Rate Data at 298°C 219
6-12 Examination of the Sensitivity of the Numerator and Denominator Terms of McGregor's Model by Using the Isothermal Rate Data at 298°C 221
6-13 Correlation of McGregor's Model Against Rate Data at Various Isothermal Runs 223
6-14 Comparing the Correlation of Various Modified McGregor's Models Containing Different Powers of the Denominator Terms 226
6-15 Models Remaining from the Preliminary Steps of Discrimination 229
6-16 Correlation Variances of the Kinetic Models Remaining from the Preliminary Steps of Discrimination 233
6-17 Results Obtained from the Correlation of the Most Successful Model Against All Rate Data 235
A-1 Least Square Fitting of GC Calibration Data for H_2S A-8
A-2 Least Square Fitting of GC Calibration Data for SO_2 A-10

LIST OF TABLES (continued)

Table		Page
C-1	Least Square Fitting of Calibration Data for the Syringe Feeder at Low Speed Range	C-2
C-2	Least Square Fitting of Calibration Data for the Syringe Feeder at High Speed Range	C-4
D-1	Least Square Fitting of IR Calibration of SO_2 at 1369 cm^{-1}	D-4
D-2	Least Square Fitting of IR Calibration of SO_2 at 1357.8 cm^{-1}	D-6
D-3	Least Square Fitting of IR Calibration of SO_2 at 1339 cm^{-1}	D-8
D-4	Least Square Fitting of IR Calibration of SO_2 at 2500 cm^{-1}	D-10
D-5	Least Square Fitting of IR Calibration of SO_2 at 2506 cm^{-1}	D-12
D-6	Least Square Fitting of IR Calibration of SO_2 at 2485 cm^{-1}	D-14
D-7	Least Square Fitting of IR Calibration of SO_2 at 1162 cm^{-1}	D-16
D-8	Least Square Fitting of IR Calibration of SO_2 at 1132 cm^{-1}	D-18
E-1	Calibrated Results for Sulfur Feed System	E-5
F-1	Results for Theoretical Estimation of Mass Transfer Coefficient	F-1

LIST OF TABLES (continued)

Table | | Page
F-2 Results of McGregor's Theoretical Pore Diffusion Limitations Calculation F-4
F-3 Results of Theoretical Pore Diffusion Limitations Calculated by Hudgin's Method F-6
G-1 Performance Data for Recirculation Pump G-4
H-1 Correlation Results for Model DOH5' against Various Isothermal Rate Data H-6
H-2 Correlation Results for Model DOH6' against Various Isothermal Rate Data H-8
H-3 Correlation Results for Model DSOH6' against Various Isothermal Rate Data H-10
I-1 Summary of Raw Rate Data I-4
I-2 Summary of Kinetic Data I-12

CHAPTER I

INTRODUCTION

1.1 Background

The involvement of the University of Alberta in the investigation of the kinetics of the Claus reaction,

$$2H_2S + SO_2 \rightleftharpoons 2H_2O + \frac{3}{x} S_x \qquad (1.1)$$

started in 1964. The investigation originated as a result of extensive use of the Claus process to convert H_2S removed from sour natural gas into elemental sulfur.

In the first study at Alberta, Cormode [26] employed Porocel (bauxite) catalyst in a differential flow reactor and used wet chemical analysis to determine reaction conversions. McGregor [84] continued Cormode's work using the same catalyst with a stainless steel recycle differential reactor and gas chromatographic analysis. He carried out 80 experimented runs, covering four different reaction temperatures from 481 to 560 °K. Dalla Lana et al. [29] re-examined McGregor's kinetic data and by using the statistical model discrimination method developed by Singh [130], concluded that the following equation provided the best fit to the rate data

$$(-r_{SO_2}) = (1.56 \times 10^{-4}) \exp\left(\frac{-7440}{RT}\right) \frac{P_{H_2S}\, P_{SO_2}^{1/2}}{1 + 0.00423\, P_{H_2O}} \qquad (1.2)$$

By statistical inference, they concluded that water exerted a retarding effect on the reaction rate. Karren [64] continued McGregor's work with the same experimental equipment and catalyst. Using the kinetic data from his 50 experimental runs, he could not obtain a good correlation to McGregor's expirical models. Upon further examination, he found that the molten sulfur collected in his sulfur condenser catalyzed the reaction between H_2S and SO_2. Hence, he suggested that since further reaction could occur in the product stream before analysis therefore, McGregor's measured rate data might not be accurate. Chuang [22] confirmed Karren's observation by bubbling a mixture of H_2S and SO_2 into molten sulfur with resulting reaction conversion.

Other published work related to the reaction between H_2S and SO_2 and not performed at the University of Alberta are described in Chapter II. Much remains unknown about the nature of the reaction and the role played by the catalyst. The mechanism of the reaction remains uncertain and a more detailed study of the catalytic reaction of H_2S with SO_2 is certainty justified.

1.2 Objectives of This Work

Due to Karren [64] and Chuang's [22] observations that molten sulfur catalyzed the reaction between H_2S and SO_2, a specially designed reactor which allowed the reaction rate measurements to be obtained "in situ" during the reaction by infrared spectrophotometry, was employed in this work. A different γ-alumina catalyst was used because the wafer prepared from this material, Alon, provided better transparency to the infrared beam than those used by earlier researchers at the University of Alberta.

Infrared spectroscopy has proven useful in determining the structures of molecules. Its application to the study of surface chemistry has provided one of the direct means of deducing the nature of adsorbed species and indirectly, the involvement of certain sites on the catalyst. By obtaining evidence about the nature of reaction intermediates, a realistic mechanism may then be constructed. Many of the advantages offered by the use of various infrared spectroscopic techniques have been exploited in this work. The main objective of the present work is to obtain a better understanding of the mechanism of the Claus reaction. Consequently the number of kinetic models to be proposed and then tested could be reduced, thus avoiding much unnecessary work. The statistical model discrimination techniques developed by Singh [130] provides a basis for discrimination between selected kinetic models and then, ultimately, for the determination of the parameters for the best model(s).

CHAPTER II

LITERATURE SURVEY

2.1 Methods of Recovering Sulfur from H_2S-Containing Gases

According to some published surveys [2,107], about 60% of the total world sulfur production comes from H_2S-containing gases. Numerous industrial processes are available for recovering elemental sulfur from H_2S. The contemporary processes may be classified into two main categories, dry-bed and wet-bed processes. Many comprehensive reviews on this subject have been published [7,19,41, 47,54,60,107,108,132,143].

2.1.1 Wet-Bed Processes

Under this category, the processes involve bubbling a gas stream consisting mainly of H_2S/SO_2 or H_2S/air into a liquid medium containing either dissolved or suspended catalysts. By using different liquid media, catalysts or process parameters, various industrial processes have been developed. These may be further classified into "liquid media absorption - direct conversion" and "liquid media absorption - air oxidation" processes.

2.1.1.1 Liquid Media Absorption - Direct Conversion

As implied by the title, the gaseous H_2S and SO_2 are first absorbed in a liquid medium and then reacted to form sulfur and water. The more common processes in this group include:

1) Lacy-Keller process
2) ASR Sulfoxide process

3) Townsend process
4) IFP process
5) Bumines Citrate process

The nature of the liquid medium in process (1) was not revealed. An aqueous sulfoxide solution is used in process (2) and according to the inventor, sulfoxide is the catalyst. In contrast with process (2), the water in an aqueous solution of triethylene glycol acts as a catalyst in the Townsend process. In the IFP process, more than one liquid medium and soluble catalysts were used. The liquid media are mainly polyalkylene, alkylene glycol, glycol ether, glycol ester or glycol ether-ester. The soluble catalysts are either a Group IA or IIA carboxylate derived from acyclic monocarboxylic or polycarboxylic acids. The preferred salts are potassium benzoate, potassium salicylate, sodium nicotinate, potassium nicotinate, sodium cinnamate and potassium fursate. In the Bumines Citrate process, an intermediate citrate complex is formed between SO_2 and citrate solution. This complex then reacts with absorbed H_2S to form elemental sulfur and water.

2.1.1.2 Liquid Media Absorption - Air Oxidation

This group differs from the preceeding one in that air replaces SO_2 in the oxidation process. The processes in this group are:

1) Thylox process
2) Perox process
3) Ferrox process
4) Giammarco-Vetrocoke process
5) Holmes-Stretford process

These processes all involve a redox reaction between air and H_2S in an aqueous medium containing inorganic salt and organic additives. In the Thylox process, H_2S is absorbed as thioarsenate in an aqueous solution containing arsenic-activated potassium carbonate or sodium arsenate. The thioarsenate then reacts with air to produce sulfur and water. The Giammarco-Vetrocoke process is quite similar except potassium arsenite instead of arsenate is used. In the Perox process, aqueous ammonia in hydroquinone acts as a catalyst. The solution oxidation of H_2S in Holmes-Stretford process involves the absorption of H_2S as bisulfide in aqueous sodium carbonate solution and with vanadate and anthraquinone disulfonic acid as oxygen carriers (The Japanese Takahox process used napthaquinone instead of anthraquinone). In the Ferrox process, a suspension of iron oxide in aqueous dilute solution of sodium carbonate is used.

The main disadvantages of the wet-bed processes are that the reaction does not proceed sufficiently rapidly and completely and sulfur is formed in a finely dispersed manner. Separation of this sulfur from the liquid medium is difficult and usually incomplete. The advantage is that the reaction can be carried out at a relatively low temperature. Equipment cost is also generally lower than that of the dry-bed processes.

2.1.2 Dry-Bed Processes

In all dry-bed processes to be discussed here, solid catalysts are used. In the "dry-bed adsorption catalytic" process, either low concentration of H_2S or SO_2 is removed from the tail gas by adsorption and then the adsorbate is subsequently reacted with the other reactant (SO_2 or H_2S). These processes are mostly used for cleanup of the tail gas rather than as a means of producing sulfur. The "dry-bed conversion" processes are those involving the simultaneous introduction of the H_2S and SO_2 over a solid catalyst for reaction.

2.1.2.1 Dry-Bed Adsorption - Catalytic Conversion

In the Westvaco or Shell process, activated carbon or molecular sieves are used to adsorb SO_2 and then the adsorbents catalyze the reaction between the adsorbate and H_2S. In the Haines process, zeolite is the adsorbent-catalyst while H_2S is adsorbate-reactant.

2.1.2.2 Dry-Bed Catalytic Conversion

Catalysts used in the processes of this group are mostly activated carbon, metal sulfide (Pilgrim), or alumina-based types (zeolite, bauxite, etc.). The names of the various processes used in this group are either too numerous or too ambiguous to merit further clarification. In some cases, a slight change in process parameters or equipment has generated another name. In most cases, the common name is still "modified Claus process" although names like Sulfreen process or Amoco CBA process are used to describe the same process but carried out under lower reactor temperature. Generally, reaction between gaseous H_2S and SO_2 takes place over the solid catalyst to form elemental sulfur and water. To ensure as close to 100% conversion as possible, the unconverted reactants are fed into further staged reactors after the removal of the sulfur by condensation.

The Dry-Bed Catalytic Conversion process is by far the most commonly applied method in North America for recovery of elemental sulfur from H_2S. Of the various catalysts, the one most commonly used is either bauxite or activated alumina. In the six years, 1971 to 1976, numerous "modified" catalysts have been made by impregnation of various inorganic salts into alumina, and claims have been made that the "new" catalysts are catalytically more active than activated alumina [19].

2.2 Review of Heterogeneous Catalytic Reactions of H_2S and SO_2

2.2.1 General Review

In 1887, the Chance brothers [18] commercialized a reaction called the Claus reaction which involved the reaction between H_2S and air over a bed of powdered catalyst at a temperature around 260°C. This reaction was named Claus reaction because of a patent issued to C. F. Claus in 1883 for his invention of a process to recover sulfur from calcium sulfides [25]. Claus treated CaS with carbonic acid to produce H_2S which then reacted with air to produce sulfur.

After the commercial application by the Chance brothers, it was generally discovered that the reactor temperature of this original Claus process was extremely difficult to control [108]. A significant advance in the art was made by I. G. Farbenindustrie in Germany in 1937 [3]. A process involving the burning of 1/3 of the H_2S with air to SO_2 which then reacts with the remaining 2/3 of the

H_2S was invented. A patent on this process was issued to Baehr and Mengdehl in 1937 [3] and to Barkholt in 1939 [5]. Hence in the reactor, the following reaction took place over a solid catalyst.

$$2H_2S + SO_2 = 2H_2O + \frac{3}{x} S_x \qquad (2.1)$$

Since then, studies of the H_2S/SO_2 reaction have gradually been gaining momentum. In fact, Reaction (2.1) has sometimes been (incorrectly) called the Claus reaction or the modified Claus reaction. The actual Claus reaction has been discussed in the previous page.

Pilgrim and Ingraham [108] provided a detailed description of the history from the Claus invention to the studies on H_2S/SO_2 reaction in 1970. Chandler [19] added to the literature survey of these subjects to cover the period from 1970 to 1975. Most of the published works covered by these reviewers dealt with the practical industrial problems. Little was known about the mechanism of the reaction and the interactions between the adsorbates and the solid catalysts. Among some publications on these topics, disagreement is evident. It is the intention in the present work to explore and hopefully clarify some of these uncertainties. Particular attention was given to the understanding of the kinetics and mechanism of the reaction. The examination of surface reaction occurring on the catalyst surface was also attempted with the hope that this might help reveal some portion of the reaction mechanism. A literature survey on the studies of the kinetics and mechanism of H_2S/SO_2 reaction will be described next.

2.2.2 Mechanistic Studies

The literature appears to be generally scanty with regard to mechanistic studies on the reaction between H_2S and SO_2, especially with γ-alumina as the catalyst. A few proposed mechanisms have been published, but none of the authors derived rate equations from the proposed mechanisms.

Murthy and Rao [91] studied the reaction between H_2S and SO_2 over cobalt thiomolybdate, cobalt sulfide, silver sulfide and molybdenum sulfide and proposed the following mechanism.

$$\left.\begin{aligned} H_2S + SO_2 &= H_2S_2O_2 \\ H_2S_2O_2 &= H_2SO + SO \\ H_2SO &= H_2O + S \\ SO + H_2S &= H_2O + 2S \end{aligned}\right\} \qquad (2.2)$$

The authors did not explain whether these reaction steps were reversible or not. They also did not specify whether this mechanism was applicable to all or only a particular one of the catalysts used. During their experimental runs, sulfur was permitted to condense on the catalyst surface. They considered the first step of their proposed mechanism to be rate-controlling but did not verify this assumption.

Hammars [55] suggested the following mechanism, which involves the dissociation of H_2S into H^+ and SH^- for the reaction between H_2S and SO_2 over cobalt-molybdenum-alumina,

$$\left.\begin{aligned} H_2S &\rightleftarrows H^+ + SH^- \\ H^+ + SH^- + SO_2 &\rightleftarrows H\,S \cdot SO \cdot OH \end{aligned}\right\} \qquad (2.3)$$

The reaction may then proceed by one of the following routes:

(i) 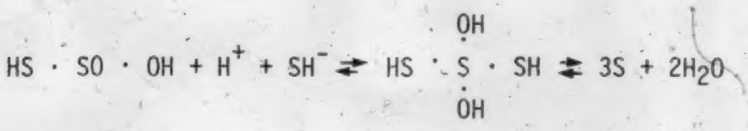 (2.4)

$$HS \cdot SO \cdot OH + H^{+} + SH^{-} \rightleftharpoons HS \cdot \underset{OH}{\overset{OH}{S}} \cdot SH \rightleftharpoons 3S + 2H_2O \tag{2.4}$$

or

(ii) 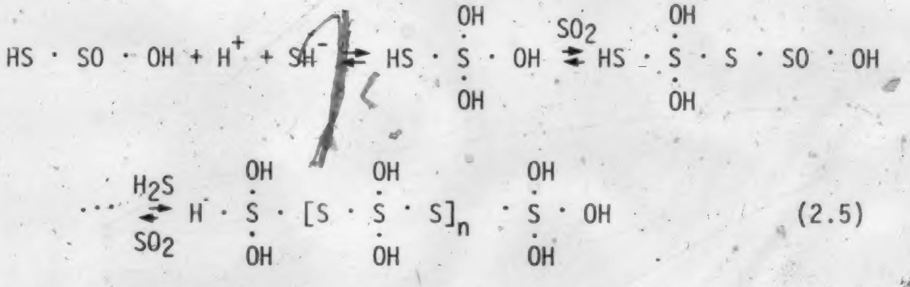 (2.5)

$$HS \cdot SO \cdot OH + H^{+} + SH^{-} \rightleftharpoons HS \cdot \underset{OH}{\overset{OH}{S}} \cdot OH \overset{SO_2}{\rightleftharpoons} HS \cdot \underset{OH}{\overset{OH}{S}} \cdot S \cdot SO \cdot OH$$

$$\cdots \underset{SO_2}{\overset{H_2S}{\rightleftharpoons}} H \cdot \underset{OH}{\overset{OH}{S}} \cdot [S \cdot \underset{OH}{\overset{OH}{S}} \cdot S]_n \cdot \underset{OH}{\overset{OH}{S}} \cdot OH \tag{2.5}$$

Water is then split off from each of the intermediates in route (ii) at different rates and the sulfur formed will be distributed into various molecular species (S_2, S_6, S_8, etc.) according to some probability function. The author did not explain the form of probability function nor did he suggest whether the function is dependent on temperature or other experimental parameters. His mechanism suggests that a distribution of polymeric hydro-sulfur species with various chain length exist on the catalyst surface during the reaction.

Several earlier researchers [32, 96] believed polythionic acid to be formed as an intermediate in the reaction between H_2S and SO_2, particularly when the reaction occurs in liquid water. They did not describe in detail the formation of polythionic acid nor the reaction steps. Zil'berman [150] proposed the following mechanism in which sulfurous acid is first produced from SO_2 and H_2O and then this further reacts with H_2S to give dihydrogen sulfoxide, which eventually decomposes to produce elemental sulfur and water.

$$\begin{aligned} H_2O + SO_2 &= H_2SO_3 \\ H_2SO_3 + 2H_2S &= 3HSOH \\ 3HSOH &= 3H_2O + 3S \end{aligned} \qquad (2.6)$$

These mechanisms, which involve the formation of polythionic acid or sulfurous acid, are based on the reaction in aqueous solution and therefore should not necessarily be considered to be applicable to systems involving solid catalysts.

George [43,44] investigated the reaction between H_2S and SO_2 on a number of solid catalysts, namely, Chromosorb-A, cobalt-molybdate on γ-Al_2O_3, porous alumina, activated alumina, Porasil and bauxite. He proposed the following ionic mechanism:

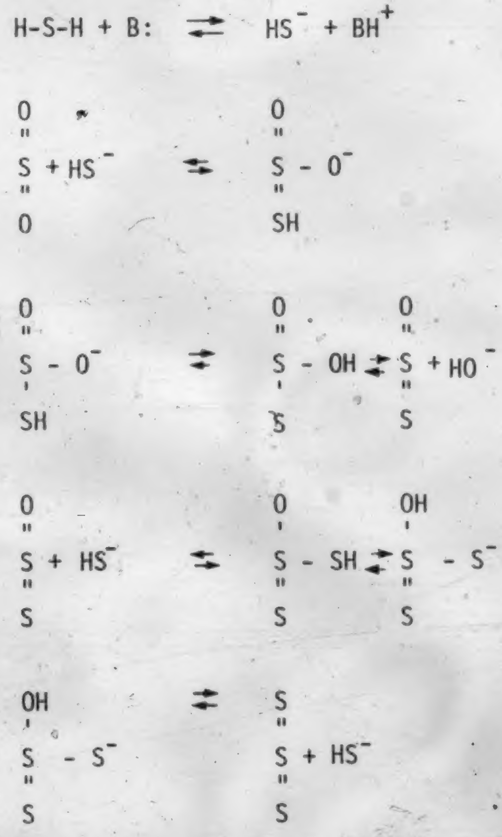

$$\begin{aligned}
&H\text{-}S\text{-}H + B: \rightleftharpoons HS^- + BH^+ \\
&\overset{\overset{O}{\|}}{\underset{\underset{O}{\|}}{S}} + HS^- \rightleftharpoons \overset{\overset{O}{\|}}{\underset{\underset{SH}{\|}}{S}} - O^- \\
&\overset{\overset{O}{\|}}{\underset{\underset{SH}{|}}{S}} - O^- \rightleftharpoons \overset{\overset{O}{\|}}{\underset{\underset{S}{|}}{S}} - OH \rightleftharpoons \overset{\overset{O}{\|}}{\underset{\underset{S}{\|}}{S}} + HO^- \\
&\overset{\overset{O}{\|}}{\underset{\underset{S}{\|}}{S}} + HS^- \rightleftharpoons \overset{\overset{O}{|}}{\underset{\underset{S}{\|}}{S}} - SH \rightleftharpoons \overset{\overset{OH}{|}}{\underset{\underset{S}{\|}}{S}} - S^- \\
&\overset{\overset{OH}{|}}{\underset{\underset{S}{\|}}{S}} - S^- \rightleftharpoons \overset{\overset{S}{\|}}{\underset{\underset{S}{\|}}{S}} + HS^-
\end{aligned} \qquad (2.7)$$

The symbol B: indicates some type of basic site on the catalyst. According to this author, basic sites were considered to be the only important sites for the reaction. The above proposed mechanism is not complete in at least two aspects. First it is stoichiometrically incomplete and second, no water is formed in the steps shown. If the reaction proceeds with this mechanism, the catalyst surface will become "saturated" with HO^- and BH^+ groups. The author did not include the step where water is formed from HO^- and BH^+. According to the author, H_2S first reacts with the basic sites (probably oxide ion sites) and dissociated into HS^- and BH^+. Gaseous SO_2 then reacts witn HS^- to continue the other reaction steps. He did not specify whether H_2S had to be adsorbed in order to react with the basic sites He also did not explain the form of HS^- and other intermediates. Finally, the proposed mechanism suggested that all of the sulfur speices produced from the catalyst surface originate in the S_3 form. If sulfur may exist in more than one form (e.g. S_2, S_6, S_8, etc.), these other species must then be produced from S_3 presumably in the vapor phase.

Other published works which briefly mentioned the reaction mechanism between H_2S and SO_2 include those by McGregor [84] and Deo et al. [34]. Both suggested that the reaction might involve hydrogen-bonding between both reactants and the surface hydroxyl groups of alumina.

From the available published work, especially with γ-alumina, and the great difference in the published proposed mechanisms, much still remains unknown regarding the mechanism of reaction between H_2S and SO_2. Little attempt has been devoted to develop rate equations from the proposed mechanisms. Many used empirical equations to fit the measured rate data.

2.2.3 Kinetic Studies

Although the reaction between H_2S and SO_2 has been applied industrially for about a hundred years, the kinetic models for this reaction are still far from conclusive. Little or no agreement exists between any two published kinetic studies. Such a situation may be attributed to the uncertainties in this field and also perhaps to the fact that the reaction is more complicated than may be expressed by the simple stoichiometric equation.

According to many researchers [21,43,44,64,84,124], the reaction between H_2S and SO_2 does not proceed homogeneously unless heated to a very high temperature (above 600°C) where decomposition accurs. The effect of condensed water on the reaction has also been studied [16,64,72,84,118,126,142] and all published results indicate that the condensed water catalyzes the reaction. Karren [64], Chuang [22] and Butler [16] observed that liquid sulfur also catalyzes the reaction. Murthy and Rao [67] found that water exhibited an auto-catalytic effect on silver sulfide catalyst. Landau and Molyneux [72] detected an increase in catalytic activity of bauxite catalyst with decrease in particle size and concluded that the reaction between H_2S and SO_2 was a diffusion-controlled process. However, during their experimental runs, the effect of reactor space velocity was not related to the catalyst particle size and therefore their result cannot conclusively indicate whether it was film or pore diffusion which was controlling the reaction rate.

The earliest empirical rate equation on the reaction between H_2S and SO_2 was published in 1927 by Taylor and Wesley [138]. They studied the kinetics over Pyrex glass at temperatures ranging from 370°C to 730°C in an integral packed bed reactor and obtained the following rate equation:

$$- dx/dt = kP_{SO_2} P_{H_2S}^{1.5} \qquad (2.8)$$

Gamson and Elkins [42] conducted kinetic measurements in an integral bed reactor over Porocel catalyst at three temperatures (230, 260 and 300°C) and four space velocities (240, 480, 960 and 1920 scf-gas/cu.ft.-catalyst h). Conversions ranging from 93% to 98% were observed. Rate data may be estimated from their plot of fractional conversion versus space velocity, but no rate equation was deduced from this kinetic data. These authors cautioned that their kinetic data was inconsistent with their thermodynamic analysis. The measured conversions were higher than thermodynamically possible under the same reaction conditions. This discrepancy may be due to the fact that they allowed both water and sulfur to condense before absorbing the unreacted H_2S and SO_2 in caustic solution for analysis. Further reaction could occur during analysis and the equilibrium conversion under analytical condition is higher than that under experimental condition. On the other hand, the thermodynamic data might be in error. The wet chemical analysis method was used by Taylor et al. [138] and by Gamson and Elkins [42] in their kinetic measurement.

Cormode [26] measured kinetic rate data of the reaction between H_2S and SO_2 using a recycle flow reactor with a commercial bauxite catalyst. An adsorption train and wet chemical analytical technique was adopted. No rate equation was deduced from the kinetic data. McGregor [84] also employed commercial bauxite catalyst (Porocel) and used a recycle differential flow reactor for his kinetic studies. A total of 80 experimental runs were carried out in the temperature range of 208-287°C. The ranges of H_2S, SO_2, H_2O and sulfur partial pressures were 11.3-63.6, 9.6-45.8, 1.2-121.0 and 0.2-9.0 mm Hg, respectively. Using a catalyst particle size of 28/35 mesh, he suggested that the reaction rate was proportional to the external and not total surface area. He approximated the external surface area from the particle mesh size by assuming that all the catalyst particles were cubical in shape. He concluded that neither pore diffusion nor film diffusion were important in the reaction, presumably all pores were filled up by condensed elemental sulfur. Both McGregor [84] and Karren [64] examined the amount of sulfur retained by the Porocel catalyst which had been in the reactor for a number of runs. Prior to cooling down the reactor for removal of the catalyst, the reactor was purged for two hours with pure nitrogen. Their analysis indicated that about 2.0% by weight of sulfur was retained by the catalyst. McGregor [84] observed that water vapor had a retarding effect at high concentration and an accelerating effect at low concentration on the forward rate of the reaction. The empirical rate expression deduced by Dalla Lana et al. [29] using a statistical-modelling method [130] and McGregor's kinetic data was

$$-r_{H_2S} = 1.212 \exp(-7440/RT)\,(P_{H_2S}\,P^{1.5}_{SO_2})/(1+ 0.00423P_{H_2O}) \tag{2.9}$$

This expression reflects the retarding effect of water vapor on the reaction rate but not the accelerating effect as observed by McGregor at low water vapor pressure. The powers of H_2S and SO_2 shown in the above rate equation were round-off values. The actual powers deduced from the statistical modelling by Dalla Lana et al. were 0.828 ± 0.0952 and 0.467 ± 0.111 for H_2S and SO_2 respectively. The figures after the ± sign show the 95% confidence limits which are 1.212 ± 0.694, 0.00423 ± 0.00246 and 7440 ± 655 for the other parameters in the rate equation. The relatively poor 95% confidence limit for the parameter of water term implies the relatively high uncertainty in the deduced value of this parameter.

George [43,44] examined the effect of impregnating a number of catalysts (Chromosorb-A, cobalt-molybdate on γ-alumina, porous alumina, activated alumina, Porasil, bauxite) with acid or base on the catalytic activities of reaction between H_2S and SO_2. The method of impregnation involved soaking the catalyst in the acid (HCl, H_2SO_4, or H_3PO_4) or base (NaOH, KOH or LiOH) solution and then decanting and drying at 100°C. The author did not specify the concentration of acid or base solutions used. His results showed that acid impregnation did not affect the catalytic activities of the catalysts studied. However, with about 4.0 weight per cent NaOH impregnation, the catalytic activities of Chromosorb-A and Porasil were improved by factors of 100 and 2, respectively, while that of other catalysts increased by at least 20%. With the hundredfold improvement, the catalytic activity of Chromosorb-A was comparable to that of a commercial Claus catalyst (alumina). The activities of all catalysts studied increased with the loading of base impregnation up to 4.5 weight per cent and then dropped off as more base was loaded. Among the various types of bases loaded, the activity of Chromosorb-A improved in the order of $K^+ < Na^+ < Li^+$. The surface area of the catalysts was not affected by base impregnation at low loading but it decreased with higher loading (i.e. greater than 5.0 weight per cent base) but no explanation was given for these results. George did not elaborate whether the catalysts were modified physically or chemically by the impregnation with bases. He concluded from these results that basic sites (presumably he meant oxide anions) were important for the reaction. If this is true, the impregnation of the catalysts with acids should change the catalytic activities. However, the author did not explain why the importance of basic sites could not account for the observation that acid impregnation did not affect the catalytic activities at all. An initial rate was obtained by fitting his three measured data points into the expression proposed by Mezaki and Kittrell [86].

$$X = A_1 \tanh[A_2(\frac{W}{F})] \tag{2.10}$$

An initial rate expression in the form of

$$-r_{H_2S} = kP_{H_2S} \tag{2.11}$$

was obtained for Chromosorb-A over three temperatures (434, 400 and 350°C). The kinetic order with respect to SO_2 was found to be zero and the activation energy was 25 Kcal/mole. For the base loaded Chromosorb-A (both 3.9 and 5.0 weight per cent base) the kinetic orders of H_2S and SO_2 were 0.7 and 0.2 respectively and the activation energy was 10 Kcal/mole. The rate expression by using commercial cobalt-molybdate on γ-alumina was found to be

$$-r_{H_2S} = \frac{kP_{H_2S}}{(1 + 0.1\ P_{H_2O})} \tag{2.12}$$

The author found that film diffusion was the rate determining step for the based loaded Chromosorb-A. He also noted sulfidation of catalyst from the change in colour of the catalyst from the original deep blue to black. This probably was due to the sulfidation of molybdenum rather than alumina.

Kerr et al. [65] studied the kinetics of H_2S/SO_2 reaction over bauxite and activated alumina catalysts in an integral bed reactor of 1-3" inside diameter and about one foot deep. The bauxite catalyst was 2-4 mesh in size while that of activated alumina was 4-6 mesh. The total volume of the catalyst used in the reactor varied from 0.2-1.2 litres. Three reaction temperatures (232, 269 and 297°C) were used. By changing the catalyst bed depth with a fixed gas flow rate, five data points were collected under each temperature. The analytical method used involved drying the product stream over P_2O_5 and then introducing it into a gas chromatograph. For bauxite, the data covered 30-70% H_2S conversion range while for activated alumina, it was 60-70%.

The authors found that the catalytic activity of bauxite catalyst was reduced by 40% after passing 1/2% O_2 for one hour over their used bauxite catalyst. In addition, they also noticed that a minimum of 4 hours of continuous operation was required before a steady-reaction rate was reached. They claimed that the catalyst could absorb (they did not use the word adsorb) 15 per cent of its weight of sulfur and therefore such a long period of time was required to reach steady-state operation. This start up behaviour was very different from that observed by Karren [64], McGregor [84] and George [43].

When developing a kinetic model for the reaction, the authors started with a general power law model without denominator terms.

$$\frac{d[H_2S]}{dt} = -k_F[H_2S]^\alpha[SO_2]^\beta + k_B[H_2O]^\gamma[S_n]^\delta \qquad (2.13)$$

They were interested only in determining the simplest values to the power coefficients. They stated that since neither the zeroeth nor first order kinetics agreed with the experimental data to a sufficient degree of accuracy to warrant their use, the following second order model was adopted

$$\frac{d[H_2S]}{dt} = -k_F[H_2S][SO_2] + k_B[H_2O][S_n] \qquad (2.14)$$

From this, they developed the following final model.

$$\frac{d[H_2S]}{dt} = k \exp \frac{-Ea}{RT} \left(-[H_2S][SO_2] + \frac{[H_2S]e[SO_2]e}{[H_2O]e[S_n]e} [H_2O][S_n]\right)$$

The above equation does not contain stoichiometric coefficients on the equilibrium terms and is thermodynamically inconsistent. The authors did not elaborate on how the values of $[S_n]$ as well as the values in equilibrium terms were determined for model correlation. After applying their 15 data points (five for each temperature) to the empirical model (2.15), the following was obtained.

$$\frac{d[H_2S]}{dx} = \frac{24148}{Va} \exp\left(\frac{-2526}{T}\right) \left\{-[H_2S][SO_2] + \frac{[H_2S]e[SO_2]e}{[H_2O]e[S_n]e} [H_2O][S_n]\right\}$$

The activation energy of 5.02Kcal/gmol H_2S was less than that obtained by McGregor (7.59Kcal/gmol H_2S). Kerr et al.[65] did not discuss the reaction mechanism at all.

2.3 Surface Properties of γ-Alumina

Because alumina has been widely employed as a catalyst or as a catalyst support, a considerable amount of research has been devoted to elucidating the nature of its catalytic properties. It is generally believed [75,109,110] that the catalytic properties are related to the surface properties of alumina. For example, the less porous alumina, called alpha alumina or corundum, has lower surface area and different crystalline structure than other aluminas and is the least catalytically active type of alumina. The crystalline structures varied not only by the pattern of arrangement of oxide ions but also by that of the aluminum ions. Due to the variations in structures, the manner by which the aluminum ions and oxide ions are exposed on the catalyst surface also differs. As a result, various "active sites" for adsorption and catalytic reaction are formed. Hence, to understand the catalytic properties of γ-alumina, it is advantageous to understand first its surface properties and a review on this topic follows.

2.3.1 The Crystalline Structure of γ-Alumina

The various types of alumina differ in crystallographic structures [75,127]. They are often prepared by precipitation of a hydrated alumina formed by mixing solutions of alkali and salts of an aluminum compound (sulfate, nitrate, acetate or occasionally chloride). The precipitate formed is gelatinous with a diffuse x-ray diagram. Subsequent heat-aging may produce boehmite, bayerite or gibbsite, depending on the treating environment. Calcination leads to elimination of water and for various temperatures of calcination, a number of intermediate structures are observed.

The thermal process can be interpreted as follows:

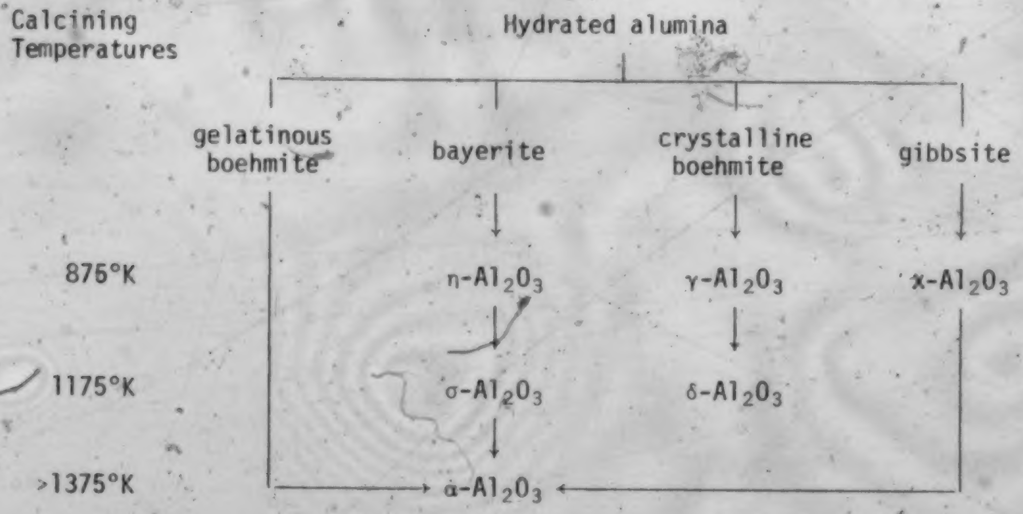

Calcining Temperatures
Hydrated alumina
gelatinous boehmite
bayerite
crystalline boehmite
gibbsite
876°K
η-Al$_2$O$_3$
γ-Al$_2$O$_3$
χ-Al$_2$O$_3$
1175°K
σ-Al$_2$O$_3$
δ-Al$_2$O$_3$
>1375°K
α-Al$_2$O$_3$

The transition aluminas still contain water, presumably entirely as hydroxyl groups on surfaces, the overall composition being $Al_2O_3 \cdot nH_2O$, with $0 < n \leq 0.6$ [127]. Lippens and de Boer [74] found by single-crystal electron diffraction studies that the oxygen lattice of α-alumina should be well-ordered. The oxygen lattice has a close-packed cubic unit cell which is stacked in layers of 1-2-3-1-2-3 unlike that of γ-Al_2O_3 which is stacked in the sequence of 1-2-1-2 as shown in Figure 2-1. In the cubic close packing of anions, there are one octahedral and two tetrahedral vacancies per anion, in which the small aluminum cation can be located. The unit cell of the crystal consists of 32 oxide ions with 21 1/3 aluminum cations arranged at random in the 16 octahedral and 8 tetrahedral positions of the spinel structure.

Since the oxygen anions are well ordered, the disorder in γ-alumina is determined by the distribution of aluminum cations. In spinels like $MgAl_2O_4$ the aluminum cations occur in octahedral sites and the magnesium cations in tetrahedral sites. Because of the similarity between the structures of the aluminas and the spinels, the former are often referred to as pseudo-spinels. Introducing a notation in which tetrahedral and octahedral Al are given as $[Al]_t$ and $[Al]_0$, the aluminas can be represented as $[Al_{2/3}]_t[Al_2]_0\ O_4$ [127]. The differences between η-, χ-, and γ-Al_2O_3 are probably related to their different ratios of $[Al]_t$:$[Al]_0$ as well as to the different distributions of $[Al]_t$ over the available tetrahedral sites and $[Al]_0$ over the octahedral sites. Saalfeld and Mehrotra [121] applied Fourier synthesis of the electron diffraction patterns to determine the cation distribution and concluded that the octrahedral aluminum

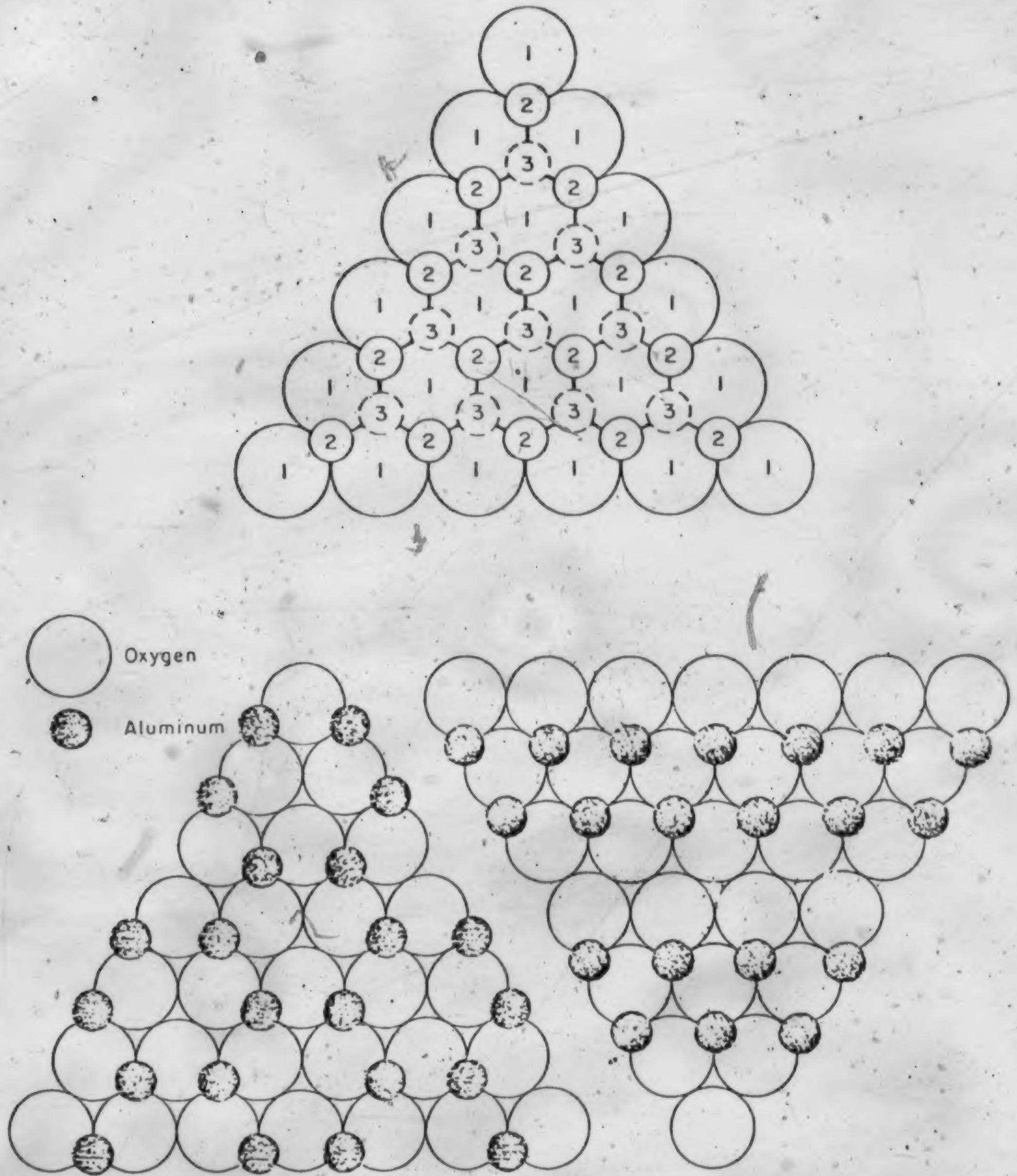
1
2
3
Oxygen
Aluminum

Figure 2-1. The Oxygen Lattice Arrangement of Alumina.

sublattice was fully occupied and that the necessary vacant sites were randomly distributed over the tetrahedral interstices. Lippens [75] provided the most detailed discussion of the crystallographic structures of aluminas.

2.3.2 The Surface of γ-Alumina

The γ-aluminas occur in the form of lamellae. From the work of Moliere et al. [90], the γ-alumina surface terminates in oxygen anions because they are more easily polarizable. Accordingly, the outermost aluminum ions lie below the oxide plane. Lippens [75] concludes from his x-ray diffractional analysis that the [110] plane forms the majority of the γ-alumina lamallae. Others [31,32] believe that the [111] plane is more energetically favored and that a greater density of oxide ions may be packed on this face.

A considerable amount of water may be adsorbed by γ-alumina. Kipling [66] evacuated hydrated γ-alumina at 25°C for 100 h and measured 13 molecules of water per 100 $\mathring{A}^2$ of surface. After drying at 120°C, 8.25 molecules per 100 $\mathring{A}^2$ were retained [32]. Initially, the water molecules are physically bonded in multilayers on the surface. As dehydration proceeds, these molecules desorb until the surface is covered with hydroxyl groups. Upon heating at higher temperature additional water can be eliminated by recombination of two adjacent surface hydroxyl groups [10,76].

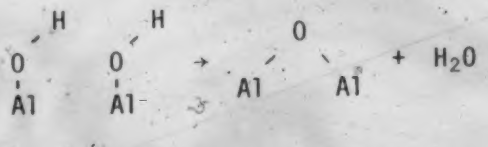

$$\underset{Al}{\overset{H}{O}} \quad \underset{Al}{\overset{H}{O}} \rightarrow Al - O - Al + H_2O \qquad (2.17)$$

This process creates aluminum and oxide ion sites. These aluminum ions are regarded by Peri and others [68,100,103,104] as Lewis-acid centers capable of adsorbing organic bases. Thus, for ammonia (pK_B=5) [109] pyridine (pK_B=9) [100], the adsorption process can be depicted as

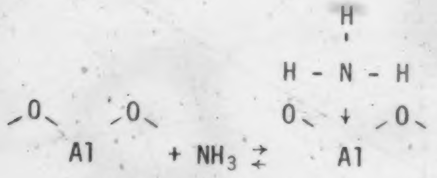

$$\overset{\diagup O \diagdown \quad \diagup O \diagdown}{Al} + NH_3 \rightleftarrows \overset{\overset{\overset{H}{|}}{H-N-H}}{\overset{O \diagdown \downarrow \diagup O}{Al}} \qquad (2.18)$$

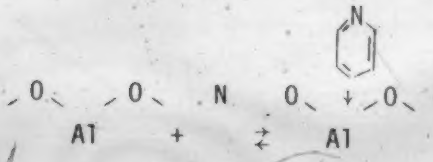

(2.19)

A model of the alumina surface obtained by Peri's computer simulation method [105] from the dehydration of a fully hydrated surface on [100] crystal planes is shown in Figure 2-2. Five different types of hydroxyl groups were predicted from the computer model and their corresponding infrared vibrational frequencies are shown in Table 2-1.

Table 2-1

Peri's IR Spectrums of Hydroxyl Groups on Alumina*

Band	Wave Number, cm^{-1}	No. of Nearest Oxide Neighbors
A	3800	4
B	3780	3
C	3744	2
D	3733	1
E	3700	0

*with reference to Figure 2-2.

The dehydration mechanism and the structure of alumina surface can be visualized from Figure 2-2. The validity of Peri's assumptions [105]

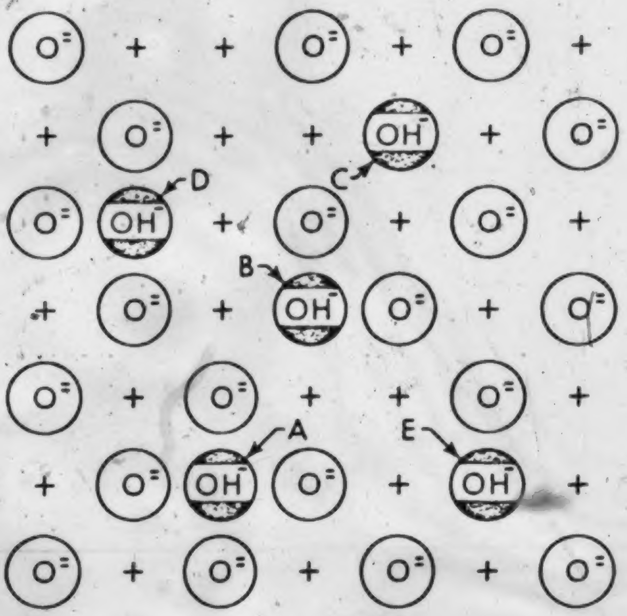

+ DENOTES Al^{3+} IN LOWER LAYER

Figure 2-2. Peri's Model on Arrangement of OH Groups of γ-Alumina.

that a spinel type alumina exposes only [100] planes on the surface at 600°C have been subjected to criticism by Lippens [74,75]. Peri [104] observed a new hydroxyl group generated by NH_3 adsorption on γ-alumina using infrared spectroscopy. The chemisorption reaction was interpreted as

$$NH_3 + O^{=} \rightarrow NH_2^{-} + OH^{-} \qquad (2.20)$$

He proposed that the above reaction was a completely ionic process involving reaction with an adjacent oxide ion. Other workers [77] explained this as simultaneous bond breaking and formation which may be shown as

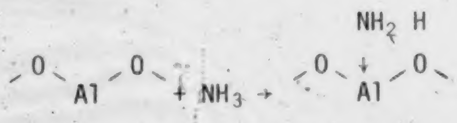

(2.21)

The hydroxyl groups on the surface of γ-alumina were reported to be very weak acidic Bronsted-acid centers, owing to the proton on the OH. These centers can react with ammonia to form ammonium ions [104] but not acidic enough to react with pyridine to form pyridinium ions [100]. From the infrared evidence of Peri [104], the hydroxyl groups are mobile on the surface of γ-alumina.

The Bronsted and Lewis acid sites are believed to be interchangeable [56,135]. The adsorption of water on the γ-alumina surface is interpreted by Tamele [135] to involve completion of the octet of alumina.

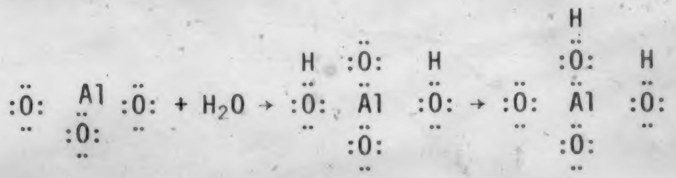

$$\begin{matrix} :\ddot{O}: & Al & :\ddot{O}: \\ & :\ddot{O}: & \end{matrix} + H_2O \rightarrow \begin{matrix} H & :\ddot{O}: & H \\ :\ddot{O}: & Al & :\ddot{O}: \\ & :\ddot{O}: & \end{matrix} \rightarrow \begin{matrix} & H & \\ & :\ddot{O}: & H \\ :\ddot{O}: & Al & :\ddot{O}: \\ & :\ddot{O}: & \end{matrix} \qquad (2.22)$$

Hence, a new hydroxyl group is created at the expense of one Lewis acid site. The reverse occurs during the dehydration process.

Comparatively little work has been done on investigating the basicity of alumina. It is generally believed [37,62,114,128] that the basicity arises from the oxide ions. Yamadaya et al. [149] have shown by means of benzoic acid titration that basic sites begin to appear on alumina when water sufficient to cover all the acid sites has been adsorbed. Basicities as high as 0.4 mmol/g have been recorded. Schwab and Kral [128] have found that 60 to 80% of the BET surface area of alumina can be covered by boron trifluoride (a Lewis acid) at 30 mm of Hg and 400°C. Since ammonia covers only from 5 to 8% for the same sample of alumina, the basicity of alumina is greater than its acidity. Pines et al. [110] have carried out a series of interesting stereochemical studies which strongly suggest that alumina contains intrinsic basic sites as well as acid sites, and acts as an acid-base bifunctional catalyst. Figote and Parera [37] visualize the adsorption of phenol on the surface of alumina in terms of occupation of adjacent pair of acid-base sites as

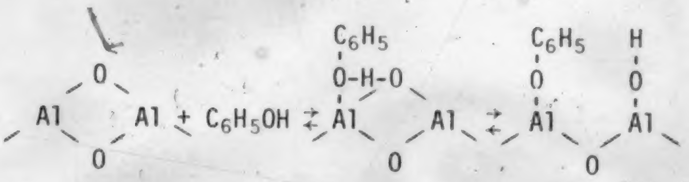

(2.23)

Attempts to correlate the acid-base properties of alumina catalyst with catalytic activities have been carried out by many researchers. Rosolovskaja et al. [116] found that the activity of alumina in the isomerization of alkylbenzene to propenylbenzene at 300°C depends on the acidity but not on the physical structure of the catalyst. Hirota et al. [58] have shown that the rate of polymerization of olefin is directly related to the acidity of alumina. For the alumina having strong acid sites, the rate drops markedly as reaction proceeds, presumably due to the poisoning of strong acid sites during reaction. However, if such strong acid sites are poisoned first with silver then the reduction in rate was not as marked. Brouwer [13,14] noted the rate of perylene oxidation and cumene cracking is greated affected by the acidity of γ-alumina catalyst.

Krylov and Fokina [70,71] obtained good correlation between the basic strength of various solids as measured by the phenol vapour adsorption method and the catalytic activity for the dehydrogenation of isopropyl alcohol. The dehydrochlorination of 1,2-dichloro-2,2-diphenylethane [1] and of 2,3-dichlorobutane [93] are promoted by the basicity of γ-alumina. Krylov and Fokina [71] investigated the reaction of acrolein with ethanol over various metal oxides and noted that the catalytic activity increases with the electronegativities of the catalysts, an indication that the reaction proceeds according to a base-type mechanism.

Since both acidic and basic sites occur on γ-alumina surface many researchers [88,89,92,96,110,111,128,137] believe that although one type of site may play a more important role for one reaction, it is not necessarily true that the other type of site does not participate in the catalytic process. They suggest that γ-alumina is more probably a bifunctional acid-base catalyst. Ohki et al.[96] studied the trans-isomerization of crotononitrite reaction over catalysts such as Al_2O_3, potassium 2-naphthol-3-carboxylate, sodium salicylate, etc., which contain both acidic and basic groups as well as NaOH, Na_2CO_3 and potassium biphthalate which have only either an acidic or basic property and found that only the acid-base bifunctional solids are catalytically active. The dehydration of various types of alcohols with alumina catalysts has been the object of intensive studies and the reaction mechanism and the nature of the alumina have been discussed by Pines and Manassen [110]. They regarded the dehydration of most alcohols (menthols, neomenthols, alkylcyclohexanols, decanols, bornanols, 2-phenyl-1-propanol, etc.) as taking the form of a trans-elimination, requiring the participation of both acidic and basic sites on the alumina. For this reason, alumina may be thought of as a "solvating" agent, in that it must surround the alcohol molecule, thereby enabling the alumina acid sites to act as proton donors or electron acceptors, and the basic sites to act as the proton acceptors or electron donors. This can be illustrated by the cis, cis-1-decanol dehydration scheme proposed by Misono and Yoneda [88].

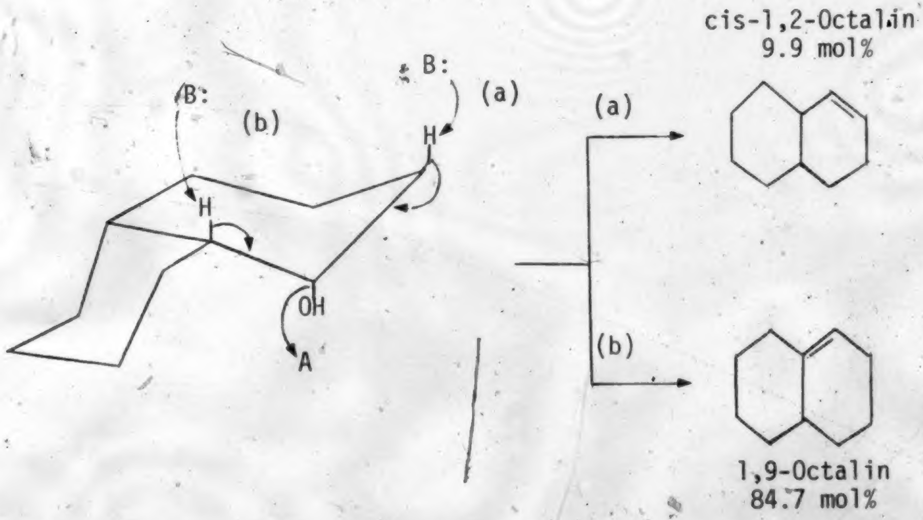

(2.24)

The hydrogen-deuterium exchange in n-propane involves both the acidic and basic sites of γ-alumina as demonstrated by Flockhart et al. [39]. The suggested mechanism is shown below.

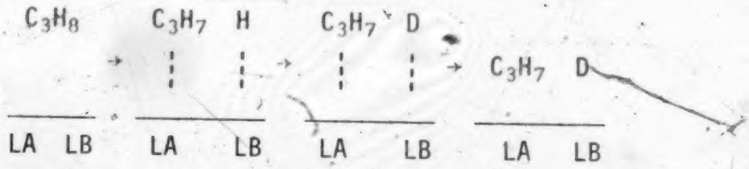

(2.25)

Dissociative adsorption of propane is followed by hydrogen exchange at the site of the active hydrogen atom, with desorption of the deuterated species from the surface as the final step. This mechanism is in accord with the mass spectrometric evidence that the exchange of hydrogen in propane is a stepwise process involving replacement of not more than one hydrogen atom per adsorption-desorption cycle. The coordinated acid-base sites on alumina are possibly associated respectively with an abnormally exposed aluminum ion and a defect centre containing oxide ions.

An excellent discussion on the acid-base properties of various catalysts has been provided by Tanabe [137].

As suggested by Weyl [145,146] and others [27] strains exist on a crystal surface. The strained sites on the γ-alumina surface are believed to result from the dehydration of the original hydrated surface [27,57]. The pattern of adsorption and reaction on the catalyst surface will then depend on the release of the strain. This is also used as one of the interpretations of the catalytic activity of γ-alumina.

2.3.3 The Adsorption Properties and Surface Chemistry of γ-Alumina

As mentioned in the previous section, the various "sites" on γ-alumina, e.g. aluminum ions, oxide ions or hydroxyl groups, provide the centres for adsorption or catalytic reaction. The chemical properties of these sites play an important role in these respects. For example, acidic sites provide the adsorption centres for basic adsorbates and vice versa.

In this work, the adsorption of the various chemicals in the studies involved on γ-alumina will be examined, as well as the surface reaction of γ-alumina with the various chemicals. A review on the published works of H_2S, SO_2 and S adsorption of γ-alumina will be presented.

2.3.3.1 Adsorption Studies: H_2S, SO_2, S

Some published work on the quantitative measurements of the adsorption of H_2S, SO_2 and S on γ-alumina are available in the literature. These will be discussed in greater detail later. Among the published work, some postulated modes of adsorption were given but experimental verification has not been attempted.

A study of adsorption should provide valuable information which improves our understanding of the mechanisms of the reaction. For example, if only one of the two reactants is found to be adsorbed under the reaction conditions, then the reaction mechanism must be of the Eley-Rideal and not Langmuir-Hinshelwood type. Moreover, from an adsorption study, the nature of sites essential for adsorption and perhaps for reaction could be understood. Whether all reactants and products or certain reactants and products compete for the sites should also be examined.

(i) Studies on H_2S Adsorption

Infrared studies on the adsorption of H_2S on γ-alumina have been reported by Slager et al. [133] and Deo et al. [34]. They observed similar (some small difference in frequencies between their recorded infrared bands) infrared bands and the observed frequencies are summarized in Table 2-2.

Table 2-2 INFRARED BANDS OF H_2S ADSORBED ON γ-Al_2O_3 OBSERVED BY DEO et al. [34]

Observed Frequencies (cm^{-1})	Gas Phase Frequencies (cm^{-1})	Assignment
1341	1290	H-S-H (bend)
1420 VW		
1568		
2568 VW	2684	S-H (stretch)
3400 Vb		O-H (hyd. bonded)

where VW=very weak, Vb=very broad

Both works reported the change of color of the catalyst from white to yellow by H_2S adsorption. The broad infrared band around 3400 cm^{-1} represents the formation of hydrogen bonding. Based on the hydrogen bonding evidence, Deo et al. proposed the following form of H_2S adsorption.

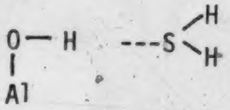

(2.26)

On the other hand, Slager et al. did not agree with this structure. They argued that a shift of -166 cm^{-1} in asymmetric stretching and +51 cm^{-1} in bending from the gas phase vibration mode of H_2S could not be explained by hydrogen bonding formation between the sulfur atom of H_2S and hydrogen atom of the hydroxyl group of γ-alumina. Instead, they suggested that the following mode of adsorption would be more appropriate

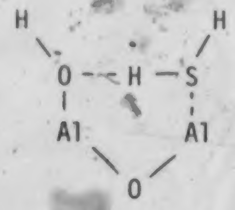

(2.27)

Through its sulfur atom, H_2S is adsorbed to the Lewis-acid site and the hydrogen bonding is formed between the hydrogen atom of the H_2S and the oxygen atom of the surface hydroxyl group of γ-alumina. In addition, they said that this type of structure is in better accord with the mechanism of surface sulfide formation which arises from the dissociation of H_2S on adsorption. Both i.r. (infrared) and gravimetric techniques were used to confirm the H_2S decomposition. When contact time between H_2S and γ-alumina was extended, they observed an increase in intensity of the i.r. band in the O-H region and also the appearance of the i.r. band at 1625 cm^{-1} arising from the H_2O bending mode. This establishes that water is one of the products of H_2S adsorption. The infrared bands of both the adsorbed H_2S and H_2O could be removed when the adsorbates and adsorbent were heated above 100°C. From gravimetric measurements, they obtained a linear relation between the total weight of the adsorbed material and the sum of the area of the i.r. bands of the adsorbed H_2S and H_2O. A mechanism in agreement with this observation is shown below

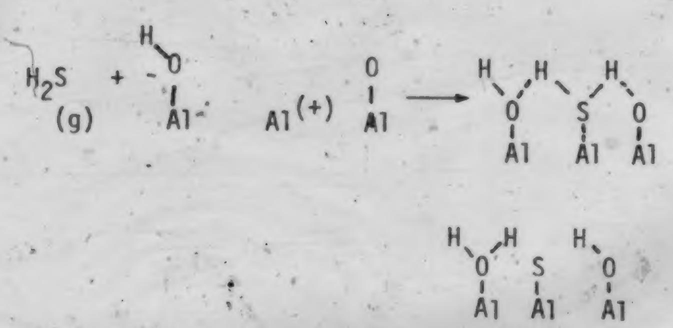

(2.28)

According to this mechanism, bond breaking in hydrogen sulfide can be thought to be coincident with the formation of an O-H bond. Rationalization for the O-H lying next to the adsorbed hydrogen sulfide can be made following Peri's work [104, 105, 106], in which a plot of the percent of O-H retained, against evacuation temperature showed that at least 50% of the surface would still be covered by hydroxyl groups after evacuation at 325° C. Thus it would be improbable that H_2S could adsorb on exposed aluminum ions without having an OH species as a neighbour. The adsorptive dissociation nature of H_2S was further demonstrated by the isotopic exchange experiments conducted by Sabtier and co-workers[122, 123, 124]. The hydroxyl group of ethyl alcohol was found to be capable of exchanging with the SH of H_2S over alumina. Other conceivable paths discussed by Slager et al. involve the breaking of the hydrogen-sulfur bonds to form H^+, H^0 or H^-, and S^{2-}, S^0 or S^{2+}. Without adequate information, they concluded that the final nature of the sulfur atom of adsorbed H_2S could not be verified. However, they said that it was unlikely for H^- or S^{2+} to be formed because subsequent reaction between H^- and OH^- or O^{2-} to form water would be inhibited by like charges and no evidence was obtained to relate to the formation of SO_2 from reaction S^{2+} and O^{2-}.

Bayley [9] noted that H_2S could not be quantitatively desorbed during adsorption-desorption cycles. Adsorption reversibility tests by Glass et al. [45, 46] showed that about 10 $\mu g/g$ of H_2S could not be desorbed from γ-alumina. DeRosset et al. [33] investigated the same system at low coverages and high temperatures and reached the conclusion that the formation of Al-S and Al-O bonds on oxygen vacancies following the adsorption of H_2S and H_2O was consistent with bulk thermodynamics. It has been reported [10, 100, 104, 135] that incompletely coordinated aluminum which possesses the Lewis-acid property occurs on the surface of γ-alumina as a result of exhaustive dehydration and readily reacts with basic adsorbents, such as NH_3 and H_2O. DeRosset found that both adsorbed H_2O or H_2S on γ-alumina prevented the development of the acid color in the case of dicinnamal acetone ($pK_A = -3.0$). While it is difficult to determine whether conversion of the dye to its conjugate acid is due to interaction with Lewis- or a Bronsted-acid site, nevertheless the experiment clearly showed that H_2S reacts as a base with the acid site of γ-alumina, whatever its nature. A high isosteric heat of H_2S adsorption (25 to 38 kcal/mol, depending on the degree of predrying of the alumina) was detected by DeRosset et al. and they argued that reaction of H_2S with a surface Bronsted-acid site (as suggested by Deo et al.) by hydrogen bonding could not account for such high heat of adsorption.

Instead, reaction of H_2S at a Lewis-acid site would create an Al-S bond and more nearly satisfy energetic requirements. They did not indicate whether such adsorbent-adsorbate interation was capable of transforming part of Al_2O_3 into Al_2S_3. Similar high isosteric heats of H_2S adsorption (16.3 and 32.5 kcal/mol at 0.02 μmol/m^2 and 0.42 μmol/m^2 at 423° K) on γ-alumina were also measured by Glass and Ross [46]. Changing of the γ-alumina color from white to pale yellow was also noted and chemical tests verified the presence of about 100 μg. of sulfur in an unknown state.

The quantitative measurement results of H_2S adsorption on γ-alumina carried out by Glass et al. and DeRosset et al. are summarized in Table 2-3.

TABLE 2-3

H_2S ADSORPTION ON γ-ALUMINA MEASURED BY VOLUMETRIC METHOD

	Adsorption Temperature (K)	H_2S Pressure (10^{-6} cm Hg)	Adsorbed Amount μmol H_2S/g	Surface Area m^2/g
DeRosset et al. [33]	300	21	22	175
Glass et al. [118]	150	350	250	490

(ii) Studies on SO_2 Adsorption

Relatively little work has been done on the adsorption of SO_2 on γ-alumina. Deo et al. [34] studied the SO_2 adsorption on γ-alumina using infrared spectroscopy. Table 2-4 shows the frequencies of the infrared bends obtained by them when 1.3 cm of Hg of SO_2 was contacted with the γ-alumina pellet at room temperature.

Table 2-4

INFRARED BANDS OF SO_2 ADSORBED ON γ-Al_2O_3 OBSERVED BY DEO et al. [34]

Observed Frequencies (cm^{-1})	Gas Phase Frequencies (cm^{-1})	Assignment
2470 w	2499	
2340 w	2305	
1330		O-S-O (stretch)
1140		O-S-O (stretch)
3400 vb		H-O-H (hyd bonded)

where w=weak, vb=very broad

The broad hydrogen bonding band at around 3400 cm^{-1} arising from SO_2 adsorption was similar to that of their observation on H_2S adsorption. The infrared band at 3785 cm^{-1}, representing the highest vibration frequencies of the surface groups disappeared as a result of SO_2 adsorption. New bands at 1685 and 1240 cm^{-1} as well as a weaker pair at 1410 and 1090 cm^{-1} were detected when SO_2 pressure was increased above 3.1 cm Hg. These were attributed to the symmetric and assymmetric stretching vibration of the perturbed adsorbed SO_2 species although the form of such species was not understood. Upon heating at higher temperature to 400° C and cooling back to room temperature, a further pair of bands at 1570 and 1440 cm^{-1} appearred. Finally, after evacuation at 400° C, only two pairs of bands remained, namely, the 1330 - 1140 cm^{-1} pair, which was observed at low SO_2 pressure (1.3 cm Hg) and shifted to 1375 - 1110cm^{-1} after high temperature evacuation, and the 1570 - 1440 pair which appearred after heating at high SO_2 pressure (above 3.1 cm Hg) and eventually stabilized at 1570 - 1470 cm^{-1}. Two interpretations were given by the authors. One is that the two pairs of remaining bands represent different chemisorbed species, each vibrating with its own characteristic frequency. The other involves the possible formation of a surface sulfate which the authors depicted as follows,

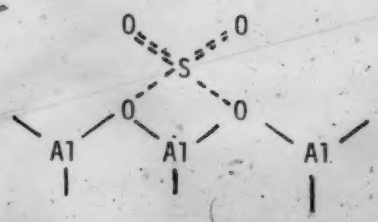

(2. 29)

The frequencies of the infrared bands of some of the inorganic sulfites, sulfates and bisulfates [113] are summarized in Table 2-5. Only those bands with frequencies less than 1700 cm^{-1} are listed. The striking feature exhibited in this table is that

Table 2-5

INFRARED BANDS OF SOME OF THE INORGANIC SULFITES, SULFATES AND BISULFATES

$(NH_4)_2SO_3.H_2O$	1410 (vs)	1105 (vs)		
Na_2SO_3	960 (vs)	1125 (w)	1215 (vw)	
$K_2SO_3\cdot 2H_2O$	943 (vs)	1100 (vs)	1175 (s)	1645 (vw)
$CaSO_3\cdot 2H_2O$	945 (vs)	947 (vs)	1100 (vw)	1210 (vw) 1625 (m)
$BaSO_3$	917 (vs)	1070 (m)	1200 (m)	1410 (vw)
$ZnSO_3$	945 (w)	1020 (s)	1160 (m)	1630 (m)
$(NH_4)_2SO_4$	1105 (vs)	1410 (vs)	1740 (vw)	
$Li_2SO_4\cdot H_2O$	1020 (vw)	1110 (vs)	1625 (m)	
Na_2SO_4	1110 (vs)			
$CaSO_4\cdot 2H_2O$	1010 (w)	1130 (vs)	1630 (s)	
$MnSO_4\cdot 2H_2O$	1025 (m)	1135 (vs)		
$FeSO_4\cdot 7H_2O$	990 (vw)	1090 (vs)	1150 (m)	1625 (m)
$CuSO_4$	805 (m)	1090 (vs)	1200 (s)	1600 (w)
$ZrSO_4\cdot 4H_2O$	920 (vw)	1080 (vs)	1630 (m)	1650 (m)
NH_4HSO_4	855 (m)	1035 (m)	1180 (m)	1410 (vw)
$NaHSO_4$	865 (s)	1075 (s)	1235 (s)	1660 (m)
$KHSO_4$	877 (s)	1065 (s)	1160 (s)	1280 (s)

where, vw=very weak, w=weak, m=medium, s=strong, vs=very strong all sulfites, sulfates or bisulfates possess the strong band at around 1100 cm^{-1}; except the ammonium member, which has one more strong band at around 1400 cm^{-1}. The band frequencies are not greatly varied by different cations. Only those members with crystallite water produce sizable bands at around 1600 cm^{-1} which represents the molecular water. None of these bands are near to those of the "sulfate" bands observed by Deo et al.

The amount of SO_2 adsorbed on γ-alumina at 20 to 80° C was found to increase monotonically with pressure by Ozawa et al. [97] (Surface area of γ-alumina = 382 m^2/g and amount of SO_2 adsorbed at 80° C and 1 atm. pressure is 180 $\mu mol/g$). Glass and Ross [45] studied the adsorption of SO_2 below monolayer coverage (0.1 - 2.0 $\mu mol/m^2$)on γ-alumina at 150°C and with SO_2 pressure to 450 mm Hg. The γ-alumina was pretreated at 500°C. A high heat of adsorption (48Kcal/mol) was detected at lowest coverage (0.1 $\mu mol/_m2$) and levelled out to 13 $Kcal/mol^{-1}$ at a coverage of 2.0 $\mu mol/_m2$. The authors believed that this high heat of adsorption was an indication of chemisorption at low coverage and agreed with the "sulfate-like" structure proposed by Deo et al.

Jones and Ross [63] investigated the SO_2 adsorption on silica gel at -10 to 50°C with a relative SO_2 pressure of 0.01 to 0.14. The isosteric heat of SO_2 adsorption at the relative pressure of 0.1 and -10°C was found to be low (9.0Kcal/mol) compared to that of ammonia [12] and ethylamine [118] in this region. The heat of liquifaction of SO_2 ("Handbook of Chemistry and Physics" Chemical Rubber Publishing Co., Cleveland, Ohio, 1959) at -10°C is 6.08 Kcal/mol.

Normally, the heat of physical adsorption of a gas on a solid surface is 1-2 times the heat of liquefaction [51]. In addition, they also noted that SO_2 adsorption was completely reversible under their experimental conditions. They considered the SO_2 adsorption on silica gel to be a physical surface process.

The adsorptive properties of SO_2 - mordenite system was presented by Roux et al. [120]. About 10% difference between adsorption and desorption curves was recorded by using H- and Na-mordenite as adsorbents. At low coverage; heat of adsorption is about 20 kcal/mol for H- mordenite and 30 kcal/mol for Na- mordenite. The authors explained this phenomenon in terms of surface heterogeneity. Initially at low loadings, the sulfur dioxide is primarily attached to specific sites in the adsorbent matrix. Once these sites are occupied, the remainder of the adsorption would proceed throughout the remainder of the adsorbent matrix by physical adsorption process. The chemisorption at low coverage was postulated to be a strong bond formation process between the SO_2 and the cation of the adsorbent. This was supported by the higher heat of adsorption on Na- mordenite than H- mordenite. The authors also suggested the unidirectional adsorptive interaction between the SO_2 and the surface with high heat of adsorption and low activation energy for adsorption so that mere evacuation would not re-establish equilibrium. They observed that the desorption activation barrier could be overcome by heating so that the amount of SO_2 irreversibly adsorbed at 160°C is only 0.4% of that at 0°C (1.2×10^{-3} mol/g H-mordenite). Strong preference for SO_2 adsorption over CO_2 adsorption even when the gas composition was over 90% CO_2 on both H- and Na-mordenite was also noted.

Table 2-6

SO_2 ADSORPTION ON γ-ALUMINA AND SILICA GEL MEASURED BY VOLUMETRIC METHOD

	Adsorption Temperature (° C)	Adsorption Pressure (mm Hg)	Amount Adsorbed (μmol/m^2)	Adsorbent
Ozawa et al. [97]	80	760	0.5	γ-alumina
Glass et al. [46]	150	500	2.0	silica gel

(iii) Studies on Sulfur Adsorption

So far, very little work has been reported on the adsorption of sulfur on solid catalysts. Barrer and Whiteman [6] investigated the sulfur adsorption on porous Ca-A, Na-X (near faujasite) and natural Ca-, Na-chabazite at 260-320° C temperature. Sulfur vapor ranges from about 0 to 70 mm Hg. In each of the zeolite, the uptake was relatively fast. There was very little difference between the uptake below 1 mm Hg and that (400 mg/g of Na-X at 320°C) at 70 mm Hg of sulfur vapor. The adsorption isotherms were found to be fully reversible, as shown by the coincidence of their sorption and desorption curves. A large isosteric heat of adsorption was detected. For Ca-A, when the sorptions were 0.32 and 0.33 g sulfur/g of adsorbent, the isosteric heats of adsorption were 24.8 and 25.3 Kcal/mol and for Na-X at sulfur sorption of 0.39 and 0.4 g/g adsorbent, they were 32.6 and 30.9 kcal/mol. These large heats of adsorption demonstrate that strong bonds were created between adsorbed sulfur and the host lattice. Despite the high affinity between the crystals and sulfur, they were able to remove all the sulfur by further heating and evacuation. Natural chabazite adsorbed sulfur very slowly compared to Ca-A and Na-X. The uptake bears a linear relation to the square root of the total sorption time. This is characteristic of a diffusion process. From the adsorption isotherms of natural zeolites, they were able to estimate approximate saturation values and it was calculated that the fractional filling of supercages of the natural zeolite by sulfur was about 0.75 to 0.80. They believed that sulfur diffused as chains in the pores.

The surface area of the bauxite catalyst used by McGregor [84] for H_2S/SO_2 reaction measurement, was decreased to 56 m^2/g after experiment compared to 148 m^2/g before use , as determined by BET-N_2 adsorption technique. The decrease in surface area was attributed to the reduction in pore diameter by sulfur. Two methods were adopted for verification of the presence of sulfur. The differential thermal analysis failed to detect sulfur in the used bauxite catalyst and it was felt that the sulfur content might be lower than the sensitivity of such measurement device. On the other hand, electron probe measurements indicated the absence of sulfur from fresh bauxite catalyst but approximately 10% sulfur content was found to be dispersed uniformly within used catalyst. Karren [64] conducted rate measurements on H_2S/SO_2 reaction over the same bauxite catalyst used by McGregor. Nitrogen was introduced into the reactor to purge the catalyst for 2 h after his experimental runs. Subsequent chemical analysis according to the procedure described by Skoog and Bartlett [131] showed that 2.0 weight per cent sulfur still remained in his catalyst.

Kerr et al. [65] concluded that elemental sulfur was found to be an effective poison (but regenerable) for Claus catalysts (bauxites or activated alumina). They found that condensed sulfur, present in levels as high as about 30 w/w %, could completely deactivate a catalyst, but this could be prevented by proper operation above the sulfur dew point.

2.3.3.2. The Oxidizing Properties of γ-Alumina

In recent years the oxidizing power of alumina has received some attention [12, 9]. Two methods have been adopted to investigate such oxidizing properties. Both of them involve contacting the γ-alumina with an adsorbate. One examines the possible formation of the oxidation product as the contacting period is extended, mostly by infrared spectroscopy. The other measures the changes in e.s.r. signal arising from the adsorbate-adsorbent interaction.

Parkyns [98, 99] studied the adsorption and oxidation of carbon monoxide on γ-alumina using infrared spectroscopic technique and observed the formation of carbon dioxide as well as surface carbonate. This was considered to indicate the presence of oxidizing centers on the surface of γ-alumina. Such centers could be removed by treatment with hydrogen and regenerate by contacting with oxygen again. In another piece of work, Parkyns [98] detected nitric oxide on the surface of γ-alumina which had been subjected to extended heating in vacuo. It was suggested as a result of this work that nitric oxide was produced from molecular nitrogen reacting with strained bridges formed by progressive dehydration [104] as also envisaged by Cornelius et al. [27]. The mechanism depicted below was proposed to account for the generation of such strained oxygen bridges.

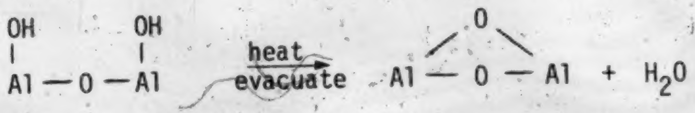

$$\underset{\text{Al}-\text{O}-\text{Al}}{\overset{\text{OH}\qquad\text{OH}}{}} \xrightarrow[\text{evacuate}]{\text{heat}} \text{Al}-\overset{\text{O}}{\text{O}}-\text{Al} + H_2O \qquad (2.\ 30)$$

Parkyns does not believe that dehydration creates oxide-type free radicals because Scott et al. [129] reported no e.s.r. signal detection in the examination of dehydrated γ-alumina. The strained oxygen bridges were regarded to be the "oxidizing centers" which were named by Parkyns earlier and capable of oxidizing CO to CO_2. A further interesting point mentioned by Parkyns is the ability of adsorbed nitric oxide to restore oxidizing properties to the γ-alumina which has been reduced by CO. Tamele [135] and Cornelius et al. [27] reported that a remarkable amount of heat was released when water was contacted at 100°C with the carefully dehydrated alumina. This may be an indication of the reverse of the creation of strain oxygen bridges by dehydration.

In fact, during such hydration-dehydration process, it is difficult to distinguish between the oxygen of water and surface oxide. This has been demonstrated by several published and unpublished works. Mills and Hindin [87] noticed that by adsorbing H_2O^{18} on hydrated alumina, H_2O^{16} could be recovered upon subsequent heating and evacuation. The oxygen isotope exchange (O^{18}/O^{16}) also takes place between CO_2 and the γ-alumina surface [38]. Using O_2^{17}, Eley and Zammitt [35] concluded that oxygen could exchange with the surface γ-alumina. Notari [95] in studying the mechanism of alcohol dehydration on γ-alumina, feels that alumina should be considered as a reactive solid, in which both cation and anion vacancies are present. The interaction of water with such surface vacancies can be depicted as follows

$$H_2O + \underset{*}{O^{=}}\ \underset{*}{\square} \rightarrow \underset{*}{OH^{-}}\ \underset{*}{OH^{-}} \qquad (2.\ 31)$$

(where * is Al and □ is a surface anion vacancy. For simplicity, the bonds between Al and O are represented as completely ionic. This, of course, is only partially true; the ionic character of the bond being very strong but not complete).

Flockhart et al. [39] studied the eletron-transfer properties of γ-alumina using e.s.r. analytical method and suggested two types of active eletron-transfer sites in existence on the surface. One type of active site which is capable of oxidizing hydrocarbon is probably of the molecular nature. The other type of oxygen which predominate in the silica-aluminas of low alumins content, would not affect the adsorbed hydrocarbon over a long period of time.

2.3.3.3 Formation of Sulfates

Marrier and Ingraham [80] did a thermodynamic study and concluded that most metallic oxides could react with SO_2 to significant levels. But in practice, many reactions could not be observed because of slow rates. They [81] also did an experimental study on the reaction between MgO and SO_2. Their results showed that MgO was sulfated by SO_3 and not by SO_2 nor the mixture of SO_2 and O_2. On the other hand, if Fe_2O_3 was impregnated into MgO, substantial sulfation of MgO by SO_2/O_2 mixture occurred. According to their explanation, this was because Fe_2O_3 catalyzed the reaction between SO_2 and O_2 to form SO_3.

Pearson [102] analyzed the used alumina catalyst of industrial Claus sulfur plants and found that sulfation on the order of 2% by weight occurred on the catalyst surface. According to Graulier et al. [50] and Pearson, this 2% sulfation occurs by the reaction of chemisorbed SO_2 and the oxide sites of catalyst surface or through dehydroxylation of the catalyst surface. Neither of them proved the nature of the real form of sulfation species. Both believed that whatever the form, sulfate could be reduced from the catalyst by H_2S. The presence of oxygen also enhanced the sulfate formation while even minute amounts of SO_3 could result in sulfate formation. They found that sulfate formation deactivated the catalyst.

Kerr et al. [65] concluded from their experimental work that the presence of H_2S and/or O_2 greatly enhanced the sulfation rates of activated alumina and bauxite by SO_2. The levels of sulfate formation measured by Kerr were lower than those measured by Pearson (2.5%). Kerr also observed that in field operations of industrial Claus sulfur plants, the sulfate concentrations on the catalyst increased in the downstream convertor beds. He could not determine the primary cause of this behavior.

All sulfate measurements in the published works discussed here were of the wet chemical analysis type. None of the published works could confirm the form of sulfation.

CHAPTER III

REAGENTS AND CATALYST

3.1 Reagents

To facilitate discussion, the reagents used in the present work may be briefly classified into three groups as described below.

3.1.1 Reagents used for Kinetic Studies

The reagents used for kinetic studies are summarized in Table 3-1 where H_2S and SO_2 are reactants, H_2O and S are products of the Claus reaction, and N_2 was used as carrier gas for reaction rate measurement.

Table 3-1 Reagents used for Kinetic Studies

Components	Suppliers	Purity (Spec.)	Impurity
N_2	Alberta Oxygen Ltd.	99.99% min	O_2
H_2S	Matheson Co.	99.50% min	CO_2, COS
SO_2	Matheson Co.	99.98% min	CO_2
H_2O	distilled water	-	-
S	J.T. Baker Co.	99.95% min	-

The nitrogen gas cylinders received were analyzed by mass spectrometer and gas chromatograph before use. An impurity of 0.01% O_2 in N_2 cylinder will produce a 0.0091/3 O_2/SO_2 ratio in a feed stream which contains 91% N_2, 6% H_2S and 3% SO_2. In other words the O_2 introduced is roughly equivalent to 0.3% of the SO_2 in the feed stream and can compete with SO_2 to react with H_2S. As a result, the reaction rate measured would not represent entirely that between H_2S and SO_2. Any cylinder of N_2 which contained more than 0.01% of

O_2 in it was rejected.

Both H_2S and SO_2 gas cylinders were used as received without further purification. One cylinder of each was sufficient for the entire kinetic study. No water could be detected by mass spectrometer in the N_2, H_2S and SO_2 cylinders used.

The distilled water was purified (mainly to remove dissolved O_2) by repeated freezing in liquid N_2 followed by thawing under vacuum. The sulfur was used as received without further purification.

3.1.2. Reagents used for Studying Adsorption and Surface Reaction on γ-Alumina

The reagents used for studying adsorption and surface reaction on γ-alumina are summarized in Table 3-2. The first two components in Table 3-2 have been described in the previous section.

Table 3-2

Reagents used for Adsorption and Surface Reaction on γ-alumina

Components	Suppliers	Purity (spec.)	Impurity
H_2S	Matheson Co.	99.50% min	CO_2, COS
SO_2	Matheson Co.	99.98% min	CO_2
H_2	Matheson Co.	99.95% min	-
O_2	Alberta Oxygen Ltd.	99.98% min	N_2
C_5H_5N	Fisher Scientific Co. Ltd.	Spectroscopic Grade	-
NH_3	Matheson Co.	Spectroscopic Grade	-

Components	Suppliers	Purity (spec.)	Impurity
BF_3	Matheson Co.	Spectroscopic Grade	-
HCl	Matheson Co.	Spectroscopic Grade	-
CH_3COOH	Fisher Scientific Co. Ltd.	Spectroscopic Grade	-

Pyridine and acetic acid were received in liquid bottles and were both subjected to repeated freezing in liquid air and thawing under vacuum before use. They were introduced into the system as vapor (amount controlled by vaporization temperature). Other chemicals in Table 3-2 were used as received in gas cylinders without further purification. Traces of nitrogen were detected in the oxygen gas cylinder but no contamination could be found in the hydrogen cylinder by mass spectroscopic and gas chromatographic analysis. No detectable impurities could be detected in NH_3, BF_3 and HCl gases by infrared spectroscopic analysis.

The hydrogen and oxygen gases were used for pretreating γ-alumina catalyst while the detailed uses of other chemicals in Table 3-2 will be described in Sections 6.1 to 6.4.

3.1.3. Reagents used for Studying Sulfate Formation on γ-alumina

The reagents used for studying sulfate formation of γ-alumina are summarized in Table 3-3. The first four components in Table 3-3 have been described in the previous two sections.

Table 3-3

Reagents used for Studying Sulfate Formation on γ-alumina

Components	Suppliers	Purity (spec.)	Impurity
H_2	Matheson Co.	99.95% min	-
H_2O	distilled water	-	-
O_2	Alberta Oxygen Ltd.	99.99% min	N_2
SO_2	Matheson Co.	99.98% min	CO_2
SO_3	J.T. Baker Co.	C.P. Grade	-
$BaCl_2$	Fisher Scientific Co. Ltd.	C.P. Grade	-
HCl	Fisher Scientific Co. Ltd.	C.P. Grade	-

The sulfur trioxide was received in liquid form sealed in a pressure glass bottle. To facilitate application, the pressure bottle had to be broken and liquid SO_3 transferred quickly into another glass container fitted with a glass stopcock. The liquid SO_3 was then isolated from the atmosphere to prevent the formation of H_2SO_4 with the water vapor in ambient air. The sulfur trioxide was then used without further purification. Both HCl and $BaCl_2$ were used as received without further purification. The detailed description on the application of the chemicals in Table 3-3 can be found in Section 6.5.

3.2 Alumina Catalysts

Only one type of catalyst was used in the present study. It is the γ-alumina supplied by the Cabot Corporation, Boston, Massachusetts under the trade-name Alon. Alon is a fumed alumina containing extremely small particles made by the hydrolysis of aluminum chloride in a flame process. The extremely small particles allowed Alon to be pressed into wafers suitable for infrared spectroscopic studies. When a wafer was compressed from about 100 mg of Alon powder and placed into the sample beam of the infrared spectroscopy with air as reference, the recorded transmittance at 4000 cm^{-1} wavelength was around 80%. This showed that Alon caused little scattering in the infrared beam and hence provided good sensitivity for infrared spectroscopic studies. The typical properties of this catalyst, as specified by the manufacturer are listed in Table 3-4. The surface area of this catalyst, after pressing into wafers was 91 m^2/g, as determined by Chuang [23] using the standard BET method (15) of nitrogen adsorption. The adsorption isotherm as measured is shown in Figure 3-1. The pore size distribution, calculated according to the procedure reported by Gregg and Sing [52], is shown in Table 3-5 and plotted in Figure 3.2.

Table 3-4

Typical Properties of Alon (from Cabot)

Color and Form = White Powder

X-Ray Structure = 90% Gamma Form

Alumina Content* = 99% minimum

Ignition Loss = 4.5% maximum

Metallic Oxides ** = 0.2% maximum

Avg. Particle Diameter = 0.03 micron

Surface Area = 100 m^2/g

pH (10% Aqueous Suspension) = 4.4

Specific Gravity = 3.6

Loose Density = 1.8 - 2.0 lbs/cu. ft.

Bag Bulk Density = 3.0 - 4.0 lbs/cu. ft.

Refractive Index = 1.70

Note: *Excludes physically and chemically combined water

**Other than Al_2O_3

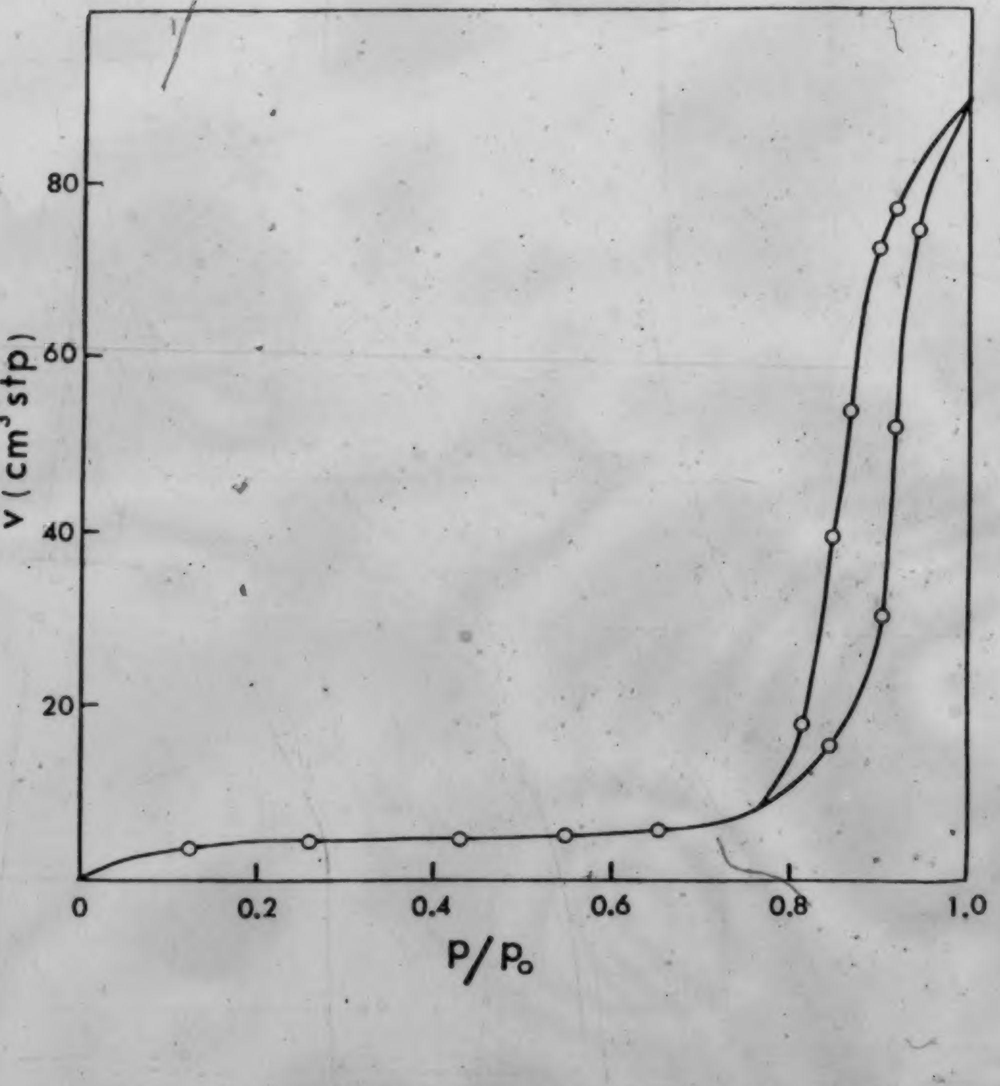

Figure 3-1. Adsorption Isotherm of γ-Alumina (Alon).

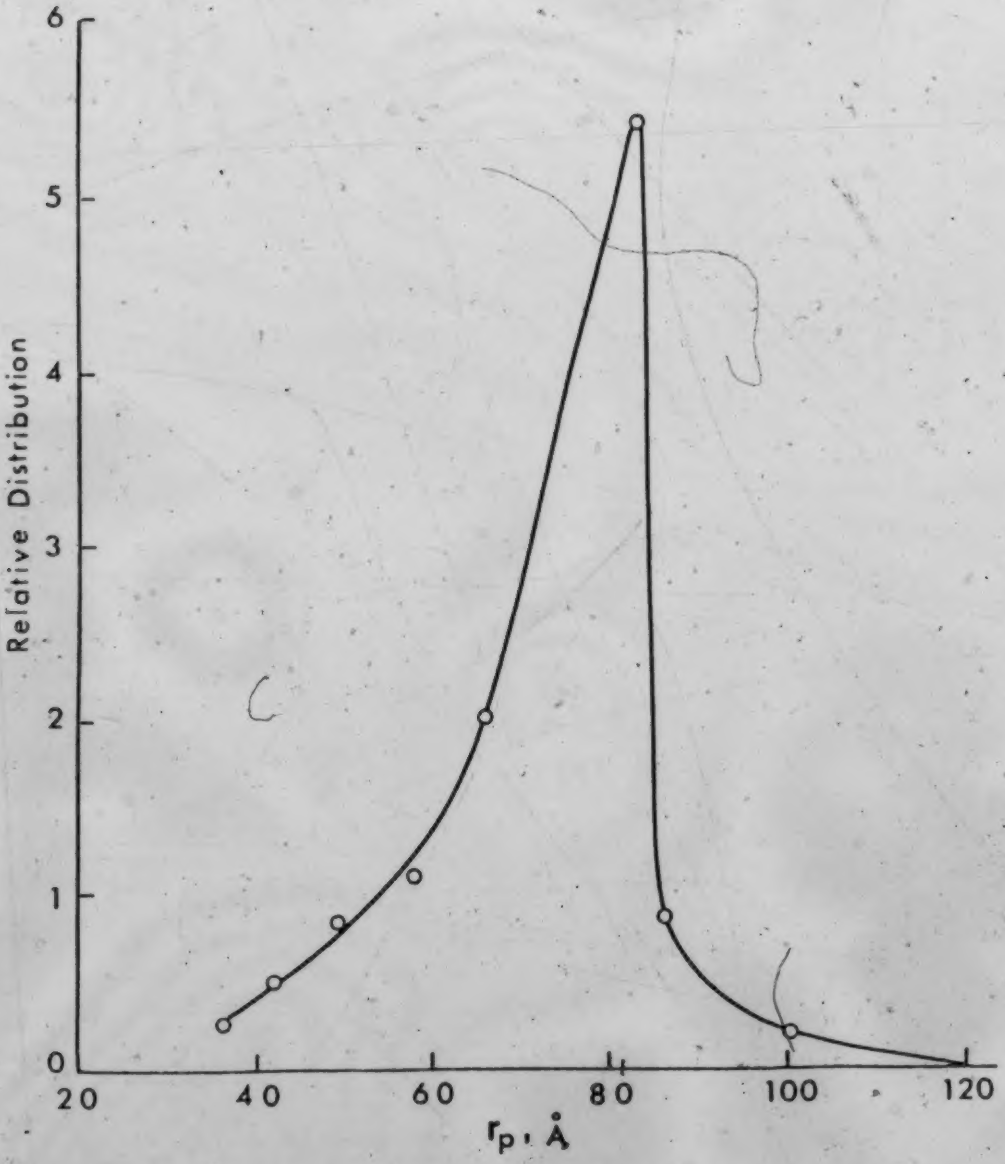

Figure 3-2. Pore Size Distribution for γ-Alumina (Alon).

Table 3-5

Pore Size Distribution for the Alumina Catalyst

P/P_o	v, cm^3 S.T.P.	r_p, Å	Relative Distribution
0.9751	86.50	398	0.0
0.9729	79.62	364	0.22
0.9177	77.46	124	0.00
0.8979	73.18	100	0.22
0.8794	62.77	85	0.90
0.8754	51.92	83	5.39
0.8428	26.42	66	2.03
0.8181	18.68	58	1.11
0.7871	13.03	49	0.82
0.7499	9.52	42	0.48
0.7106	7.40	36	0.26
0.6079	5.66	27	0.13

Notes: P/P_o = adsorbate gas phase pressure/saturation vapor pressure

v = volume of the adsorbate adsorbed

r_p = pore radius of the adsorbent.

According to the plot, the majority of the pore had a size of around 84 Å.

CHAPTER IV

ADSORPTION AND SURFACE REACTION OF γ-ALUMINA

4.1. Experimental Equipment

The experimental equipment employed in the study of adsorption and surface reactions on γ-alumina included mainly the infrared cell and the vacuum system. The simple design and its easier handling was advantageous because of the numerous repeated steps needed for introducing gases into the infrared cell, for evacuation of the infrared cell and the catalyst wafer, and for inserting the infrared cell into the infrared spectroscopic compartment.

4.1.1. Infrared Cell

A sketch of the infrared cell, consisting of two sections, is indicated in Figure 4-1. The bottom section of T-shape was fabricated from two 34 mm ID quartz tubes. The shorter 3 inch long arm of the "T" is used as an analytical compartment. The two ends of the "T" are sealed by two NaCl disc-shaped windows. These NaCl discs, transparent to infrared light in the range of frequencies used in the present work, are the windows of the analytical compartment. A silicone rubber potting compound (Fisher Scientific Co., Catalogue No. 4-769-5) was used to cement the windows to the quartz body with vacuum-tight joints. The procedure of sealing included:

1) Ensuring that the circular edges of the analytical compartment are clean, flat and dry.
2) Applying a layer of the potting compound about 1.5 mm thick to one of the analytical compartment circular edges.

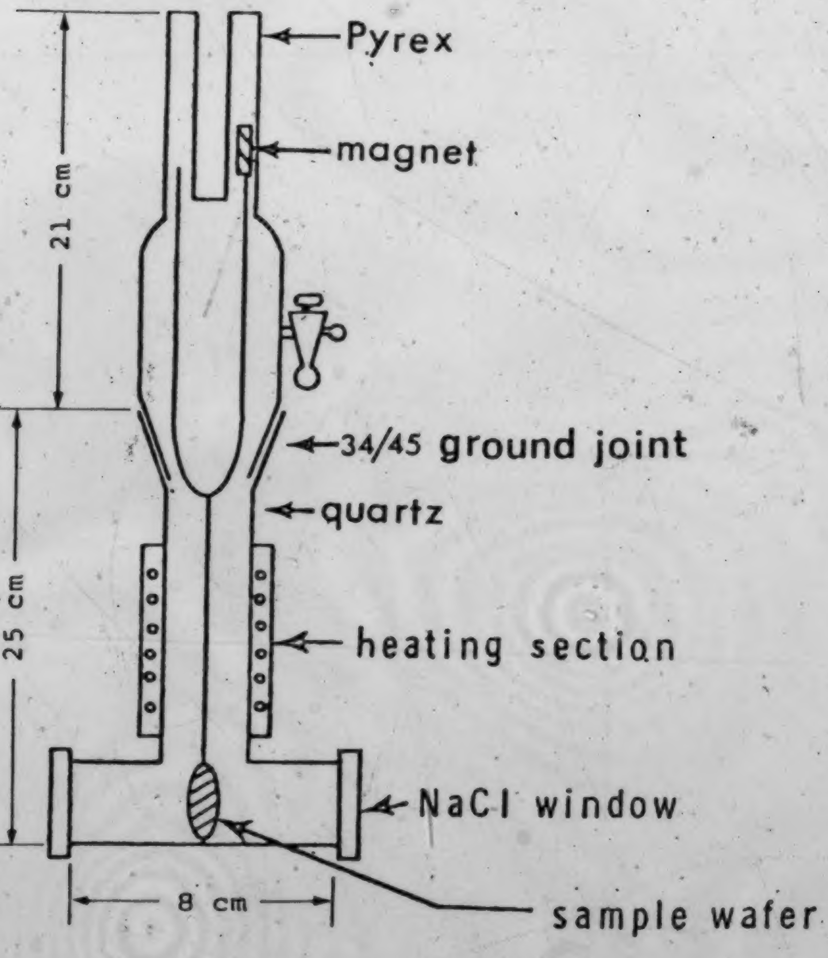
Pyrex
magnet
21 cm
34/45 ground joint
quartz
25 cm
heating section
NaCl window
8 cm
sample wafer

Figure 4-1. Infrared Cell for Adsorption Studies.

3) Clamping the T-shaped cell to a stand so that the circular edge to be cemented with potting compound is horizontal upwards.

4) Ensuring that the surface of the NaCl window to be bonded is clean (avoid contacting fingers with the flat surfaces of the window) and then press the window gently and firmly to the quartz surface with potting compound. No air bubbles should remain between the contacting surfaces.

5) Re-adjusting the T-shaped equipment until the NaCl window sits horizontally. Place a 50 gm weight on it and let it sit for 6 h.

6) Repeat steps 1) to 5) for the second NaCl window.

7) The complete assembly should be allowed to cure for 12 h.

The sealing compound will maintain 10^{-6}mm of Hg vacuum and its elasticity cushions against thermal shock from differences in thermal expansion between the quartz tube and the NaCl windows. Its physical and chemical stabilities were good up to 250°C. To dismantle the windows, the T-shaped compartment was placed within an oven and the oven temperature was increased from room temperature to 400°C in 3 h. After 10 h in the oven at 400°C, the potting compound disintegrated and the NaCl windows would drop from the sealed joint. About 12 h of annealing time should be allowed while the NaCl windows cool to room temperature in the oven.

The longer arm of the T-shape compartment is used as a heating section. The heating zone could not be located in the analytical section of the cell because of the thermal limitation of the potting compound. The heating section was wrapped with nichrome heating coil (25 ohm) externally insulated with 1/2 inch thick asbestos. This section could be heated to any temperature up to 650°C by changing the voltage supplied to the coil. The end of this section is equipped with an open ground glass joint.

The upper section of the cell was equipped with a stopcock for introducing gases or for evacuating the cell. The two prongs projecting upwards house the two extensions from the sample holder. This design allows the sample holder to glide up and down from the infrared cell without rotating by means of an external magnetic lift.

The lower portion of the sample holder consisted of two quartz rings 2.52 cm I.D. and 2.54 cm O.D. The two rings are joined together with a 2mm thick slit between the rings.. The catalyst wafer was supported between the two rings inside the slit.

When a catalyst wafer was prepared, it was placed onto a thin surface (such as a clean razor blade) and then inserted horizontally into the slit of the sample holder. Keeping the sample holder and contained wafer horizontal, the two arms of the sample holder were then inserted into the two corresponding enclosures of the infrared cell cover. The cover and the sample holder were then attached to the main body of the infrared cell with a well-greased vacuum tight joint. By rotating the cover inside the infrared cell, the catalyst wafer could be positioned parallel with the cell windows and normal to the incident IR beam. After clamping the cell to a stand (the catalyst wafer being kept in a horizontal position), the sample holder and the catalyst wafer were moved to the lower portion of the cell by lowering with the external magnet. As required, the catalyst wafer could be located in either the heating or the analytical sections of the cell. It is imperative that all movement of the wafer carriage be slow to prevent the catalyst wafer from falling off or colliding with the inner wall of the infrared cell. The catalyst wafer and/or the sample holder was always lowered to the bottom of the cell before the infrared cell is rotated to the vertical position.

4.1.2. Vacuum System

The vacuum system consisted of a mechanical roughing pump (Welch Scientific Company, Skokie, Illinois, Model No. 1405), a two-stage mercury diffusion pump, one Pirani vacuum gauge (Edwards High Vacuum Limited, Model G9) and a glass vacuum rack. The glass rack was equipped with four one-liter glass reservoirs, a mercury manometer and several glass stopcocks. The liquid nitrogen trap was installed to prevent the oil or mercury vapour from diffusing backwards into the infrared cell. The trap also prevented undesirable gases such as hydrogen sulfide or sulfur dioxide from entering the vacuum system or the vacuum pump. The thermos-insulated traps were refilled with liquid nitrogen every 12 h to ensure continuous operation. The vacuum system could be evacuated to 5×10^{-6} mm Hg absolute pressure as measured by the Pirani gauge. This pressure increased to 1×10^{-5} mm Hg after the vacuum system was isolated continuously for 24 h from the liquid nitrogen traps and the vacuum pump.

4.2 Preparation and Pretreatment of Catalyst Wafer

About 100 mg of the catalyst powder were pressed between two pieces of smooth firm paper (such as recording-chart paper, Perkin-Elmer Co., Part No. 221-1613) by stainless steel dies (2.54 cm dia.) at about two tons/cm^2 pressure for about 10 sec. The wafer was then ready to be pretreated in the infrared cell.

The infrared cell with catalyst wafer was evacuated for about 10 min at room temperature before being heated and degassed at 400°C for 2 h. It is imperative that evacuation be carried out prior to heating or else the water retained by the γ-alumina, after its long exposure to the atmosphere, would vapourize upon heating and would condense on the relatively cool infrared windows. The water will etch the NaCl surface reducing it IR transparency necessitating repolishing of the windows. The heating of infrared cell should be carried out slowly (about 5°C per min) and dry cool air should be blown on windows during the heating process. After the wafer in the infrared cell had been degassed for 2 h at 400°C, it was then heated with 10 cm Hg ocygen for 2 h followed by degassing for 2 h, all at 400°C. This step was repeated with hydrogen in place of oxygen. Subsewuently, the cell was degassed overnight at 400°C and then cooled slowly to room temperature. At this stage, the catalyst wafer was ready for experiments using the infrared spectrophotometer.

4.3 Experimental Procedure

Different experimental procedures were used during the studies of adsorption and surface reactions of γ-alumina, Some standard procedures were followed in all the studies, for example, the methods of recording infrared spectra or of comparing the baseline spectra of γ-alumina with those absorbates. Other procedures were only used for a particular study, for example the impregnation of sulfate containing γ-alumina into NaBr or NaCl. These latter experiments will be discussed in detail in the following sections.

4.3.1 Recording Infrared Spectrum

After a catalyst wafer was prepared and pretreated (as mentioned in Section 4.2), it was lowered carefully to the bottom of the infrared cell and positioned parallel to the infrared cell windows. The infrared cell was then transferred slowly to the infrared spectrophotometer for recording of the baseline spectrum. The method of recording a baseline spectrum is the same as that used for recording spectra of any adsorbate plus adsorbent.

4.3.1.1. Without Gas Phase Interference

The infrared cell was placed in the sample-beam side of the analytical compartment of the infrared spectrophotometer and was clamped in vertical position. Because the infrared beam is higher than the platform of the analytical compartment of the infrared spectrophotometer, the catalyst wafer was carefully aligned to the center of the infrared sample beam. The position of the infrared cell was then adjusted carefully so that its longitudinal axis was parallel to the infrared team.

The correct detailed operating instructions for recording the infrared spectrum, etc., are described in the Perkin-Elmer Model 621 Manuals. In essence, after the infrared spectrophotometer was switched on and satisfactory operating conditions were achieved, the drum chart paper was synchonized to the starting frequency (4000 cm^{-1}) of the infrared spectrophotometer, and matched with the pen reading on the chart paper of the recorder. The position of the infrared cell was readjusted in two directions both normal to the IR beam to produce the highest transmittance.

The Perkin-Elmer model 621 infrared spectrophotometer is equipped with an attenuator in the reference beam. This was used in cases where substantial scattering of the infrared beam is caused by the catalyst wafer (especially in 3000-4000 cm^{-1} frequency range of the infrared beam). The slit opening, which is directly proportional to the square root of the reciprocal of the original transmittance, can then be decreased to compensate for the loss in energy (intensity of light) from scattering. On the other hand, decreases in slit opening reduce the total amount of light in the reference beam and would also reduce the sensitivity of analysis.

By adjusting the slit opening, the transmittance indicated by the pen reading should be set at about 80%. For best results, the transmittance reading should lie between 10% and 90% throughout the entire range of infrared scan. This is achieved by stopping the scan and readjusting the slit opening as needed from time to time. The scanning range of a Perkin-Elmer Model 621 infrared spectrophotometer is from 4000 to 200 cm^{-1} frequency and the scanning speed is variable. Since the γ-alumina shows strong infrared absorption at frequencies below 1000 cm^{-1}, scans involving γ-alumina were terminated at 1000 cm^{-1}. For better accuracy, slower scanning speeds should be used. In spectral frequency ranges of no interest, the scanning speed was increased. In general, the speed of the entire scan for an unknown analysis should preferably be on the slow rather than fast side.

For thin relatively transparent γ-alumina wafers, the slit opening in the attenuator should be increased until the transmittance readings lie between 10% and 90%. The disadvantage of using a thin wafer is that it is more difficult to prepare, easier to break, and reduces the amount of adsorbate. For wafers which are either thicker or darker colored, the transparency is greatly reduced and the slit opening in the attenuator should be decreased. The reduced sensitivity from using a thick wafer is balanced against the need to obtain an increased amount of adsorbate.

Figure 6-1 shows a typical baseline spectra for γ-alumina. The reproducibility of the baseline spectra was very good for diffenent γ-alumina wafers. The only observable difference between the different equal-weight γ-alumina wafers was in the intensity of the spectral bands of the hydroxyl groups around 3600-3800 cm^{-1}. The maximum difference measured in this work, about 10%, was largely attributable to the speed of heating and evacuation of the catalyst wafers. If the analysis of the gas phase in contact with the γ-alumina wafer was required, the wafer could be lifted out of the infrared beam with the external magnet.

4.3.1.2 With Gas Phase Interference

During the recording of a spectral scan mentioned in Section 4.3.1.1, air was used in the reference beam of the infrared spectrophotometer. Because carbon dioxide in the atmosphere could affect the spectral results, when critical, an identical evacuated infrared cell was placed in the reference beam. On the other hand, if the infrared spectrum for γ-alumina in contact with a gas was required, the spectral bands of the gas could interfere with the surface spectra. Under such circumstances, an identical infrared cell containing the same gas at the same pressure as in the infrared cell in the sample beam could be placed in the reference beam. In this way, the infrared signal from the gaseous adsorbate registered by the sample beam is cancelled by that of the reference beam.

4.3.2. Adsorption-Desorption Studies

After the baseline spectrum of the catalyst wafer was recorded, the infrared cell was secured to the vacuum rack for adsorption-desorption experiments. All sections upstream of the infrared cell stopcock were thoroughly evacuated before introducing any adsorbate gases. When the vacuum level was adequate, the stopcock of the infrared cell was opened to the vacuum rack. With the cold traps and vacuum pump isolated from the system, adsorbate(s) could then be introduced into the infrared cell. The pressure of the adsorbate could be measured by the manometer. During the initial contact with the wafer, the gas pressure could drop quite significantly due to adsorption. The readings on the manometer were constantly observed until the pressure stabilized. The final pressure was then recorded. During this period, any change in the color of the wafer was carefully observed. After the required time of adsorption, the infrared cell was isolated and transferred to the infrared spectrophotometer for analysis. Spectra so recorded, could be compared to the baseline spectrum.

The adsorption could be carried out at higher than room temperature by lifting the catalyst wafer into the temperature-controlled heating section.

After the spectra were recorded, the infrared cell containing the adsorbate(s) was transfered to the vacuum rack. Further evacuation could be performed over any desired period of time and at any selected temperature. The infrared spectra from the catalyst wafer which had been under such treatment could then be recorded.

These spectra were compared to those from the adsorption study and to the baseline spectrum.

4.3.3. Surface Reaction of γ-alumina

The surface reactions of γ-alumina, as investigated herein, included three main studies: (1) oxidizing property of γ-alumina, (2) adsorption and reaction sites for H_2S and SO_2; and, (3) formation of sulfate on γ-alumina. The experimental procedures, being rather involved, will be described separately in Section VI with the results and discussions.

The analytical method used in the studies of the oxidizing property of γ-alumina and in the examination of the adsorption and reaction sites for H_2S and SO_2 was the same as that described in Section 4.3.2. Two methods used in the study of the formation of sulfate on γ-alumina, different from that in Section 4.3.2., will be described here.

Since the γ-alumina shows a strong spectral band near 1000 cm^{-1}, spectral bands in this frequency range from other possible surface species could be masked by the strong band. To overcome this problem, two methods could be used. One method uses a small portion of the γ-alumina, previously used in the required experiments, mixed with NaCl or NaBr powder. A wafer prepared from this powder mixture according to the method described in Section 4.2, even though a smaller amount of γ-alumina was used, resulted in spectral bands which were smaller but which were well inside the detection range of the infrared spectrophotometer. The disadvantage of this method is that the quantity of that species under investigation being reduced, proportionally decreases the sensitivity of analysis. The second method involved preparation of an equivalent (same size and weight) pure Υ-alumina wafer which could place in the reference beam of the infrared spectrophotometer. The strong infrared band of Υ-alumina detected by the sample beam could then be compensated by that in the reference beam. Only the spectral bands of those components present on the sample side Υ-alumina wafer but not on the pure Υ-alumina wafer in the reference beam could be recorded. In this manner, spectra could be recorded without interference from the strong alumina band around 1000 cm^{-1}. The weakness of this method arises from the difficulty encountered in the preparation of two equivalent wafers.

CHAPTER V

STUDIES ON KINETICS AND MECHANISM

5.1 Experimental Equipment

A schematic diagram of the experimental equipment used in the studies of kinetics and mechanism is shown in Figure 5-1. It comprises a feed system, an infrared cell-reactor, a recirculation pump, water and sulfur condensers, a temperature control and recording system, and flow measurement devices. Other than the infrared cell windows which were either C_aF_2 or NaCl, all material of equipment construction was 316 stainless steel.

McGregor [84] studied the kinetics of the same reaction system but he used a bauxite catalyst. His conversion results were calculated by analyzing and comparing the reactant concentrations in the feed and product streams using gas chromatography. To analyze the product stream, the sulfur vapor was first condensed. Karren [64] continued McGregor's work by using the same reaction apparatus but a larger sulfur condenser and discovered that liquid sulfur could catalyze the reaction between the unconverted H_2S and SO_2 in the gaseous product stream. This effect was also observed by Chuang [22] later. As a result, the calculated conversions would include both the bauxite catalytic effect and the added conversion obtained in the sulfur condenser. To avoid this problem, the equipment used in the present work was designed so that reaction conversion could be measured *in situ* in the reactor using an infrared spectrophotometer. Hence, the chemical analysis could be done without changing the condition, i.e. composition, of any streams.

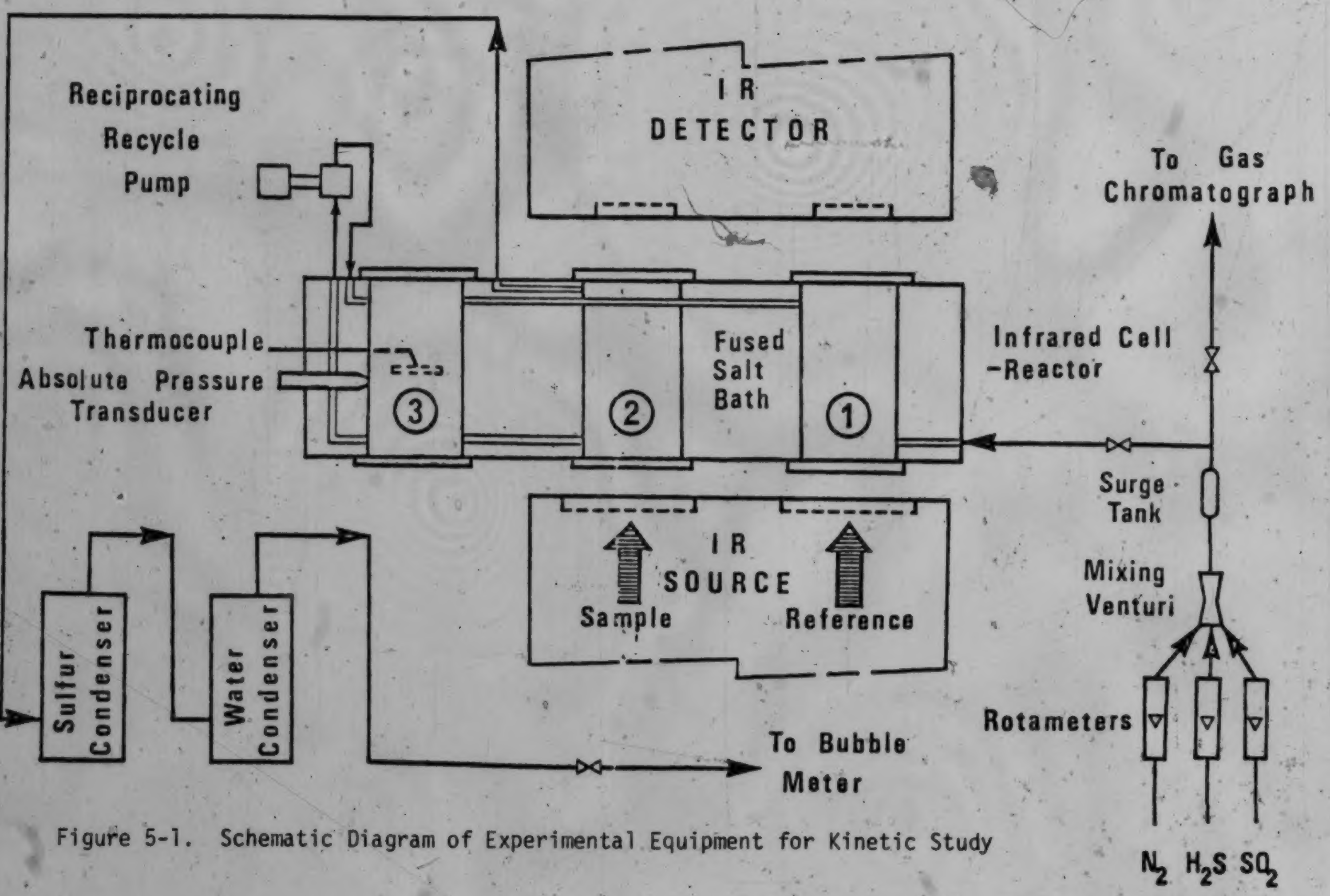
Reciprocating
Recycle
Pump
I R
DETECTOR
To Gas
Chromatograph
Thermocouple
Absolute Pressure
Transducer
③
②
Fused
Salt
Bath
①
Infrared Cell
-Reactor
Surge
Tank
I R
SOURCE
Sample
Reference
Mixing
Venturi
Sulfur
Condenser
Water
Condenser
Rotameters
To Bubble
Meter
N_2
H_2S
SO_2

Figure 5-1. Schematic Diagram of Experimental Equipment for Kinetic Study

The equipment depicted in Figure 5-1 was mounted on a mobile rack which could be moved up to the infrared spectrophotometer when an analysis was required. This arrangement was used to prevent the need of stationing the hot reactor permanently in the analytical compartment of the infrared spectrophotometer. It would, thus, also free the infrared spectrophotometer for other analytical uses whenever required and to prevent excessive heat radiated from the hot reactor to the sensitive components of the infrared spectrophotometer. The decision on whether the infrared spectrophotometer or the equipment should be mobile was made solely on the basis of convenience. Moreover, the desirability of levelling the infrared spectrophotometer in a horizontal plane was facilitated by keeping it stationary.

The various components of the experimental equipment will be described in the following sections, except the water and sulfur condensers which were similar to those used by McGregor [84].

5.1.1. Feed System

The feed system allowed blending of various chemical species which were of interest in the present work prior to their introduction into the reaction system. Gaseous reactants (hydrogen sulfide and sulfur dioxide) and diluent (nitrogen) were supplied from cylinders and the supply pressure was determined by gas regulators. The flow of each gas was controlled by a needle valve. A Matheson 601 rotameter was used for nitrogen and Matheson 602 rotameters were used for hydrogen sulfide and sulfur dioxide to provide a visual indication of the rate as well as the steadiness of the continuous flow. The reactants and nitrogen were combined and mixed first in a manifold and then a surge vessel. This set up was capable of providing a continuous constant composition feed stream, as confirmed by repeated continuous analysis using gas chromatograph and infrared spectrophotometry. Hence, the venturi mixer as used by McGregor [84] was unnecessary. The gas dryers were also not installed because from mass spectrometric analysis, even traces of water could not be detected in the various gases used. After the surge tank, a small fixed portion of the feed stream was continuously bled to the gas chromatograph for analysis while the major portion went to the reactor. The reason for using a gas chromatograph in addition to the infrared spectrophotometer for chemical analysis will be explained in Section 5.2. The flow rate of the feed stream to the reactor could be varied by monitoring the size of the portion to the gas chromatograph without upsetting the feed composition. The feed stream entered the preheat section before proceeding to the reactor. The preheat section consisted of a two feet long 1/4 inch diameter tubing wound with nichrome wire and insulated by 1/4 inch thick asbestos tape. The feed stream could be preheated to the reactor temperature at the reactor entrance. The heat load to the preheat section could be varied by the voltage input to the nichrome wire using a Variac. A manifold with three lines was installed at the entrance of the preheat section to allow the introduction of water, sulfur or other reagents into the reactor. These supply lines were also wound with nichrome wire and insulated with asbestos tape so that water, sulfur or other liquid reagents could be vaporized before entering the preheating section. It is of utmost importance that all the liquid reagents be vaporized before they enter the infrared cell-reactor. If not, the CaF_2 or NaCl windows could be shattered by the thermal shock imposed by the vaporization of these liquid reagents.

One of the lines on the manifold before preheat section was fitted with a Matheson 602 rotameter to allow the introduction of the gaseous reagents like NH_3 or HCl.

A Sage Model 355 syringe pump (Sage Instruments, Inc., White Plains, New York) was employed to inject water and other liquid reagents into the feed system. A set of driving gears in the syringe pump enables one to infuse liquid continuously at various flow rates using any single syringe with a ratio of 25,000 to 1 at the maximum and minimum settings. A pair of gears on top of the pump engage the mating racks on the drive carriage and push it to force the syringe piston forward smoothly. The speed of movement of the syringe piston ensured reproducibility of ± 0.3% full scale regardless of the difference in back pressure. This means that a continuous constant liquid feed supply could be guaranteed independent of the reactor pressure. This was possible because an electronic feed back circuit regulated the permanent magnetic DC motor to drive the pump. A Hamilton 50 c.c. glass-wall syringe (Catalogue No. 1050) was employed to hold the liquid reagent. A Teflon-coated piston enabled the gas-tight movement during the feeding of liquid. The calibration of the syringe feeder is shown in Appendix C.

The sulfur was introduced into the feed system by bubbling nitrogen gas through a molten sulfur reservoir which was a 3 in. diameter 8 in. long cylinder fabricated from 316 stainless steel. It was wound with nichrome wire and insulated with asbestos tape. The temperature of the sulfur reservoir could be changed by manipulating the voltage supply to the nichrome wire using a variac. A fixed flow rate of nitrogen gas was bubbled into the molten sulfur in the reservoir to carry a finite amount of sulfur into the reaction system. By changing the temperature of the sulfur reservoir, various amounts of sulfur could be introduced into the feed system. The sulfur feed was calibrated at various temperatures at a fixed nitrogen gas flowrate and the results are shown in Appendix E.

5.1.2. Recirculation Pump

A double-acting magnetic solenoid reciprocating pump constructed by the machine shop, Department of Chemical Engineering, University of Alberta, was employed to recycle the gases around the recirculation loop of the reactor. The construction of the pump has been described elsewhere [23]. All material of construction of the pump, except the check-valves, o-rings and pump piston, is of 316 stainless steel. The check valves and o-rings were made of Teflon and the pump piston was machines from mild steel. Both suction and discharge check-valves were formed from Teflon disks which were back seated with stainless steel springs.

The pump cylinder was made of one inch I.D. tubing screwed into a 2-1/2 inch O.D., 2 inch long head at each end. Two straight-thread connectors of 1/4 inch I.D. were bored in each of these two heads. The check-valve disks were seated against the threaded end of the connectors. A "Swagelock" fitting was screwed onto each of the four straight-thread connectors. Through the "Swagelock" fittings, the two suction check-valves were connected to a common tee by 1/4 inch O.D. tubing, so as the two discharge check-valves. One tee was connected to the external suction line and the other was connected to the external discharge line. The total length of the pump body was 13-3/4 inch and the overall piston length was four inches.

During the pumping operation, the piston travels reciprocally from end to end in the pump body tubing. Under such motion, one end of the pump body is under compression while the other end under suction. The check-valves were designed in such a way that the suction check-valves were opened with the suction and closed with the compression in the pump body. The opposite pattern applied to the discharge valve, i.e. closed under suction and opened under compression. Since there is one suction check-valve at each end of the pump body and the two suction valves as well as the two discharge valves are connected to a common suction and discharge line respectively, gases can be continuously sucked into and discharged from the pump by the reciprocating motion of the piston.

Three coils, each occupying a 3 2/3 inch length of pump body and separated from each other by a 1/4 inch asbestos fiber disk, were wound around the pump cylinder. Each coil consisted of approximately 2500 turns of No. 25 enameled copper wire. The enameled coating on the copper wire was stable to a temperature of 275°C. The three coils were separate coils and were not connected to each other. As DC power was supplied alternately in sequence to the three coils, the piston could be reciprocated between the ends of the pump cylinder through the magnetic force generated by the electric current.

The external electronics of the pump consisted of a DC power supply, a master clock, three wave shaper, counters, decoders, delays and power stages. The actual power supply was from the 110 volts AC current which was then converted by a rectifier into the 25 volts DC current. The master clock determined the speed of the reciprocating motion of the pump by transmitting electric pulses at various preset frequencies to switch on and off the three pump coils alternately. Each pulse transmitted would switch on one coil once. The wave-shaper was a device that modified the electric pulses into rectangular shape. The counters and decoders converted the analog pulses into digital pulses which provided the on-off operations. The delays determined the span of time in which each pump coil should be on the off position before it was switched on again. They were adjusted so that the adjacent delays were off-phase by 90°. The current transmitted by the decoders was not powerful enough to activate the pump coil. As a result, the power stages were employed. They connected each pump coil to the 25 DC volts power supply every time a signal was decoded to that coil by the decoder. At the construction stage of the pump electronic components (decoders, wave shapers etc.), the problem of overheating of these components was not expected and as a result, no fan-cooling system was built in. A continuous air-purge cooling system was added later when this was found to be necessary to assure stable pump operation at the trial run stage.

The temperature in the pump cylinder could reach 135°C after the piston had been reciprocating over a long period of time even without external heat supply. Besides the pump coil section, the whole pump plus the tubings were wound with nichrome wire and then insulated with asbestos tape. By varying the voltage input to the nichrome wire using a Variac, the temperature of the pump cylinder could be operated between 135°C to 275°C. As mentioned earlier, the 275°C temperature limitation was imposed by the thermal stability of the pump coil. In most of the kinetic runs, the reactor temperature was generally higher then the pump temperature. To minimize the temperature differential, additional heating using nichrome wire was provided to the discharge line of the recirculation pump. The 275°C temperature limitation of the pump imposed a restriction on the operation at high sulfur partial pressure.

The pump was mounted horizontally to provide a more uniform reciprocating action even though the lower surface of the piston was constantly rubbing against the pump cylinder. Vertical mounting could reduce the friction between the piston and cylinder but such arrangement resulted in a faster downward than upward movement of the piston. With careful manipulation, it was possible to operate the pump continuously over at least a few days. However, due to the narrow clearance between the piston and cylinder, it was necessary to purge the pump thoroughly with pure nitrogen while the temperature was maintained at about 250°C after the termination of each experimental run (purging time was approximately 3h). Cooling the pump without adequate purging might cause the residual sulfur vapor in the pump to condense. This eventually resulted a difficult or impossible start up of the next experimental run due to the loss of free piston motion. According to the experience from the present work, the situation could be so bad that a complete dismantling of the pump for cleaning was necessary.

5.1.3. Infrared Cell-Reactor and Catalyst Holder

The infrared cell-reactor employed in the kinetics measurements of the present work is shown in Figure 5.2. It consisted of a 3 inch wide, 13 inch long and 9 inch deep rectangular tank with three infrared cells, an electric stirrer and four electric heating elements.

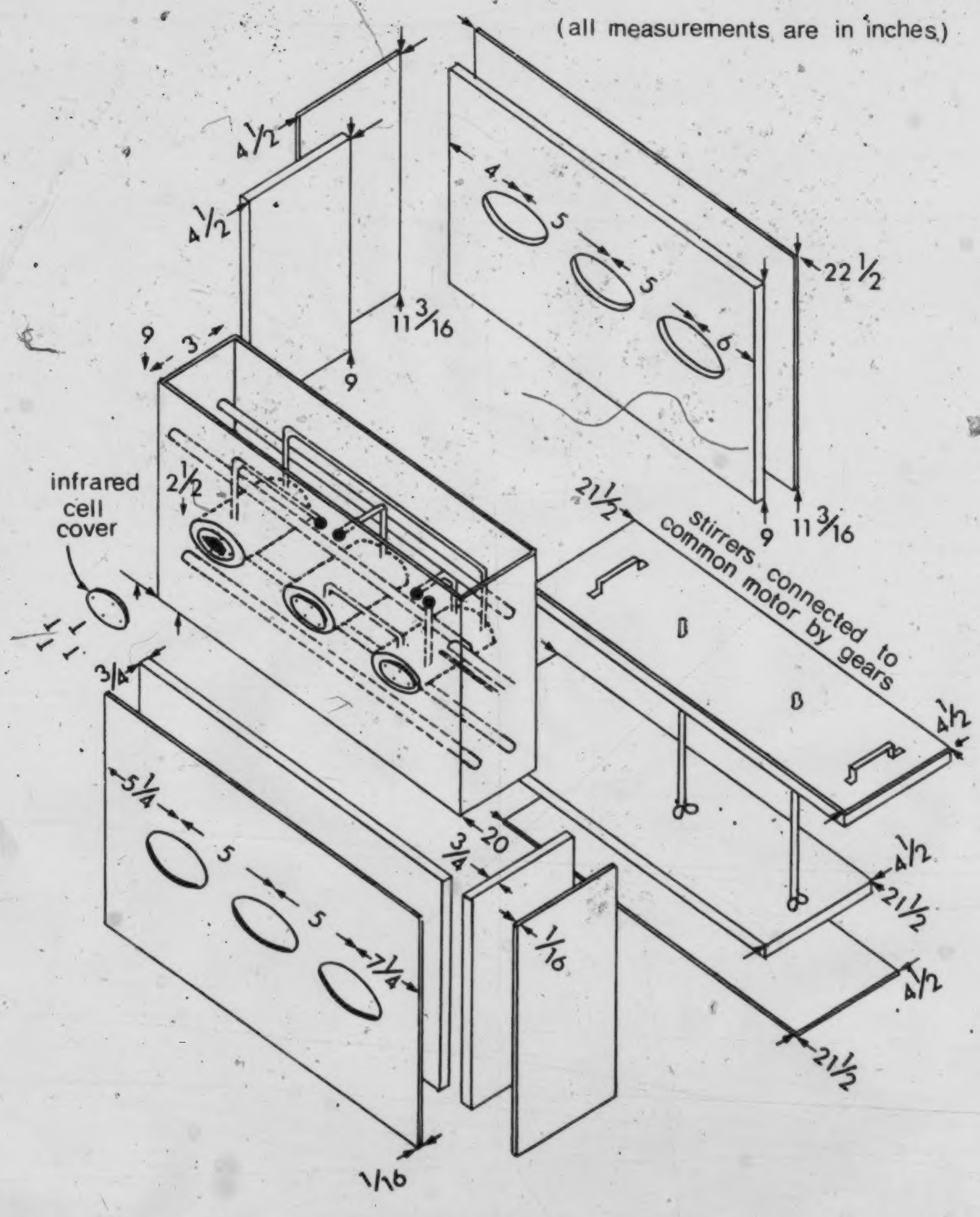
(all measurements are in inches)
4 1/2
4 1/2
11 3/16
9
4
5
5
6
22 1/2
9
11 3/16
9
3
9
infrared cell cover
2 1/2
1
1 1
21 1/2
stirrers connected to common motor by gears
4 1/2
3/4
5 1/4
5
5
7 1/4
1/16
20
3/4
1/16
4 1/2
21 1/2
4 1/2
21 1/2

Figure 5-2. Infrared Cell-Reactor.

As can be seen in Figure 5.2, three 1 1/2 inch diameter holes were cut on each of the two largest vertical faces of the rectangular tank. A 3 inch long infrared cell with 1 1/2 inch O.D. and 1 1/4 inch I.D. was inserted between each pair of these holes. The infrared cell was welded to the inner faces of the tank wall along the edges of the cut holes. The ends of the infrared cell were then exactly flushed with the outer faces of the tank walls. A 1/8 inch wide groove was machined on each end face of the infrared cell to accommodate a Teflon o-ring. Four threaded holes with 3/32 inch diameter were made along a circle 1/8 inch outside the outer circumference of the infrared cell. These four holes were separated from each other by equal distances and whose depth was about 3/4 of the tank wall thickness. The function of these holes was to hold the infrared cell cover. Six identical covers were fabricated for the three infrared cells. These covers were made from 3/8 inch thick disks with 1 3/4 inch diameter. A 1 3/8 inch I.D. and 11/32 inch deep trough was cut from the disk for the accomodation of the infrared cell window. A hole with 1 inch diameter was then cut from the bottom of the trough. This allowed the passage of the infrared beam. Four holes with 3/32 inch diameter and separated equal-distance from each other were drilled along a wide 1 5/8 inch in diameter on the cover. By employing four screws, the cover together with the NaCl (or CaF_2) window could be fastened onto the infrared cell. The screws were tightened snugly into the holes on the tank wall mentioned earlier so that the NaCl (or CaF_2) window was pressed against the o-ring to provide a good seal. If the operating temperature was below 250°C, the Teflon o-ring could last for a long time. However, at a higher temperature of 350°C, it could be used for about 200 h, beyond which it started to deform slowly. Hence, all the o-rings used in the present work were replaced before the 200 h of service life was reached.

The three infrared-cells were arranged in such a way that the two cells at the ends were used as feed and reactor cells, respectively, while the middle one was used as the product cell. The centers of the cells were separated by 5 inches from each other. This was to match with the distance between the reference and sample beams of the infrared spectrophotometer used in the present work. The centers of the cells were located 2.5 inch from the base of the infrared cell-reactor tanks and the width of the tank was 3 inch in order to match with the geometric configuration of the analytical compartment of the infrared spectrophotometer. During analysis, the entire infrared cell-reactor tank had to be inserted into the analytical compartment. Two 1/4 inch holes were drilled on top of both the feed and product cells. Tubing of 1/4 inch O.D. was welded to one hole on the feed cell and to one hole on the product cell. This tubing was then connected to the feed system outside the reactor tank from the feed cell, and to the product system for the product cell. Four 1/4 inch diameter holes were drilled on top of the reactor cell, two on each end. Two holes, one from each end, were welded to the 1/4 inch O. D. suction and discharge lines of the recycle pump to allow for recirculation of gases through and around the reactor. The remaining two holes were each connected by 1/4 inch O.D. tubing to the holes on the feed and product cells, respectively. With the set up described so far, the gases could flow through the feed system via the feed cell. They could then enter the reactor cell at one end via the tubing connecting the feed and reactor cells. If the recycle pump was switched on, the gases could be recirculated after passing through the reactor cell. Finally, the product stream could flow from the reactor cell to the product cell and then from the product cell to the external product system. In addition to the recirculation line from the pump, all flow lines from the feed system to the product system were positioned within the reactor tank. The tank was filled with a fused salt heating media of eutectic composition prepared by mixing equal amounts of $NaNO_3$ and KNO_3 by weight. As a result, the gases could be maintained at a uniform temperature while they flowed from the feed to the product system.

Two 1/8 inch diameter holes were made at the side of the reactor cell to permit introduction of a thermocouple and a absolute pressure transducer (Statham 600 absolute pressure transducer) through the side of the reactor tank. The heat supply to the fused-salt bath was from four stainless steel-clad 750 watt heating elements (Type T tubular heating element, Chromalox, Toronto, Ontario, Canada), installed two above and two below the infrared cells in the reactor tank. Three variable voltage transformers (Variac, Fisher Scientific Company) were used to adjust the power supply to the three heating elements. The power supply to the fourth heating element which was situated above the infrared cell was manipulated by a temperature controller (Foxboro Model 625M). The reason for such an arrangement was twofold. First, a single temperature controller could not be used to control the total power input to the four heating elements.

Second, the speed of increasing the temperature of the fused salt bath would be decreased if one temperature controller was used for four heating elements. Such an arrangement enabled the temperature of the fused-salt bath to be raised relatively rapidly to the vicinity of the required temperature. The eventual fine adjustment and control of the desired temperature was then performed by the temperature controller. The input to the temperature controller was supplied by a thermocouple located above the feed cell.

Two stirrers driven by a single motor on the top cover of the reactor tank were employed to circulate the fused-salt bath. The stirrers were positioned in the spaces between the infrared cells. The pattern of circulation was to push the fused-salt to the bottom of the tank and then upwards around the ends of the tanks through deflection. The stirrers were necessary because the temperature difference of the bath between a point near the surface of the heating element and another point at the bottom corner of the tank was reduced from about 6°C to 0.1°C by the stirrers. One disadvantage of the stirrer design in the present work was that the fused-salt bath had to be heated above melting point (190°C) before the stirrer could be removed from the bath. Another disadvantage was that a continuous rattling noise was produced by the gears on the stirrers during experimental runs. However, the movement of stirrers created negligible vibration on the reaction tank.

The infrared cell-reactor was insulated by a 1/8 inch thick asbestos plate followed by a 1/2 inch thick air gap and then another 1/8 inch thick asbestos plate. The entire set-up was then mounted on a projecting arm attached to a mobile rack. The position of the arm could be shifted vertically or horizontally. Such a design allowed the infrared cell-reactor tank to be introduced smoothly into the analytical compartment of the infrared spectrophotometer. Another two fine adjustments were also added so that the infrared cell-reactor tank could be placed at the desired depth and made parallel to the side-wall of the analytical compartment.

Some pinpoint leaks on the welded joints between the infrared cell and tank walls developed due to the corrosive action of the fused-salt bath and the thermal stress from the frequent heating and cooling of the equipment. Throughout the experimental work, the leaks were detected once and after repairing they did not reoccur.

The catalyst sample holder shown in Figure 5-3 was fabricated from 316 stainless steel, 2 15/16 inch long and 1 1/4 inch diameter at both ends but 1/8 inch smaller in the central portion. A groove with 1 1/64 inch diameter and 1/16 inch width was cut at the central portion for holding the catalyst wafer. The catalyst sample holder was designed to allow the vertical positioning of catalyst wafer and provide ample space for the passage of gases in the infrared reactor cell.

Before an experimental run, a catalyst wafer was placed into the groove of the sample holder. This was accomplished by picking the wafer up with a flat device such as a razor blade and inserting it horizontally into the groove of the sample holder. It should be done with great care in order not to break the thin wafer. The sample holder with catalyst wafer was then introduced into the reactor cell and positioned in such a way that the tip of the thermocouple in the

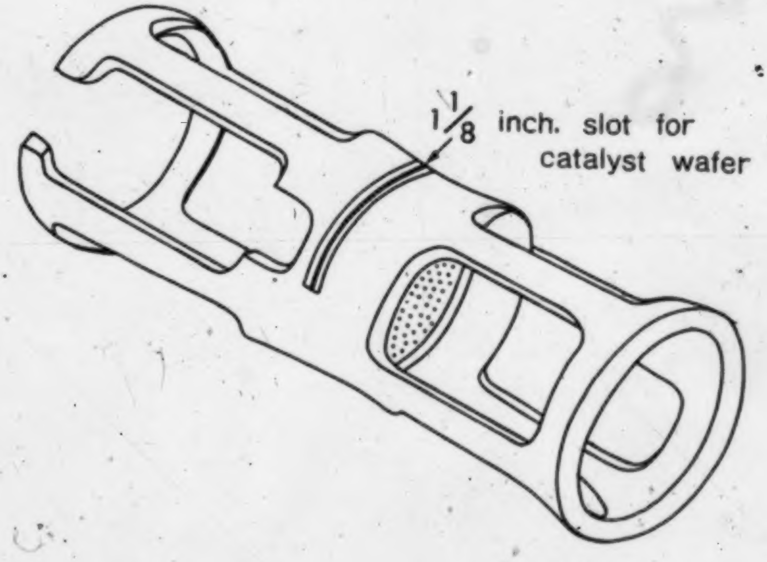

$2\frac{15}{16}$ inch. long

$1\frac{1}{4}$ inch. diameter at ends

1 inch. diameter in the middle

$1\frac{1}{8}$ inch. slot for catalyst wafer

Figure 5-3. Catalyst Wafer Holder in Infrared Cell-Reactor.

reactor pressed very lightly against the surface of the wafer. This operation was delicate because the catalyst wafer could be broken if pressed too strongly against the tip of the thermocouple. When placed in the reactor cell heated up to 300°C, the temperature of the central and edge portion of the catalyst wafer differed by about 0.4°C which was reduced to about 0.1°C after the recirculation pump had been switched on. The temperature difference between the fused-salt bath which was kept at 400°C and the center of the catalyst wafer was about 0.5°C with the stirrers in the fused-salt bath in operation. Although Claus reaciton is exothermic, the heat generated from reaction was so small compared to the capacity of the heat sink of the fused-salt bath that the temperatures of the three infrared cells in the reaction were essentially the same.

5.2 Process Measurements

The major process measurements include reactor temperature (at catalyst surface), reactor pressure (in the vicinity of the catalyst) and the feed flow rate. These recorded measurements were used for calculation of reaction conversions.

5.2.1 Reactor Temperature

An 1/8 inch diameter 316 stainless steel shielded iron-constantan thermocouple was introduced into the infrared-reactor cell with its tip touching the surface of the catalyst wafer to measure the reaction temperature. The thermocouple was connected to a Leeds and Northrup temperature recorder (Speedomax Type G). The recorder reading was calibrated against a known voltage input by potentiometer and the thermocouple was calibrated in a bath of known temperature before installation. The readings of the isothermal temperature bath bore a linear relation with those of the voltages measured by the thermocouple. By applying a least square fit to the readings, an equation in the form of $y = 5.6001 + 18.000x$ was deduced, where

y = temperature of the isothermal temperature bath, °K

x = signal measured by the recorder, mv.

at the end of each experimental run, a known voltage from the potentiometer was fed into the recorder to check the voltage indicated by the reading on the recorder. Throughout the whole experimental runs, no noticeable drift in temperature recording was experienced.

5.2.2 Reactor Pressure

A Statham 600 stainless steel absolute pressure transducer was installed at a port situated just beside the catalyst wafer in the infrared-reactor cell to measure the reaction pressure. The body of the absolute pressure transducer was located outside the reactor tank and was not in contact with the fused-salt heating bath. Therefore, there was a temperature difference of about 90°C between the catalyst wafer and the body of the absolute pressure transducer during the experimental run. The electronic components located in the body of the absolute pressure transducer limit the operating temperature to 316°C as recommended by the manufacturer, but with the set up used in the present work, the maximum operating temperature could be increased further by about 90°C. The absolute pressure transducer was connected to a Honeywell recorder. After the termination of each experimental run, a manometer whose reading was measured with a cathetometer was connected to the reactor to enable the reliability of the pressure transducer performance to be checked. The accuracy and reliability of the pressure transducer used in the present work was found to be very satisfactory.

5.2.3. Process Flow Rate

After the sulfur and water in the product stream were removed from the sulfur and water condensers, respectively, the remaining stream was passed into a cold slush bath to remove the unreacted reactants. The cold slush bath was formed by mixing n-propanol with liquid nitrogen in a Dewar flask. When properly mixed, a fluid slush at a constant temperature of -127°C was obtained. The slush was maintained by adding more liquid nitrogen into the Dewar flask occassionally. A more detailed description of such a cold slush bath has been reported by Rondeau [115]. The removal of the unreacted hydrogen sulfide and sulfur dioxide was so successful that the exit stream from the cold slush bath contained only the nitrogen diluent, as analyzed by mass spectroscopy. The exit stream from the cold slush bath was heated back to room temperature before entering the soap bubble meter for measurement of the nitrogen flow rate. A mercury thermometer was installed at the entrance of the soap bubble meter to measure the temperature of the nitrogen. From the measured nitrogen flow-rate and the feed composition analyzed by the gas chromatograph, the flow-rate through the reactor of all the feed components could be calculated.

When the cold slush bath was introduced to the cold trap, care must be taken to ensure that the solution level in the soap bubble meter was below the inlet nozzle. This prevented the soap solution from being sucked into the cold trap when a sudden temperature drop in the system was experienced upon the introduction of the cold slush bath.

5.3 Operation of Equipment and Experimental Procedure

Before the start of an experimental run, all components of the equipment were checked for proper conditions (especially the reciprocating recycle pump) and the reactor infrared cells and windows were inspected for cleanliness. If required, the Teflon O-rings of the infrared cells were replaced. If such replacement was not necessary, careful examination to make sure that all infrared windows were properly sealed was carried out. Depending on whether a "new" piece of catalyst wafer was needed, the preparation of it might or might not be necessary before the start of an experimental run. If it was necessary, the method of preparation was the same as that described in the previous chapter. The weight of catalyst wafer was found by weighing the sample holder with and without the wafer. This was not done by weighing the wafer directly because a loose portion of the wafer would usually drop off when placed in the sample holder. Before the catalyst wafer plus the holder were introduced into the reactor cell, they were carefully inspected for loose particle again. If loose particles were detected, they were gently blown free by compressed air and the weighing of catalyst wafer and holder repeated. The introduction of sample holder with catalyst wafer into the reactor cell should be done according to the way mentioned in Section 5.3.

5.3.1 Start-up and Catalyst Pretreatment

At start-up, the nitrogen flow was turned on by setting the regulator pressure at 100 psig. By adjusting the needle valve on the nitrogen feed rotameter, a slow stream of about 20 ml/min of pure nitrogen was purged through the reactor for about 1/2 h. During this time, the operation of process measurement and analytical equipment could be tested. The cold slush bath (mentioned in Seciton 5.2.3) could be prepared in a dewar by mixing n-propanol with liquid nitrogen. The operation of the soap bubble meter could also be checked with the pure nitrogen flowing. As soon as the bubble meter had been checked, all the soap solution was drained out of the meter into a bulb at the bottom. When the cold slush bath was prepared, it was placed onto the cold trap at the outlet of the sulfur and water condenser. A sudden decrease in the temperature of the cold trap could hence be created and a suction could occur. The soap bubble meter was drained earlier to prevent the soap solution from being sucked back into the cold trap. About 10 minutes after the introduction of the cold slush bath, the temperature in the cold trap became steady.

The power supply to the sulfur condenser, to the product lines at the outlet of the reactor and to the four heating elements in the fused-salt bath of the reactor tank was turned on. It is of utmost importance that the reactor be heated with nitrogen gas flowing because in doing so, the large quantity of water preadsorbed on the alumina from the atmosphere would vaporize and in turn would ruin the NaCl infrared windows by making them non-transparent. This was mandatory regardless of whether the start-up was performed with a "new" or "used" piece of catalyst wafer. The heat supply to the reactor should also be slow (about 3-4°C per minute) in order not to create a sudden thermal expansion which would crack the infrared cell windows. As soon as the temperature of the reactor started to increase, the temperature recorder could be turned on. After the temperature in the fused-salt bath exceeded 200°C (the eutectic point of the fused-salt bath was 190°C), the sitrrers in the bath were switched on to provide a good circulation of the fused-salt. The temperature controller on the reactor cell as well as the power supply to the Statham absolute pressure transducer were activated. Power was also supplied to the heating coils on all the lines in the reaction system (including feed preheater, recycle pump and the recirculation lines). With all the operations completed so far, the equipment was then at the stage for pretreatment of catalyst (if pretreatment is necessary).

In the present work, the methods of catalyst pretreatment (evacuated at 400°C for 24 h under a vacuum of 10^{-5} cm of Hg, heated at 400°C with a continuous stream of N_2, or H_2, or O_2 for 24 h, or just heated at 250°C with a continuous stream of N_2 for 24 h) did not affect the eventual steady state conversion. After this discovery, all pretreatment of catalyst were performed by heating at 250°C under a continuous flow of N_2 for 24 h. During the pretreatment, liquid nitrogen and/or n-propanol (depending on requirement) should be added to the dewar at 12 h intervals to make up for vaporization losses. Occasionally, the bath had to be stirred to maintain the slushy state.

At the beginning of a kinetic run, the reactor temperature on the controller was set at about 1-2°C below the desired temperature. Later, when the reaction had been started and steady state was approaching, fine adjustment could then be made to provide the final desired reaction temperature. The temperature of the recycle pump was lower than that of the reactor as mentioned in Section 5.1.2. When the recycle pump was switched on, the discharge line of the pump was heated to provide a uniform temperature between the three infrared cells. The air purge to the solid state pump control was also turned on. With only nitrogen flowing, the portion of feed stream branched to the gas chromatograph for analysis and the vent valve on the product stream were manipulated to provide an approximate required values of feed rate and reactor pressure. The nitrogen feed needle valve was readjusted if total flow was found to be too high or too low. The feed rate was measured by the soap bubble meter and the reactor pressure by the recorder reading of the absolute pressure transducer.

The operation of the gas chromatograph together with its sampling valve was then checked with pure nitrogen. The infrared spectrophotometer could be switched on and set up for analysis with a new recording chart paper. After every piece of experimental equipment was found to be operating in good condition, the flow of hydrogen sulfide gas was introduced at a rate near the desired level. The pressure regulator of hydrogen sulfide cylinder was set at 50 psig. The flow was maintained for about 1/2 h. If a new cylinder of nitrogen was used and it was desired to examine for the oxygen impurity in it, the feed and product cells of the reactor could be inserted into the analytical compartment of the infrared spectrophotometer for the possible detection of sulfur dioxide. Next, the sulfur dioxide gas cylinder was turned on with its pressure regulator set at 50 psig. As soon as the sulfur dioxide gas was introduced into the feed stream, both the needle valves of the hydrogen sulfide and sulfur dioxide rotameters were adjusted until the desired feed composition was achieved. The adjustment was performed on the basis of repeated comparison of the analytical results reported by the gas chromatograph. When the desired feed composition had been obtained, a final adjustment on the portion of feed flow that branched off to the gas chromatograph and the product vent valve to provide the desire reactor pressure and feed rate.

With the feed composition, flow rate and reactor pressure fixed, the reactor temperature controller set point was adjusted to give a final desired reaction temperature. While the reaction steadied out, the reactor temperature and pressure readings were constantly watched. The feed stream was also constantly analyzed by the gas chromatograph to ensure that the feed composition was reproducible. A steady feed flow rate as measured by soap bubble meter should also be ensured. The reaction was allowed to proceed for 1.5 h before the infrared spectroscopic analysis was taken. With the feed cell aligned with the sample beam and the reference beam of the infrared spectrophotometer opened to the atmosphere, the partial pressure of sulfur dioxide in the feed cell could be calculated (the method of calculation is mentioned in Section 5.5). A complete scan from 4000 cm^{-1} was performed and the attenuator of the infrared spectrometer was adjusted to provide a transmittance of about 80 to 90% through the feed cell at 4000 cm^{-1}. From the spectrum so recorded, the frequency set for reaction conversion analysis could be determined (as mentioned in Section 5.5). Moreover, any reaction occurring in the feed system upstream of the feed cell could be confirmed from the detection of water bands in such a spectrum. A typical gaseous SO_2 spectrum is shown in

Figure 5-4 and the frequencies of the characteristic bands are listed in Table 5-2.

5.3.2. Steady-State

When all process variables were fixed, a new recording chart paper was put on the infrared spectrophotometer to prepare for the reaction conversion analysis. The reactor tank was inserted into the analytical compartment of the infrared spectrophotometer. The feed cell of the reactor was aligned with the reference beam and the product cell aligned with the sample beam of the infrared spectrophotometer. A complete infrared scan from 4000 cm^{-1} to 500 cm^{-1} was performed. Due to reaction, the amount of SO_2 in the product cell was lower than that in the feed cell. As a result, the differential infrared scan would produce a spectrum with inverse bands. The magnitude of the inverse band reflected the extent of reaction occurring in the reactor cell at that particular instant. If the catalyst wafer was required to be analyzed in the hope of observing surface species or reaction intermediates, the product cell could be aligned with the reference beam and the reactor cell aligned with the sample beam of the infrared spectrophotometer. With such an arrangement, the infrared bands attributed to the species in the gaseous phase were compensated because of the equal and simultaneous signals detected by the reference and sample beam of the infrared spectrophotometer. Only the signals attributed to the catalyst wafer plus its surface species were recorded.

To determine the attainment of steady reaction state, the frequency at which the best sulfur dioxide spectral band was recorded was selected and set on the frequency knob of the infrared spectrophoto-

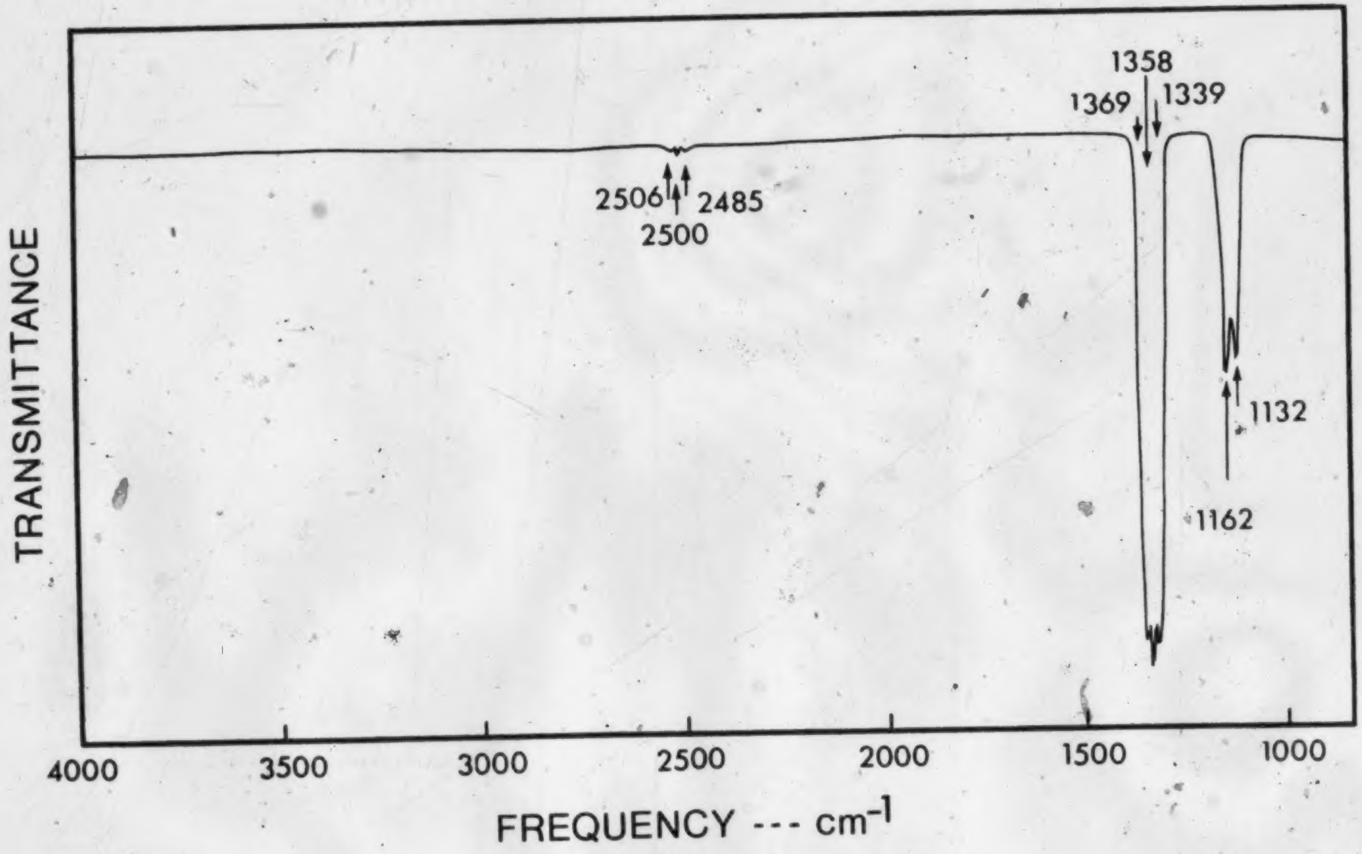

Figure 5-4. Infrared Spectrum of Gaseous SO_2.

meter. After the selection, the scan clutch control of the infrared spectrophotometer was turned to the "out" position. An infrared spectral scan was carried out at this single frequency of interest. A steady reaction state was considered to be reached when the magnitude of the inverse spectral band remained constant. The steady reaction state was maintained for at least an additional 1/2 h before a final complete infrared spectral scan was performed from 4000 cm^{-1} to 500 cm^{-1} with the scan clutch control of the infrared spectrophotometer turned to the "in" position. This scan was the same as that performed earlier to measure the reaction conversion. If the magnitude of the spectral bands recorded in the final scan was equal to that measured earlier, the recorded value was accepted and used for the kinetic calculations. Otherwise, the value was rejected and the reason for the discrepancy was investigated. One possible reason may be the contamination of the windows of the feed or product cell. This resulted in drift of the baseline of the spectrum and produced a change in the magnitude of the SO_2 bands. Naturally, this could also be due to a change in the process conditions.

The time spent to achieve a single data point was about 3-1/2 h after a "fresh" catalyst wafer had been pretreated. In the process of continuous kinetic runs, about 40 min. should be allowed to elapse starting from the time the reaction temperature was changed to another level before one more analysis on reaction conversion was taken. In cases where the feed flow rate was varied, about 30 min. were required before the reaction reached another steady state. For each "new" steady state, the check on attainment of constant reaction conversion as mentioned earlier was carried out before the analysis result was accepted.

5.3.3. Shutdown

On the termination of a kinetic run, the hydrogen sulfide and sulfur dioxide gas flow were the first to be terminated while maintaining the nitrogen gas flow and the equipment operating conditions. The residual hydrogen sulfide and sulfur dioxide in the reaction system could be flushed out by nitrogen in about 1/2 h as could be found by spectroscopic analysis. After the removal of sulfur dioxide and hydrogen sulfide from the reaction system, the cold trap which was accumulated with condensed H_2S and SO_2 was removed from the equipment together with the cold slush bath dewar and kept in the fan-hood. This was to allow the temperature in the cold trap to rise slowly to room temperature and to permit the condensed hydrogen sulfide and sulfur dioxide to be gradually and safely evaporated from the cold trap. After the removal of the cold trap, a manometer could be connected to the reactor to check the reliability of the pressure measurement by the Statham 600 absolute pressure transducer. The whole reaction system plus the sulfur and water condensers should be purged continuously with pure nitrogen while hot for about 3 h before being allowed to cool. To shut down the equipment, the temperature of the reaction system, especially the infrared cell should be allowed to cool slowly (at about 2°C per minute) to prevent the cracking of the NaCl (or CaF_2) infrared cell windows. This was done by slowly decreasing the power supply to the fused salt bath and to the nichrome wire on the discharge line of recirculation pump. Power supply to other heating systems as well as to the absolute pressure transducer could be turned off completely. The stirrers in the fused salt bath could be switched off while the recirculation pump should be in operation until the whole system returned to room temperature. When the whole system was cooled to room temperature, the recirculation pump was switched off. The sulfur and water condensers could be removed for cleaning if required (to remove condensed sulfur). The conditions of the Teflon O-rings on the infrared cells should be inspected. If a brownish color was observed, the O-ring was replaced by a new one. If required, the reactor cell could be opened for the removal of the catalyst wafer and its holder.

If another run is planned for the next day, it is recommended that the whole system be maintained near the desired "new" operating conditions but without the flow of hydrogen sulfide and sulfur dioxide. This is to minimize unnecessary thermal stress being imposed on the equipment (particularly on the infrared cell windows) due to the heating and cooling of the system and also to save time required to energize and stabilize the system. The introduction of a feed with only hydrogen sulfide and sulfur dioxide without nitrogen into the heated reactor containing the catalyst should strictly be discrouaged. The excessive sulfur so generated could condense on the recirculation pump and the infrared cell windows and might be very difficult to remove.

After shutdown, the catalyst wafer could be removed for examination of its condition if necessary. The infrared cell windows (NaCl or CaF_2) should also be removed and repolished if they had been contaminated and their transparency reduced.

The power to the infrared spectrophotometer should be switched off to prevent the overheating of its light source. Preferably, the gas chromatograph should be kept at operating condition during the period at which the experimental equipment was shutdown because it took about a day for the gas chromatograph to reach a steady operating condition after its start-up.

5.4. Analysis and Data Evaluation

5.4.1. Analysis

In the present work, both the infrared spectrophotometer and a gas chromatograph were employed as analytical tools. The reasons for not using the infrared spectrophotometer alone were twofold. First, the nitrogen gas which was used as diluent is infrared-inactive and second, the hydrogen sulfide gas which was one of the reactants, failed to provide a strong enough signal to allow reliable interpretation although it is infrared-active. On the other hand, the type of experiment conducted in the present work did not permit the employment of gas chromatography to analyse the reaction product because the sulfur in it had to be removed before the analysis. As sulfur was condensed and removed, it could catalyze the reaction between the unconverted hydrogen sulfide and sulfur dioxide. This created the uncertainty in the determination of the reaction rate previously described in Chapter II. Consequently, the gas chromatograph was used to analyze the feed stream which was free of sulfur and the infrared spectrophotometer was used to measure the conversion.

5.4.1.1. G. C. Analysis

Two columns connected in series were used in the gas chromatographic analysis. Both were made from 1/8 inch diameter 316 stainless steel tubing. The first column 4 ft long was packed with Chromosorb

104 and the second column 6 ft long was packed with Porapak Q-S. These columns were developed by the Chemical Laboratory, Department of Chemical Engineering, University of Alberta through trial-and-error and it was not clear which column accomplished which separation. Presumably, according to the nature of the packing, the first column separated H_2O from other components while both columns contributed to the separation of N_2, H_2S and SO_2. Before use, these columns were conditioned by purging with a flow of 40 ml/min helium at 200°C for 48 h. The column packings were found to be non-catalytic towards the reaction between hydrogen sulfide and sulfur dioxide because no water peak was detected when a gaseous mixture of nitrogen, hydrogen sulfide and sulfur dioxide was injected into the columns. The operating conditions of the gas chromatograph are summarized in the following table.

TABLE 5-1

OPERATING CONDITIONS OF GAS CHROMATOGRAPH

Chart speed:	0.5 inch/min
Sample size:	0.63 ml
Attenuation:	H_2S, SO_2 x 1; N_2 x 32
Bridge current:	250 mA
Detector temperature:	120°C
Column temperature:	80°C
Helium flow rate:	40 ml/min for both sample and reference

Among the chemicals analyzed, the columns provided the best analysis for hydrogen sulfide and the worst for water. With the same sample, the repeatability of the peak areas was better than 0.2%. The long-term analytical reliability of the columns was also periodically checked against samples with known compositions and a repeatability of better than 0.2% could be maintained. The gas chromatographic columns were calibrated by contrasting prepared standard gas samples against the peak areas. The calibration procedure and results are presented in Appendix A. Essentially, the area ratio of the gas chromatographic peaks of the hydrogen sulfide (or sulfur dioxide) and nitrogen gas was calibrated against the molar concentration ratios of these gases in the prepared samples. During experimental runs, the concentration ratio of hydrogen sulfide to nitrogen as well as sulfur dioxide to nitrogen could be calculated from the measured gas chromatographic area ratio by using the calibration results. Since ratio rather than absolute values of gas chromatographic area and concentration were calibrated, the sample size introduced into the gas chromatograph did not affect the analytical results. During calibration, various sizes of the same gas sample were injected into the gas chromatograph and it was found that the gas chormatographic area ratio for hydrogen sulfide (or sulfur dioxide) to nitrogen was not affected by the sample size nor the total pressure of the gas sample.

If the partial pressure of sulfur dioxide gas in the reactor is known (it was measured by the infrared spectrophotometer in the present work), the partial pressures of the hydrogen sulfide and nitrogen could be calculated from the concentration ratio recorded by the gas chromatograph. In conventional analytical approaches, the partial pressures of each species may be affected by the unknown partial pressure of sulfur vapor present in the system. This objectional procedure is eliminated when P_{H_2S} or P_{SO_2} may be measured directly.

5.4.1.2. I.R. Analysis

Unlike Chapter IV where the use of IR analysis was qualitative, the service from the infrared spectrophotometer in this chapter was mainly quantitative enabling for the measurement of reaction conversions and the partial pressures of SO_2 in the reaction system. During the simultaneous kinetic and mechanistic study in this chapter, qualitative IR analysis (essentially for detection of reaction intermediates on catalyst surface) was performed occasionally with quantitative IR analysis. The infrared cells used in this chapter were different from those used in Chapter IV as outlined separately in Section 4.1 and 5.1. In the kinetic runs involving low water and sulfur concentrations, NaCl windows were used on the infrared cell and for higher concentrations, CaF_2 windows were used.

Many excellent books [113, 137] have been written on infrared spectroscopic analysis. However, a brief discussion on infrared pectroscopic analysis will be provided in the following sections.

Generally, the quantitative analysis using infrared spectroscopy involves relating the absorbance to the concentration. If a pure component is analyzed and the extinction coefficient of this compound is known, its concentration in the infrared cell can be calculated from the measured absorbance by the following relation:

$$A_\lambda = \log[I_{o\lambda}/I_\lambda] = \epsilon C \ell \qquad (5.1)$$

Using ideal gas law, the expression, $A_\lambda = \varepsilon l P/(RT)$ results. This relation is called the Lambert-Beer law and is the same one used in routine colorimetric analysis,

where	A_λ	is the absorbance at wavelength
	$I_{o\lambda}$	the intensity of the incident beam
	I_λ	the intensity of the transmitted beam
	C	the concentration
	l	the length of the infrared cell
	ε	the extinction coefficient
	P	partial pressure of the gas sample
	T	absolute temperature under which analysis is carried out
	R	the gas constant

According to equation (5.1) for a given pure sample in a fixed infrared cell, the absorbance is related linearly to the concentration. The validity of this linear relation may not always be true over the entire pressure range under investigation. Until this validity is checked, the use of equation (5.1) for quantitative analysis should not be recommended. The most widely used procedure is to calibrate concentration versus absorbance.

In most experiments, gaseous mixtures rather than pure gas samples are analyzed. Under these situations, the recorded spectrum is a combination of those of all individual components. It is not uncommon that two or more components of the mixture absorb at the same wavelength. The total adsorbance of the recorded spectral band at this wavelength is equal to the sum of the adsorbance of each of the individual components. If the Lambert-Beer law is applicable, the total adsorbance is related to the concentration or partial pressure of each component as:

$$A_\lambda = \sum_i (\varepsilon_i C_i \ell) = \sum_i [\varepsilon_i P_i \ell / (RT)] \qquad (5.2)$$

where the subscript i refers to a particular species. Another interference includes the broadening effect on the spectral bands. Rao [113] has discussed several methods such as the ratio method to overcome the problems of overlapping bands. However, overlapping absorption bands often tend to decrease the accuracy of the analysis. Fortunately, many gaseous compounds have more than one absorption band. The overlapping of one or a few bands at the same frequencies between the gaseous component does not necessarily mean that all of the recorded bands are overlapping. As long as one isolated intense absorption band can be located for each compound, this band can be used for the analysis (qualitative and quantitative) of that particular component. If the Lambert-Beer law is applied, equation (5.2) reduces to:

$$A_{i\lambda} = \varepsilon_{i\lambda} C_i \ell = \varepsilon_i P_i \ell / (RT) \qquad (5.3)$$

As may be seen from the Lambert-Beer law, the magnitude of the absorbance does not depend solely upon the concentration. It varies also with the length of the infrared cell and the extinction coefficient of the sample. Since the length of the infrared cell is fixed, the range of concentration (or partial pressure) under which the analysis would be accurate depends on the value of the extinction coefficient. In infrared quantitative analysis, too large or too small an absorbance will both reduce the accuracy. If a sample has a large extinction coefficient, it would be most accurately analyzed at low pressures or concentrations, and vice versa. Hence, the range of partial pressures useful for infrared quantitative analysis may also be limited. For some gases, more than one absorption band appears in its infrared spectrum, each with a different intensity at the particular concentration. When the analysis is performed at a low concentration, the most intense suitable band should be chosen. As the concentration increases, the magnitude of this band would reach a value where the accuracy of analysis becomes questionable. At this value, a less intense band may then be used and the range extended. This greatly broadens the pressure range under which one can conduct experiments.

Another difficulty in the infrared quantitive analysis is encountered when the gas sample is infrared non-active. The absence of absorption bands is usually encountered by symmetric diatomic gases whose molecules are formed by two similar atoms, e.g. nitrogen, oxygen etc. If no dipole moment change resulted from atomic vibrations, infrared absorption bands do not appear. If only certain components in the gas mixture are infrared active, then the combined analysis must be obtained by the use of not only an infrared spectrophotometer but also other instruments, such as a gas chromotograph.

In the product stream, the absorption band of the sulfur species was not detectable from the recorded spectrum and that of water was found too noisy to provide an accurate analysis. As a result, sulfur dioxide was chosen as the key component for analysis. The partial pressures of other components in the product were then calculated from the stoichiometry of the reaction (2.1). Since no evidence for the occurrence of reaction other than the reaction (2.1) was observed under the experimental conditions in the present work, this approach seemed reasonable.

Three distinctive ioslated absorption bands around 2500, 1350 and 1150 cm^{-1} frequencies, respectively, appear in the recorded spectrum of sulfur dioxide, as shown in Figure 5-4. All three bands of SO_2 spectrum are of a type where the magnitude of P,Q,R bands are comparable. The frequencies of the peak of these bands are summarized in Table 5.2 together with the applicable partial pressure range. The band at around 1350 cm^{-1} possessed the highest extinction coefficient and was used for the lowest partial pressure range and that at around 2500 cm^{-1} for the highest partial pressure range.

The calibration curves indicated in Appendix C were prepared by introducing different amounts of SO_2 vapor into a quartz infrared cell identical to the stainless steel one used in the reactor as mentioned in Section 5.1.3. The reason for using a separate infrared cell and not that in Section 5.1.3 for calibration is because of the greater maneuverability of the former cell. The ability of this cell to maintain a vacuum for more than 36 h had been carefully checked and since the cell was required to hold a gas sample for less than 24 h in all the calibrations, inaccuracy due to leakages may be neglected. During calibrations, the infrared cell was connected to the vacuum rack equipped with a manometer. The cell was thoroughly evacuated before each introducion of gas sample. The pressure in the cell was measured from the manometer by reading with a cathetometer after a certain amount of SO_2 vapor was fed into the cell. In the first few calibrations, an initial pressure was recorded immediately after the introduction of gas sample into the cell and two readings were again

TABLE 5-2

FREQUENCIES AND PRESSURE RANGE EMPLOYED FOR QUANTITATIVE ANALYSIS OF SO_2

Frequency of Spectral Bands	Pressure Range Used
2480 2497 cm^{-1} 2509	6 cm Hg - 1 atm
1159 1130 cm^{-1}	1.8 - 20 cm Hg
1365 1351 cm^{-1} 1342	0.02 - 3.0 cm Hg

taken every 2 h. A final reading was taken after the SO_2 vapor had been in the cell for 14 h. It was observed from the first few calibrations that the pressure measured at 2 h after the introduction of gas sample was the same as those measured later. This showed that the amount of gas adsorbed on the wall was negligible compared to the total amount in the quartz infrared cell. After the first few calibrations, all other pressures were recorded at 3 h from the introduction of the gas sample. All the calibrations were carried out at 200°C. To examine the possibility of applying the calibration curves obtained at 200°C to other temperatures by using the ideal gas law, three calibrations were carried out, each at 200, 300 and 400°C, respectively. It was learned that the absorbances observed from these four calibrations were equal to those calculated from the calibration curves at 200°C by applying corrections based upon ideal gas behavior.

The compartment of the Perkin-Elmer Model 621 infrared spectrophotometer used in the present work was larger than that of the length of the infrared cell. During calibrations, the infrared cell was moved first closer to one end and then closer to the other end of the compartment of the infrared spectrophotometer. It was found that such variation of the position of the infrared cell in the compartment did not affect the recorded absorbance.

The pressure-broadening effect was found to be insignificant. This was checked by introducing mixtures of SO_2/N_2 or SO_2/H_2O vapor into the infrared cell and then comparing the recorded absorbance to that shown by the calibration curve. If the partial pressure of SO_2 in the mixture was the same as the presence of pure SO_2 at a similar temperature, the absorbance was found to be identical. The pressure-broadening effect by H_2S and sulfur vapor on sulfur dioxide was not examined. This was because hydrogen sulfide and sulfur dioxide could react slowly in the quartz cell and the introduction of sulfur vapor could create a danger of ruining the cell-window transparency by condensation.

Generally two methods may be used to relate the spectral band intensity to the partial pressure of gas. One is by peak height and the other is by the area of the spectral band. In the present work, since the peaks of the spectral band are quite sharp and a good straight line could be obtained from plotting peak height against partial pressure, the peak height method was thus adopted.

5.4.2. Data Evaluation

This section is devoted to an explanation of the procedure by which the reaction rates were derived from the experimental measurements. The descriptions on the methods of process measurements and the analysis by the gas chromatograph and infrared spectrophotometer have been mentioned in Sections 5.1 to 5.4.1.

A stainless steel infrared cell recirculation reactor was employed to generate experimental values of the reaction rate. Consider the recirculation reactor in Figure 5-5 where a reactant stream of fixed composition and flow rate is fed to the reactor loop. Let the conversion of the selected reactant, A, be zero at the reactor inlet, X_{A1}, just before the catalyst bed and, X_{Af} just after the catalyst bed. Also, assume that the rate of reaction is the same at all points in the differential catalyst bed for a specific run. A steady state material balance over the entire reaction suggests

$$X_{Af}F_{AO} = (-r_A)_{AV} (W) \qquad (5.4)$$

where $(-r_A)_{AV}$ is measured at some average conversion, i.e. at average reactant concentration values, of the streams entering and leaving the catalytic bed. Thus, X_{Af} X_{AV} X_{A1}. Since $(X_{Af} - X_{A1})$ may be large, the assumption of an average rate may lead to serious error.

Now suppose that a part of the product stream is recycled. As the recycle rate increases, the incoming feed is mixed with some

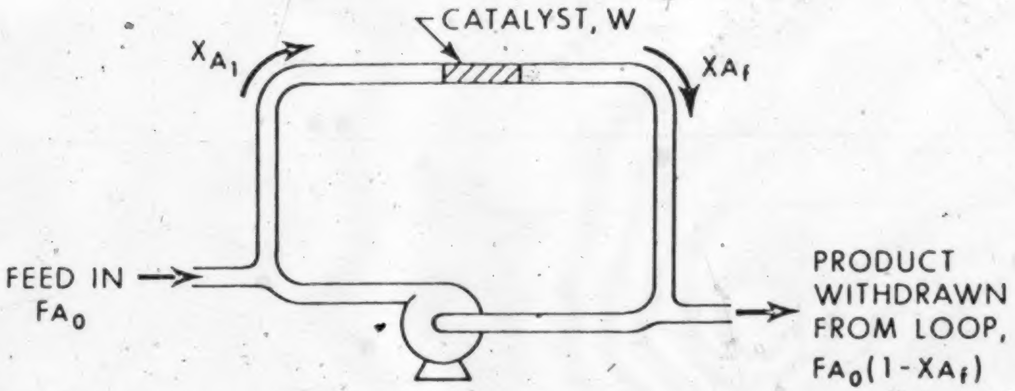
CATALYST, W
X_{A_1}
X_{A_f}
FEED IN
F_{A_0}
PRODUCT
WITHDRAWN
FROM LOOP,
$F_{A_0}(1-X_{A_f})$

Figure 5-5. Sketch of Recirculation Reactor Loop for Calculation of Reaction Conversion,

product stream causing X_{A1} to approach X_{Af}. Thus the error in the assumption of an average rate decreases accordingly and so at a high recycle ratios of R/(1-R),

$$(-r_A)_{AV} \quad (-r_A)_f = X_{Af}F_{Ao}/W$$

where the rate is measured at the exit stream conditions. At high recycle rates, this type of reactor may properly be considered to be a perfectly mixed backmix reactor. At high recycle ratios, the conversion of A per pass through the catalyst is small and the reactant concentration before and after the catalyst may be almost equal and the approximation of the above equation becomes more reasonable.

The capacity of the recirculation pump used in the present work was 45.1 /min and the volume in the entire recycle loop was 0.67 litres. The highest reactant feed rate (H_2S or SO_2) employed in the kinetic experiments was less than 0.1 ℓ/min. The recycle rate was therefore more than 60 times that of the feed rate throughout the entire kinetic runs. Accouding to Zwietering's [151] concept of "maximun mixedness", a recirculation reactor with a recycle ratio of over 20 approaches the behavior of backmix reactor.

In the present work, the reactor was designed in such a way that $(P_{Ao}-P_{Af})$ could be measured directly. By placing the feed cell of the reactor in the reference beam and the product cell in the sample beam of the infrared spectrophotometer, and by setting the infrared wavelength at which the SO_2 absorbance was most intense (refer to Table 5-2), an inverted spectral band which represents $(P_{Ao}-P_{Af})$ could be recorded. From the magnitude of this inverted spectral band, $(P_{Ao}-P_{Af})$ could be calculated. Before this method was adopted for use, the possibility of a difference in magnitude of the normal and the inverted spectral band had been carefully checked. A known partial pressure of SO_2 was introduced into the infrared cell. The cell was first placed in the sample beam of the infrared spectrophotometer to provide a normal spectral band. Then this cell was switched to the reference beam and an inverted spectral band was recorded. It was observed that the absolute magnitude of the positive end negative band was exactly equal. By knowing $(P_{Ao}-P_{Af})$, the fractional conversion of component A was approximated as,

$$X_{Af} = \frac{P_{Ao} - P_{Af}}{P_{Ao}}$$

By placing the feed cell of the reactor in the sample beam of the infrared spectrophotometer and using atmospheric air in the reference beam, a spectral band that represents the partial pressure of component A in the feed could be recorded. From the magnitude of the band and the calibration curve the "calibrated" partial pressure of component A in the feed could be calculated. The actual partial pressure of component A in the feed is then given by:

$$P_{Ao} = P_{A,calibrated} \times \frac{T}{473}$$

where T is the reaction temperature in degrees Kelvin. From the fractional conversion and the prartial pressure of A in the feed stream, the partial pressure of component A in the reactor was approximated by $P_{Af} = P_{Ao}\,(1-X_{Af})$. The partial pressures of other components in the reactor were calculated by the stoichimometry of the reaction, the feed stream composition and the correction for the change of modal flow rate due to chemical reaction. Since sulfur may exist in more than one form at the reaction condition, an equilibrium distribution among its different forms, $S_2 - S_6 - S_8$, was assumed and the partial pressure of each individual species calculated accordingly. McGregor [84] also used this assumption in his determination of the distribution of various sulfur species and concluded that such assumption was not in serious error. It was unfortunate in the present work that the various sulfur species were not detectable by infrared spectroscopy or else the equilibrium distribution assumption would not be necessary.

The material balance was checked by comparing the sum of the partial pressure of each individual species in the reactor with the measured total pressure of the reactor and it was found that the material balance was better than 98%. From the rate of reaction calculated and the partial pressures of all the species in the reactor, a set of data in the form of $(-r_A) = f(P_i)$ could be gathered under various experimental conditions and then employed for correlations of kinetic models.

An example showing step-to-step calculation of reaction rate together with material balance is exhibited in Appendix I.

CHAPTER VI

RESULTS AND DISCUSSION

6.1 Oxidizing Property of γ-Alumina

The Oxidizing Property of γ-alumina has been investigated [98,99,129] as mentioned in Section 2.3.3.2. Parkyns and Patterson [98] found that CO could be oxidized to CO_2 by γ-alumina. Flockhart et al. [39] observed that upon heating alumina aerogel previously in contact with air, nitric oxide might be given off in substantial amounts. Some investigators [97,135] related the catalytic activity of γ-alumina to its oxidizing property, especially towards reactions of a redox nature.

In the present work, the oxidizing property of γ-alumina was investigated by using infrared spectroscopic techniques. The γ -alumina catalyst was subjected to two types of pretreatments. Pretreatment (I) followed the steps described in Section 4.2 but pretreatment (II) consisted of an additional step of reducing the catalyst wafer with H_2 for 2 h followed by evacuation overnight, all at 400°C. The γ-alumina subjected to pretreatment (I) will be referred to as "oxidized-alumina" and the other referred to as "reduced-alumina". Figure 6-1 (A) and (B) represent the baseline spectra of the "oxidized-alumina" and "reduced-alumina". Only three spectral bands attributed to hydroxyl stretching frequencies in the 3650 to 3800 cm^{-1} region plus the alumina band at around 1000 cm^{-1} were recorded. No significant difference could be noticed between these two spectra.

To study the oxidizing property, the "oxidized-alumina" and

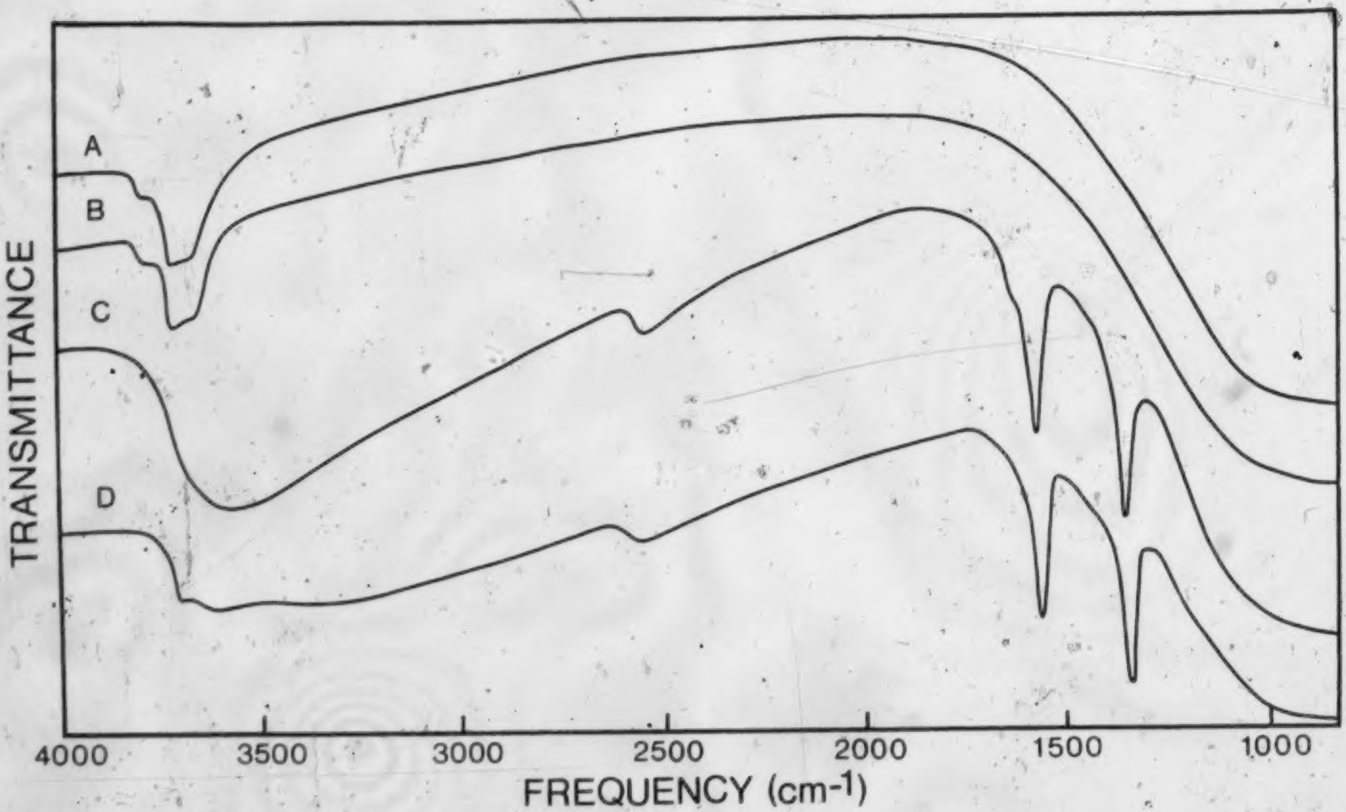

Figure 6-1. Infrared Spectra of (A) Oxidized γ-Alumina (B) Reduced γ-Alumina (C) H_2S Adsorbed on Oxidized γ-Alumina (D) H_2S Adsorbed on Reduced γ-Alumina.

"reduced-alumina" were exposed separately to an adsorbate and then the results were compared. Two types of adsorbates were used. Since H_2S is one of the reactants in the present work, it was chosen as one of the adsorbates. The other assorbate was CS_2. When H_2S is oxidized, water can be formed and it can further dissociate to form hydroxyl groups on the γ-alumina surface. The increase in surface hydroxyl groups may have resulted from dissociation rather than from oxidation of H_2S. By using CS_2 in place of H_2S, more information on the oxidizing property of γ-alumina could be obtained.

6.1.1 Oxidizing Property Demonstrated by H_2S Adsorption

Upon contacting H_2S at room temperature, the surface color of "oxidized-alumina" immediately changed from its normal white to violet-green, an observation previously noted [34] with the use of oxygen-pretreated γ-alumina. The violet-green color eventually changed into yellow after prolonged contact with H_2S at room temperature. An infrared spectrum of the "oxidized alumina" wafer recorded right after the contact with H_2S is shown in Figure 6-1 (C). This spectrum consists of a broad band at roughly 3550 cm^{-1} plus three other bands at 2560,1568 and 1345 cm^{-1}. The latter three bands are attributed to the adsorbed H_2S as suggested by earlier workers [34,133]. The broad band could be attributed to either H_2S or H_2O hydrogen-bonding, the latter resulting from the possible surface reaction,

$$H_2S + [O] \rightleftharpoons H_2O + [S] \qquad (6.1)$$

The states of [O] and [S] are unknown.

Comparing this psectrum with the baseline spectrum (6-1 A) of the "oxidized alumina", the spectral band at 3790 cm^{-1} was found to disappear upon contacting H_2S with "oxidized alumina". On the other hand, it was very difficult to conclude whether the other two hydroxyl stretching bands at 3720 and 3680 cm^{-1} disappeared as well or were covered by the broad band around 3550 cm^{-1}. Disappearance of the 3790 cm^{-1} hydroxyl band results from hydrogen-bonding of H_2S and H_2O. The weak band at around 1625 cm^{-1} could be the adsorbed H_2O.

The occurrence of the suspected reaction (6.1) was confirmed by mass spectral analysis of gases desorbed from the "oxidized alumina" after evacuation of the infrared cell to 10^{-3} Torr. Both water and elemental sulfur were detected. In addition, the introduction of sulfur vapor into a cell containing newly pretreated "oxidized alumina" or "reduced alumina" at room temperature produced the same color change. As adsorbed sulfur increased, the color changed from violet to green-yellow to yellow.

Upon repeating the H_2S adsorption experiment using "reduced alumina" at room temperature, the infrared spectrum of Figure 6-1 (D) was reduced. The three bands at 2560, 1568 and 1345 cm^{-1}, representing the adsorbed H_2S were again detected but the broad band at around 3550 cm^{-1} which was found upon contacting H_2S with "oxidized alumina" did not appear. Instead another weak broad band at around 3300 cm^{-1}, was observed. This may possibly be the hydrogen-bonding band of adsorbed H_2S. Unlike the "oxidized alumina", the hydroxyl stretching band at 3785 cm^{-1} was still present upon contacting the "reduced alumina" with H_2S. Neither product of reaction (6.1) could be detected by mass spectral identification, thus confirming that the occurrence of reaction (6.1) was the result of oxygen pretreatment of the γ-alumina. The color of the "reduced alumina" was unchanged by the contact with H_2S.

By comparing the results of the "oxidized alumina" and "reduced alumina", it seems that certain type(s) of surface oxygen exist on γ-alumina. Their states are unknown but capable of oxidizing H_2S according to reaction (6.1) and could be consumed by reduction with H_2.

6.1.2 Oxidizing Property Demonstrated by CS_2 Adsorption

Similar experiments were repeated by using CS_2 in place of H_2S. Figure 6-2 (A) and (B) represent the result of spectral scans obtained upon contacting CS_2 with "oxidized alumina" and "reduced alumina" at room temperature. The spectral bands at 2156 and 1495 cm^{-1} are in both cases attributed to physically adsorbed CS_2. Unlike the H_2S adsorption, the broad band at around 3500 cm^{-1} was not detected upon contacting CS_2 with γ-alumina. The band at 2000 cm^{-1} observed in Figure 6-2 (A) only reveals the formation of adsorbed COS, a species not previously present. Infrared spectral analysis of the gas-phase surrounding the catalyst wafer confirmed the formation of COS according to the possible surface reaction,

$$CS_2 + [O] \rightleftharpoons COS + [S] \qquad (6.2)$$

As in the case of H_2S adsorption, the states of [O] and [S] are unknown. An independent spectral scan for pure COS adsorbed on "oxidized alumina" confirmed the assignment of the 2000 cm^{-1} band. The white color of the catalyst changed to green-yellow, presumably caused by adsorption of

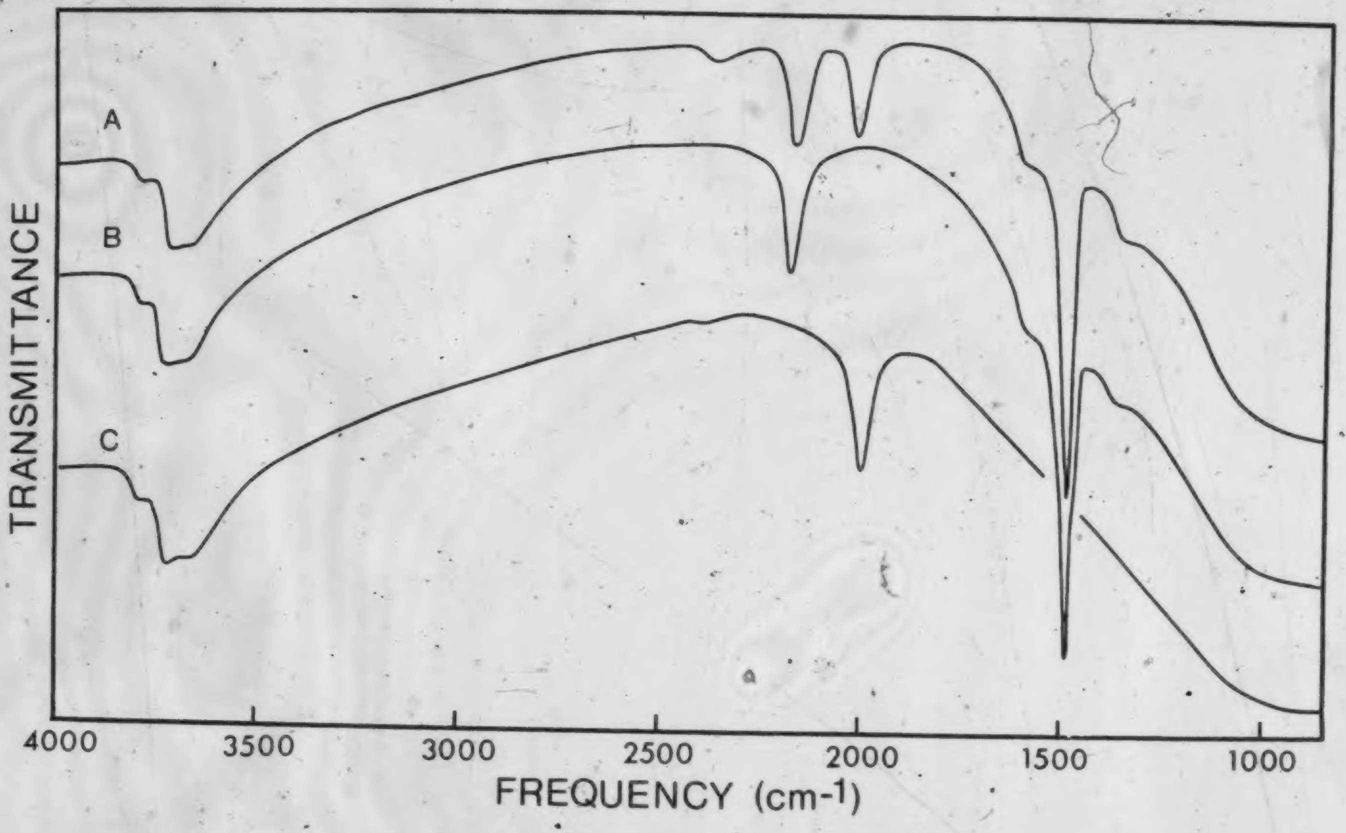

Figure 6-2. Infrared Spectra of (A) CS_2 Adsorbed on Oxidized γ-Alumina (B) CS_2 Adsorbed on Reduced γ-Alumina (C) COS Adsorbed on Reduced γ-Alumina.

elemental sulfur. These did not occur upon adsorption of CS_2 on "reduced alumina", as indicated by Figure 6-2 (B).

By examining Figure 6-2 (A) and (C) more closely, the 2365 cm^{-1} and 2200 cm^{-1} bands which are attributed to the adsorbed CO_2 and CO on γ-alumina are not detected in Figure 6-2 (A) while the 2365 cm^{-1} band is barely visible in Figure 6-2 (C). This probably means that the following reactions were not detected in the presence of excess CS_2 (in comparison to other components).

$$CS_2 + [O] \rightleftarrows CO + 2[S] \qquad (6.3)$$

$$CS_2 + 2[O] \rightleftarrows CO_2 + 2[S] \qquad (6.4)$$

6.1.3 The Postulated Forms of "Oxygen" on γ-alumina

When repeated doses of H_2S or CS_2 were exposed to "oxidized alumina", a diminishing extent of reaction (6.1) or (6.2) was observed. This was done by comparing the progressive increase in the magnitudes of H_2O (1625 cm^{-1}) and COS (2000 cm^{-1}) bands. Such result implies that this oxidizing character is associated with the finite amount of [O] available on the alumina surface. The "surface oxygen" could be restored by treating with gaseous O_2 or SO_2, ("used" wafer evacuated at 400°C for 10 h, treated with O_2 or SO_2 at 400°C for 2 h, again evacuated at 400°C for 10 h) although it is not certain in the case of SO_2 because of the possible formation of sulfate by SO_2 on γ-alumina surface. Water and sulfur could be formed by reacting sulfate with H_2S without the surface [O].

Two different interpretations may be suggested to explain the forms of [O] mentioned in reactions (6.1) and (6.2). The first is adsorbed "molecular" oxygen, a source suggested from studies of

Hydrocarbon oxidation [17,35], and the second is "strained-bridge" surface oxygen as proposed by Parkyns [99]. The strained oxygen bridge was envisaged by Cornehius et al. [27] as formed by progressive dehydration of alumina. The mechanism depicted below was proposed to account for the generation of such strained oxygen bridges from dehydration,

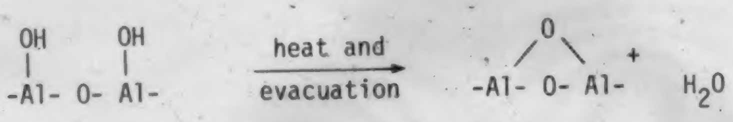

$$\begin{array}{c}\mathrm{OH}\\|\\-\mathrm{Al}-\end{array}\ \mathrm{O}-\ \begin{array}{c}\mathrm{OH}\\|\\\mathrm{Al}-\end{array}\ \xrightarrow[\text{evacuation}]{\text{heat and}}\ -\mathrm{Al}-\ \overset{\overset{\mathrm{O}}{/\ \ \backslash}}{\mathrm{O}-}\ \mathrm{Al}-\ +\ H_2O \qquad (2.30)$$

Tamele [135] and Cornelius et al. [27] reported that a remarkable amount of heat was released when water was contacted at 100°C with the carefully dehydrated alumina. This may be an indication of the reverse of the creation of strained oxygen bridges by dehydration. Parkyns [99] believed that these strained oxygen bridges were the "oxidizing centers" capable of oxidizing CO to CO_2 and could be restored by adsorbing NO to the γ-alumina which has been reduced by CO. On the other hand, Parkyns noted that degassing of alumina at temperatures above 450°C removed the active centers for oxidation of CO to CO_2. This temperature is relatively low for short-term surface recrystallization or annealing effects but degassing at this temperature should effectively desorb most of the molecular oxygen. The published results discussed so far seem to favor both interpretations.

Others used H_2O^{18} [57], O_2^{18} [38] and O_2^{17} [35] to investigate the isotope exchange with surface oxygen of alumina. All concluded that exchange of oxygen took place between the alumina and the adsorbate at relatively low temperature (around 100°C). Although such observations do not demonstrate beyond doubt which interpretation is correct, they seem to favor the strained oxygen bridge interpretation. It is more difficult to envisage how the strong bond of the molecular oxygen could be broken without the participation of the catalyst surface.

6.2 Adsorption of H_2S on γ-alumina

There are basically three types of adsorption sites on the surface of γ-alumina, namely: (i) the Lewis-acid sites made up of aluminum ions, (ii) the basic sites made up of oxide ions and (iii) the Bronsted-acid sites formed by the surface hydroxyl groups. The adsorption of the hydrogen sulfide involve one or more of these three types of sites and there still remains much controversy about which type of site is involved.

The adsorption of H_2S on γ-alumina at room temperature produces an infrared spectrum as indicated in Figure 6-1 (D). The spectrum is characterized by a broad hydrogen bonding band at around 3300 cm^{-1} plus three other bands at 2565, 1568 and 1345 cm^{-1} which are attributed to the various vibration modes of the adsorbed H_2S. Similar spectra have also been observed [34,133] but based on the IR spectrum alone, it is difficult to conclude on what sites and how H_2S is adsorbed.

The infrared band frequencies for H_2S and D_2S adsorbed on γ-alumina at room temperature are shown in Table 6-1.

TABLE 6-1

INFRARED BAND FREQUENCIES FOR H_2S AND D_2S ADSORBED ON γ-ALUMINA AT ROOM TEMPERATURE

Compound	Observed Frequencies (cm^{-1})	Gas-Phase Frequencies (cm^{-1})	Assignment
H_2S	1345	1290	H-S-H (bend)
	1568		
		2422	H-S-H (bend)
	2565	2611	S-H (stretch)
		2684	S-H (stretch)
D_2S	1860	1999	S-D (stretch)
		934	D-S-D (bend)

6.2.1 Selective Adsorption Method to Evaluate Sites of Adsorption

The approach adopted in the present work to study the adsorption of H_2S on γ-alumina involved the quantitative infrared spectroscopic method. The population of a particular type of surface site was selectively varied. The effect of such a variation upon the amount of H_2S adsorbed under a similar set of adsorption conditions was then evaluated. From the results so obtained, the type of sites involved in H_2S adsorption could then be determined.

The population of the surface Bronsted-acid sites was varied by evacuating the catalyst at different temperatures. After a γ-alumina wafer had been subjected to the pretreatment procedure mentioned in Section 4.2, pure water vapor was introduced to rehydrolyze the catalyst at room temperature. The "hydrolyzed" catalyst wafer was then evacuated under various temperatures. As temperature increased, the population of the Bronsted-acid sites (represented by the magnitudes of the hydroxyl bands of the infrared spectrum as indicated in Figure 6-3) decreased according to the following reaction

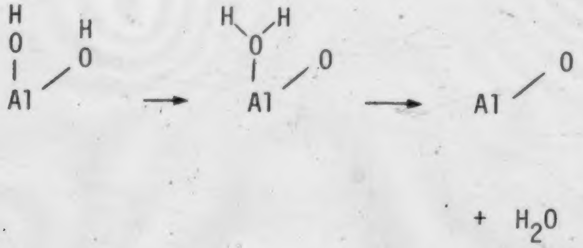

(6.5)

One the completion of evacuation at each temperature, the catalyst wafer was cooled back to room temperature for H_2S adsorption.

The aluminum ion sites on γ-alumina surface exhibit Lewis-acid behavior. An adsorbate with uncoordinated electrons is capable of interacting with aluminum ion sites (Lewis-acid sites). Both pyridine and ammonia molecules have an unshared pair of electrons on the nitrogen atom and hence are Lewis-bases. Parry and others [100, 104] have used pyridine and ammonia for selective adsorption on γ-alumina surface. Presumably, these two Lewis-bases are adsorbed on the Lewis-acid sites in the following manner

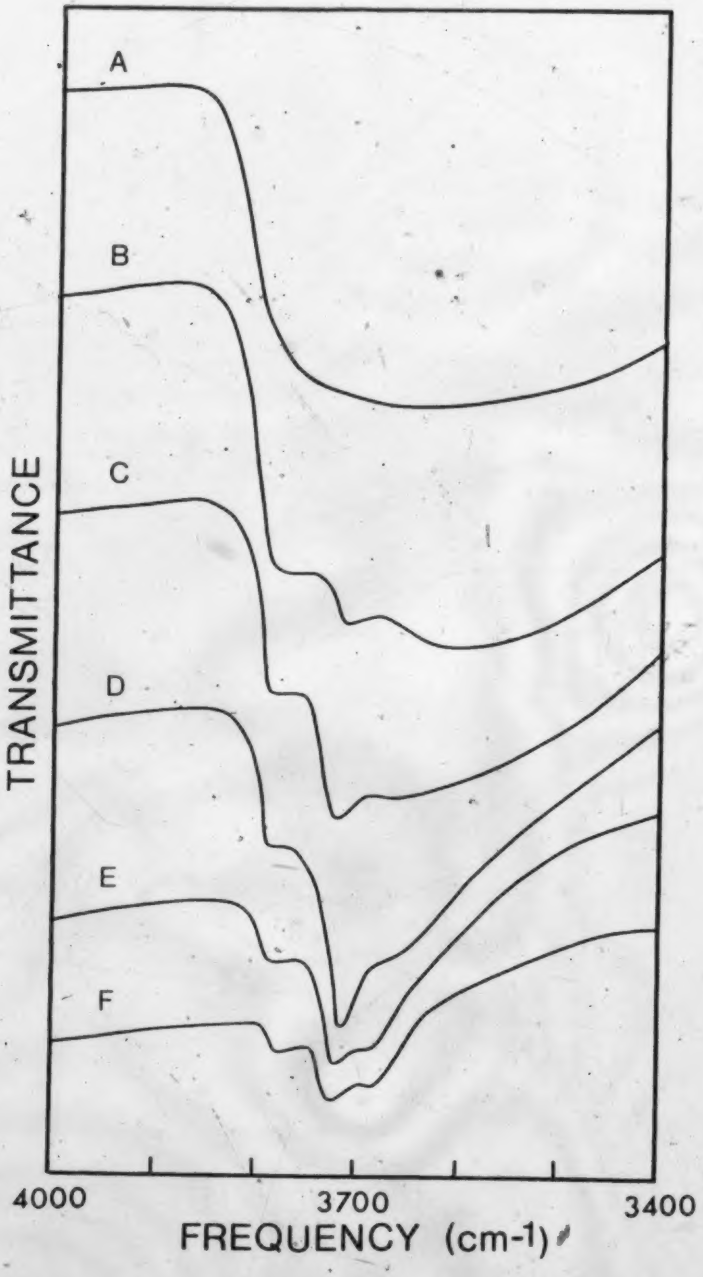

Figure 6-3. Infrared Spectra of OH Groups of γ-Alumina Evacuated at (A) Room Temperature (B) 100°C (C) 200°C (D) 300°C (E) 400°C (F) 500°C.

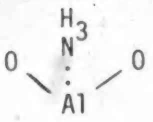

(2.18)

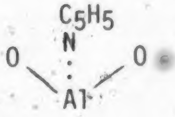

(2.19)

The infrared spectra of adsorbed ammonia and pyridine on γ-alumina are shown in Figure 6-4 (B) and (C). A broad hydrogen-bonding band at around 3500 cm^{-1} was observed with the disappearance of the hydroxyl band at 3785 cm^{-1} in both spectra. Both ammonia and pyridine were believed [104] not to adsorb on the Bronsted-acid sites through hydrogen-bonding. Rather, the hydrogen-bonding was formed between the adsorbate and the neighbouring Bronsted-acid sites. Other spectral bands of the adsorbed NH_3 occur at 3841, 3280, 1620 and 1442 cm^{-1}. The relative magnitudes of the latter two bands, were much larger than the former ones. For the adsorbed pyridine, the spectral bands were at 3085, 3064, 1617, 1575, 1490 and 1458 cm^{-1}. All bands but those at 1617 and 1458 cm^{-1} were weak.

The magnitude of the spectral bands of the adsorbed species could be varied in two ways: first, by using different pressures of adsorbate and second, by performing adsorption at different tempratures. In the present work, an arbitrary amount of pyridine or ammonia was contacted with the catalyst wafer at room temperature to provide an initial magnitude of spectral bands. The catalyst wafer was then evacuated at room temperature and eventually, by evacuating at progressively higher temperatures, it exhibited spectral bands of smaller magnitude.

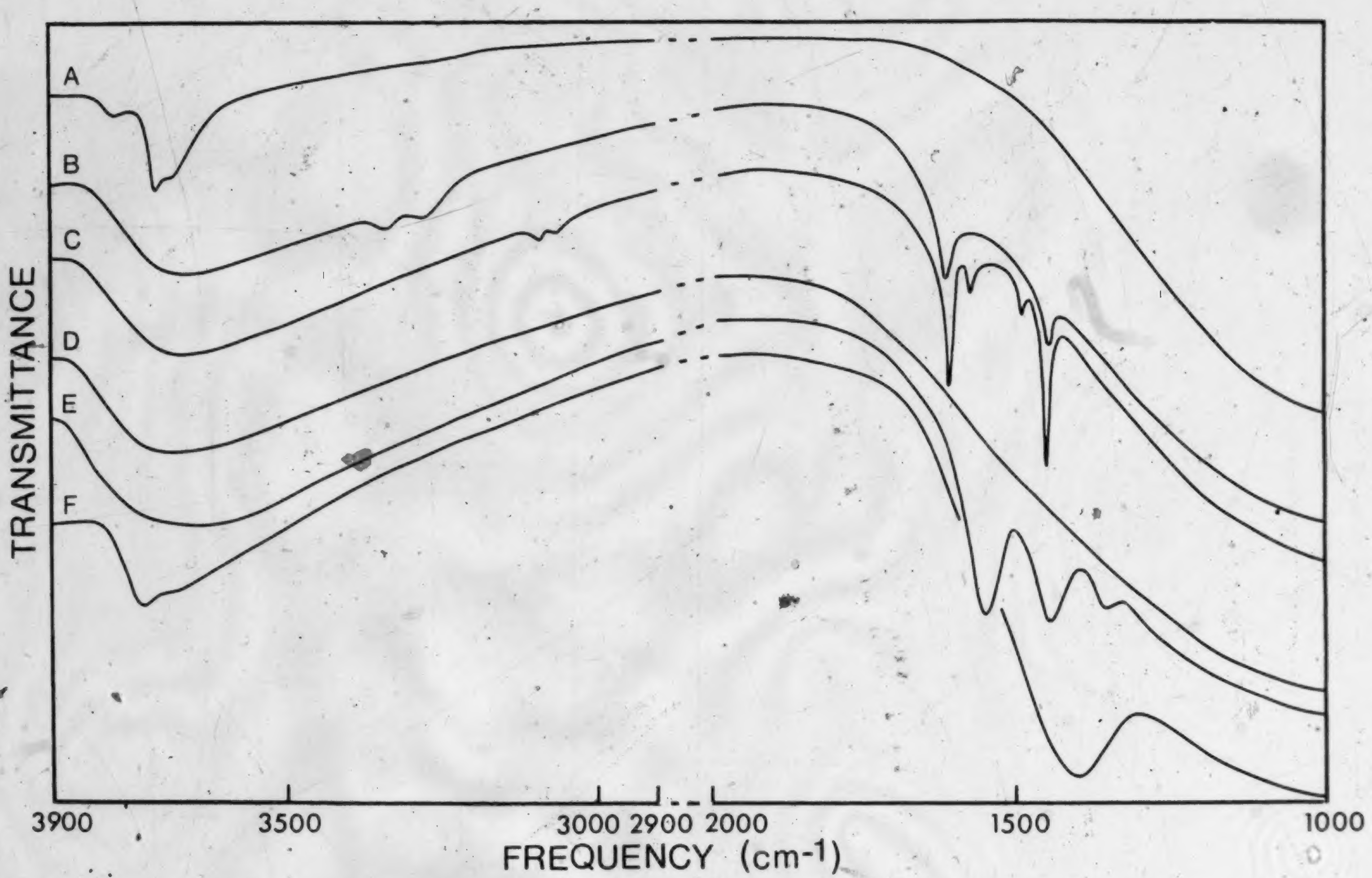

Figure 6-4. Infrared Spectra of Some Acidic and Basic Gases Adsorbed on Υ-Alumina (A) Baseline, (B) Ammonia, (C) Pyridine, (D) Hydrochloric Acid, (E) Acetic Acid, (F) Boron Trifluoride.

The intensities of the 1620 cm^{-1} and 1617 cm^{-1} spectral bands were chosen to represent the amounts of adsorbed ammonia and pyridine. This was due to their relatively strong intensity and freedom from interference of the spectral bands of adsorbed H_2S (and the adsorbed SO_2 discussed in Section 6.3). Both ammonia and pyridine were found not to react with hydrogen sulfide on Υ-alumina, as confirmed by the infrared spectroscopic analysis. Since ammonia and pyridine are both adsorbed on the Lewis-acid sites, the 1260 cm^{-1} or 1617 cm^{-1} spectral band could be used as a measure of Lewis-acid site occupation.

In the case of oxide ion sites, Schwab and Kral [128] found that boron trifluoride and acetic acid could be selectively adsorbed. Presumably, adsorption took place in the following manner.

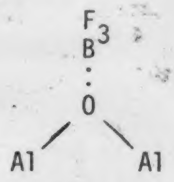

(6.6)

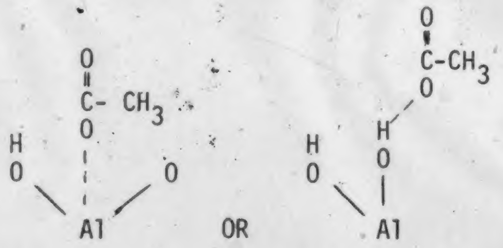

(I) (II)

(6.7)

The infrared spectrum of adsorbed acetic acid on Υ-alumina (Figure 6-4 E) is characterized by a broad hydrogen bonding band at around 3500 cm^{-1} and three other bands at 1561, 1468 and 1355 cm^{-1}. For adsorbed boron trifluoride (Figure 6-4 F), a spectral band at 1402 cm^{-1} is detected but not the broad hydrogen bonding band. In this work, the 1561 cm^{-1} band was chosen to represent the amount of adsorbed acetic acid on γ-alumina because of its relatively larger magnitude. For the adsorbed boron trifluoride, there was no choice but to pick the only band, 1402 cm^{-1}. Since acetic acid and boron trifluoride are adsorbed on the oxide-ion sites of γ-alumina, the magnitude of the 1561 cm^{-1} or 1402 cm^{-1} bands could be used as a measure of the occupation of these sites. The method of varying the amount of adsorbed acetic acid and boron trifluoride on γ-alumina was the same as that used for ammonia and pyridine. No reaction was found between hydrogen sulfide and acetic acid or boron trifluoride on γ-alumina surface, as confirmed by the infrared spectroscopic analysis.

With every variation in the amount of each adsorbate on γ-alumina, 5 cm Hg pressure of H_2S vapor was allowed to contact with the catalyst wafer later at room temperature for 2 h. An infrared spectrum of the adsorbates on γ-alumina was then recorded at room temperature. For each spectral scan, there are mainly two types of adsorbates on the catalyst surface. One is H_2S and the other is the species preadsorbed prior to H_2S exposure (ammonia, boron trifluoride etc.). Since each adsorbate (excluding H_2S) could be used as a measure of the occupation of a particular type of sites, by plotting the magnitude of the spectral band of this adsorbate and that of the adsorbed H_2S, the importance of a particular type of sites towards H_2S adsorption could be examined. When the Bronsted-acid sites are examined. When the Bronsted-acid sites are examined, only one adsorbate H_2S is present on the catalyst surface and the magnitude of the adsorbed H_2S spectral band is plotted against that of the surface hydroxyl groups. All results are summarized in Figure 6-5. There is not much significance on the absolute value of the infrared absorbance

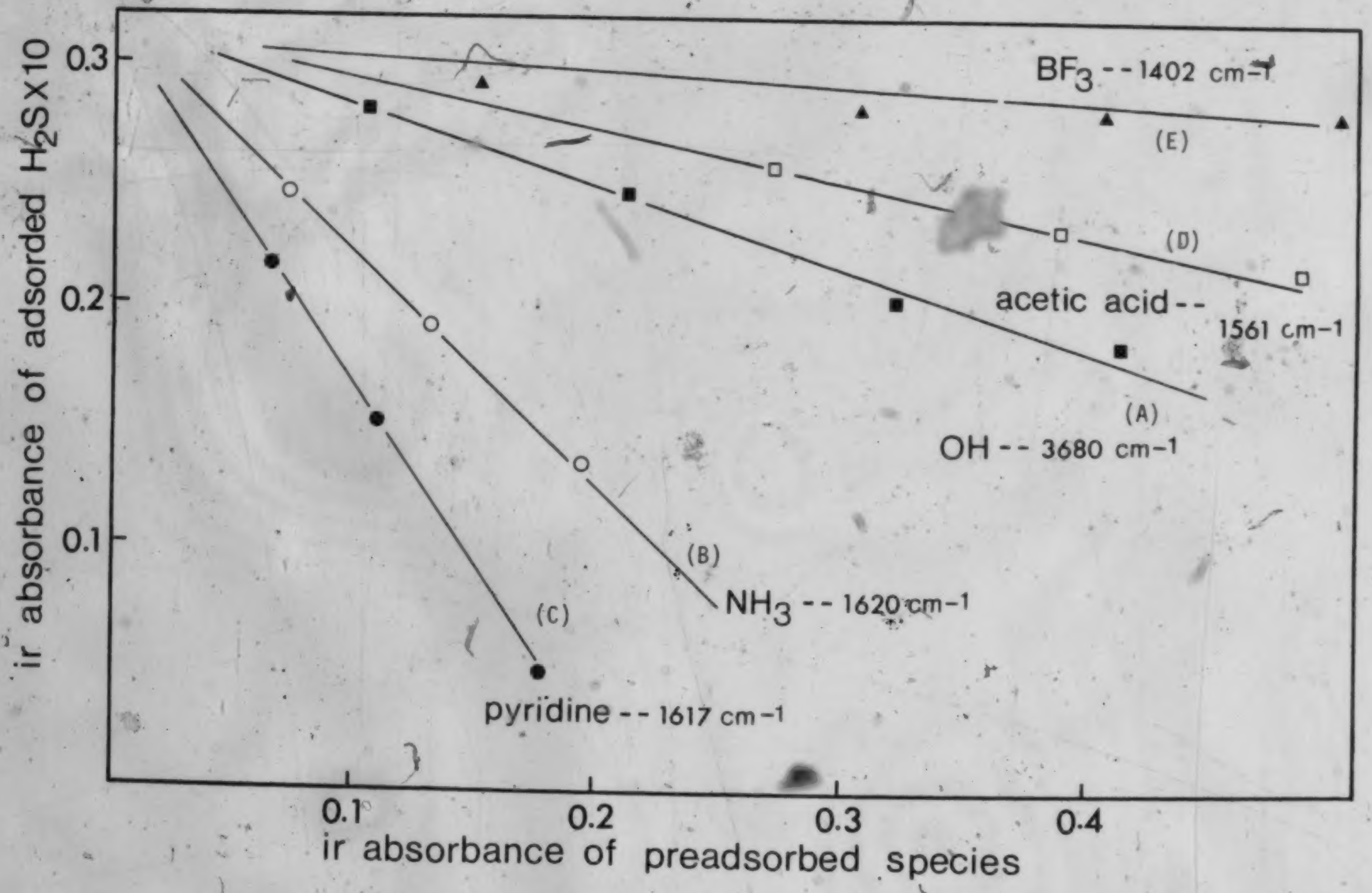

Figure 6-5. Effect of Preadsorption of Some Acidic or Basic Gases Upon H_2S Adsorption on γ-Alumina.

of the adsorbates shown. More important are the slopes of the lines, which will be used for discussion in the next section.

6.2.1.1 Bronsted-acid Sites

Deo et al. [34] proposed the following model for H_2S adsorption on the Bronsted-acid sites of γ-alumina based on the broad hydrogen bonding band and the disappearance of the hydroxyl band observed in his infrared spectrum of adsorbed H_2S.

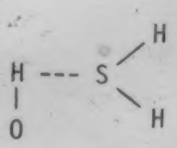

(2.26)

The hydrogen bonding was formed between the bydrogen atom of the Bronsted-acid site and the sulfur atom of H_2S.

The broad hydrogen bonding spectral band is not sufficient to verify the model proposed above. Peri [104] provided experimental evidence to prove that the broad spectral band around 3500 cm^{-1} could be attributed to the hydrogen bonding between hydrogen and oxygen. Deo et al. did not provide evidence or explanation about any difference in the spectral bands between the hydrogen bonding formed by hydrogen-oxygen and that by hydrogen-sulfur. The following models probably can also account for the same observation of the broad hydrogen bonding band produced by adsorbed H_2S on γ-alumina.

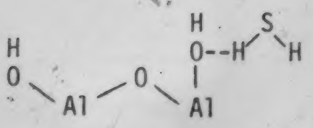

(II)

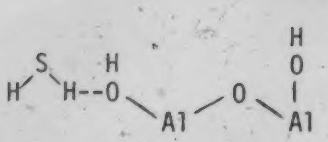

(III)

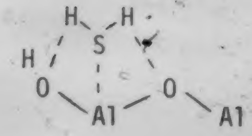

(IV)

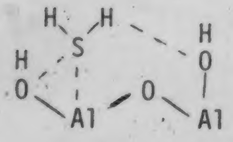

(V)

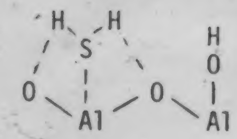

(VI)

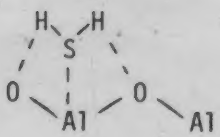

(VII)

(6.8)

On the surface of a catalyst, one type of site may not be completely isolated from the influence of other types of sites in the neighboring area. As measured by Peri [104], there is always a significant quantity of hydroxyl groups on the surface of γ-alumina, even at temperature as high as 500°C. Hydrogen bonding formation need not proceed via the adsorption of adsorbates on the surface hydroxyl groups.

Figure 6-5 (A) shows that as the magnitude of surface hydroxyl band (population of Bronsted-acid sites) increases, the magnitude of the adsorbed H_2S band (population of adsorbed H_2S) decreases. If H_2S is adsorbed on the Bronsted-acid sites, as proposed by Deo et al. [34], the reverse situation should happen. The results in Figure 6-5 (A) clearly demonstrate that H_2S is not adsorbed on the Bronsted-acid sites of γ-alumina. As a result, the broad hydrogen bonding band and the disappearance of the 3785 cm^{-1} hydroxyl band recorded by Deo and also in the present work should be interpreted as the interaction of adsorbed H_2S with the neighboring oxide-ion sites and Bronsted-acid sites of γ-alumina.

On the other hand, if H_2S is not adsorbed on Bronsted-acid sites, then the line in Figure 6-5 (A) should be horizontal. This means that a fixed amount of H_2S may be adsorbed regardless of the population of Bronsted-acid sites. This will be explained in greater detail in Section 6.2.1.3.

6.2.1.2 Oxide-ion Sites

Very little has been discussed in the literature about H_2S being adsorbed on the oxide-ion sites of γ-alumina. Deo et al. [34] proposed that SO_2 could interact with the surface oxide-ion sites to produce a sulfate like structure shown below

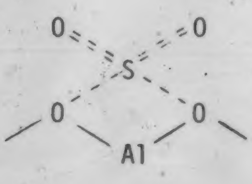

(2.29)

Using similar model, the interaction of H_2S with oxide-ion sites was suggested by Deo et al. [34] as shown below

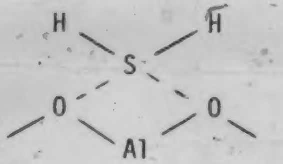

(6.9)

Figure 6-5 (D) and (E) both exhibit the relation between the extent of occupation of oxide-ion sites (magnitude of the spectral bands of adsorbed acetic acid or boron trifluoride) and the population of adsorbed H_2S. The almost horizontal straight line of Figure 6-5 (E) implies that no matter how many oxide-ion sites were occupied by boron trifluoride, about the same amount of H_2S can be adsorbed on the γ-alumina surface. The results clearly demonstrated that H_2S is not adsorbed on the oxide-ion sites. The more negative slope of the line indicated by Figure 6-5 (D) will be explained in greater detail in Section 6.2.1.3.

6.2.1.3 Lewis-acid Sites

De Rosset et al. [33] found that adsorbed H_2O or H_2S both presented the development of the acid color by dicinamal acetone ($pK_a = -3.0$) on γ-alumina surface. While it is difficult to determine whether conversion of the dye to its conjugate acid is due to interaction with a Lewis- or Bronsted-acid site, the experiment clearly showed that H_2S reacts as a base with the acid sites of γ-alumina. High isosteric heats of adsorption for H_2S (25 to 38 Kcal/mol, depending on the degree of predrying of the alumina) were detected by De Rosset et al. and they argued that reaction of H_2S with a surface Bronsted-acid site (as suggested by Deo et al.) by hydrogen bonding could not account for a high heat of adsorption. Instead, reaction of H_2S at a Lewis-acid site would create an Al-S bond and more nearly satisfy energetic requirements. They did not indicate whether such adsorbent-adsorbate interaction was capable of transforming part of Al_2O_3 into Al_2S_3. Similar high isosteric heats of H_2S adsorption (16.3

and 32.5 Kcal/mol at 0.02 mol/m^2 and 0.42 mol/m^2 at 423°K) on γ-alumina were also measured by Glass and Ross [46].

In the present work, the strong interaction of adsorbed H_2S with γ-alumina surface was also noticed. The magnitude (absorbance) of the spectral bands at 2565, 1568 and 1345 cm^{-1}, which represent the adsorbed H_2S on γ-alumina, could not be diminished by prolonged evacuation at room temperature.

Figure 6-5 (B) and (C) exhibit the relation between amount of adsorbed ammonia and pyridine (which represents the extent of occupation of Lewis-acid sites) and that of adsorbed H_2S and γ-alumina. The plot shows that as more Lewis-acid sites are occupied (more adsorbed ammonia or pyridine) less H_2S could be adsorbed. This implies that Lewis-acid sites are important for H_2S adsorption, a conclusion which coincides with that of De Rosset et al. The H_2S adsorption can be represented by any one of the following models depending upon which sites are in the immediate vicinity of the adsorbed H_2S.

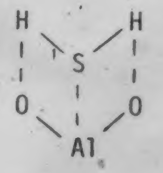
(I)

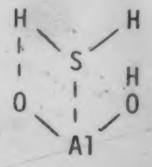
(II)

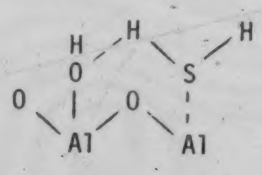
(III)

(6.10)

All three models could exist simultaneously on the catalyst surface and all could involve hydrogen bonding and agree with the results of infrared spectrum for adsorbed H_2S on γ-alumina.

Slager and Amberg [133] did not believe that H_2S is adsorbed on Bronsted-acid site of γ-alumina by hydrogen-bonding, as proposed by Deo et al. [34]. They observed a shift of -166 cm^{-1} asymmetric stretching frequency and +51 cm^{-1} bending frequency from the gas-phase to adsorbed H_2S by using infrared spectroscopic measurements. Such a shift could not be explained by the hydrogen bonding formation between the sulfur atom of the Bronsted-acid site. They proposed the following model for H_2S adsorption.

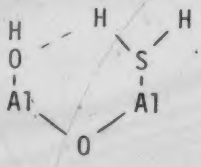

(2.27)

In this model, H_2S is adsorbed on the Lewis-acid site which agrees with the experimental results of the present work. Hydrogen bonding is formed between the hydrogen atom of the H_2S and the oxygen atom of the Bronsted-acid site.

In addition, they also observed the increase in intensity of the spectral bands in the hydroxyl and hydrogen bonding region of around 3600 cm^{-1} as well as the appearance of the spectral band at 1625 cm^{-1} which represents the bending mode of the adsorbed water. They proposed that adsorbed H_2S decomposes to produce hydroxyl groups and water as shown below,

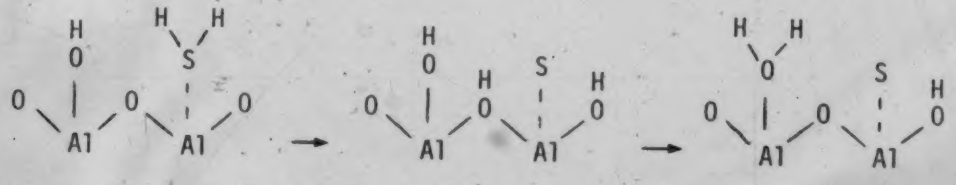

(2.28)

These were supported by infrared spectroscopic and gravimetric measurements. The authors could obtain a linear relation between the total weight of the adsorbed material and the sum of the area of the infrared spectral bands of the adsorbed H_2S and H_2O.

The γ-alumina catalyst used by Slager and Amberg was pretreated in the same way as the "oxidized-alumina" in the present work mentioned in Section 6.1. Results similar to those observed by Slager and Amberg were discussed in Section 6.1 upon adsorption of H_2S on "oxidized alumina", although a broad hydrogen-bonding band at around 3300 cm^{-1} band was recorded. It was difficult to confirm whether there was any increase in hydroxyl groups upon H_2S adsorption on "reduced alumina" because all spectral bands of the hydroxyl groups (except that of 3785 cm^{-1}) were covered by the broad hydrogen bonding band. From the close similarity of the molecular structures of H_2S and H_2O and the slight difference between the dissociation energies of OH and SH bonds, it is quite possible that some adsorbed H_2S can dissociate in a similar way to that of H_2O upon dehydrated γ-alumina as confirmed by many published works [100,104]. The possible dissociation of H_2S on γ-alumina was demonstrated in the present work by isotopic exchange method. First, the surface OD groups which have infrared bands at around 2700 cm^{-1} were created by contacting D_2O vapor with γ-alumina. On contacting the γ-alumina with H_2S, the magnitude of the OD bands diminished while that of OH groups increased. The qualitative adsorption-dissociation nature of H_2S has also been investigated by Sabatier and coworkers [122,123]. De Rosset measured H_2S adsorption on γ-alumina and from the energy of adsorption, concluded that some adsorbed H_2S dissociated with the formation of surface aluminum sulfide.

Little is known about the nature of H_2S dissociative adsorption, e.g. what percentage of the adsorbed H_2S is dissociated and under what conditions. However, it has been demonstrated in the present work that dissociation of adsorbed H_2S on γ-alumina, if it occuurs, did not proceed far enough to produce adsorbed H_2O because the spectral band of adsorbed H_2O at 1625 cm^{-1} was not detected upon adsorption of H_2S on "reduced alumina".

6.2.2 Adsorption Model Concluded from the Present Work

From the results mentioned in Section 6.2.1, it has been concluded that H_2S is not adsorbed on the Bronsted-acid or the oxide-ion sites of γ-alumina. It is adsorbed on Lewis-acid site and presumably a strong chemical bond is formed between the adsorbate and adsorbent because adsorbed H_2S could not be removed by evacuation at room temperature. The postulated adsorption model is shown below, which is similar to that by Slager and Amberg [133].

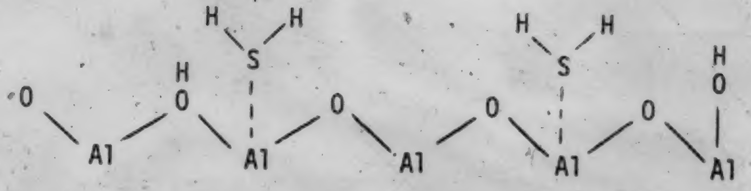

(6.11)

The H_2S is adsorbed on Lewis-acid site via its sulfur atom and various hydrogen bonds can be formed as shown depending on the types of sites in the immediate vicinity of the adsorbate. The above model also agrees with the experimental evidence collected from a number of other published works [33,133].

Partial decomposition of adsorbed H_2S on dehydrated γ-alumina is possible although the extent of decomposition is not certain and it does not proceed far enough to produce adsorbed water. Immediate formation of water upon adsorption of H_2S on dehydrated alumina is not likely without the presence of surface oxygen (Section 6.1). Some of these results agree with those of past workers [34,133].

The adsorption of H_2S on Lewis-acid sites can be used to explain the results in Figure 6-5 (A), which shows that although Bronsted-acid sites are not responsible for H_2S adsorption, they do affect the amount of adsorbed H_2S on γ-alumina. As Bronsted-acid sites increase, the amounts of adsorbed H_2S on γ-alumina decreases. As proposed by Peri [104] and Parry [100], the hydration of γ-alumina by water involves the creation of two Bronsted-acid sites and the occupation of one Lewis-acid and one oxide-ion site.

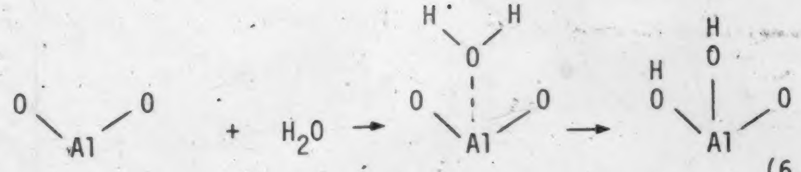

(6.5)

Therefore, as more Bronsted-acid sites are created by increasing hydration, more Lewis-acid sites are occupied. With H_2S being adsorbed on Lewis-acid sites, it explains why the amount of adsorbed H_2S decreases with increase in Bronsted-acid sites.

A similar explanation applies to Figure 6-5 (D), which shows that progressively less H_2S could be adsorbed if the γ-alumina surface is preadsorbed with increasing amounts of acetic acid. As acetic acid is adsorbed, one Lewis-acid and one oxide-ion site are occupied

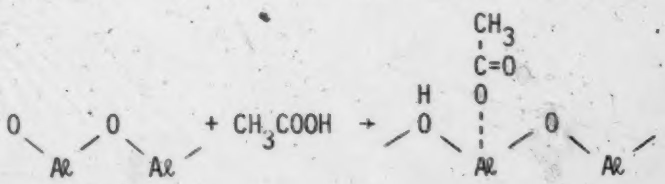

(6.7)(I)

6.2.3 The Effect of Temperature on H_2S Adsorption

In the previous Sections, the measurements of H_2S adsorption were carried out at room temperature. To provide more informations, the adsorption was also investigated at higher temperatures. Figure 6-6 shows the infrared spectra of the adsorbed H_2S on γ-alumina wafer at various temperatures. At each temperature, about 5 cm Hg absolute pressure of H_2S vapor was allowed to contact the wafer for 2 h before an infrared spectrum was recorded.

As indicated in Figure 6-6, the magnitude of the infrared spectral bands of adsorbed H_2S decreases as the adsorption temperature increases. At temperatures above 100°C, these bands become almost undetectable. This may or may not indicate the absence of adsorbed H_2S at temperatures higher than 100°C. It depends on the sensitivity of the infrared spectroscopic analysis of adsorbed H_2S. With less than half a gram of γ-alumina in the wafer the amount of adsorbed H_2S may be too low to allow infrared spectroscopic detection. From the volumetric measurements of H_2S adsorption on γ-alumina by de Rosset [33] and Ross [45], significant amounts of H_2S could be adsorbed at a temperature as high as 500°C. Table 2-3 shows some of the adsorption data collected by De Rosset and Ross. The reason suggested why the volumetric method could detect H_2S adsorption on γ-alumina but the infrared spectroscopic method could not is that a much larger sample of γ-alumina could be used in the volumetric method. In the infrared spectroscopic method, too large a sample would produce a wafer with a thickness that would substantially reduce its transparency to the infrared beam and this, in turn, greatly reduces the analytical sensitivity.

6.3 Adsorption of SO_2 on γ-alumina

The work described in this Section parallels that described in Section 6.2 except that SO_2 instead of H_2S was used.

The adsorption of SO_2 on γ-alumina at room temperature produced an infrared spectrum characterized by a broad hydrogen bonding band around 3500 cm^{-1} with the disappearance of the hydroxyl band at 3785 cm^{-1} as shown in Figure 6-8 (A). Three other spectral bands at

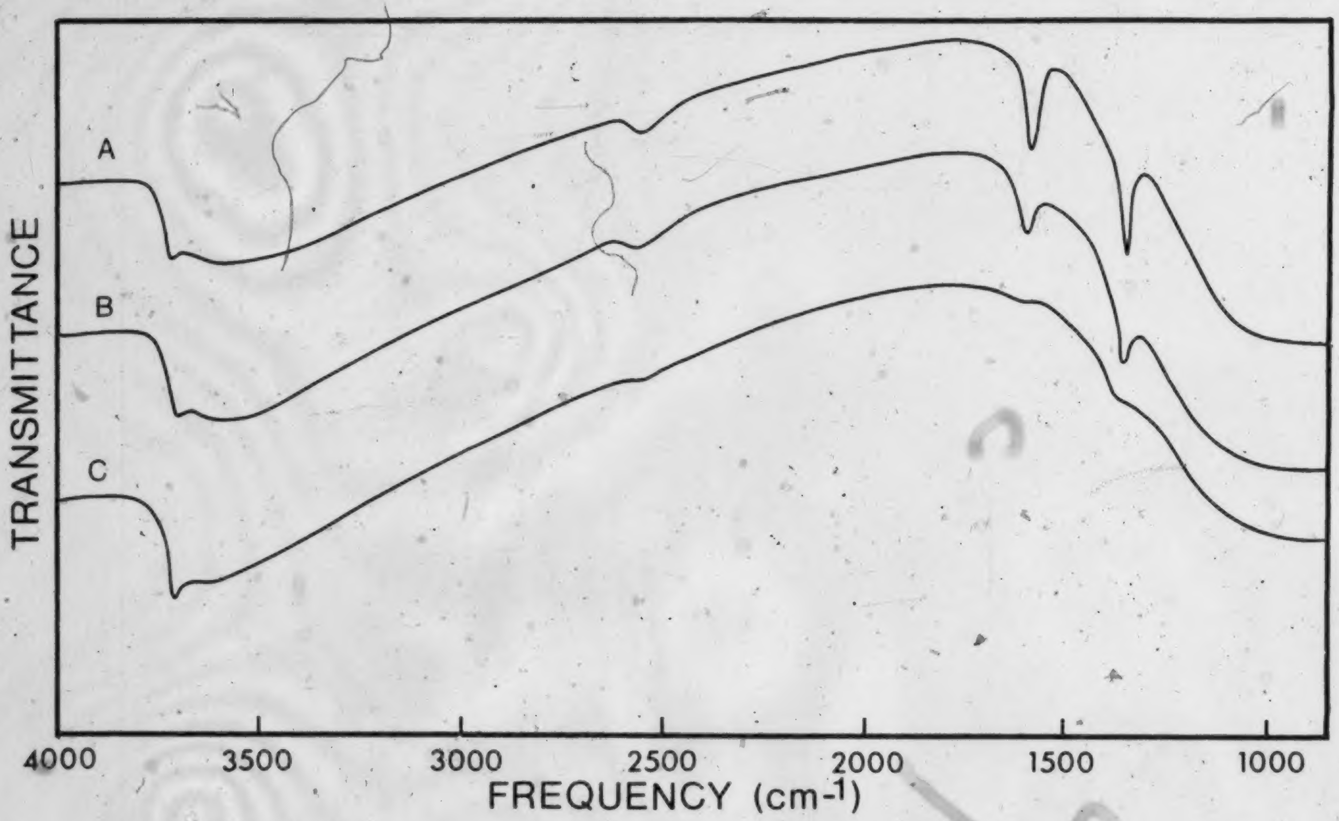

Figure 6-6. Adsorption of H_2S on γ-alumina at Various Temperatures.
(A) Room Temperature, (B) 50°C, (C) 100°C

2499, 1335 and 1140 cm^{-1} attributed to adsorbed SO_2 were also detected. These agree with other observations [34,78]. From the infrared spectrum alone, it is difficult to conclude what type of site which SO_2 is adsorbed on γ-alumina. Unlike the H_2S adsorption, the color of γ-alumina wafer did not become yellow. Identical results were obtained regardless of whether SO_2 is adsorbed on "oxidized alumina" or "reduced alumina". The infrared spectral band frequencies for gas-phase SO_s and SO_2 adsorbed on γ-alumina are summarized in Table 6-2.

TABLE 6-2

INFRARED BAND FREQUENCIES FOR SO_2 ADSORBED ON γ-ALUMINA AT ROOM TEMPERATURE

Compound	Observed Frequencies (cm^{-1})	Gas Phase Frequencies (cm^{-1})	Assignment
SO_2	1140 1335	1130 1159 1342 1351 1365	S-O (stretch)
	2499	2480 2497 2509	S-O (bend)

6.3.1 Selective Adsorption Method to Evaluate Sites of Adsorption

The methods and experimental steps used in this Section to evaluate the type of site for SO_2 adsorption on γ-alumina were exactly the same as those described in Section 6.2.

From the infrared spectroscopic analysis, it was found that no reaction occurs between the adsorbed SO_2 and any other absorbate used in the present work. The results for SO_2 adsorption on γ-alumina which are analagous to those of H_2S adsorption in Section 6.2 are summarized in Figure 6-7.

6.3.1.1 Bronsted-acid Sites

Deo et al. [34] studied the SO_2 adsorption on γ-alumina using infrared spectroscopic techniques and with the broad hydrogen bonding spectral band at around 3500 cm^{-1} plus the disappearance of the hydroxyl band at 3785 cm^{-1}, they proposed that SO_2 may be adsorbed according to the following schemes:

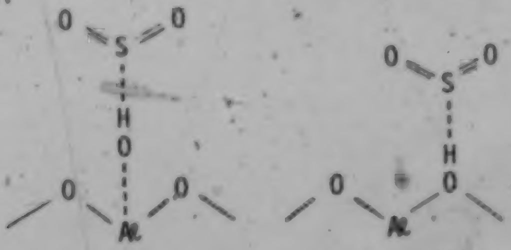

(I) (II) (6.12)

Actually, the infrared spectral observations by Deo et al. are insufficient to support the above two schemes. The following alternatives can also account for their infrared spectral observations,

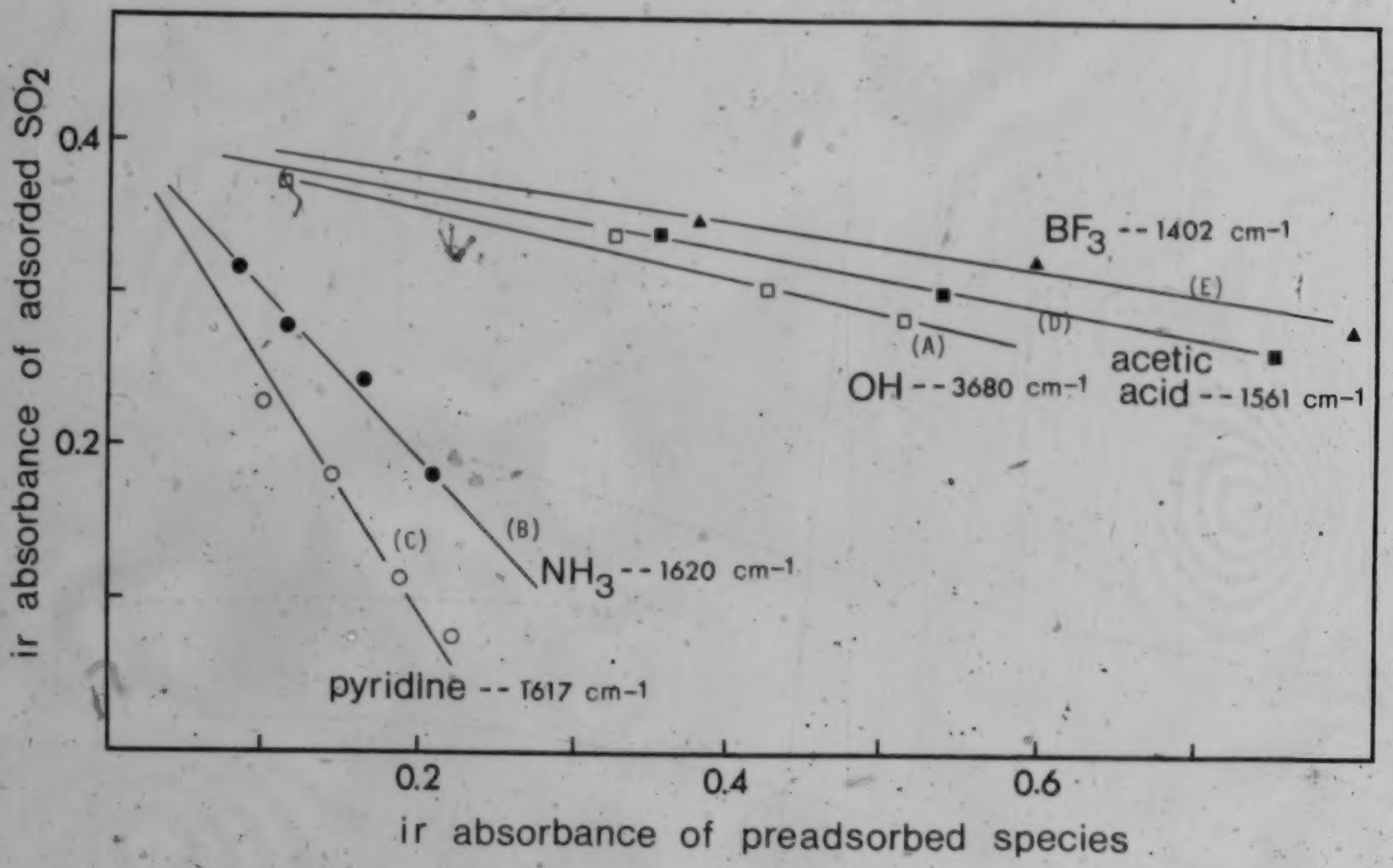

Figure 6-7. Effect of Preadsorption of Some Acidic or Basic Gases Upon SO_2 Adsorption on γ-Alumina.

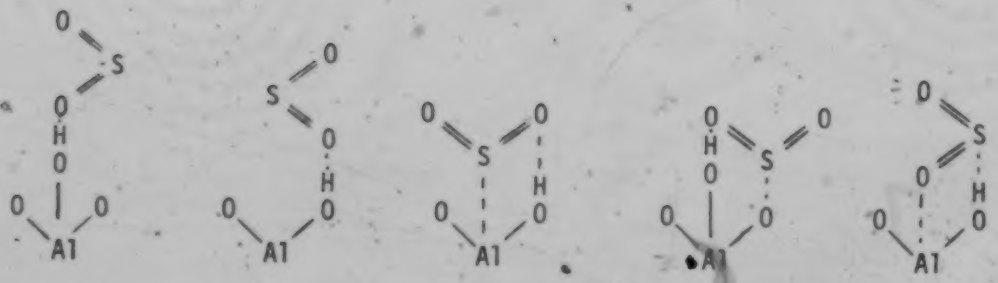

(III) (IV) (V) (VI) (VII)

(6.13)

Figure 6-7 (A) shows that as the surface Bronsted-acid sites increase, the amount of adsorbed SO_2 on γ-alumina decreases. This demonstrates that SO_2 is not adsorbed on the Bronsted-acid sites. The detection of a broad hydrogen-bonding band and the disappearance of the hydroxyl band at 3785 cm^{-1} upon SO_2 adsorption,as observed by the infrared spectroscopic technique, are believed to be due to the interaction of adsorbed SO_2 with the neighboring Bronsted-acid sites.

On the other hand, if SO_2 is not adsorbed on Bronsted-acid sites, Horizontal lines should be shown in Figure 6-7 (A) and not lines with negative slopes. The explanation will be discussed in Section 6.3.1.3.

6.3.1.2 Oxide-ion Sites

Deo et al. [34] found that when the absolute pressure of SO_2 vapor in contact with the γ-alumina was increased to 3.1 cm Hg., new infrared spectral bands at 1685 and 1250 cm^{-1} as well as a weaker pair at 1410 and 1090 cm^{-1} were detected. They attributed these to the symmetric and asymmetric stretching vibrations of the perturbed adsorbed SO_2. Upon increasing the temperature of adsorption to 400°C and cooling to room temperature, a further pair of bands at 1570 and 1440 cm^{-1} appeared. Finally, after evacuation at 400°C and cooling to room temperature, two pairs of bands at 1375-1110 cm^{-1} and 1570-1440 cm^{-1} remained. They suggested two interpretations. One was that the two pairs of remaining bands represent different chemisorbed species, each vibrating with its own characteristic frequency. They did not elaborate on the forms of the hypothetical chemisorbed species and the types of sites involved in the adsorption. The other explanation involves the possible formation of surface sulfate which the authors depicted as follows:

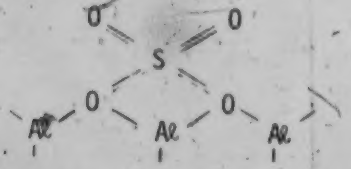

(2.29)

The infrared spectral bands of some inorganic sulfites, sulfates and bisulfates are listed in Table 2-5. A strong spectral band at around 1100 cm^{-1} exists in every compound listed. Only those members with crystallite water produce a sizeable band around 1600 cm^{-1} which represents molecular water. None of them possess the two pair of bands at 1375-1110 cm^{-1} and 1570-1440 cm^{-1} as observed by Deo et al. This shows that the two pairs of bands observed by Deo et al. may not be sulfate bands.. The experimental exploration of sulfate formation on γ-alumina in the present work will be discussed in Section 6.4.

Figure 6-7 (B) and (C) exhibit that when the adsorbed BF_3 and CH_3COOH increase (oxide-ion sites decrease), the amount of adsorbed SO_2 decreases only very slightly. Although these results did not prove that SO_2 is not adsorbed on oxide-ion sites, they do show that the oxide-ion sites are not very important for SO_2 adsorption. Section

6.3.1.3 will provide further clarification on this point.

6.3.1.3 Lewis-acid Sites

Figure 6-7 (D) and (E) show that as the surface Lewis-acid sites decrease (amount of adsorbed NH_3 and pyridine increase), the amount of adsorbed SO_2 decreases. This clearly demonstrates that Lewis-acid sites are important for SO_2 adsorption. The adsorption may be depicted by the following scheme:

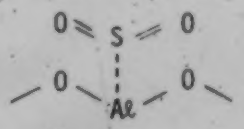

(6.14)

In the above scheme, SO_2 is adsorbed on Lewis-acid site via its sulfur atom. Low et al. [79] observed a shift of 24 cm^{-1} in the spectral band frequency from gas-phase SO_2 to the adsorbed SO_2 on CaO via sulfur atom and a similar shift of 32 cm^{-1} was observed in the present work. With this type of adsorption scheme, it is possible to explain the results in Section 6.3.1.1 and the arguments used are the same as those in Section 6.2.2 Similarly, it could explain the results in Section 6.3.1.2 by using the arguments in Section 6.2.2.

6.3.2 Adsorption Model Concluded from the Present Work

From the present work, the model concluded for SO_2 adsorption on γ-alumina is shown below,

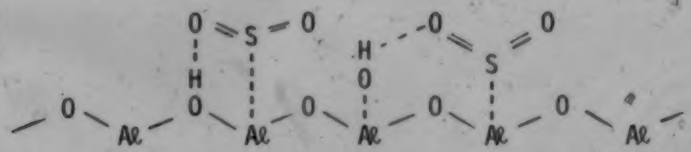

(6.15)

The SO_2 is adsorbed via its sulfur atom on the Lewis-acid site of γ-alumina and various forms of hydrogen bonding could be formed, as shown in the model, depending on the types of Bronsted-acid sites surrounding the adsorbate.

Unlike the adsorbed H_2S, the majority of the adsorbed SO_2 could be desorbed by evacuation at room temperature. Such physical adsorption has also been noted by other workers using the volumetric measurement method. Ozawa et al. [97] found that the amount of SO_2 adsorbed increased monotonically with pressure. Ross et al. [118] considered the SO_2 adsorption to be a physical surface process.

On the other hand, Roux et al. [120] observed a high heat of adsorption at initial low loading and then the heat dropped and leveled off quickly with increase SO_2 adsorption on H-mordenite. They attributed this to the surface heterogeneity of the catalyst. Strong chemical adsorption could occur on some specific sites and when these sites are occupied, the remainder of the adsorption would proceed by physical process. A similar phenomenon was observed by Glass and Ross [46] from their investigation of SO_2 adsorption below monolayer coverage on silica gel.

6.3.3 The Effect of Temperature on SO_2 Adsorption

Figure 6-8 shows the effect of temperature on SO_2 adsorption. The infrared spectra were recorded with the γ-alumina wafer in contact with 5 cm Hg absolute pressure of SO_2 at various temperatures. Each contact was allowed to proceed for 2 h before the recording of infrared spectrum. From Figure 6-8, it may be seen that as temperature increases,

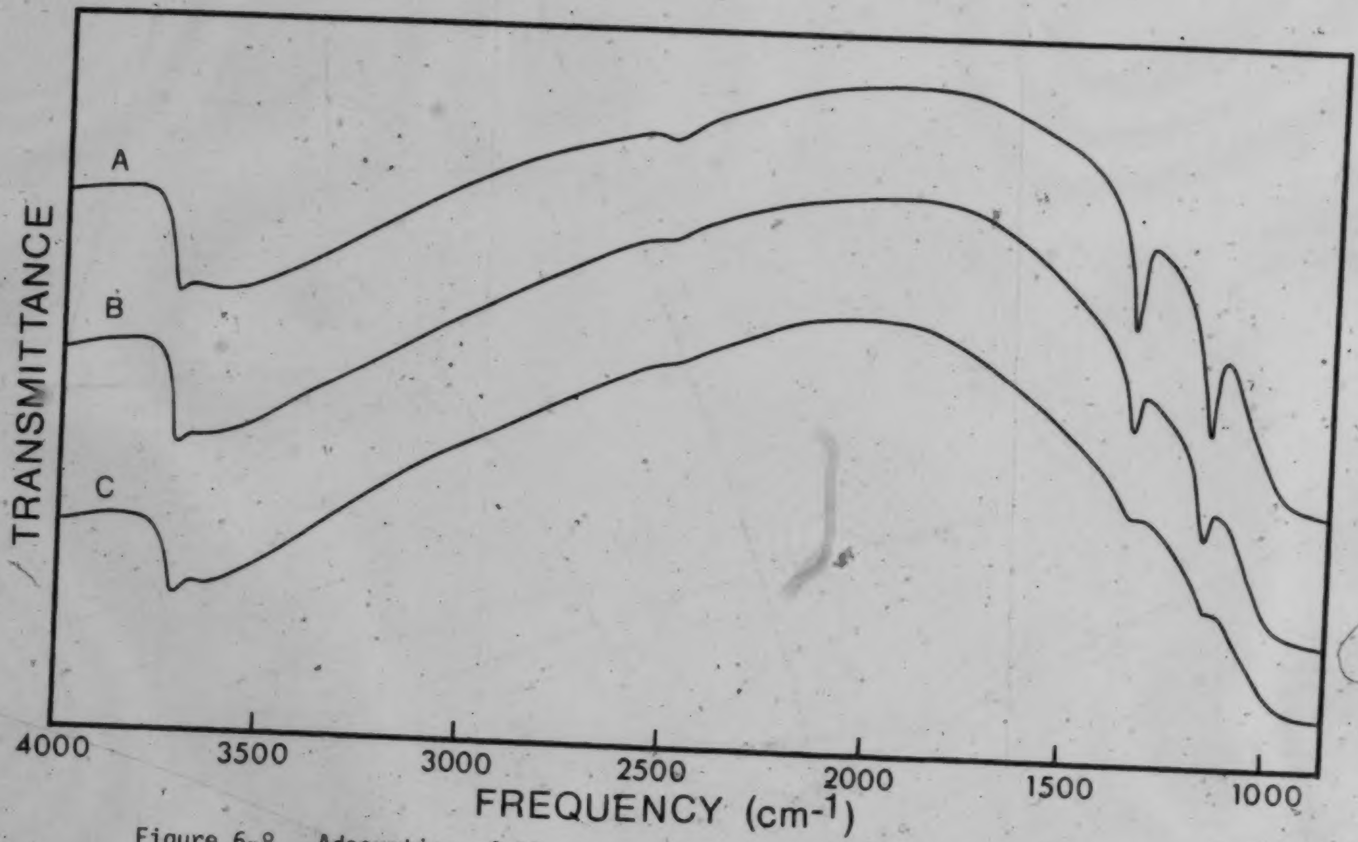

Figure 6-8. Adsorption of SO_2 on -alumina at Various Temperatures. (A) Room Temperature, (B) 50°C, (C) 100°C

the amount of adsorbed SO_2 decreases. At 100°C or higher, the spectral bands of adsorbed SO_2 become non-detectable. This may infer that negligible amount of SO_2 adsorption occurs at temperatures higher than 100°C. The decrease in SO_2 adsorption with increase in temperature was also noted by Roux et al. [120]. They found that the amount of adsorbed SO_2 at 160°C on H-mordenite is only 0.4% that of 0°C. Other published works, listed in Table 2-6 show that 0.5 - 2.0 mol/m^2 of SO_2 could be adsorbed on Υ-alumina and Silica Gel at 80 - 150°C as measured by the volumetric method. Comparing the published results with those of the present work, the failure to detect infrared spectral bands of adsorbed SO_2 above 100°C probably means that the quantity of Υ-alumina used is too little and hence the amount of adsorption too small to allow detection by infrared spectroscopic techniques.

6.4 The Relative Importance of Various Types of Sites for Reaction

In Section 6.3, it has been concluded that both H_2S and SO_2 are primarily adsorbed on the Lewis-acid site of Υ-alumina via their sulfur atoms. It is the purpose of this section to investigate whether Lewis-acid sites (or any other types of sites) are essential for the reaction between H_2S and SO_2.

In heterogeneous solid-catalyzed gas-phase reactions, several physical and chemical steps may be involved before reactants are converted into products. The physical steps involve mass transfer processes whereas the chemical steps involve adsorption-desorption processes or chemical reactions. The latter may be a simple transformation of reactants directly into products or may involve several steps in which more than one reaction intermediate may be formed. After two reactants are adsorbed, they produce a number of reaction intermediates and in doing so, often require the participation of other catalytic surface sites not related to the adsorption. Depending on which reaction step is rate controlling, the type of sites which are responsible for adsorption may not be as critical as those sites which take part in the intermediate reaction steps.

In this section, the results of addition of various chemicals to the feed which are selectively adsorbed on a particular type of sites on γ-alumina were presented to the reactor. The reaction rates under a fixed set of conditions and with the presence of different chemicals for selective adsorption are then compared. Pyridine and ammonia were chosen for selective adsorption on Lewis-acid sites and HCl, BF_3 and CH_3COOH for oxide-ion sites. If the reaction rate between H_2S and SO_2 in the presence of pyridine or ammonia is lower than that in the presence of HCl or BF_3 or CH_3COOH, then Lewis-acid sites would be expected to be more critical than oxide-ion sites.

A uniform catalyst weight of 100 mg was used in all the runs while all the reaction temperatures and pressure were set at 256°C and 715 mm Hg. The feed stream contained 4.0 mol % H_2S, 2.0 mol % SO_2 and 94.0 mol % N_2. In cases where a "selective adsorption" agent was used.

10.0 mol % N_2 in the feed stream was replaced by that agent. Due to the possible irreversible adsorption of these agents on γ-alumina, the used catalyst wafer was always replaced by a new one whenever the agent was changed. The analysis was done by the infrared spectroscopic method and the extent of SO_2 consumed was chosen to measure the reaction conversion.

The results are summarized in Figure 6-9. Curve (A) represents a series of runs without any "selective adsorption" agent and was used as a basis for comparison. Highest reaction conversions were achieved in this as compared to other series of runs. Before the commencement of other series of runs, the possible reaction between any of the "selective adsorption" agents and the reactants (H_2S or SO_2) was carefully examined and the results showed that no reactions occurred.

Curves (B) and (C) represent the runs where the feed streams contained NH_3 and pyridine, repectively. The SO_2 conversions shown were less than those depicted in curve (A). Two interpreations may be given to such observations. One is that pyridine and NH_3 competed with the reactants for adsorption while the other is that Lewis-acid sites may participate in the reaction (besides adsorption) and hence being partly occupied by pyridine or NH_3, the reaction rate is lowered.

Curves (C), (D) and (E) are results of runs when the feed Streams contained HCl, CH_3COOH and BF_3 respectively. The SO_2 conversions indicated by these curves are much lower than for the previous curves. This is most clearly demonstrated by curve (E) where the SO_2 conversion is almost zero. Both HCl and CH_3COOH are adsorbed on the Lewis-acid and oxide-ion sites while BF_3 is adsorbed on oxide-ion sites only.

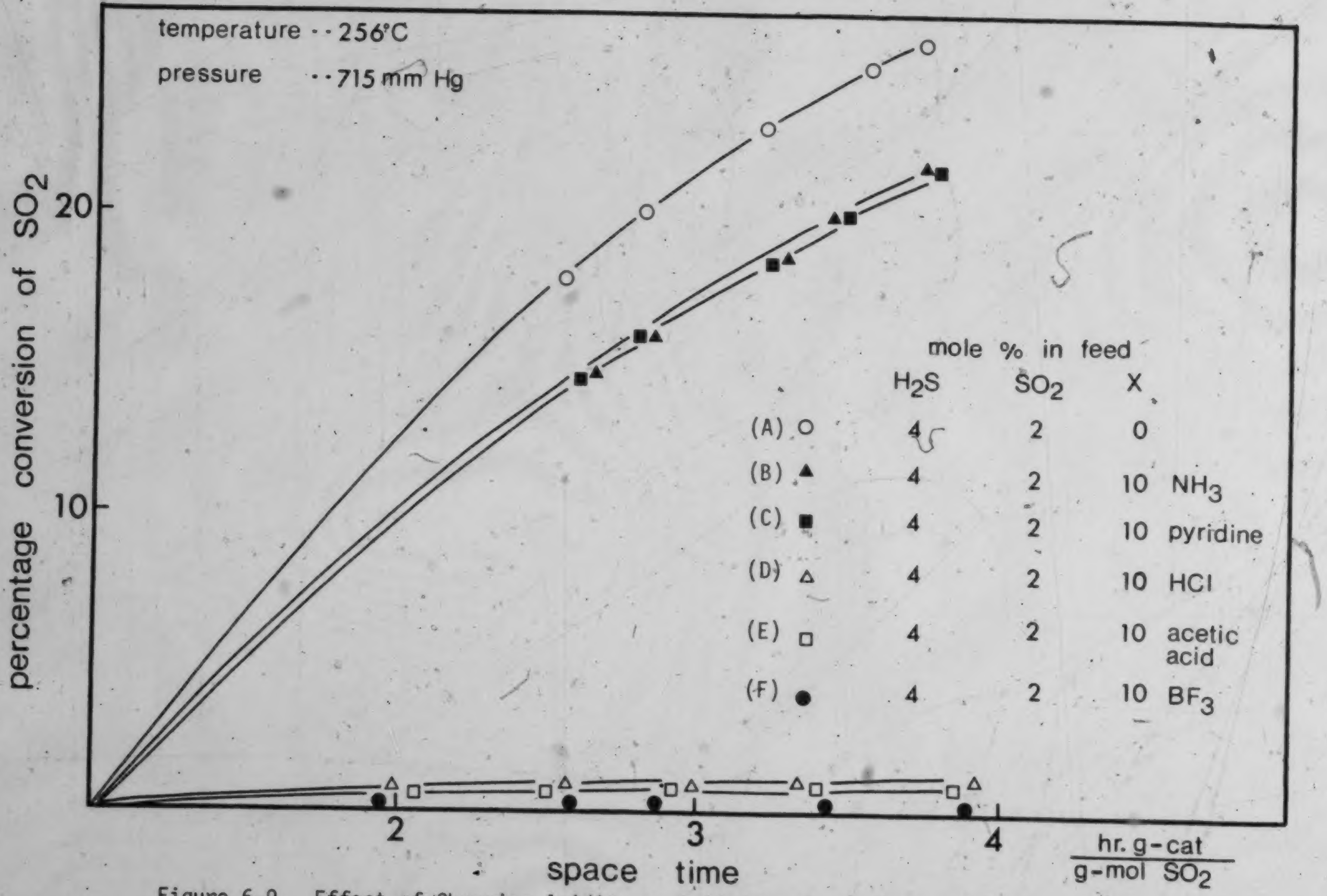

Figure 6-9. Effect of Changing Acidity or Basicity of γ-alumina Upon Its Catalytic Activity.

From the results of the curves shown in Figure 6-9, the extreme importance of oxide-ion sites for the reaction between H_2S and SO_2 has been clearly demonstrated although these sites are not responsible for the adsorption of either reactants as shown in Sections 6.2 and 6.3. Such experimental evidence may imply that the reaction mechanism between H_2S and SO_2 is not of the simple Hougen-Watson type where the two reactants are adsorbed on the adjacent Lewis-acid sites and then react with each other to form the products. Some sort of intermediate reaction steps which involve the participation of oxide-ion sites may be the rate-determining step(s).

It was very difficult to evaluate the importance of the Bronsted-acid sites on the reaction in the present work. Although by NaOH impregnation, the Bronsted-acid sites can be decreased and there are some chemicals which can be selectively adsorbed on Bronsted-acid sites, the results so produced can be ambiguous. The reason is that Bronsted-acid sites can be continuously generated by water which is a product from the H_2S/SO_2 reaction. Moreover, water vapor pressure (which in turn is related to reaction conversion) and reaction temperature also play an important role in affecting population of Bronsted-acid sites.

6.5 Sulfate Formation on γ-alumina

The sulfate formation on γ-alumina has been investigated by others [65,102], as mentioned in Section 2.3.3.3. Two approaches were adopted in the present work for such an investigation. The first approach involved the use of infrared spectroscopic method. A wafer containing 100 mg of γ-alumina was contacted with SO_2, O_2 or SO_3 vapor under various conditions and then the presence of sulfate was analyzed by taking an infrared spectral scan at room temperature. The second involves wet chemical analytical methods. A 5 g batch of γ-alumina was exposed to gaseous SO_2, O_2 or SO_3 at various conditions. The catalyst was then removed and boiled in 50 ml 1N HCl solution, filtered and washed with 100 ml of boiling water twice. The filtrate and wash-solution were combined and cooled to room temperature. Excess $BaCl_2$ solution was added, the mixture stirred and allowed to sit overnight. The mixture was then filtered and washed through an ashless filter paper. The filter paper was ignited in a crucible whose weight was measured before and after the ignition to determine any ash present. Sufficient KBr was added to the crucible to mix with any ash present and a wafer was prepared from the mixture. The infrared spectroscopic method was used to detect any presence of $BaSO_3$ or $BaSO_4$ on the wafer.

6.5.1 Sulfate Formation from SO_2

First, the experiments performed by Deo et al.[34] were repeated twice to determine whether the pair of infrared spectral bands at 1570-1470 cm^{-1}, which they attributed to possible sulfate formation, could be detected here. The experimental procedures were the same as outlined in Section 2.3.3.1. The γ-alumina catalyst used by them and in the present work was of the same type (Alon). Sufficiently slow scanning speed was used to ensure an adequate sensitivity of the analysis by the infrared spectrophotometer.

Attempts to locate the 1570-1470 cm^{-1} pair of spectral bands were completely unsuccessful. Eventually much higher SO_2 pressure (50 cm Hg) and longer contact time (36 h) than those in Deo's work were used and similarly, it was not possible to observe any spectral bands around 1570-1470 cm^{-1}.

The experiments were repeated using 5 g stead of 100 mg of catalyst and wet chemical plus infrared spectroscopic analysis were adopted. Again, neither $BaSO_3$ nor $BaSO_4$ nor any other sulfite/sulfate could be detected. Apparently, contacting of SO_2 with γ-alumina under the experimental conditions adopted in the present work does not generate observable amounts of sulfite or sulfate.

6.5.2 Sulfate Formation from SO_2 and O_2

Since sulfate formation could not be detected by contacting the γ-alumina with SO_2 alone, another series of experiments involving both SO_2 and O_2 was carried out. The experiment consisted of two parts. First, alternate 100 cm Hg doses of SO_2 and O_2 were contacted with the same γ-alumina wafer at 400°C for 2 h, after which the treatment gas was evacuated. After a total of ten consecutive doses (five for SO_2 and five for O_2), the wafer was evacuated and cooled to room temperature to be scanned by the infrared spectrophotometer. The acanning speed as well as sensitivity were carefully controlled during recording of the spectrum. The second part of the experiment involved using three gaseous mixtures of 10:90, 50:50 and 90:10 SO_2 to O_2 ratio to contact with γ-alumina separately for 12 h at 400°C and under a 600 mm Hg total pressure. For each mixture, a separate γ-alumina wafer was used. After each contact, the wafer was evacuated, cooled to room temperature and analyzed by infrared spectrophotometry. These experiments were repeated by using batches of 5 gm γ-alumina and with the wet chemical plus the infrared spectroscopic method of analysis as mentioned in Section 6.5.

All results failed to produce the pair of infrared bands at 1570-1470 cm^{-1} as observed by Deo et al. [34] but formation of sulfate was detected as shown in Figure 6-10. These bands bear a close resemblance to those of pure $BaSO_3$, $BaSO_4$, $Al_2(SO_3)_3$ or $Al_2(SO_4)_3$ and indicate that in the presence of oxygen, formation of sulfate on γ-alumina by contacting with SO_2 is possible.

6.5.3 Sulfate Formation from SO_3

Since sulfate formation on γ-alumina was indicated by contacting with the gaseous mixture of SO_2 and O_2, the next objective was to investigate the formation of sulfate from SO_3. A 100 mg of γ-alumina wafer was placed in the infrared cell, subjected to the normal pretreatment used in this work and then exposed to about 5 mm Hg absolute pressure of anhydrous SO_3 vapor at room temperature. The contact was maintained for 1/2 h and then the infrared cell was first evacuated for 2 h at room temperature followed by degassing at 400°C for 2 h. The infrared cell was allowed to cool slowly to room temperature and an infrared spectrum was taken on the γ-alumina wafer. During the infrared scan, the SO_3-treated wafer was placed in the sample beam while another equal size pure γ-alumina wafer was in the reference beam of the infrared spectrophotometer. This matching was required since both the sulfite and sulfate bands are near the alumina band. By placing an equal size wafer in

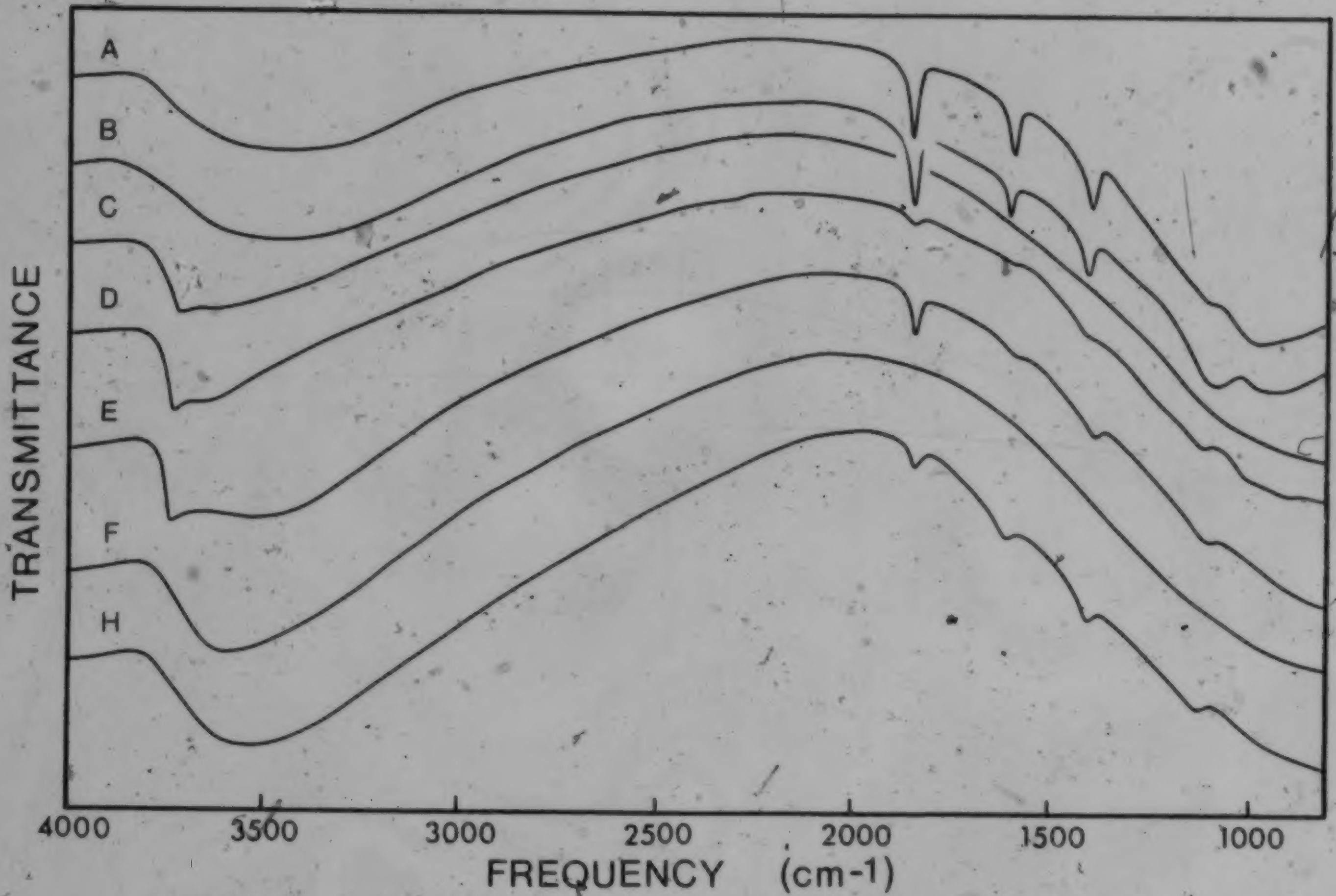

Figure 6-10. Infrared Spectra of Sulfate Formation on γ-alumina. (A) $Al_2(SO_3)_3$ (B) $Al_2(SO_4)_3$; γ-alumina Contacted with (C) SO_2, (D) $SO_2 + O_2$, (E) SO_3, (F) $SO_2 + H_2O$, (H) $SO_2 + H_2O + O_2$

the reference beam, the intense Al-O band could be compensated enabling any sulfate or sulfite present to be observed. The spectrum, as shown in Figure 6-10, contains both the sulfite and sulfate bands at around 1100 cm^{-1}. These bands bear a close resemblance to those of pure $BaSO_3$, $BaSO_4$, $Al_2(SO_3)_3$ or $Al_2(SO_4)_3$.

The experiment was repeated by using 5 g γ-alumina and wet chemical plus infrared spectroscopic analysis. When excess $BaCl_2$ was added to the filtrate in the wet chemical analysis, a white precipitate was obtained. As analyzed by the infrared spectroscopic method, this white precipitate was found to contain both $BaSO_3$ and $BaSO_4$ as shown in Figure 6-10.

By comparing the results in this section with those in the previous section, it appears that SO_3 and the SO_2/O_2 mixture were strong enough chemically to form sulfate and/or sulfite on γ-alumina while SO_2 alone was not. In the case of SO_2/O_2 mixture, it was not clear whether SO_2/O_2 reacted directly on the γ-alumina surface to produce sulfate or indirectly via the formation of SO_3 first.

6.5.4 Sulfate Formation in the Presence of Water Vapor

Since water vapor is always present in the industrial reactors involving the Claus reaction, the possibility of sulfate formation by SO_2 or the mixture of SO_2 and O_2 on γ-alumina in the presence of water vapor was also investigated. A 100 mg γ-alumina wafer was contacted at 400°C for 12 h with 30 cm Hg of SO_2 vapor which had been saturated with water at room temperature. The wafer was degassed for 12 h and cooled to room temperature for an infrared scan. During the scan, an identical wafer of γ-alumina was placed in the reference beam of the infrared spectrophotometer. No sulfite or sulfate could be detected in the analysis. The same result was obtained by repeating the experiment with 5 g γ-alumina together with wet chemical plus infrared spectral analysis.

The spectrum shown in Figure 6-10 was recorded after an experiment identical to the above but which involved 50 mol % of SO_2 and O_2 in place of the SO_2. Both sulfite and sulfate bands, although weak, were detected. The presence of sulfite and sulfate was confirmed by repeating the experiment with 5 g γ-alumina and using wet chemical plus infrared spectral analysis.

From the results, it appears that formation of sulfite or sulfate on γ-alumina was feasible with the mixture of SO_2, O_2 and H_2O whereas the absence of O_2 or SO_2 reduced the formation, if any,to a negligible rate.

In order to evaluate whether the sulfite or sulfate formation on γ-alumina was feasible under the experimental conditions of kinetic runs in the present work, the three γ-alumina wafers employed in testing the catalytic activity in Section 6.10 were examined. These wafers all had a service history of 63 h (each with seven 9 h continuous runs). No sulfite or sulfate could be detected in any one of these wafers by wet chemical plus infrared spectroscopic analysis. Since any one batch of γ-alumina used in the present kinetic runs had less than 40 h service, the possible effect of sulfite or sulfate on reaction rates could be neglected.

6.6 Preliminary Kinetics Experiments

Before commencing the kinetics study in depth, preliminary experiments were carried out. In a "blank" run, possible homogeneous reaction or catalytic effect of the equipment walls were examined. The reversibility of the reaction was then tested to determine whether the reverse reaction occurred at a detectable rate. The significance of mass transfer effects in gas-film or pore diffusion was also investigated. Finally, the stability of the catalyst activity was checked to ensure the reliability of the kinetics data. These experiments will be discussed in the following sections.

6.6.1 Blank Run

The possible catalytic effect of the surface of the experimental equipment was evaluated by using a feed containing 10.0 mol % H_2S, 5.0 mol % SO_2 and 85.0 mol % N_2, first, without the recycle pump and then with the recycle pump in operation. Before the introduction of feed the reactor and feed system were cleaned carefully to eliminate particles of catalyst. During this test, the reactor pressure was maintained near one atm. and the reactor temperature was increased from 200°C to 350°C in steps of 50°C. At each temperature, the operation was allowed to proceed for at least one hour before the feed and product analysis were performed.

By measuring the water vapor content in the feed cell by infrared spectroscopy (according to Section 5.1.3), it was possible to determine if reaction had occurred in the system upstream from the feed cell. On the other hand, by comparing the concentration of SO_2 in both feed and product cells (again as per Section 5.1.3), the occurrence of chemical reaction in the reactor or recycle pump could be found. In all runs, no evidence of reaction could be detected.

The absence of reaction without catalyst was true only if reactants and products in the system remained in the vapor state. If either water or sulfur was allowed to condense, reaction between H_2S and SO_2 could be observed to occur in the resulting liquid phase. This effect has previously been observed [22,64]. McGregor [84] studied the kinetics of the reaction between H_2S and SO_2 over a bauxite catalyst and also reported that the surface of his equipment fabricated from 316 stainless steel was non-catalytic.

6.6.2 The Reversibility of the Reaction

The reaction between H_2S and SO_2 is reversible, although the forward reaction is much more dominant at industrial catalytic reaction temperatures. To understand the reaction mechanism and to develop a kinetic model, it will be useful to ascertain the significance of reverse reaction within the range of reaction conditions adopted for the rate measurements. In the present work, experiments were designed to investigate the equilibrium conversion of reaction (2.1) and to evaluate the extent of reverse reaction occurring at the conditions used.

6.6.2.1 Equilibrium Conversion

Gamson and Elkins[42] studied the rate of H_2S/SO_2 reaction over bauxite and found the measured H_2S conversion was higher than their theoretical equilibrium conversion for the same conditions. Cho [21] calculated theoretical equilibrium conversions by using the free energy minimization method [84] and published thermodynamic data [83,144]. He considered a stoichiometric ratio of H_2S/SO_2 in his feed compositions.

At 400°C, he found that as the N_2/SO_2 ratio in feed compositions increased from 3 to 200, the equilibrium SO_2 conversion increased from 76 to 89 %.

Cho also measured the rate of reaction between H_2S and SO_2 over a commercial γ-alumina (Kaiser S-201) in a packed-bed reactor. Using a feed stream containing 95.5 mol % N_2, 3.0 mol % H_2S and 1.5 mol % SO_2 and space velocities of 100 or 4 h^{-1}, his measured SO_2 conversions were 5 and 10% higher than his calculated equilibrium conversions. The discrepancy between measured and calculated equilibrium conversions, as reported by both Cho [2] and Gamson [42], may be explained in two ways. First, the theromodynamic data used for theoretical equilibrium calculation may not be accurate. Secondly, both authors allowed the sulfur to condense in order to remove it from the product stream before undergoing chemical analysis. As a result, it may be possible that their observed conversions are excessive.

In this work, the equipment shown in Figure 6-11 was used to examine the estimation of equilibrium conversion for the H_2S/SO_2 reaction. The equipment consisted of an infrared cell connected to a reaction chamber containing some catalyst pellets. The CaF_2 infrared windows at both ends of the infrared cell were sealed with the silicon potting compound. Except for the infrared windows, the only material of construction used for the equipment was 316 stainless steel. To heat this cell externally, two separate sets of nichrome wire were wound around the equipment and insulated with asbestos tape. The first coil of nichrome wire heated the infrared cell and the needle valve above it.

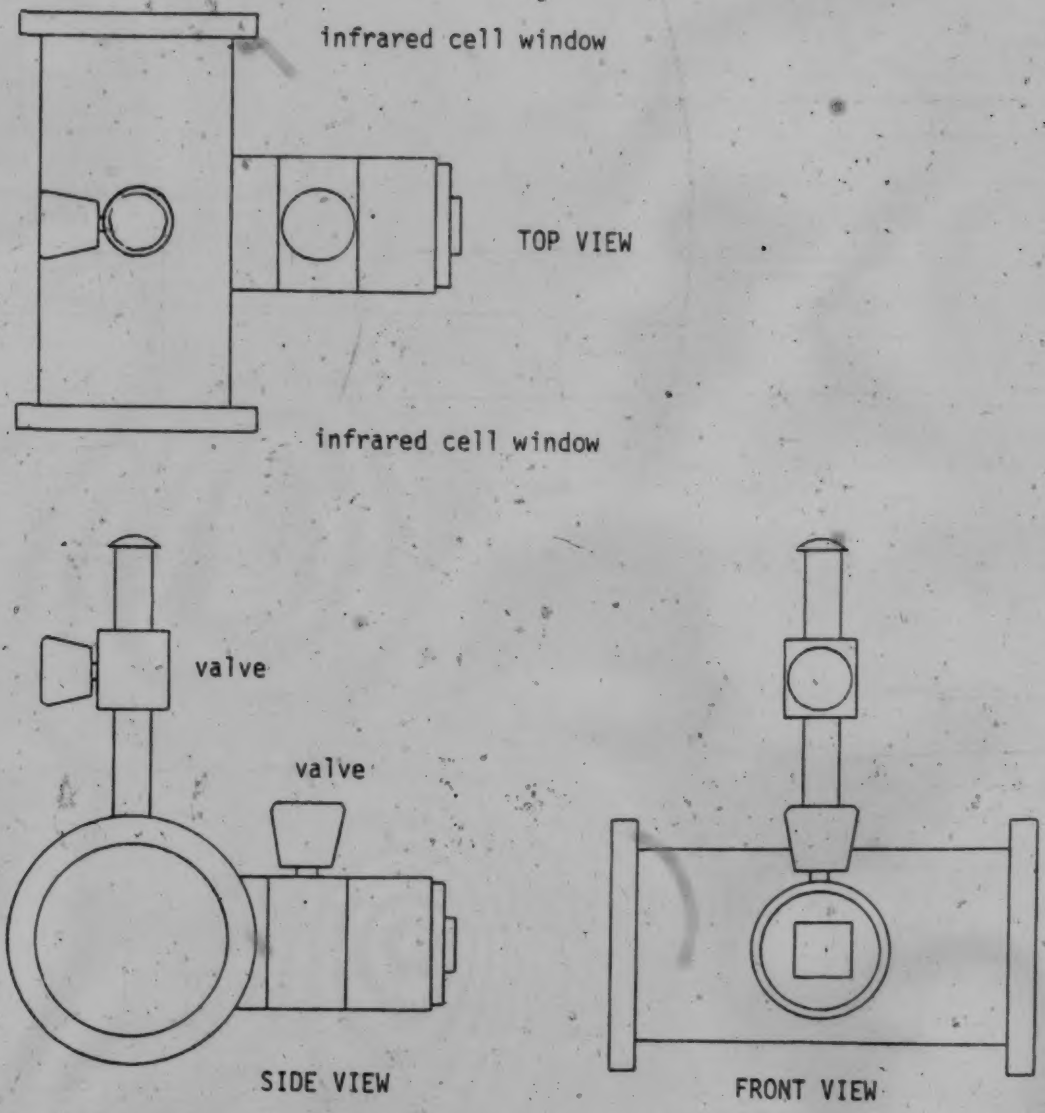
infrared cell window
TOP VIEW
infrared cell window
valve
valve
SIDE VIEW
FRONT VIEW

Figure 6-11 Equipment Used for Reaction Equilibrium Study

The second coil of nichrome wire heated the reaction chamber and the needle valve located between the infrared cell and the reaction chamber. The voltage input to the nichrome wire could be varied and the temperature in the infrared cell (or the reaction chamber) was calibrated against the Variac settings. The two nichrome wire heaters allowed the infrared cell and the reaction chamber to be heated separately.

The equipment was carefully checked for the absence of leaks. To start an experiment, a known weight of γ-alumina was introduced into the reaction chamber by removing the plug at the end. After the plug was carefully secured, the entire equipment was connected to the vacuum system through the ball joint. The valve on the inlet line was slowly opened so that the infrared cell could be evacuated. Next, the valve on the reaction chamber side was opened to evacuate the chamber. After the system pressure was reduced below 0.01 mm Hg, the temperature of the infrared cell was gradually raised. The infrared cell could be heated to 250°C by setting the Variac at 50 V. When the temperature of the infrared cell was above 100°C, heating of the reaction chamber was commenced. It was important that the infrared cell temperature be above 100°C before the reaction chamber was heated because the water vaporized from the catalyst could recondense on the CaF_2 windows. The catalyst was degassed at 400°C for 16 h and then cooled back to the temperature at which the experiment was to be conducted. The temperature of the infrared cell was maintained at 250°C throughout.

A gaseous mixture containing 4.0 mol % H_2S, 2.0 mol % SO_2 and 94.0 mol % N_2 was then introduced into the infrared cell (250°C). During the introduction, the needle valve to the reaction chamber was closed to prevent catalytic reaction. After the introduction, the total pressure in the infrared cell was measured by a manometer and the entire apparatus was transferred to the sample compartment of the infrared spectrophotometer for analysis. A complete infrared spectrum of the SO_2 in the infrared cell was recorded and this is shown in Figure 6-12 (A). Then, the valve leading to the reaction chamber, which contained the catalyst maintained at 210°C, was opened, allowing the gases to contact the catalyst. During this contact, the partial pressure of SO_2 in the infrared cell was determined at intervals. After about 6 h of reaction, the SO_2 partial pressure in the infrared cell was less than 5% of that present originally. The partial pressure of SO_2 increased slightly when the temperature of the reaction chamber was raised to 350°C.The results are shown in Figure 6-12. The accuracy of the equipment was inadequate for determining the exact extent of equilibrium conversion. However, it was quite evident that more than 90% of the reactants had been consumed after the 6 h contact with the catalyst. The measured equilibirum conversions are slightly higher than the theoretically calculated value [84,21] but lower than those measured by Cho [21].

The greater reliability of infrared spectrophotometry over gas chromatography for measuring the equilibrium conversion results from eliminating the need to condense sulfur for the IR analysis. To improve the reliability of equilibrium composition measurements, the equipment described herein should include a small magnetic centrifugal pump. By circulating the gases between the reaction chamber and infrared cell, a more rapid approach to equilibrium by reduction of concentration gradient would be anticipated.

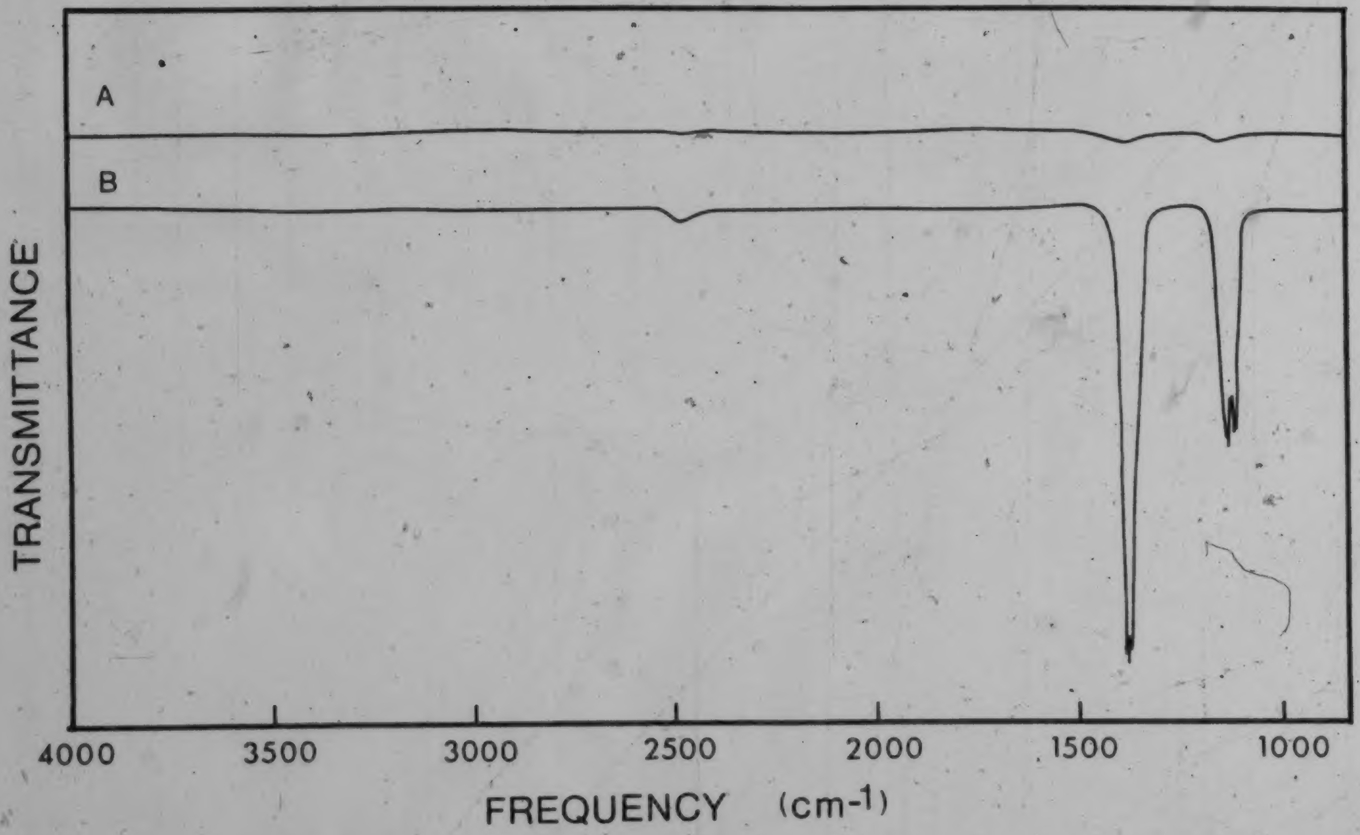

Figure 6-12. Infrared Spectra for Reaction Equilibrium Study
(A) Before Reactants were Contacted with γ-alumina
(B) After Reactants were Contacted with γ-alumina for 6h.

6.6.2.2 The Extent of Reverse Reaction

An experiment was carried out with the equipment mentioned in Section 5.1 to examine whether the reverse reaction was significant under the reaction conditions being studied. The approach adopted was to introduce S_x and H_2O diluted with a carrier gas (N_2) into the reaction chamber containing γ-alumina catalyst and then to observe the formation of H_2S and SO_2. A catalyst wafer containing 1.0351 g of γ-alumina was employed in this experiment (compared to less than 0.13 g used during all of the kinetics studies). A flow-rate of 40 ml/min of pure nitrogen was bubbled through liquid sulfur in a reservoir kept at 300°C. This mixture was then combined with a continuous stream of 1.95×10^{-4} g mol/min of water vapor in the preheater. The combined gaseous mixture then entered the infrared-cell reactor and flowed over the γ-alumina wafer. The 40 ml/min nitrogen carrier gas flow rate was lower than the lowest one (62 ml/min) used in the kinetic measurements. The reactor was maintained at 210°C and 805 mm Hg. The continuous flow of gaseous mixture (nitrogen, water and sulfur) over the catalyst was allowed to proceed for over 1.5 h before any analysis was attempted. To prevent condensation of sulfur, the recycle pump was disconnected prior to this experiment. Then both feed and product cells of the reactor loop were introduced into the sample and reference beams of the infrared spectrophotometer, respectively, to detect the presence of SO_2 in the gaseous stream which had been in contact with the catalyst. The resulting analysis revealed the absence of SO_2 indicating that the H_2O and S_x had not reacted. This experiment suggested that the reverse reaction,

$$\frac{3}{x} S_x + 2H_2O \rightarrow 2H_2S + SO_2 \qquad (2.1)$$

does not occur measurably at 210°C and 805 mm Hg. The experiment was then repeated at a reaction temperature of 320°C and once again SO_2 was not detected. Since this experiment employed a larger quantity of catalyst, a lower carrier gas flow-rate, and comparable if not higher sulfur and water partial pressures, than used in any of the kinetic measurements, it would therefore be reasonable to assume that the reverse reaction rate may be ignored in the kinetic runs carried out in the present work.

Some published rate equations proposed for the Claus reaction, e.g. $(-r_{H_2S}) = kP_{H_2S}^{1.5} P_{SO_2}$ by Taylor and Wesley [138] using Pyrex glass as catalyst, and $(-r_{H_2S}) = kP_{H_2S}$ by George [25] using various alumina-based catalysts, are also expressed without reverse reaction terms.

6.6.3 Mass Transfer Consideration

The investigation of catalytic reactions is complicated by the fact that the process frequently involves diffusion as well as chemical phenomena. The likelihood of encountering significant diffusion effects is greatest in the case of the most active catalyst. Interpretation of experimental kinetics results becomes difficult when mass transfer resistances are significant in comparison to chemical resistences. Satterfield [125] and Carberry [17] have extensively reviewed the effect of mass transfer upon observed reaction kinetics. Carberry [17] expressed the various rate-controlling domains as a function of key experimental variables, as summarized in Table 6-3.

TABLE 6-3

BEHAVIOR OF VARIOUS KINETIC PARAMETERS IN EACH DOMAIN OF CONTROL (17)

Domain	Activation Energy	Order	Pellet Size*	Fluid Velocity
Chemical Reaction	E	n	independent	independent
Pore diffusion-reaction	$\frac{E}{2}$	$\frac{n+1}{2}$	$(-r_A)=f(\frac{1}{L})$	independent
Bulk Mass Transfer		first	$(-r_A)=f(\frac{1}{L})^{3/2}$	$(\text{velocity})^{1/2}$

*1/L = external surface area-to-volume ratio for the wafer.

Before measuring the kinetics of reaction (2.1) using the IR cell-reactor, the influence of mass transfer on the rates of reaction must first be evaluated. Accordingly, the effects of both gas-film diffusion and pore diffusion on the reaction rate were investigated.

6.6.3.1 Gas-film Diffusion

A reaction is considered to be gas-film diffusion controlled if the rate of diffusion through the gas-film is much slower than any of the competing chemical reaction, pore diffusion, adsorption or desorption steps. Theoretical as well as experimental methods exist for examining whether gas-film diffusion is significant in a reaction. In the theoretical methods, the rate (or flux) of gas film diffusion is predicted using the relation,

$$N_i = k_G (P_i - P_i^S) \qquad (6.16)$$

If the predicted N_i is much greater than the observed rate of reaction (either measured experimentally or calculated from a rate equation) then the reaction is probably not gas-film controlled.

From dimensional analysis, Chilton and Colburn [20] developed the correlation shown below for k_G

$$\frac{k_G d_P}{D_{12}} = f(N_{R_e}, N_{S_c}) \qquad (6.17)$$

Such an empirical correlation allows one to estimate k_G (which is used to calculate N_i) if the physical properties of the gases including diffusivity data are known. They suggested that in the absence of diffusivity data, the following Chapman-Enskog expression can be used to estimate the diffusivities,

$$D_{12} = \frac{0.001858\ T^3\ [(M_1+M_2)/M_1M_2]^{1/2}}{P\ \sigma_{12}^2\ \Omega_D} \qquad (6.18)$$

In addition, they also provide a graphical correlation of j_D versus N_{R_e} which then is very useful for obtaining k_G from the following equation,

$$j_D = \frac{k_G \ P}{G_M} N_{S_c}^{2/3} \tag{6.19}$$

McGregor [84] performed the theoretical calculation for gas-film diffusion in his study of Claus reaction over bauxite catalyst by using two examples. The first was by using the conditions used in one of his kinetic runs while the second was done by adopting the operating conditions of one of the industrial sulfur plant chosen by him. In both examples, gas-film diffusion was not found to be rate-controlling. A similar theoretical calculation is described in Appendix F and the result again suggests that gas-film diffusion was not rate-controlling.

Experimentally, the significance of gas-film diffusion in a reaction can be examined by varying the feed rate while keeping both the feed composition and space-time constant [73]. If the reaction conversion is not affected by the different fluid velocities in the bed, the reaction is probably not gas-film diffusion controlled. With a recycle reactor, the gas-film diffusion is tested by varying the recycle ratio and holding other reaction conditions constant. If the bulk flow rate in the recirculation loop does not affect the rate of reaction, the gas-film diffusion is probably not significant. Since a recycle reactor was used in these kinetic measurements, the gas-film diffusion was investigated by changing the recycle ratio.

About 0.1105 g of γ-alumina was employed in this experiment carried out under the reaction conditions outlined in Table 6-4. During the experiment, the recycle flow was varied from 28.3 to 45.1 l/min by changing the recirculation pump speed.

TABLE 6-4

REACTION CONDITIONS USED FOR EXAMINING GAS-FILM DIFFUSION

Catalyst Weight (g)		0.1105	0.1105
Feed Flow Rate (ml/min)		80	80
Feed Composition	N_2	94.0	94.0
(mol %)	H_2S	4.0	4.0
	SO_2	2.0	2.0
Reactor Temperature (°C)		210	320
Reactor Pressure (mm Hg)		801	801

The reaction conversion was found to be unaffected by the volumetric flow rate in the recycle loop.

Normally, gas-film diffusion controlled is more probable when the reaction rate is high and/or when the reactant partial pressure is low in the system. More generally [125], the probability of gas-film diffusion control is proportional to the ratio of the reaction rate to the reactant partial pressure. The two sets of conditions in Table 6-4 had the highest ratio of reaction rate to reactant partial pressure. In addition, the recycle rates used in kinetic measurements were all higher than those used in the gas-film diffusion investigation. Repeating the experiments by changing a 0.1085 g wafer from a position perpendicular to the direction of gas flow to a position parallel to the direction of gas flow also indicated that the gas-film diffusion was not significant. Therefore, it is reasonable to assume that the bulk diffusion was probably negligible in all the kinetic runs in the present work. (one may also speculate that the reactive area of the extremely thin wafer was rapidly accessible to gas flowing on either side of the wafer. This has implications concerning pore-diffusion).

6.6.3.2 Pore Diffusion

Pore diffusion may occur by one or more of three mechanisms: ordinary diffusion, Knudsen diffusion and surface diffusion. Satterfield [125] in his study of these subjects reports that surface diffusion becomes significant only when the partial pressure of the reacting species is an appreciable fraction of the vapor pressure and available published data indicate that it contributes very little to the overall transport processes through a porous media.

Ordinary gas diffusion occurs in pores if gas-gas molecular collisions predominate. The effective diffusivity $D_{12,eff}$, may be used to relate the mass flux to the total cross-section of the porous solid, as

$$D_{12,eff} = \frac{D_{12}\,\theta}{\tau} \tag{6.20}$$

where θ is the porosity and τ is the tortuosity factor. The overall diffusivity D_{eff} in the pore is then related to the effective diffusivity $D_{12,eff}$ and Knudsen diffusivity $D_{K,eff}$ according to equation (6.21),

$$\frac{1}{D_{eff}} = \frac{1}{D_{K,eff}} + \frac{1}{D_{12,eff}} \tag{6.21}$$

Knudsen diffusion predominates when the gas density is low, and/or when the pores are quite small . Under this situation, the molecules collide with the pore wall much more frequently than with each other. The molecules hitting the wall are momentarily adsorbed and then given off in random directions (diffusively reflected). The gas flux is reduced by the wall "resistance" which causes a delay since both the diffuse reflection and the finite time the molecules are adsorbed. Kinetic theory provides the following relations for Knudsen diffusion in gases in a straight round pore,

$$D_k = 9700\, r_e \sqrt{T/M} \qquad (6.22)$$

where r_e is the pore radius in cm, T the temperature in K and M the molecular weight.

Normally, the internal geometry of consolidated porous solids are poorly understood, and the following relation has been proposed [125] to account for this unknown,

$$D_{K,eff} = 19400 \frac{\theta^2}{\tau_m S_g \rho_p} \sqrt{I/M} \qquad (6.23)$$

where τ_m is the tortuosity factor calculated from a mean pore radius, S_g is the total surface area in cm^2 measured by BET method and $_p$ is the density in g/cm^3 of the solid.

From a practical point of view, one would like to have a criterion which used measured values of reaction rate, effective diffusivity, reaction order, and so forth, which could then be used to discern whether a reaction is operating near the pore-diffusion controlled regime. The more commonly used [84,125] and simpler criteria for such purpose are

Hudgin's method [59] and the effectiveness factor method [125]. Hudgin's method is considered to be conservative, perhaps more than necessary [84]. The pore diffusion is insignificant if the following relation is satisfied.

$$\frac{L_r^2}{D_{eff}} < \frac{1}{r'(C_o)} \qquad (6.24)$$

where L_r is the radius of the solid in cm and r' is the first derivative of the rate of reaction with respect to the reactant concentration.

For the effectiveness factor method, Satterfield [125] provides plots of effectiveness factor, η (the actual ratio to the ratio which would be observed in the absence of diffusion limitations), versus the Thiele diffusion modulus for reactions with different activation energies. If the effectivenss factor η of a reaction is near unity, the reaction is probably not pore-diffusion controlled. The following equations are required to calculate the values used for determining the effectiveness factor:

$$\Phi_L = \frac{L^2}{D_{K_A}} (-r)/C_A \qquad (6.25)$$

$$D_{K_A} = 9700\, \gamma_e\, (T/M)^{1/2} \qquad (6.26)$$

$$K = [K_A - D_K\, \Sigma_i\, (K_i\, \nu_i/D_{K_i})]/\omega \qquad (6.27)$$

and

$$\omega = 1 + \sum_i K_i\, (P_i + (\tau_A\, \nu_i\, D_{K_A}/D_{K_i})] \qquad (6.28)$$

Examples demonstrating the calculation method are described by Chuang [23] and also in Appendix F of the present work.

McGregor [84] used Hudgin's method to examine the significance of pore diffusion in his experimental runs by using the values from one of his kinetics runs. He found that the value of his $L_r^2/D_{K,eff}$ was about three and one-half times that of his $1/r'$ and hence, according to Hudgin's criterion, pore diffusion could not be ignored in his experiments. Dalla Lana et al.[29] correlated McGregor's kinetics data by using statistical modelling method [130] and obtained a different set of rate constants. McGregor's calculation was repeated in this work (Appendix F) using the rate constants obtained by Dalla Lana et. al [29] and it was found that the value of $L_r^2/D_{k,eff}$ was close to $1/r'$(CO). This may indicate that whether the pore diffusion is significant in McGregor's experiment or not is very difficult to confirm from this calculation. (especially considering that Hudgin's method is very conservative in any case). Furthermore, the value of $L_r^2/D_{K,eff}$ becomes smaller than $1/r'$(CO) when a pore diameter of 80A° was used to repeat McGregor's calculation. This, in turn, shows that pore diffusion may be ignored in McGregor's kinetic run.

Both Hudgin's method and the effectiveness factor method were used to calculate theoretically the significance of pore diffusion in the kinetic runs of this work. The data for a kinetic run in which the highest r/C_A ratio applies was used for such calculations(shown in Appendix F). It would be anticipated that the higher the rate of reaction r and the lower the reactant concentration C_A, the more significant the pore diffusion. The calculation shows that it is reasonable to assume that pore diffusion was probably negligible.

The effects of pore diffusion can be determined experimentally measuring the reaction rates for various particle sizes catalyst under otherwise identical conditions [73]. If the reaction conversion remains constant when the catalyst particle size is varied while keeping the ratio of catalyst weight to the feed flow rate as well as other reaction conditions constant, then the pore diffusion is probably not significant.

Accordingly, three different weights of γ-alumina wafers, and correspondingly, three different catalyst wafer thicknesses were investigated. The experimental conditions and results from these runs are shown in Figure 6-13. The results indicate that pore diffusion is probably negligible as long as the catalyst weight is kept below 250 mg.

From the results of these theoretical calculations and the experimental investigation, it is reasonable to assume that pore diffusion limitations were probably negligible in the range of kinetics studied in the present work as long as the catalyst weight is less than 250 mg.

6.6.4 Stability of the Catalyst Activity

In heterogeneous catalytic reactions, the problem of catalyst poisoning by either a reactant or a product is not uncommon. The catalyst activity could deteriorate with use and eventually become completely inactive. For example, Liu [78] found that γ-alumina could be poisoned by the product CO_2 in the reaction between COS and SO_2 Pearson [102] reported that the γ-alumina catalyst used in the industrial Claus sulfur plants could be poisoned by sulfate formation.

Successful kinetic measurements require reproducible catalytic activities during the experiments. Therefore, while taking kinetics measurements in this work, the maintenance of a constant

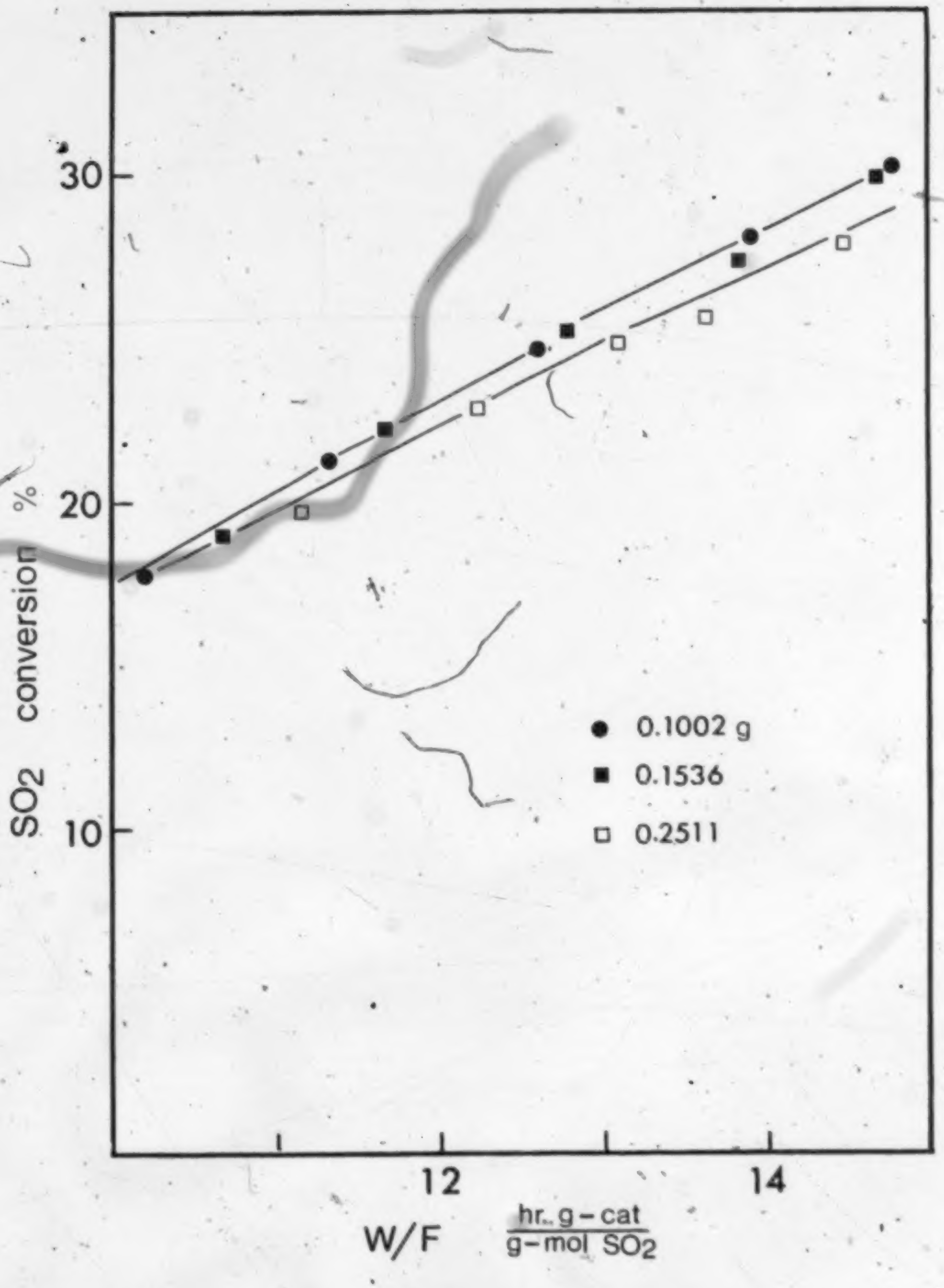

Figure 6-13. Evaluation of Pore Diffusion.

catalytic activity was carefully checked. Two approaches were followed: in the first approach, the activity of a catalyst wafer which was subjected to a long period of service was compared the activity of a "fresh" catalyst ; the second appraoch involved examining the activity of a catalyst wafer under a fixed set of experimental conditions and with a total service time longer than any to be employed actual kinetic runs.

Three series of experimental runs at 220, 260 and 300°C were carried out to check the catalyst activity. For each series, a new γ-alumina wafer was used and seven runs which constituted 9 h each were performed. Therefore, each catalyst wafer had a total of 63 h service. It was found that in all of the runs, the repeatability of reaction conversion in each 9 h period was within one percent. The overall repeatability for all three series of runs was approximately two percent. The reaction conditions used for these experiments are summarized in Table 6-5 while the results are shown in Figure 6-14.

At the end of these experiments, the three catalyst wafers were removed and analyzed for the presence of sulfate according to the method mentioned in Section 6.5. Negligible amounts of sulfate were found in each of the wafers which suggested that the sulfate formation within 63 h of use might not be significant.

Throughout these experiments, none of the catalyst wafers had been used for a total time exceeding 63 h. As a result, the problem of catalyst deactivation could be ignored.

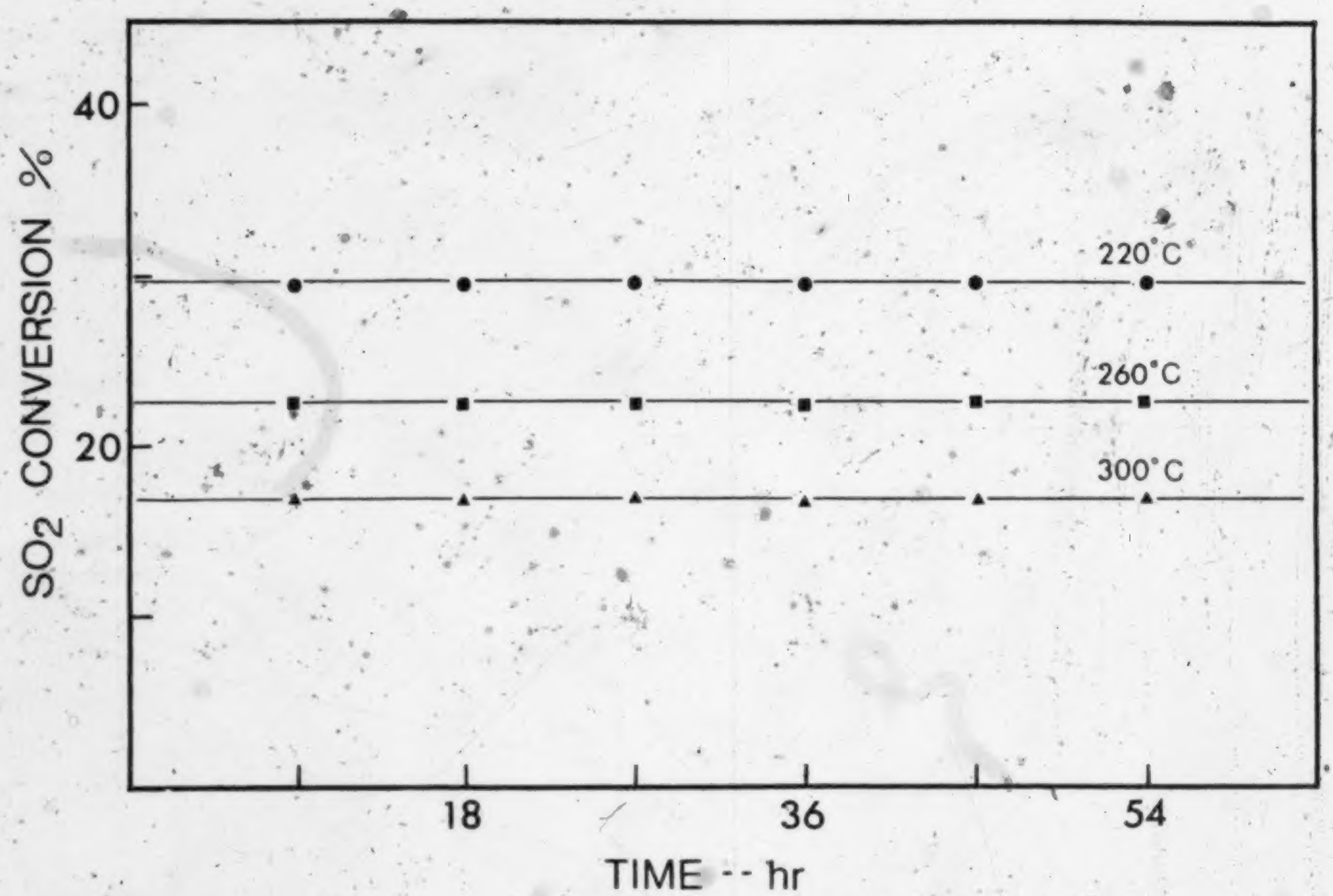

Figure 6-14. Examination of Stability of the Catalyst Activity.

TABLE 6-5

EXPERIMENTAL CONDITIONS USED FOR EXAMINING THE STABILITY OF THE CATALYST ACTIVITY

Temp. (°C)	Cat. Wt. (g)	N_2 Flow Rate x 10^3 $(\frac{g\text{-mol}}{min})$	SO_2 Conv. (%)	Reactor Partial Pressures (mm Hg)				
				N_2	H_2S	SO_2	H_2O	S_x
220	0.1240	4.7740	29.36	735.8	26.10	11.60	26.52	1.80
260	0.1071	9.8849	22.57	707.0	36.02	33.11	20.00	3.88
300	0.1152	6.8122	17.55	737.0	9.02	37.45	15.41	3.09

6.7 Infrared Spectra of γ-alumina under Reaction Condition

The infrared spectroscopic technique has been applied to examine the adsorption of reacants and products on a catalyst surface without interruption of the reaction. It has also been proven useful to identify the presence of intermediates (if they are sufficient in quantity and are infrared-active) during reaction. Hopefully, such information could be revealing on the reaction mechanism.

The reactor designed for the present work enabled the observation of catalyst surface phenomena without affecting the steady-state of the reaction. Two infrared spectra shown in Figure 6-15 were recorded at 275°C. Curve (A) was one taken when a stream of pure nitrogen was passed through the reaction system with the recirculation pump in operation. A broad hydrogen-bonding band at 3500 cm^{-1} and a band at 1000 cm^{-1} representing the Al-O bond of γ-alumina were detected. Curve (B) was recorded when a stream containing 91.0 mol % N_2, 6.0 mol % H_2S and 3.0 mol % SO_2 was introduced into the reaction system with the recirculation pump switched on. This spectrum, recorded "in situ" during the reaction, was identical to curve (A). It was not certain whether this was due to the absence of adsorbates on catalyst surface or the amount of adsorbate were too low to allow detection.

6.8 Kinetics and Mechanism

A total of 118 data points were collected from the kinetic measurements, covering six reaction temperatures from 200°C to 323°C. The data points and the partial pressure range of the components in the reactor under each of the six temperatures are summarized in Table 6-6:

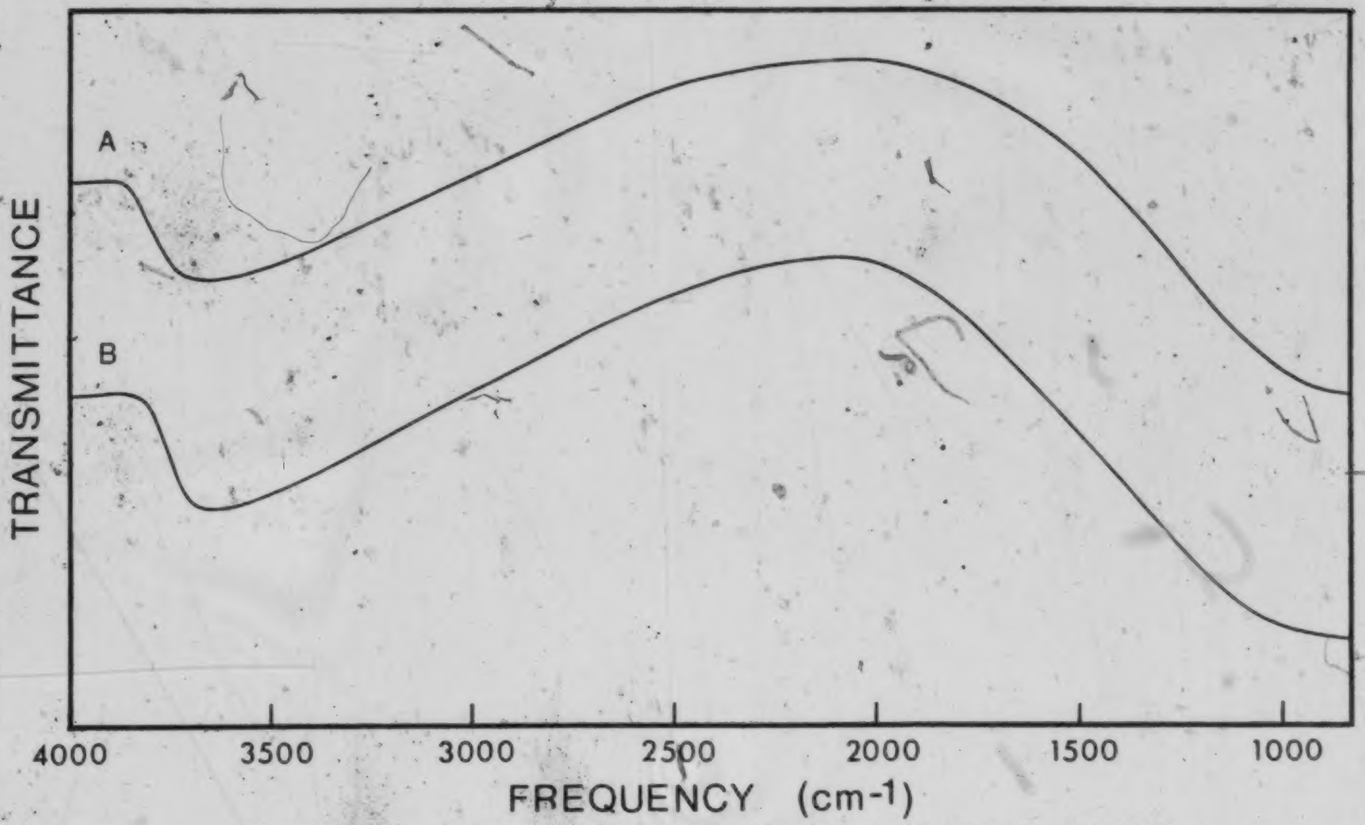

Figure 6-15. Infrared Spectra of γ-Alumina Under Reaction Conditions. (A) Without Reactants (B) With Reactants

TABLE 6-6

PARIAL PRESSURE RANGE OF THE COMPONENTS IN KINETIC RUNS

Temperature (°C)	No. of Data Points	Partial Pressure (mm Hg) Range: P_{H_2S}	P_{SO_2}	P_{H_2O}	P_{S_x}
200.0	19	11.92-33.40	11.47-32.59	5.21-36.01	0.99-4.19
212.3	19	12.07-39.07	10.71-31.87	9.06-40.31	1.44-2.33
235.18	16	9.33-28.43	8.96-28.89	8.14-58.86	1.51-2.34
261.5	14	8.97-35.01	8.56-35.01	7.64-65.32	0.84-3.20
298.24	36	5.52-55.97	7.96-55.97	7.01-41.30	1.38-5.39
323.0	14	8.53-29.40	8.28-28.81	10.57-60.02	1.76-3.64

More details on the 118 data point are to be found in Appendix I.

In the following sections, several plausible reaction mechanisms, ones which are in agreement with the overall chemistry and observations, will be proposed. Kinetic models will then be deduced from the various mechanisms. A model discrimination technique was then applied to test these rival models with the aid of experimental data. Hopefully, the model producing the "best" correlation with the experimental data could be chosen to represent the reaction.

6.8.1 General Methods for Developing and Testing Kinetic Models

Basically, the success in developing a kinetic model for a given reaction system relies on the effectiveness of the model discrimination technique. At the same time, it is affected by how the models are developed and whether adequate models have been considered. If an adequate model is not included among those models proposed for the system, any sophisticated model discrimination technique will generate a meaningless correlation. In fact, all statistical discrimination techniques are developed on the basic assumption that one adquate model must be contained among the rival models to be discriminated.

Generally, there are two methods for developing and testing kinetic models.

6.8.1.1 Empirical Models

Some empirical models are written down (e.g. power-function models) and then correlated with the data as a function of the various operating conditions. This method does not consider the nature of the reaction or rate-determining steps although, by coincidence, the model that produces the"best" correlation may reflect the rate-determining step or some characteristic of the reaction. The two major disadvantages of this method include: firstly, it does not provide any insight into the reaction mechanism anda good correlation can only be interpreted to mean a good correlation. The best such model does not necessarily reveal the true nature of the reaction. Secondly, with a lack of understanding on the nature of the reaction, it is not safe to extrapolate the range of application beyond the range of the experimental data and the models to be included for discrimination cannot be prescreened on the basis of the chemistry of the reaction. As a result, the number of rival models to be discriminated isusually large. This is very tedious and the chance of ending up with more than one equally good models after the discrimination process are also higher. Moreover, this method does not generally provide an understanding of the catalytic nature of the solid catalyst.

6.8.1.2 "Mechanistic" Models

This method involves obtaining as much knowledge as possible on the mechanism of the reaction and then developing the rate models (if more than one is feasible) which best describes the plausible mechanism. The following are the advantages of this method over the previous one. It provides some understanding of the nature of the reaction and the catalyst, which allows one to reject some rival models least conform with the accumulated knowledge. It may also allow one to extrapolate the range of application beyond the experimental range although one should still do this with caution. The reason of caution is that when the range is extended by simple extrapolation, the rate-controlling step might change. For example, the bulk gas-phase diffusion step may not be rate-controlled in the range of the experimental data but may be rate-controlled at some point in the extrapolated range.

In this method, the models most widely used to describe the mechanism of gaseous reactions on solid surfaces are the Eley-Rideal and Langmuir-Hinshelwood type models. The Eley-Rideal type model assumes that the reactant adsorbed on the catalyst surface reacts with another components in the gas-phase adjacent to the catalyst surface. The Langmuir-Hinshelwood models assumes that the reactants are adsorbed on one type of active site on the catalyst surface where they react, either with themselves or with other adjacent adsorbed species. Further assumptions in formulating Langmuir-Hinshelwood rate models include the existence of a single rate-controlling step, such as adsorption, surface reaction, or desorption, within a mechanism involving a series of reaction steps, and the absence of interactions between adsorbed molecules.

Although the approach followed in developing rate equation of the Langmuir-Hinshelwood type is straightforward, the task involved in determining the best rate expression for a complex reaction system is immense. If all possible reaction models are listed within the assumption of the Langmuir-Hinshelwood scheme, a relatively large number of models is obtained. For example, 84 empirical models have been postulated for methane oxidation by Mezaki et al. [85] and 47 models for ethanol dehydration by Kittrell [67]. The number of models could be increased if the assumptions applied in the formulation of Hougen-Watson rate equation are modified in various ways (for example, using more than one type of adsorption sites).

The presently available model discrimination techniques cannot be easily applied to a large groups of rival models due to the prohibitive amount of computer time that would be required. Consequently, it is desirable if not necessary to eliminate obviously inadequate models before utilizing the better model discrimination procedures.

In those cases where intermediate reaction steps are involved, the infrared spectroscopic technique has provided considerable insight into the identity of chemisorbed species which may act as intermediates in catalytic reactions, and also the nature of the interaction between an active site and an adsorbed molecule. According to the nature of surface intermediates observed, various intermediate reaction steps could then be formulated. Such information accumulated by infrared spectroscopic technique at the molecular rather than the macroscopic level, should serve as a good screening method because the mechanisms proposed according to infrared data would incorporate more detailed knowledge of the mechanism taking place on the catalyst surface.

After such prescreening, the remaining models could be tested by a model discrimination technique and hopefully one model that provides the "best" correlation with the experimental data could be evolved. Not frequently, the results of the discrimination procedure turn out to be ambiguous in that no one model is shown to be clearly superior. This dilemma may possibly be resolved by measuring more experimental rate data under reaction conditions outlined by a statistical design of experiment [130].

6.8.2 Development of Kinetic Models

The "mechanistic" approach for developing kinetic models was adopted in the present work. In the process of writing reaction mechanism for developing the kinetic models, the experimental evidence accumulated in Section 6.1 to 6.6 was taken into consideration.

In Sections 6.2 and 6.3, both H_2S and SO_2 were found to be adsorbed on Lewis-acid sites and their adsorption nature were found to be quite similar. In Section 6.6.1, it was found that no reaction was detected without the presence of catalyst under the reaction conditions employed in this work. Therefore, by combining the experimental observation in these three sections both H_2S and SO_2 are assumed to be adsorbed on the Lewis-acid sites of γ-alumina before they react with each other according to the reaction mechanisms proposed in the subsequent sections.

In Section 6.5, the importance of oxide-ion sites (which were not responsible for the adsorption of H_2S or SO_2) towards the reaction has clearly been demonstrated. This means that some intermediate step(s) must be included in the reaction mechanism to allow for the vital participation of the basic oxide sites. There are several possible intermediate steps that could enable the involvement of the basic sites. In Section 6.1, it was shown that a certain amount of "oxygen" or "oxide" is present on the surface of γ-alumina but whose state is still not clearly understood. This surface "oxygen" or "oxide" has oxidation capability at room temperature as demonstrated by the oxidation of H_2S into water plus sulfur and CS_2 into carbon dioxide plus sulfur. The quantity of this surface "oxygen" or "oxide" is finite and can be restored by heating γ-alumina with oxygen or SO_2. Such oxidation capability of γ-alumina has also been observed by others [23, 87, 115]. Considering the heterogeneity of the catalyst surface, perhaps some of the surface oxide-ions are more active and possess oxidation capability while others do not. This could explain the experimental observations in Section 6.1 that the amount of surface "oxygen" or "oxide" is finite. Parkyns [98, 99] interpreted the form of this surface "oxygen" or "oxide" in terms of a "strained oxygen bridge".

Other published results have revealed that the "oxygen" or "oxide" on the γ-alumina, regardless of its forms, can be exchanged with isotopic oxygen like H_2O^{18} [87], O_2^{18} [38] and O_2^{17} [35]. The exchange reaction seemed to imply that some surface "oxide" or "oxygen" is removable and replaceable. Presumably, when the removable surface oxides are consumed, a structural strain is created on the catalyst and this strain can be removed when the oxygen from an adsorbate is donated to the catalyst surface. This is demonstrated by the hydration and dehydration process of γ-alumina,

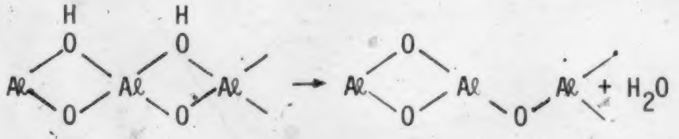

(6.29)

The above scheme does not represent the actual picture because it is not three-dimensional. Tamele [135] and Cornelius [27] reported that a remarkable amount of heat was released when water was contacted at 100°C with carefully dehydrated alumina. The release of heat was also detected by adsorbing H_2S on γ-alumina [33,84]. Perhaps, the consumption of oxygen by H_2S and restoration of oxygen by SO_2 on the γ-alumina surface is a continuous oxidation-reduction process. This oxidation-reduction process may be depicted by the following scheme,

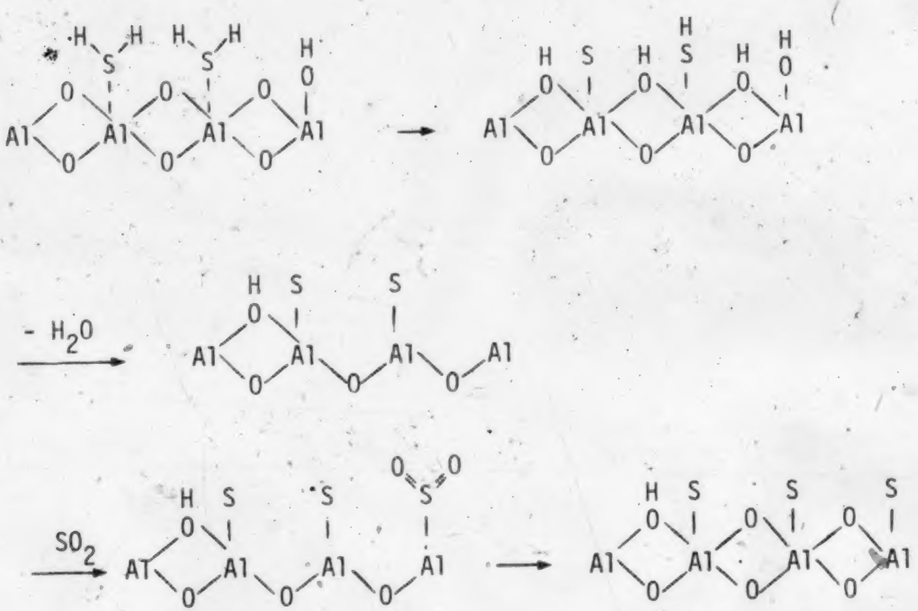

The above scheme may not represent the actual picture on the surface of γ-alumina because it is not three-dimensional where the final step may not be impossible. As has been shown by Tamele [135] and Cornelius [27], the exposed aluminium-ion on the dehydrated alumina is quite unstable and readily covers itself with hydroxyl group on hydration and may proceed in one of the following manners,

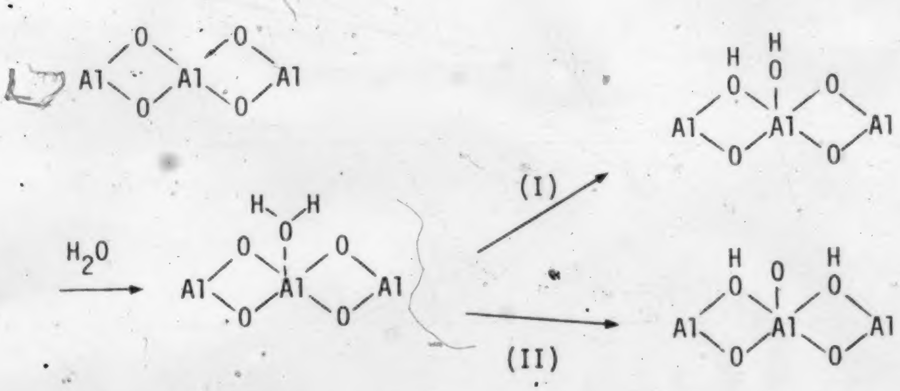

Case (II) can be shown taking place on the 110-plane of γ-alumina as below.

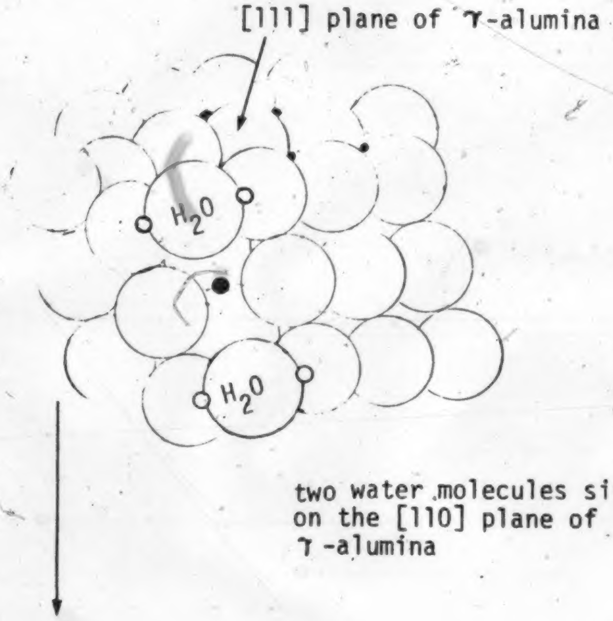
[111] plane of γ-alumina
H_2O
H_2O

two water molecules sitting on the [110] plane of γ-alumina

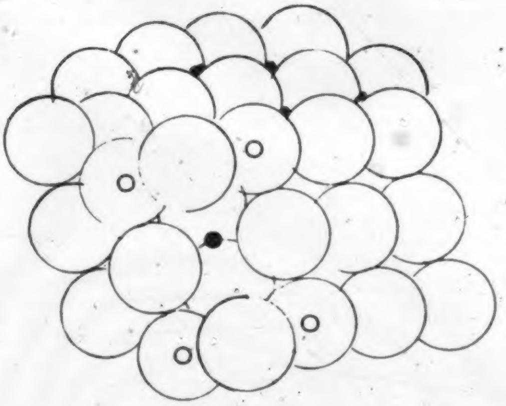

two hydrogen atoms dissociated from each water molecules sitting on [110] plane of γ-alumina

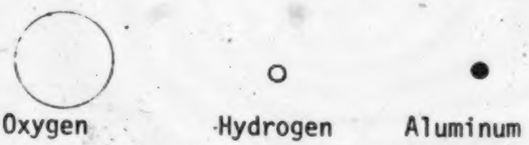
Oxygen
Hydrogen
Aluminum

If partial dissociation of two adsorbed water molecules occurs, followed by desorption of one water molecule, then

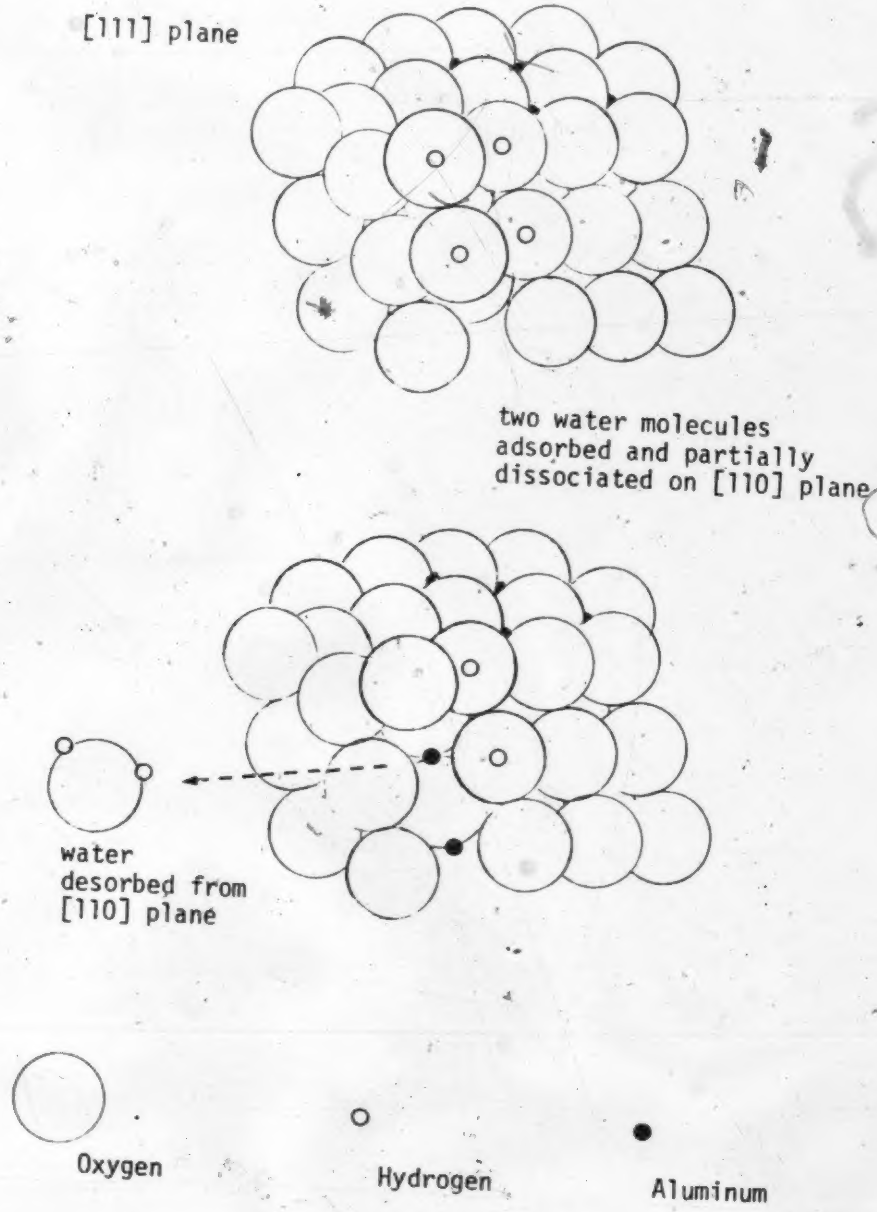
[111] plane
two water molecules
adsorbed and partially
dissociated on [110] plane
water
desorbed from
[110] plane
Oxygen
Hydrogen
Aluminum

A "surface oxygen" thus remains on the surface of the 110 planes. By the same analogy, such "surface oxygen" could be created by dissociation of SO_2 on 110 plane as shown below.

[111] plane of -alumina

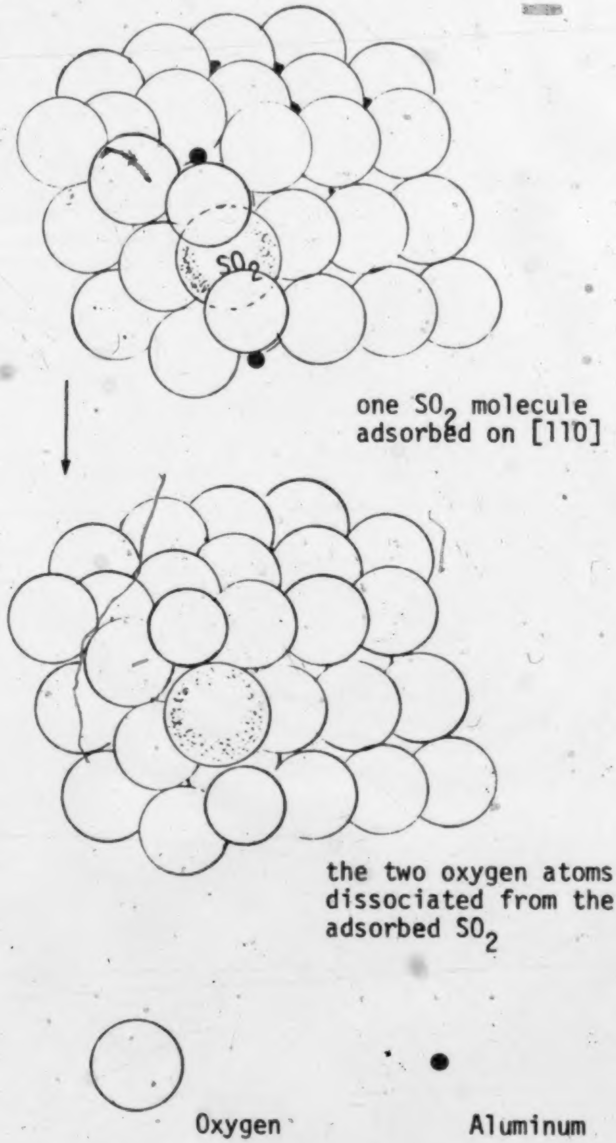

one SO_2 molecule adsorbed on [110] plane

the two oxygen atoms dissociated from the adsorbed SO_2

It is not certain whether the oxidation-reduction reaction between H_2S and SO_2 takes place via the "lattice" oxygen or the "surface" oxygen of γ-alumina. However, the experimental evidence in Section 6.1 shows that a finite amount of "surface oxygen" (whatever its form) exists on γ-alumina. Such an alumina exhibits strong oxidation power, which effect has also been observed by others [23,86,87,115] and SO_2 dissociation is a means of supplementing this "surface oxygen" in its process of reaction with H_2S. Therefore, in developing the reaction mechanism in the subsequent sections, SO_2 adsorption followed by dissociation will be considered as a reaction step. Other steps in the mechanisms involved the adsorption-desorption of the products sulfur and water.

The major differences among the various sets of mechanisms developed in the later sections include dissociation of adsorbed H_2S as observed by others [33,133], the various surface species located in the closest vicinity of the reactants, and the possible participation of the surface sulfur (as adsorption sites or reaction intermediates) in the reaction. All of these will be discussed in greater detail when the specific mechanisms involving them are developed.

6.8.2.1 Kinetic Models Derived from a Reaction Mechanism Involving Dissociation of Adsorbed H_2S into Hydroxyl Groups

The dissociation of adsorbed H_2S on γ-alumina was observed by de Rosset et al. [33] and Slager and Amberg [133]. The way by which adsorbed H_2S dissociates depends very much on what is located around its closest vicinity. The various arrangements of the "OH" and "O" groups have been discussed extensively by Peri's computer simulated models plus his infrared spectroscopic and micro-gravimetric studies [67]. Briefly, the different ways by which adsorbed H_2S dissociates on γ-alumina surface are shown below:

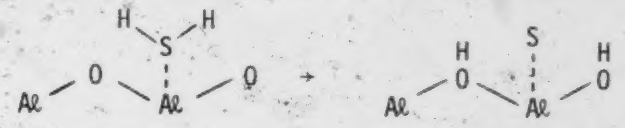

(6.35)

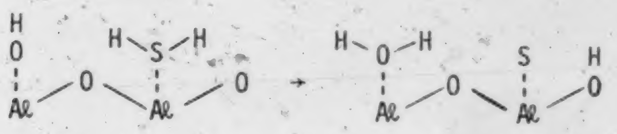

(6.36)

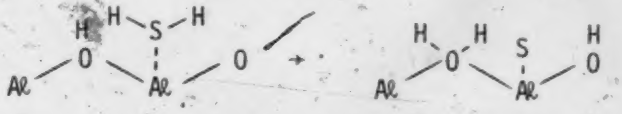

(6.37)

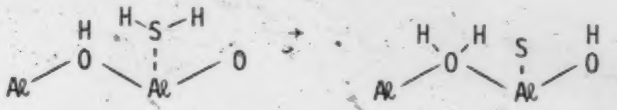

(6.38)

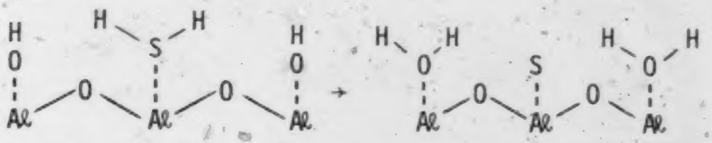

(6.39)

Therefore, after the adsorption and dissociation of H_2S, adsorbed water is formed which then desorbs and each water molecule takes along with it one oxygen atom from the surface of γ-alumina. The oxygen is then replenished by the dissociation of adsorbed SO_2. In terms of mechanistic equations shown in Table 6-7, to maintain the stoichiometric balance, it was assumed that one H_2S molecule dissociates to produce one sulfur atom and two hydroxyl groups (regardless of whether according to that shown by the left hand term of 6.36 or 6.37) which eventually react with one more H_2S molecule to produce water and sulfur.

By assuming various alternative step(s) as rate-controlling in the mechanism, more than one kinetic models could be derived, as shown in Table 6-7. During the derivation of each of the kinetic models, all reaction steps in the proposed mechanism were originally assumed to be reversible and examples of the derivation can be found in Appendix H. In Section 6.6.2.2, the reverse reaction was found to be practically insignificant under the process conditions employed in this work. The insignificance of the reverse term was also noted by others[84,43,64,138] consequently, the reverse terms of the derived kinetic models were dropped and the resulting models are listed in Table 6-7, where the sulfur is represented by S_x and x represents the number of sulfur atom (1,2,.... 8) of various sulfur molecules. No reliable method of measuring the distribution of various sulfur species (S_1, S_2, etc.) during reaction is yet available. In this work, a pseudosulfur species S_x was calculated by assuming an equilibrium distribution among the various sulfur species. McGregor[84] concluded from the material balance calculation around his reaction system that the selection of S_x from equilibrium distribution calculation to represent the various sulfur species in his reactor was quite reasonable. When more than one step is considered to be rate-controlling, overcomplication of the derived kinetic models results. To avoid this problem only the relatively simple models were used.

6.8.2.2 Kinetic Models Derived from Reaction Mechanisms Involving Adsorbed H_2S Reacting with Surface "Oxygen" and Hydroxyl Groups

As pointed out in Section 6.7, a broad hydrogen bonding band was recorded by the infrared spectrophotometer during the reaction. A significant quantity of hydroxyl groups were present on the catalyst surface

TABLE 6-7

KINETIC MODELS DERIVED FROM REACTION MECHANISM INVOLVING DISSOCIATION OF ADSORBED H_2S INTO HYDROXYL GROUPS

Proposed Mechanism

(1) $2H_2S + 2\,\# \rightleftharpoons 2H_2S\cdot\#$

(2) $SO_2 + \# \rightleftharpoons SO_2\cdot\#$

(3) $SO_2 + \# + 2\# \rightleftharpoons S\,.\,\# + 2O\,.\,\#$

(4) $H_2S\cdot\# + 2O\cdot\# \rightleftharpoons S\,.\,\# + 2HO\,.\,\#$

(5) $H_2S\cdot\# + 2HO\cdot\# \rightleftharpoons S\,.\,\# + 2H_2O\,.\,\#$

(6) $2H_2O\,.\,\# \rightleftharpoons 2H_2O + 2\#$

(7) $3S\,.\,\# \rightleftharpoons 3/x\ S_x + 3\#$

where # is the Lewis acid site

S_x is a pseudo sulfur species representing S_2, S_6, S_8 etc.

(mostly S_8 under the process condition used here)

TABLE 6-7 (Continued)

Controlling Step(s)	Rate Expression ($-r_{SO_2}$)	Assigned Model No.
(1)	$b_7\, P_{H_2S}^{\;2} / Y^2$	HS1
(2)	$b_8\, P_{SO_2}/Y$	HS2
(3)	$b_9\, P_{SO_2}/ Y^3$	HS3
(4)	$b_{10}\, P_{H_2S}\, P_{SO_2}/ P_{S_x}^{\;1/x}\, Y^3$	HS4
(5)	$b_{11}\, P_{H_2S}^{\;2}\, P_{SO_2} / P_{S_x}^{\;1/x}\, Y^3$	HS5
(6)	same as HS5	
(7)	same as HS5	
(1) + (2)	same as HS5	

where b_1,b_2,b_3,b_4 are adsoprtion equilibrium constants for H_2S,SO_2,H_2O, S_x; K_i is the equilibrium rate constant for reaction step i.

k_i is the forward rate constant for reaction step i

$b_5 = \sqrt{K_2K_3K_7}$, $b_6=K_1\sqrt{K_3K_4K_2}$, $b_7 = k_1$, $b_8 = k_2$, $b_9 = k_3k_2$,

$b_{10}= k_4K_1K_2\, K_7K_3$, $b_{11} = k_5K_1^{\,2}\, K_7^{\,2}\, K_2K_3$

$$Y = [1 + b_1P_{H_2S} + b_2P_{SO_2} + b_3\, P_{H_2O} + b_4P_{S_x}^{\;1/x} + b_5P_{SO_2}^{\;1/2}/P_{S_x}^{\;1/2x} + b_6P_{H_2S}^{\;1/2}\, P_{SO_2}^{\;1/2}/P_{S_x}^{\;1/x}]$$

during reaction. Under a temperature comparable to that used in the kinetic runs of the present work, Peri [104] observed a large number hydroxyl groups on the γ-alumina surface. Therefore, because of their population, it is logical to consider that the hydroxyl groups may also participate in the reaction.

In this mechanism, the adsorbed H_2S is assumed to transfer its two hydrogen atoms to the two neighbouring hydroxyl groups to produce two adsorbed molecules of water and sulfur. This has been considered in the mechanism in Section 6.8.2.1. At the same time, the adsorbed H_2S is assumed to be oxidized by "surface oxygen" to produce one adsorbed molecule of water and sulfur but in the mechanism in Section 6.8.2.1, the adsorbed H_2S was oxidized to two hydroxyl groups. Another difference between this mechanism and the one in Section 6.8.2.1 is that the hydroxyl groups were not generated by the dissociation of adsorbed H_2S but by the dissociation of the adsorbed H_2O.

Other reaction steps for the two mechanisms are practically the same. The proposed mechanism and the kinetic models derived from it by assuming various step(s) to be controlling are listed in Table 6-8. Again, to conform with the experimental observations in Section 6.6.2.2, the reverse terms of all derived kinetic models were dropped before writing them down in Table 6-8, although all steps were considered reversible during the model derivation process. This practice will be the same in all subsequent model derivations and will not be emphasized again.

TABLE 6-8

KINETIC MODELS DERIVED FROM REACTION MECHANISM INVOLVING ADSORBED H_2S REACTING WITH SURFACE "OXYGEN" AND HYDROXYL GROUPS

Proposed Mechanism

(1) $2\ H_2S + 2\ \# \rightleftarrows 2H_2S\cdot\#$

(2) $SO_2 + \# \rightleftarrows SO_2\cdot\#$

(3) $SO_2\ .\ \# + 2\ \# \rightleftarrows S\cdot\# + 2O\cdot\#$

(4) $H_2S\cdot\# + 2HO\cdot\# \rightleftarrows 2\ H_2O\ .\ \# + S\ .\ \#$

(5) $H_2S\ .\ \# + O\ .\ \# \rightleftarrows H_2O\ .\ \# + S\ .\ \#$

(6) $H_2O\ .\ \# + O\ .\ \# \rightleftarrows 2HO\ .\ \#$

(7) $2H_2O\ .\ \# \rightleftarrows 2H_2O + 2\#$

(8) $3S\ .\ \# \rightleftarrows 3\# + 3/x\ S_x$

TABLE 6-8 (Continued)

Controlling Step(s)	Rate Expression ($-r_{SO_2}$)	Assigned Model No.
(1)	$b_7 P_{H_2S}^{2} / Y^2$	DOH1
(2)	$b_8 P_{SO_2} / Y$	DOH2
(3)	$b_9 P_{SO_2} / Y^3$	DOH3
(4)	$b_{10} P_{H_2S} P_{H_2O} P_{SO_2}^{1/2} / P_{S_x}^{1/2x} Y^3$	DOH4
(5)	$b_{11} P_{H_2S} P_{SO_2}^{1/2} / P_{S_x}^{1/2x} Y^2$	DOH5
(6)	same as DOH4	
(7)	same as DOH4	
(8)	same as DOH4	

where b_1, b_2, b_3, b_4 are the equilibrium adsorption constants for H_2S, SO_2, H_2O and S_x

K_i is the equilibrium constants for reaction step i

k_i is the forward rate constant for reaction step in $b_5 = (K_2K_3K_8)^{1/2}$

$b_6 = (k_2K_3K_8)^{1/4}(K_7)^{1/2}$ $b_7 = k_i$, $b_8 = k_2$, $b_9 = k_3K_2$,

$b_{10} = k_4K_1K_6K_7(K_2K_3K_8)^{1/2}$

$$Y = [1 + b_1P_{H_2S} + b_2P_{SO_2} + b_3P_{H_2O} + b_4P_{S_x}^{1/x} + b_5P_{SO_2}^{1/2} / P_{S_x}^{1/2x} + b_6P_{SO_2}^{1/4} P_{H_2O}^{1/2} / P_{S_x}^{1/4x}]$$

6.8.2.3 Kinetic Models Derived from Reaction Mechanism Involving Dissociation of Adsorbed H_2S by the Sulfur on Catalyst Surface But Without the Participation of Hydroxyl Groups in Reaction

In the mechanism, the adsorbed sulfur is assumed to participate in the reaction. The adsorbed H_2S is assumed to have a choice to react with the adsorbed sulfur or "surface oxygen" depending on which is in the nearest vicinity. If it reacts with the former, it dissociates to produce two adsorbed SH groups. These then react with the "surface oxygen" to form adsorbed sulfur and water. On the other hand, if it reacts directly with "surface oxygen" then adsorbed sulfur and water will be produced without going through the formation of SH groups. The following scheme demonstrates how adsorbed H_2S dissociates on adsorbed sulfur and then reacts with "surface oxygen"

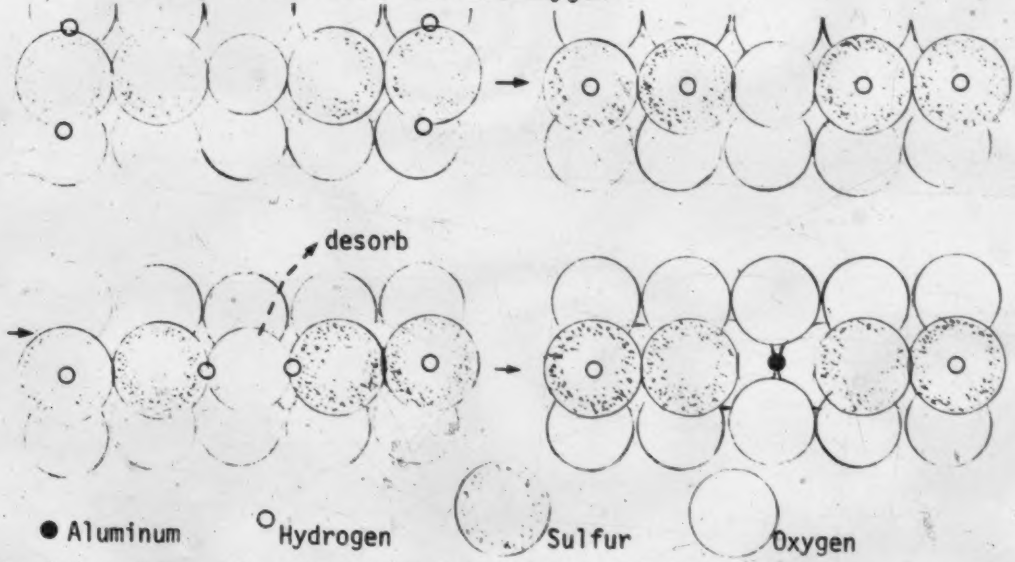

In this scheme, the adsorbed H_2S transfers one of its hydrogen atoms to a neighbouring adsorbed sulfur to form a SH group. Two of these SH groups are assumed to be located next to a "surface oxygen" and could then transfer their hydrogen atoms to the "surface oxygen" to form an adsorbed water. The two SH groups are hence transferred into sulfur.

The possible dissociation of adsorbed H_2S has been suggested by De Rosset et al.[33] and Slager and Amberg [133]. Wiewiorowski and Toure [147,148] studied the experiment of bubbling H_2S into molten sulfur by using infrared spectroscopy. They observed possible dissociation of H_2S in the molten sulfur and found that the total concentration of H_2S in molten sulfur varied from 0.0544 to 0.145 % in the temperature range of 125 to 181°C. Their experimental evidence included the detection of the formation of polysulfide, HS....S....SH. They detected the band at 2570 cm^{-1} which represents the H_2S in molten sulfur from the infrared spectrum at about 5 minutes after bubbling H_2S into molten sulfur, but only after more than 30 minutes later did they detect the 2498 cm^{-1} band which indicated the presence of polysulfide. After bubbling 20 hours of H_2S into the molten sulfur, the H_2S was removed and nitrogen was used to continue the bubbling. This time, the more volatile H_2S which was represented by the 2570 cm^{-1} band disappeared 15 minutes after the bubbling started but the 2498 cm^{-1} band polysulfide was removed from the molten sulfur only 20 hours later. Hyne [60] theorized the formation of H_2S_n as a step of producing sulfur from H_2S. This will be discussed in Section 6.9.

6.8.2.4 Kinetic Models Derived from Reaction Mechanism Involving Dissociation of Adsorbed H_2S by the Sulfur on Catalyst Surface But With the Participation of Hydroxyl Groups in Reaction

This mechanism is the same as that mentioned in Section 6.8.2.3 except that the surface hydroxyl groups are assumed to participate in the reaction. They do so by reacting with the adsorbed H_2S to generate HS

TABLE 6-9

KINETIC MODELS DERIVED FROM REACTION MECHANISM INVOLVING DISSOCIATION OF ADSORBED H_2S BY THE SULFUR ON CATALYST SURFACE BUT WITHOUT THE PARTICIPATION OF HYDROXYL GROUPS IN REACTION

Proposed Mechanism

(1) $2H_2S + 2\,\# \rightleftharpoons 2H_2S\cdot\#$

(2) $SO_2 + \# \rightleftharpoons SO_2\cdot\#$

(3) $SO_2\,.\,\# + 2\,\# \rightleftharpoons S\cdot\# + 2O\cdot\#$

(4) $H_2S\,.\,\# + O\cdot\# \rightleftharpoons H_2O\,.\,\# + S\,.\,\#$

(5) $H_2S\,.\,\# + S\cdot\# \rightleftharpoons 2HS\,.\,\#$

(6) $2HS\,.\,\# + O\cdot\# \rightleftharpoons H_2O\,.\,\# + 2S\,.\,\#$

(7) $2H_2O\,.\,\# \rightleftharpoons 2H_2O + 2\,\#$

(8) $3S\,.\,\# \rightleftharpoons 3/x\ S_x + 3\,\#$

TABLE 6-9 (Continued)

Controlling Step(s)	Rate Expressions ($-r_{SO_2}$)	Assigned Model No.
(1)	$b_7 P_{H_2S}^2 / Y^2$	DS01
(2)	$b_8 P_{SO_2} / Y$	DS02
(3)	$b_9 P_{SO_2} / Y^3$	DS03
(4)	$b_{10} P_{H_2S} P_{SO_2}^{1/2} / P_{S_x}^{1/2x} Y^2$	DS04
(5)	$b_{11} P_{H_2S} P_{S_x}^{1/x} / Y^2$	DS05
(6)	$b_{12} P_{H_2S} P_{SO_2}^{1/2} P_{S_x}^{1/2x} / Y^3$	DS06
(7)	combination of DS04 and DS06	
(8)	combination of DS04 and DS06	

where b_1, b_2, b_3, b_4 are the equilibrium adsorption constants for H_2S, SO_2, H_2O and S_x

K_i is the equilibrium constant for reaction step i and

k_i is the forward rate constant for reaction step i

$b_5 = (K_3K_8K_2)^{1/2}$, $b_6 = (K_5K_1K_8)^{1/2}$, $b_7 = k_1$, $b_8 = k_2$, $b_9 = K_3K_2$

$b_{10} = k_4\, K_1(K_3K_2K_8)^{1/2}$ $b_{11} = k_5K_1/K_8$, $b_{12} = k_6K_5K_1\, (K_2K_3/K_8)^{1/2}$

$$Y = [1 + b_1P_{H_2S} + b_2P_{SO_2} + b_3\, P_{H_2O} + b_4P_{S_x}^{1/x} + b_5P_{SO_2}^{1/2} / P_{S_x}^{1/2x} + b_6\, P_{H_2S}^{1/2} / P_{S_x}^{1/2x}]$$

groups and water. The HS groups are oxidized by the "surface oxygen" to water and sulfur or to hydroxyl groups and sulfur. The kinetic models derived from this mechanism are summarized in Table 6-10.

6.9 Model Discrimination

The model discrimination process generally involves selecting the best candidate out of the various eligible models under the assumption that an adequate model has been included among the models proposed for the system studied. The various useful model discrimination techniques have been reviewed extensively by others [4,67]. Basically, after the prescreening to eliminate some poor models according to the observed chemistry of the reaction, the following three steps were carried out:

1. parameter estimation.
2. computing the model discrimination index - likelihoods of the data, and
3. sequential design of experiments.

In the present work, the statistical model discrimination technique developed by Singh [130] was adopted. Details of this technique are summarized below.

6.9.1 Statistical Model Discrimination Technique

6.9.1.1 Model Discrimination Procedure

Out of the various criteria for classifying model performance, the earliest one was the minimum sum of errors squared. One of the most successful criteria is the Bayesian expected likelihood procedure based on a Bayesian interpretation of probability described below.

TABLE 6-10

KINETIC MODELS DERIVED FROM REACTION MECHANISM INVOLVING DISSOCIATION OF ADSORBED H_2S BY THE SULFUR ON CATALYST SURFACE BUT WITH THE PARTICIPATION OF HYDROXYL GROUPS IN REACTION

Proposed Mechanism

(1) $2H_2S + 2\,\# \rightleftarrows 2H_2S\cdot\#$

(2) $SO_2 + \# \rightleftarrows SO_2\cdot\#$

(3) $SO_2\,.\,\# + 2\,\# \rightleftarrows S\cdot\# + 2O\cdot\#$

(4) $H_2S\,.\,\# + S\,.\,\# \rightleftarrows 2\,HS\cdot\#$

(5) $H_2S\,.\,\# + HO\cdot\# \rightleftarrows H_2O\,.\,\# + HS\,.\,\#$

(6) $2HS\,.\,\# + O\,.\,\# \rightleftarrows H_2O\,.\,\# + 2S\,.\,\#$

(7) $HS\,.\,\# + O\,.\,\# \rightleftarrows HO\,.\,\# + S\,.\,\#$

(8) $2H_2O\,.\,\# \rightleftarrows 2H_2O + 2\,\#$

(9) $3S\,.\,\# \rightleftarrows 3/x\;S_x + 3\,\#$

TABLE 6-10 (Continued)

Controlling Step(s)	Rate Expression ($-r_{SO_2}$)	Assigned Model No.
(1)	$b_8 P_{H_2S} / Y^2$	DSOH1
(2)	$b_9 P_{SO_2} / Y$	DSOH2
(3)	$b_{10} P_{SO_2} / Y^3$	DSOH3
(4)	$b_{11} P_{H_2S} P_{S_x}^{1/x} / Y^2$	DSOH4
(5)	$b_{12} P_{H_2S}^{3/2} P_{SO_2}^{1/2} / P_{S_x}^{1/x} Y^2$	DSOH5
(6)	$b_{13} P_{H_2S} P_{SO_2}^{1/2} P_{S_x}^{1/2x} / Y^3$	DSOH6
(7)	$b_{14} P_{H_2S}^{1/2} P_{SO_2}^{1/2} / Y^2$	DSOH7
(8)	combination of (5) and (6)	
(9)	combination of (5) and (6)	

where b_1, b_2, b_3, b_4 are adsorption equilibrium constants

K_i is the equilibrium constant for reaction i

k_i is the forward rate constant for reaction i

$b_5 = (K_2K_3K_9)^{1/2}$, $b_6 = (K_4K_1/K_9)^{1/2}$, $b_7 = K_7(K_4K_3K_1K_2)^{1/2} K_9$

$b_8 = k_1$, $b_9 = k_2$, $b_{10} = k_3K_2$, $b_{11} = k_4K_1/K_9$

$b_{12} = k_5K_1K_7K_9(K_1K_2K_3K_4)^{1/2}$ $b_{13} = k_6K_4K_1(K_2K_3/K_9)^{1/2}$

$b_{14} = k_7\,(K_1K_4K_2K_3)^{1/2}$

$$Y = [1 + b_1 P_{H_2S} + b_2P_{SO_2} + b_3P_{H_2O} + b_4P_{S_x}^{1/x} + b_5P_{SO_2}^{1/2}/P_{S_x}^{1/2x}$$

$$+ b_6 P_{H_2S}^{1/2} P_{S_x}^{1/2x} + b_7P_{H_2S}^{1/2}P_{SO_2}^{1/2} / P_{S_x}^{1/x}]$$

Assuming that m models have been left for discrimination after the preliminary screening which comprises the metamodel:

$$\begin{aligned} y &= \phi_1 (\underline{x}, \underline{a}_1) + \varepsilon_1 \\ &\vdots \\ y &= \phi_k (\underline{x}, \underline{a}_k) + \varepsilon_k \\ &\vdots \\ y &= \phi_m (\underline{x}, \underline{a}_m) + \varepsilon_m \end{aligned} \quad . \qquad (6.40)$$

where metamodel is defined as the model space containing all the potential mechanisms which are considered simultaneously, and

$\underline{x}$ = vector of independent variables

$\underline{a}_k$ = vector of unknown parameter corresponding to the k^{th} model

y = dependent variable

ε_i = error term in the i^{th} model.

The models may be in differential rather than algebraic form but that will not affect the argument to follow.

Uncertainty about which model form is the true one is expressed quantitatively in the form of a discrete probability distribution, where P_k is the probability that the k^{th} model form is correct. Obviously, the set of P_k's satisfy the axioms of probability, i.e.

$$0 \leq P_k \leq 1.0 \; ; \; \sum_{k=1}^{m} P_k = 1.0 \qquad (6.41)$$

Conceptually, the P_k's are personal or subjective probabilities in the Bayesian sense and not objective or frequency probabilities in the classical sense. Bayesian probabilities are a measure of our current state of knowledge about an uncertain quantity or hypothesis; they are modified with the acquisition of new information in accordance with Baye's Theorem.

Probabilities are assigned to the different models before taking data and without strong information about the reaction, it is conventional to make these "prior probabilities" all equal. Similarly, lacking specific information about the parameters, their values are assumed to be distributed over the range - to + (called the improper uniform distribution).

With n sets of observations $\{y_i, \underline{x}_i; i = 1, 2, \ldots\ldots n\}$, the posterior probabilities, P_j'', can be calculated by the Bayes' Theorem.

$$P_j'' = \frac{P_j' \, L\,(\underline{y}/\phi_j)}{\Sigma_j P_j' \, L\,(\underline{y}/\phi_j)} \qquad (j = 1, 2, \ldots\ldots n) \qquad (6.42)$$

Where P_j' designates the probability prior to observing the data of and $L(\underline{y}/\phi_j)$ is the expected likelihood which is used to designate the probability of observing the data, given that the model form ϕ_j is correct.

Ball [4] mentioned that the excessive computations involved in evaluating the expected likelihoods when the number of observations is more than 20 has been a disadvantage for the Bayesian discrimination procedure. This has been overcome by Singh[130] by developing new expressions for the expected likelihoods and thus simplifying the computations. They proposed the following expressions for computing the expected likelihood for j^{th} model when the prior information about the parameters in each model form is so vague that it can be approximated by the improper uniform distribution,

$$L(\underline{y}/\phi_j) = (2\pi\,\sigma_j^2)^{-n/2}\,(1/2)\,\exp\left\{-\frac{\hat{S}_j^2}{2\sigma_j^2}\right\} \qquad (6.43)$$

where r = number of parameters involved in the j^{th} model.

$\hat{S}_j^2$ = the minimum sum of errors squared;

$$\hat{S}_j^2 = \min_{\underline{a}_j} \sum_{i=1}^{n} (y_{\text{observed}, i} - y_{\text{calcd}, i})^2$$

$\hat{\underline{a}}_j$ = parameter vector that minimize the sum of errors squared.

$\sigma_j^2 = \hat{S}_j^2/(n-r)$; the unbiased estimate of error variance.

The posterior probabilities of success for the competing models can now be computed from equation (6.42) and the parameters, $a_{j,k}$ with 95% confidence intervals, are calculated from following equation:

$$a_{j,k} = \hat{a}_{j,k} \pm 2\sqrt{C_{j,kk}} \tag{6.44}$$

where $\hat{a}_{j,k}$ = k^{th} element of the parameter vector $\hat{\underline{a}}_j$ that minimize the sum of errors squared for the j^{th} model.

$C_{j,kk}$ = the diagonal element of the variance covariance matrix of the parameters, $\underline{c}_j$ for the j^{th} model.

In order to compute c_j, the following equations are refined:

$$\underline{X}_{jik} = \left.\frac{\partial\phi_j(\underline{X}_i, \underline{a}_j)}{\partial a_{jk}}\right|_{a_j = \hat{\underline{a}}_j} \tag{6.45}$$

$$\underline{X}_j = X_{jik}, \{i = 1,2,\ldots.\ n;\ k = 1,2,\ldots..r\} \tag{6.46}$$

$$= n \times r \text{ design matrix}$$

$$\underline{A}_j = \underline{X}_j^t\, \underline{X}_j \tag{6.47}$$

The $\underline{C}_j$ can now be obtained by

$$\underline{C}_j = \sigma_j^2\, \underline{A}_j^{-1} \tag{6.48}$$

6.9.1.2 Design of Experiments

The idea of planning of experiments is to explore the entire operating space to locate a region in which predicted responses of the various competing models, based on existing information, will provide maximum discrimination. The expected entropy changes criterion used for design of experiments in this thesis is due to Singh [130] and is both exact and analytically simple unlike the earlier criteria that were only approximately correct [4].

For a set of m models after observing n data points, the entropy may be defined as:

$$E_n = -\sum_{i=1}^{M} P_{i,n} \ln P_{i,n}$$

where $P_{i,n}$ is the probability of the i^{th} model being true after n observations. A hypothetical $(n+1)^{st}$ experiment is carried out and the expected posterior probabilities $P_{i,n+1}$ are now used to compute E_{n+1}. It is the difference, $-R = E_n - E_{n+1}$, that is a measure of the improvement in our knowledge. The following expression for -R gives the negative of expected entropy change.

$$-R = 0.5 \sum_{i=1}^{M} P_{i,n} \left[-\ln \frac{\sigma^2 + \sigma^2_{i,n+1}}{\sigma^2 + \sigma^2_{n+1}} + \frac{(\hat{y}_{i,n+1} - \hat{y}_{n+1})^2}{\sigma^2 + \sigma^2_{n+1}} + \frac{\sigma^2_{i,n+1} - \sigma^2_{n+1}}{\sigma^2 + \sigma^2_{n+1}} \right]$$

where σ^2 = error variance of a single measurement.

$$\sigma^2_{i,n+1} = \underline{X}_D (\underline{X}^t_{i,n} - \underline{X}_{i,n}) \underline{X}^t_D \sigma^2$$

$\underline{X}_D$ = 1 x r design vector for $(n+1)^{st}$ row of the design matrix $\underline{X}_{n+1}$

$\hat{y}_{i,n+1}$ = prediction from the i^{th} model corresponding to $\underline{X}_D$

$$\sigma^2_{n+1} = \sum_{i=1}^{M} P_{i,n}\,{}^{2}\,\hat{y}_{i,n+1}$$

$$\hat{y}_{n+1} = \mathop{}\limits_{i=1}^{M} P_{i,n}\ \hat{y}_{i,n+1}$$

The hypothetical $(n+1)^{st}$ experiment is carried out at various experimental conditions and the negative value of the expected entropy change is examined to obtained a region where -R is maximum.

Computer programs used for the above calculations are listed in Appendix B.

6.9.2 Some Published Models on Claus Reaction

Before the kinetic models developed in Section 6.8 are considered, it would be interesting to correlate some of the published models on Claus reaction with the rate data measured in the present work. Such correlation can provide a comparison of the published result against that in this thesis. The published models selected are:

(1) Hammar's [55] models

(a) $-r_{SO_2} = b_1\ P_{H_2S}\ \ P_{SO_2}\ /(1 + b_2P_{H_2S} + b_3P_{SO_2})^2$

(b) $-r_{SO_2} = b_1\ P_{H_2S}{}^2\ P_{SO_2}\ /(1 + b_2P_{H_2S} + b_3P_{SO_2})^2$

(c) $-r_{SO_2} = b_1\ P_{H_2S}\ \ P_{SO_2}\ /(1 + b_2P_{H_2S} + b_3P_{SO_2})^3$

(2) George's [44] best model

$$\text{(a)} \quad -r_{H_2S} = b_1 P_{H_2S}$$

(3) McGregor's [84] best model

$$\text{(a)} \quad -r_{SO_2} = b_1 P_{H_2S} P_{SO_2}^{1/2} / (1 + b_2 P_{H_2O})$$

The statistical model discrimination techniques mentioned in Section 6.9.1 were employed for the correlation. To minimize complications, the rate data collected in a set of isothermal kinetic runs were used for preliminary correlation tests. There are 36 data points in the isothermal kinetic experiment at 298°C and less than 20 data points in each of the other five sets of isothermal experiments. Therefore, the 298°C run was employed for the preliminary correlation tests against the selected published kinetic models and the results are summarized in Table 6-11.

TABLE 6-11

CORRELATION OF SOME PUBLISHED KINETIC MODELS WITH RATE DATA AT 298°C

Kinetic Models	b_1	b_2	b_3	Variance
Hammar's Model (a) $b_1 P_{H_2S} P_{SO_2}/(1+b_2 P_{H_2S}+b_3 P_{SO_2})^2$	6.1945×10^{-8} $\pm1.4657\times10^{-8}$	-0.0014 ±0.0038	0.0141 ±0.0103	3.1847×10^{-12}
Hammar's Model (b) $b_1 P_{H_2S}^2 P_{SO_2}/(1+b_2 P_{H_2S}+b_3 P_{SO_2})^2$	1.4335×10^{-8} $\pm1.2315\times10^{-8}$	0.0517 ±0.0613	0.0299 ±0.0481	7.5801×10^{-12}
Hammar's Model (c) $b_1 P_{H_2S} P_{SO_2}/(1+b_2 P_{H_2S}^{0.5}+b_3 P_{SO_2})^3$	6.062×10^{-8} $\pm2.0508\times10^{-8}$	-0.0060 ±0.0432	0.0089 ±0.0095	3.3197×10^{-12}

TABLE 6-11 (Continued)

Kinetic Models	b_1	b_2	b_3	Variance
George's Best Model $b_1 P_{H_2S} /(1 + b_2 P_{H_2O})$	6.7713×10^{-7} $\pm5.8321\times10^{-8}$	0.007 ±0.021		1.3983×10^{-11}
McGregor's Best Model $b_1 P_{H_2S} P_{SO_2}^{1/2}/(1 + b_2 P_{H_2O})$	2.0006×10^{-7} $\pm5.5648\times10^{-10}$	0.0051 ±0.0001		5.4180×10^{-15}

Table 6-11 shows the values of the parameters and variances together with their 95% confidence limits for the various kinetic models tested. McGregor's model exhibits the best fit while George's model is the worst. From the statistical model discrimination technique, it was found that the posterior probability of McGregor's model is very nearly 100% whereas those for the other models are almost zero. The clear superiority of McGregor's model is also shown by its relatively narrow 95% confidence limits of the correlated parameters in contrast to those of other models.

The form of McGregor's model differs from that of the other four models not only in denominator but also in numerator terms. To test for the sensitivity of the numerator and the denominator terms in McGregor's models, the following two models were correlated using the same 298°C isothermal rate data.

$$-r_{SO_2} = b_1 P_{H_2S} P_{SO_2} /(1 + b_2 P_{H_2O}) \qquad \text{Model No. DEM 2}$$

$$-r_{SO_2} = b_1 P_{H_2S} P_{SO_2}^{1/2} / (1 + b_2 P_{H_2O})^2 \qquad \text{Model No. DEM 3}$$

Model DEM 2 was established by changing the power of the SO_2 term in McGregor's model (DEM 1) from 1/2 to 1 while models DEM 2 was obtained by changing the power of the denominator terms in McGregor's model (DEM 1) from 1 to 2. The results for the correlation of model DEM 2 and DEM 3 with the 298°C isothermal data are shown in Table 6-12.

TABLE 6-12

EXAMINATION OF THE SENSITIVITY OF THE NUMERATOR AND DENOMINATOR TERMS OF MCGREGOR'S MODEL BY USING THE ISOTHERMAL RATE DATA AT 298°C

	MODEL DEM1	MODEL DEM2	MODEL DEM3
	$b_1P_{H_2S}P_{SO_2}^{1/2}/(1+b_2P_{H_2O})$	$b_1P_{H_2S}P_{SO_2}/(1+b_2P_{SO_2})$	$b_1P_{H_2S}P_{SO_2}^{1/2}/(1+b_2P_{H_2O})^2$
b_1	2.0006×10^{-7} $\pm 5.5648 \times 10^{-10}$	4.3711×10^{-8} $\pm 6.1586 \times 10^{-9}$	1.9883×10^{-7} $\pm 4.6796 \times 10^{-10}$
b_2	0.0051 ± 0.0001	0.0050 ± 0.0051	0.0023 ± 0.0001
Variance	5.4180×10^{-15}	1.2001×10^{-11}	4.4370×10^{-15}

As exhibited in Table 6-12, both the values of the variance and the 95% confidence limits of the parameters are poorer for model DEM 2 than DEM 1 while those of DEM 3 and DEM 1 are about equal. This illustrates that changing the power of SO_2 term in the denominator term from 1/2 to 1 is more sensitive in affecting the results of correlation than changing the power of whole denominator terms from 1 to 2. In George's model, the SO_2 term was completely left out and as a result, his model fitted poorly.

The clear superiority of McGregor's model over other published model suggests that the powers of P_{H_2S} and P_{SO_2} terms in the numerator should be 1 and 1/2. This can be verified by the correlation of the following model,

$$-r_{SO_2} = b_1 P_{H_2S}^{b_2} P_{SO_2}^{b_3} / (1 + b_4 P_{H_2O}) \quad \text{Moedl No. DEMX1}$$

against the isothermal rate data at 298°C and then examine whether the values of parameter b_2 and b_3 are 1 and 1/2. The values of the parameters obtained from such correlation are:

$$b_1 = 1.9899 \times 10^{-7} \pm 4.7919 \times 10^{-9}$$

$$b_2 = 1.0008 \pm 0.0040$$

$$b_3 = 0.5010 \pm 0.0047$$

$$b_4 = 0.0051 \pm 0.0001$$

$$\text{Variance} = 5.7199 \times 10^{-15}$$

which also strongly indicate the powers of P_{H_2S} and P_{SO_2} to be 1 and 1/2 respectively. To investigate whether this is also true for other temperatures, the model DEMX1 was correlated against the isothermal rate data at other temperatures. The results are summarized in Table 6-13.

As can be seen in Table 6-13, the powers on P_{H_2S} and P_{SO_2} terms (that is, b_2 and b_3) in model No. DEMX1 are 1 and 1/2 regardless of temperature. The 95% confidence limits on all parameters deduced from the correlation are relatively small as are the variances. The goodness of fit for McGregor's model against the rate data collected in this work has apparently been demonstrated. Although the values of the parameters of P_{H_2O} term (b_4) do not show a good correlation as a function of

TABLE 6-13

CORRELATION OF MCGREGOR'S MODEL AGAINST RATE DATA AT VARIOUS ISOTHERMAL RUNS

Model DEM1 $-r_{SO_2} = b_1 P_{H_2S} P_{SO_2}^{1/2} / (1 + b_4 P_{H_2O})$	Model DEMX1 $-r_{SO_2} = b_1 P_{H_2S}^{b_2} P_{SO_2}^{b_3} / (1 + b_4 P_{H_2O})$
T = 200°C $b_1 = 5.2951 \times 10^{-8} \pm 1.3392 \times 10^{-9}$ $b_4 = 0.0153 \pm 0.0017$ Variance = 5.3788×10^{-15}	$b_1 = 4.7758 \times 10^{-8} \pm 4.7508 \times 10^{-9}$ $b_2 = 1.0200 \pm 0.0271$ $b_3 = 0.5164 \pm 0.0201$ $b_4 = 0.0160 \pm 0.0018$ Variance = 4.5569×10^{-15}
T = 212.3°C $b_1 = 6.4821 \times 10^{-8} \pm 6.2329 \times 10^{-10}$ $b_4 = 0.0154 \pm 0.0006$ Variance = 2.3113×10^{-15}	$b_1 = 6.9613 \times 10^{-8} \pm 2.2839 \times 10^{-9}$ $b_2 = 0.9826 \pm 0.0078$ $b_3 = 0.4958 \pm 0.0008$ $b_4 = 0.0154 \pm 0.0004$ Variance = 1.0235×10^{-15}
T = 235.2°C $b_1 = 8.6649 \times 10^{-8} \pm 4.3002 \times 10^{-10}$ $b_4 = 0.01132 \pm 0.00024$ Variance = 1.0262×10^{-15}	$b_1 = 8.5498 \times 10^{-8} \pm 1.7734 \times 10^{-9}$ $b_2 = 0.9811 \pm 0.0301$ $b_3 = 0.5066 \pm 0.0193$ $b_4 = 0.01121 \pm 0.00031$ Variance = 1.2004×10^{-15}

TABLE 6-13 (Continued)

Model DEMI1 $-r_{SO_2} = b_1 P_{H_2S} P_{SO_2}^{1/2} / (1 + b_4 P_{H_2O})$	Model DEMX1 $-r_{SO_2} = b_1 P_{H_2S}^{b_2} P_{SO_2}^{b_3} / (1 + b_4 P_{H_2O})$
T = 261.5°C	
$b_1 = 1.3323 \times 10^{-7} \pm 1.5718 \times 10^{-9}$	$b_1 = 1.2806 \times 10^{-7} \pm 1.4995 \times 10^{-9}$
	$b_2 = 1.0107 \pm 0.0055$
	$b_3 = 0.4986 \pm 0.0087$
$b_4 = 0.0134 \pm 0.0006$	$b_4 = 0.0141 \pm 0.0008$
Variance = 1.5988×10^{-14}	Variance = 1.5369×10^{-14}
T = 298.2°C	
$b_1 = 2.0006 \times 10^{-7} \pm 5.5698 \times 10^{-10}$	$b_1 = 1.9899 \times 10^{-7} \pm 4.7919 \times 10^{-9}$
	$b_2 = 1.0008 \pm 0.0040$
	$b_3 = 0.5010 \pm 0.0047$
$b_4 = 0.0051 \pm 0.0001$	$b_4 = 0.0052 \pm 0.0001$
Variance = 5.4180×10^{-15}	Variance = 5.7199×10^{-15}
T = 323°C	
$b_1 = 2.6767 \times 10^{-7} \pm 2.9830 \times 10^{-9}$	$b_1 = 2.5773 \times 10^{-7} \pm 1.6717 \times 10^{-9}$
	$b_2 = 1.10102 \pm 0.0145$
	$b_3 = 0.5021 \pm 0.0171$
$b_4 = 0.0103 \pm 0.0005$	$b_4 = 0.0102 \pm 0.0005$
Variance = 2.7501×10^{-14}	Variance = 2.7244×10^{-14}

temperature, they do indicate that the retarding effect of water vapor against the rate of reaction is significant. This may be due to the greater experimental errors in the runs with high water vapor partial pressures.

Because of the relatively good correlation of McGregor's model against the rate data collected in the present work, it would be interesting to proceed a step further. The powers of the denominator terms will be varied and the models so obtained will be called Modified McGregor's models. Rate data will then be correlated against these models to find out the best power for the denominator terms. This will be described in the following section.

6.9.3 Correlation of Modified McGregor's Model

Table 6-14 shows the results of the correlation of various isothermal rate data collected in the present work against following models.

$$-r_{SO_2} = b_1 P_{H_2S} P_{SO_2}^{1/2} / (1 + b_2 P_{H_2O}) \quad \text{Model No. DEM 1}$$

$$-r_{SO_2} = b_1 P_{H_2S} P_{SO_2}^{1/2} / (1 + b_2 P_{H_2O})^2 \quad \text{Model No. DEM 12}$$

$$-r_{SO_2} = b_1 P_{H_2S} P_{SO_2}^{1/2} / (1 + b_2 P_{H_2O})^3 \quad \text{Model No. DEM 13}$$

which were obtained by assigning the 1st, 2nd and 3rd power to the denominator terms of McGregor's model.

The model DEM 1 fitted best at 235.2°C, 261.5°C and 323°C; the model DEM 12 at 298.2 °C; and the model DEM 13 at 200 °C and 212.3 °C. It may appear that the first power model DEM 1 emerges to be the best model because it fits best with most isothemal runs. However, among the three isothermal runs that it fits best, the values of the variance were somewhat larger than those where DEM 12 and DEM 13 fit best. Therefore it is really

TABLE 6-14

COMPARING THE CORRELATION OF VARIOUS MODIFIED McGREGOR'S MODELS CONTAINING DIFFERENT POWERS OF THE DENOMINATOR TERMS

Temperature	Model DEM1	Model DEM12	Model DEM13
200°C	$b_1 = 5.2951 \times 10^{-8} \pm 1.3392 \times 10^{-9}$ $b_2 = 0.0153 \pm 0.0017$ Variance = 5.3788×10^{-15}	$5.274 \times 10^{-8} \pm 1.1567 \times 10^{-9}$ 0.0070 ± 0.0006 5.1333×10^{-15}	$5.1838 \times 10^{-8} \pm 1.0228 \times 10^{-9}$ 0.0042 ± 0.0004 4.5398×10^{-15}*
212.3°C	$b_1 = 6.4821 \times 10^{-8} \pm 6.2329 \times 10^{-10}$ $b_2 = 0.0154 \times 10^{-8} \pm 0.0006$ Variance = 2.3113×10^{-15}	$6.3847 \times 10^{-8} \pm 5.0058 \times 10^{-10}$ 0.0066 ± 0.0002 1.9495×10^{-15}	$6.351 \times 10^{-8} \pm 4.7688 \times 10^{-10}$ 0.0042 ± 0.0001 1.9192×10^{-15}*
235.2°C	$b_1 = 8.6649 \times 10^{-8} \pm 4.3002 \times 10^{-10}$ $b_2 = 0.1132 \pm 0.00024$ Variance = 1.0262×10^{-15}*	$8.5393 \times 10^{-8} \pm 4.4459 \times 10^{-10}$ 0.0048 ± 0.0001 1.367×10^{-15}	$8.5032 \times 10^{-8} \pm 4.5272 \times 10^{-10}$ 0.0030 ± 0.00006 1.4958×10^{-15}
261.5°C	$b_1 = 1.3323 \times 10^{-7} \pm 1.5718 \times 10^{-9}$ $b_2 = 0.0134 \pm 0.0006$ Variance = 1.5988×10^{-14}*	$1.3105 \times 10^{-7} \pm 1.6628 \times 10^{-9}$ 0.0055 ± 0.00025 2.195×10^{-14}	$1.3043 \times 10^{-7} \pm 1.6955 \times 10^{-9}$ 0.0035 ± 0.00016 2.413×10^{-14}

Temperature	Model DEM1	Model DEM12	Model DEM13
298.2°C	$b_1 = 2.0006 \times 10^{-7} \pm 5.5648 \times 10^{-10}$	$1.9883 \times 10^{-7} \pm 4.6796 \times 10^{-10}$	$1.9826 \times 10^{-7} \pm 4.7312 \times 10^{-10}$
	$b_2 = 0.0051 \pm 0.0001$	0.0023 ± 0.00007	0.0015 ± 0.00002
	Variance $= 5.4180 \times 10^{-15}$	4.4371×10^{-15}*	4.7577×10^{-15}
323.0°C	$b_1 = 2.6767 \times 10^{-7} \pm 2.983 \times 10^{-9}$	$2.6433 \times 10^{-7} \pm 2.827 \times 10^{-9}$	$2.6335 \times 10^{-7} \pm 2.8006 \times 10^{-9}$
	$b_2 = 0.01025 \pm 0.0005$	0.0044 ± 0.0002	0.0028 ± 0.0001
	Variance $= 2.7501 \times 10^{-14}$*	3.0127×10^{-14}	3.1323×10^{-14}

(where * is the best model in that isothermal run)

TABLE 6-14 (Continued)

difficult to conclude which of these three model fits best. However, all models illustrated the significance of P_{H_2O} term on the retarding effect of the reaction rate.

6.9.4 Discrimination Among Models Derived in the Present Work

Among the various models derived in Section 6.8, some are similar to Hammar's model or George's best model, while others are similar to McGregor's best model. It has already been illustrated in Section 6.9.2 to 6.9.4 that basically McGregor's model correlates extremely well with the rate data collected in the present work. It has also been shown that it was vital to have the $P_{H_2S}\ P_{SO_2}^{1/2}$ terms in the numerator of the model in order to achieve good correlation. Based on these results, the models derived in Section 6.8 which do not contain the $P_{H_2S}\ P_{SO_2}^{1/2}$ terms in their numerators are rejected during this preliminary steps of the model discrimination. The requirement of the $P_{SO_2}^{1/2}$ term in the numerator of the model may indicate that the reaction mechanism should be one that involves the dissociation of adsorbed SO_2 into two "oxygen" which then react separately (shown in Table 6-8 to 6-10 as intermediate steps). This may also mean that the simple Eley-Rideal and Langmuir-Hirshelwood type of mechanisms which do not include these intermediate steps could not be the representative mechanisms for the reaction system studied. The whole mechanism depicted in Table 6-7 must hence be rejected. The models which remained from these preliminary steps of discrimination are listed in Table 6-15.

All models listed in Table 6-15 contain seven or more parameters. Substantial computer time would be required for the correlation process

TABLE 6-15

MODELS REMAINING FROM THE PRELIMINARY STEPS OF DISCRIMINATION

Model No.	Rate Expressions ($-r_{SO_2}$)
DOH4	$b_1 P_{H_2S} P_{SO_2}^{1/2} P_{H_2O}/P_{S_x}^{1/2x} (Y+b_6 P_{SO_2}^{1/2}/P_{S_x}^{1/2x} + b_7 P_{SO_2}^{1/4} P_{H_2O}^{1/2}/P_{S_x}^{1/4x})^3$
DOH5	$b_1 P_{H_2S} P_{SO_s}^{1/2}/P_{S_x}^{1/2x} (Y + b_6 P_{SO_2}^{1/2}/P_{S_x}^{1/2x} + b_7 P_{SO_2}^{1/4} P_{H_2O}^{1/2} / P_{S_x}^{1/4x})^2$
DS04	$b_1 P_{H_2S} P_{SO_2}^{1/2} / P_{S_x}^{1/2x} (Y + b_6 P_{SO_2}^{1/2} / P_{S_x}^{1/2x} + b_7 P_{H_2S}^{1/2} / P_{S_x}^{1/2x})^2$
DS06	$b_1 P_{H_2S} P_{SO_2}^{1/2} P_{S_x}^{1/2x} / (Y + b_6 P_{SO_2}^{1/2} / P_{S_x}^{1/2x} + b_7 P_{H_2S}^{1/2} / P_{S_x}^{1/2x})^3$
DSOH6	$b_1 P_{H_2S} P_{SO_2}^{1/2} P_{S_x}^{1/2x} / (Y + b_6 P_{SO_2}^{1/2} / P_{S_x}^{1/2x} + b_7 P_{H_2S}^{1/2} P_{S_x}^{1/2x} + b_8 P_{H_2S}^{1/2} P_{SO_2}^{1/2} / P_{S_x}^{1/x})^2$

where $Y = 1 + b_2 P_{H_2S} + b_3 P_{SO_2} + b_4 P_{H_2O} + b_5 P_{S_x}^{1/x}$

bi are constants and not necessarily equal between two different models in order to determine the values of these parameters. Without first knowing whether all terms in the bracket of the denominator of the models are significant, it seems not worthwhile to invest the amount of computer time at this stage. Therefore, all bracketed terms in the denominators of the model are first reduced to only Y,

$$\text{where } Y = 1 + b_2 P_{H_2S} + b_3 P_{SO_2} + b_4 P_{H_2O} + b_5 P_{S_x}^{1/x}$$

This step reduces the number of parameters in all models to five instead of seven and the model Nos. are modified to DOH4', DOH5' etc.

These modified models were then correlated with the rate data of all isothermal runs performed in the present work. Model DOH4' is dropped at this stage because of the P_{H_2O} terms in the numerator. Only the values of the variances achieved from such correlation are summarized in Table 6-16 while the correlated values of the various parameters are listed in Table H-1 of Appendix H. From the correlated values of the various parameters, it can be notices that the terms P_{H_2S} and P_{SO_2} in the denominator of the models are not significant. This is exhibited by two points: first, some of the correlated constants for P_{H_2S} and P_{SO_2} are negative and second, the values of these constants are negligible in comparison to their 95% confidence limits in most cases. The insignificance of the P_{H_2S} and P_{SO_2} terms in the denominator may be due to the relatively weak adsorption of H_2S and SO_2 compared to that of water or sulfur. The strong adsorption capability of H_2O as compared to H_2S or SO_2 had been verified at room temperature in the present work by using infrared spectroscopic technique. The experiment to support this view included the preadsorption of 1 cm Hg pressure H_2S(or SO_2) on a γ-alumina wafer which was then exposed to a mixture of H_2S(or SO_2) and H_2O

vapor at room temperature. Figure 6-16 shows the infrared spectra recorded in such an experiment. It can be seen that the infrared bands at 2565, 1585 and 1335 cm^{-1} indicated in spectrum (A) and characteristic of adsorbed H_2S are no longer present in spectrum (B) after the exposure of that wafer to water vapor. Instead a broad hydrogen bonding band around 3600 cm^{-1} plus the scissors-like bending vibration band of adsorbed water at 1625 cm^{-1} were detected in spectrum (B). Apparently, the adsorbed H_2S was displaced by the adsorption of water. A similar result was obtained, as depicted in spectra (C) and (D) when SO_2 was used in place of H_2S. In both cases, the complete displacement took about 3 h.

From Table 6-16, it can be seen that the models DSO4' and DOH5',

$$-r_{SO_2} = b_1 P_{H_2S} P_{SO_2}^{1/2} / P_{S_x}^{1/2x} (1+b_2P_{H_2S}+b_3P_{SO_2}+b_4P_{H_2O}+b_5P_{S_x}^{1/x})^2$$

provided the best correlation for all isothermal runs. These two models were derived, according to Section 6.8, with the mechanism which involves the,

$$H_2S\,.\,\# + O.\# \rightarrow H_2O\,.\,\# + S.\# \qquad (6.51)$$

surface reaction step as rate-determining, where # represents Lewis-acid site. Hence the adsorption of H_2S and SO_2 on Lewis-acid sites and the importance of oxide-ion site for the reaction had been observed experimentally and verified by the results of model correlation. Among all the models listed in Table 6-16, the water term in the bracket of the denominator was proven to be significant irrespective of the model or set of isothermal data. Therefore, the retarding effect of water on the rate of reaction was not only demonstrated by experiments but also illustrated by the data-fitting results.

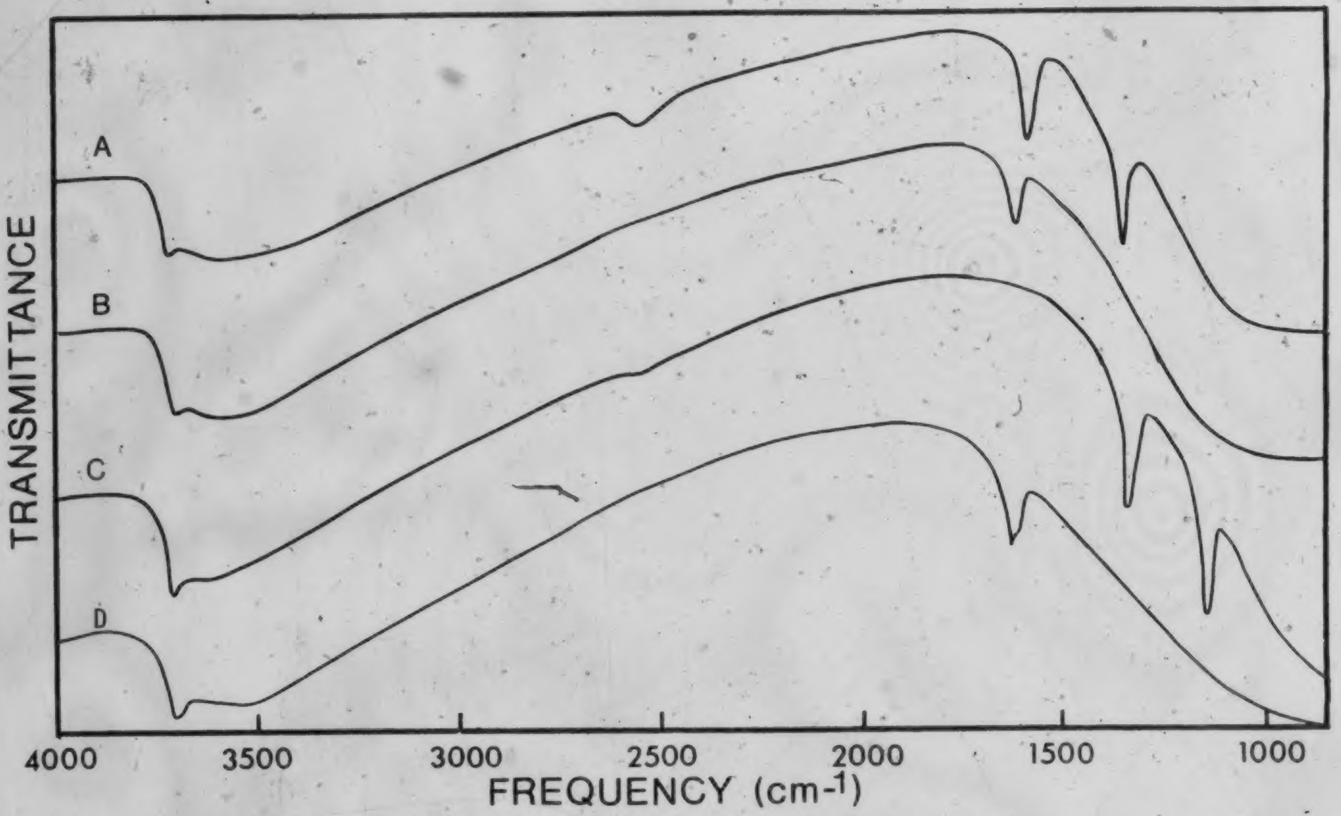

Figure 6-16. Displacement of H_2S and SO_2 by H_2O on γ-alumina (A)=H_2S on γ-alumina;(B)=(A)+H_2O; (C)=SO_2 on γ-alumina;(D)=(C)+H_2O.

TABLE 6-16

CORRELATION VARIANCES OF THE KINETIC MODELS REMAINING FROM THE PRELIMINARY STEP OF DISCRIMINATION

Kinetic Models / Temperature (°C)	200.0	212.3	235.2	261.5	298.2	323.0
Model No. DOH5' = No. DS04'						
$-r_{SO_2}=b_1P_{H_2S}P_{SO_2}^{1/2}/P_{S_x}^{1/2x}\ Y^2$	1.353×10^{-5}	2.999×10^{-19}	2.077×10^{-17}	4.589×10^{-15}	1.232×10^{-18}	1.363×10^{-18}
Model No. DS06'						
$-r_{SO_2}=b_1P_{H_2S}P_{SO_2}^{1/2}/P_{S_x}^{1/2x}\ Y^3$	4.106×10^{-15}	2.624×10^{-17}	2.850×10^{-17}	4.663×10^{-15}	1.934×10^{-16}	1.576×10^{-16}
Model No. DSOH6'						
$-r_{SO_2}=b_1P_{H_2S}P_{SO_2}^{1/2}P_{S_x}^{1/2x}/Y^2$	3.854×10^{-15}	2.437×10^{-17}	1.718×10^{-15}	4.656×10^{-15}	7.827×10^{-16}	6.706×10^{-16}

where $Y = (1 + b_2P_{H_2S} + b_3\,P_{SO_2} + b_4\,P_{H_2O} + b_5\,P_{S_x}^{1/x})$

On the other hand, the sign of desorption equilibrium constant for sulfur $P_{S_x}^{1/x}$ in the bracket of the denominator term was negative for some models and positive for others. The 95% confidence limit on this parameter could be considered as good or bad depending on the model. But as far as the best model is concerned, the $P_{S_x}^{1/x}$ term in the bracket of the denominator is insignificant. As a result, the best model is reduced to the following form:

$$-r_{SO_2} = b_1 P_{H_2S} P_{SO_2}^{1/2} / P_{S_x}^{1/2x} (1 + b_2 P_{H_2O})^2 \quad \text{Model No. FHS1}$$

after the terms P_{H_2S}, P_{SO_2} and P_{S_x} were dropped from the bracketed terms of the denominator of the model.

6.9. 5 Kinetic Model with Temperature Dependency

The most successful model, FHS1, obtained from the model correlation process using isothermal data at different temperatures, is rewritten below according to Arrhenius expression:

$$-r_{SO_2} = \frac{k_0 \exp(-E_1/RT) P_{H_2S} P_{SO_2}}{P_{S_x}^{1/2x} [1 + K_{A0} \exp(E_2/RT) P_{H_2O}]^2} \quad \text{Model No. FHS2}$$

This model is then correlated with all the rate data collected in the present work and the results are listed in Table 6-17.

TABLE 6-17

RESULTS OBTAINED FROM THE CORRELATION OF THE MOST SUCCESSFUL MODEL AGAINST ALL RATE DATA

$k_0 = 9.72 \times 10^{-5} \pm 4.37 \times 10^{-5}$

$E_1/R = 3509 \pm 254$

$K_{A0} = 1.15 \times 10^{-5} \pm 2.18 \times 10^{-5}$

$E_2/R = 3158 \pm 1049$

$\text{Variance} = 7.15 \times 10^{-13}$

These final results indicate the significance of retarding effect of H_2O on rate of reaction although the 95% confidence limit of the P_{H_2O} term parameter obtained here is worse than those deduced from the correlation against isothermal rate data in Section 6.9.5.

CHAPTER VII

CONCLUSIONS AND RECOMMENDATIONS

7.1. Conclusions

7.1.1 Adsorption of H_2S and SO_2 on γ-Alumina

Contrary to other reports [34, 84], this work suggests that both H_2S and SO_2 are not adsorbed on γ-alumina via the formation of hydrogen bonding with the surface hydroxyl groups. Rather, they are adsorbed through their sulfur atom on the Lewis-acid sites and the adsorption is reversible. The broad hydrogen bonding band detected by infrared spectrophotometry upon the adsorption of H_2S or SO_2 on γ-alumina is due to the interaction of the adsorbate with the neighbouring sites like surface hydroxyl groups or oxide-ion sites.

With a wafer less than 150 mg, the amount of H_2S or SO_2 adsorbed at temperatures above 150°C could not be detected by infrared spectroscopy although detection of these adsorbed species was achieved at room temperature. By using the volumetric method, others [33, 45, 46] were able to measure significant H_2S or SO_2 adsorption easily at temperatures as high as 500°C because they could employ substantially larger quantity of γ-alumina in their experiments.

Upon adsorption of H_2S (or CS_2) on γ-alumina pretreated by heating in oxygen or air followed by degassing at 400°C, the H_2S (or CS_2) was found to be oxidized to sulfur by a finite amount of "surface oxygen' on γ-alumina. Heating the catalyst with hydrogen at 400°C after the "normal' pretreatment process could prevent the oxidation of the adsorbate. The exact form (molecular, lattice or other forms) of such "surface oxygen" is still unknown. This finite amount of "surface oxygen" could be restored by heating the γ-alumina again with oxygen or SO_2. Others [35, 38, 57] reported that the surface oxygen of γ-alumina could be exchanged with the isotopic oxygen or H_2O^{18}.

No sulfate formation could be detected upon adsorption of SO_2 on γ-alumina from room temperature to 400°C regardless of which catalyst pretreatment method was adopted. It was found that the presence of oxygen was necessary for the formation of sulfate on γ-alumina from SO_2 although the formation of sulfate could be enhanced by adsorbing only SO_3 on γ-alumina. Among the various ways of forming sulfate, the adsorption of SO_3 vapor on γ-alumina was found to be the most effective and fastest. It is still unknown whether the formation of sulfate from SO_2 and O_2 proceeds directly or via the formation of SO_3. No surface sulfate could be detected on the used catalyst produced in the kinetic experiments.

7.1.2 The Catalytic Role Played by γ-Alumina in Claus Reaction

The Lewis-acid sites of γ-alumina were found to be important for the adsorption of both H_2S and SO_2. On the other hand, the oxide-ion sites were more essential than the Lewis-acid sites in affecting the catalytic activity of the reaction. Hence, somehow the oxide-ion sites should be expected to play a vital role in the reaction.

In the model discrimination process, it was found that those models which were derived by assuming a reaction mechanism involving the simple reaction step between two adsorbed reactants at adjacent sites or between one adsorbed reactant and the other in gaseous phase produced poor correlation results. Models with mechanisms involving intermediate reaction steps generated better correlation results and those with dissociation of adsorbed SO_2 as a step gave best results.

The catalytic role played by γ-alumina in the Claus reaction is one that involves adsorption of the reactants and acts as a medium for the oxidation-reduction process to take place. The adsorbed H_2S is oxidized by the "surface oxygen" on the γ-alumina which in turn is replenished by the dissociation of the adsorbed SO_2. Hence the continuous consumption of the "surface oxygen" by H_2S and replenishment by SO_2 hence accounts for the Claus reaction.

7.1.3 Kinetics and Mechanism of Claus Reaction

The use of "in situ" quantitative infrared spectroscopy was found to be able to eliminate the possibility of error attributable to the catalytic effect of molten sulfur. In agreement with Karren [64], molten sulfur was found to exhibit a catalytic effect on the reaction.

The general form of the kinetic model determined from the rate measurements of the present work matches surprisingly well with that by McGregor [84], who used bauxite as a catalyst. This implies that it is the skeletal structure of γ-alumina in bauxite that is responsible for the catalytic action. In agreement with McGregor, water was observed to have imposed a retarding effect on the reaction rate. The rate data derived from the present work demonstrated the retarding effect of water more emphatically than those of McGregor.

This is because the water concentrations in the present work were varied over a wider range. McGregor did not mention about the effect of sulfur on rate of reaction but in the present work, sulfur was statistically found to exert a retarding effect on reaction rate.

McGregor concluded from his rate data fitting process that the reverse reaction term was probably not significant under the experimental conditions employed. In the present work, the negligible effect of the reverse reaction was also observed experimentally.

By using a Bayesian approach to model discrimination, the following model was found to describe the reaction system studied

$$(-r_{SO_2}) = \frac{b \exp(-E_{10}/RT)\, P_{H_2S}\, P_{SO_2}^{1/2}}{[1+ b_{20} \exp(-E_{20}/RT) P_{H_2O}]^2\, P_{sx}^{1/2x}}$$

where $b_{10} = 9.72 \times 10^{-5} \pm 4.37 \times 10^{-5}$

$E_{10}/R = 3509 \pm 254$

$b_{20} = 1.15 \times 10^{-5} \pm 2.18 \times 10^{-5}$

$E_{20}/R = 3158 \pm 1049$

This model was derived from the mechanisms shown in Table by omitting the P_{H_2S}, P_{SO_2} and $P_{sx}^{1/x}$ from the bracketed denominator terms. In these mechanisms, the reaction between the adsorbed H_2S and "surface oxygen"

$$H_2S \cdot \# + O \cdot \# \rightleftharpoons H_2O \cdot \# + S \cdot \# \qquad (6.51)$$

is rate-determining. The "surface oxygen" is replenished (after being consumed by H_2S) by the dissociation of adsorbed SO_2. In parallel with reaction step (6.51), adsorbed H_2S could also be dissociated by the surface sulfur into SH or S_xH groups which were in turn oxidized by "surface oxygen" into sulfur and water. On the other hand the adsorbed H_2S could also be oxidized by surface hydroxyl groups into water and sulfur. These steps were assumed not to be rate-determining because the models derived by considering these as rate-determining produced poorer correlation results. Mechanisms involving the dissociation of adsorbed H_2S into water and SH group did not generate models that correlate satisfactorily with the measured rate data.

The apparent rate constant and activation energy are only slightly different from those obtained by McGregor. This implies again the similarity of catalytic activity between pure γ-alumina and bauxite towards the Claus reaction.

7.2 Recommendations

7.2.1 Equipment

7.2.1.1 Reactor

There are several items on the reactor that can be improved and these are listed below

(1) The gears on the stirrers of the reactor fused salt bath were too noisy during experimental runs. Although this did not affect the results of the experiment, the noise pollution should definitely be reduced. This could possibly be accomplished by

redesigning the gear or by using other types of driving devices (for example, a belt drive instead of a gear drive).

(2) The Teflon O-rings employed on the infrared cell windows could withstand a finite period of application beyond which they started to deform. Which type of O-ring would be the more suitable is not known but a search for a better O-ring should be continued.

(3) The screw threaded holes for holding the infrared cell windows were tapped right onto the wall of the fused salt bath container of the reactor. Since the container wall is relatively thin (1/8 inch), very little metal was left in the wall on the tapped spot. Thermal stress plus corrosion could generate a crack easily and hence fused salt could leak out through those tapped holes and could damage the infrared cell windows. This problem could be overcome by either increasing the wall thickness at that region or by adopting other methods of holding the infrared cell windows.

(4) Although the catalyst sample holder seemed not to have created significant mass transfer or flow restriction to the reaction, it could certainly be improved by reducing the weight and to have more clearance for the access of reactants to the catalyst.

7.2.1.2 Recirculation Pump

There were mainly three types of difficulties encountered in the operation of the reciprocating recirculation pump in the present work. First, the electric coils wound around the pump could not be heated above 275°C and hence this limited the amount of sulfur vapor pressure tolerable in the pump. Second, the method of insulating the pump by winding asbestos tape around it was poor and new insulation had to be used every time the pump was dismantled for cleaning. Third, due to carelessness, sulfur could be condensed in the pump by inadequate purging prior to shutdown. The first problem could be overcome by selecting an electric wire for the winding whose insulation would withstand higher temperature. The second problem could be resolved by placing the pump in a temperature-controlled compartment and by doing so, it would eliminate the use of the asbestos tape. As for the third problem, more careful operation will be required although some safety device like switching on an auxiliary nitrogen purge to the pump whenever the pump is shutdown or its temperature lowered to some prset point could be installed.

7.2.2 Studies on Equilibrium Conversion

The infrared spectrophotometric technique has been proven to be very useful for the measurement of equilibrium conversions of the Claus reaction. This is because the analysis could be done "in-situ" in the reactor and does not require the removal of a sample from the reactor for analysis like gas chromatograph. Very often, sulfur has to be eliminated from the sample before analysis by gas chromatography and in so doing the sample composition may be affected. This is due to the possibility that condensed sulfur either to adsorb the reactants or catalyzes further reaction. The equilibrium conversion so measured may possibly be in error.

The method and equipment used for measurement of equilibrium conversion in Section 6.6.2 could be used for a more detailed study on equilibrium conversion of the Claus reaction. Some modifications on the equipment should be made before attempting such a study. This includes the installation of a small recirculation pump between the reactor and the infrared cell so that equilibrium could be reached sooner. The infrared cell should also be lengthened to provide more sensitive analysis.

7.2.3 Kinetics and Mechanism

Several unclarified points still remain concerning the kinetics and mechanism of Claus reaction. The suggusted future work is summarized below:

(1) The nature of "surface oxygen" on the γ-alumina surface which is capable of oxidizing adsorbed H_2S at room temperature and is an intermediate for Claus reaction is still unknown. The clarification of this point could provide further understanding of Claus reaction and also, more important, increase the knowledge on the catalytic nature of γ-alumina. The exact method of achieving this is not clear at this stage. Perhaps by comparing the heat of reaction of hydrogen with alumina and with pure oxygen accurately, it may be possible to find out whether the "surface oxygen" is of the molecular or "strain-bridge" type [99].

(2) It has been assumed that SO_2 dissociates on the surface of γ-alumina in this thesis and in the process of model discrimination, only models derived from mechanisms assuming the dissociation of SO_2 provided good correlation with rate data. However it has not been demonstrated conclusively by experiment that SO_2 dissociation actually takes place. Two methods are porposed here for such investigation. First, by contacting SO_2 with the "reduced-alumina" at temperatures

from 200°C - 400°C and then evacuating the resultant gases into a mass spectrometer for the analysis of sulfur. If a trace of sulfur is detected, this should be from the dissociation of SO_2. Second, by using isotopic SO_2 like SO_2^{18} for adsorption on -alumina and if SO_2^{16} is detected exchange of oxygen and hence dissociation of SO_2 should have occurred.

(3) The catalytic effect of molten sulfur on Claus reaction has been detected qualitatively [22, 64]. To gain more knowledge in this field, quantitative measurements are needed. Goddin et al. [48] reported a higher Claus unit efficiency by operating the reaction temperature lower than the sulfur dew point. The additional research on molten sulfur-catalyzed Claus reaction can provide valuable information to the design and operation of a Claus process involving the removal of sulfur by condensation before the unreacted H_2S and SO_2 are introduced to downstream reactors.

(4) If molten sulfur is capable of catalyzing the Claus reaction, so should the condensed sulfur in the pores of the catalyst. It appears that the type of experiment required for such investigation is not too complicated. First, a porous solid which is inert to the Claus reaction could be chosen as a medium for sulfur condensation in the pores. In the present work, α-alumina was found to be inert to Claus reaction and could be used for such purpose. To carry out the experiment, sulfur vapor (at as high a concentration as possible) should be introduced with H_2S, SO_2 and N_2 (which acts as a carrier gas) over α-alumina of the reaction temperature. If reaction between H_2S and SO_2 is detected, this should be from the catalytic effect of condensed

sulfur (of course, it should be absolutely established that the porous solid is catalytically inert).

BIBLIOGRAPHY

1. Andreu, P., Heunisch, M., Schmitz, E., and Noller, H., Naturforsch, 196, 649 (1964).
2. Anon, Sulfur, Nov./Dec. 1973 (109) 37-39
   Jan./Feb. 1973 (110) 35-53.
3. Baehr, H., and Mengdehl, H., I.G. Farbenindustrie Aktiengesellochaft, US Pat. 2092386 Sep. 7, 1937.
4. Ball, F.J., Hydrocarbon Processing, 51. 125 (1972)
5. Barkholt, H., US Pat. 2169379, August 15, 1939.
6. Barrer, R.M., and Whiteman, J.L., J. Chem. Soc. (A), 13 (1967).
7. Barry, C.B., Hydrocarbon Proc. 102-106, April, 1972.
8. Barthel, Y. , "The IFP Gas Cleaning Processes" Session 2, Paper 3, Proceedings of International Conference held at Univ. of Salford, 10-12th April, 1973.
9. Bayley, C.H., Can. J. Res. 10, 19 (1934).
10. Bhasin, M.M., Curran, C., and John, G.S., J. Phys. Chem. 74, 3973 (1970).
11. Bischoff, K.B., and Fromant, G.F., Ind. Eng. Chem. Fund., 1, 195 (1962).
12. Boyle, T.W., Gaw, W.J. and Ross, R.A., J. Chem. Soc.,(A)240(1965)
13. Brouwer, D.M., J. Catalysis, 1, 372 (1962).
14. Brouwer, D.M., Chem. Ind. (London), 177 (1961).
15. Brunauer, S., Emmett, P.H., and Teller, E., J. Am. Chem. Soc., 60, 309 (1938).

16. Butler, J.R., Dew, J.E., and Zink, D.G., US Pat. 2724641, Nov. 22, 1955.

17. Carberry, J.J., Catalysis Reviews, 3, 62 (1970).

18. Chance, A.M., and Chance, J.F., Brit. Pat. 8666 June 16, 1887.

19. Chandler, R.H., "The Claus Process-Review" R.H. Chandler Ltd., Braintree England, 1976.

20. Chilton, T.C., and Colburn, A.P.,Ind. and Eng. Chem. 26,1183(1934)

21. Cho, B.K., M. Sc. Thesis, Dept. of Chemical Engineering, Univ. of Alberta, Edmonton, Alberta, Fall, 1975.

22. Chuang, T.T., unpublished data (1972).

23. Chuang, T.T., Ph. D. Thesis, Dept. of Chemical Engineering, Univ. of Alberta, Edmonton, Alberta, Fall, 1971.

24. Chuang, T.T., and Dalla Lana, I.G., Trans. Faraday Soc.69,643(1973)

25. Claus, C.F., Brit. Pat. 5958, Dec. 31, 1883.

26. Cormode, D.A., M. Sc. Thesis, Dept. of Chemical Engineering, Univ. of Alberta, Edmonton, Alberta, Fall, 1965.

27. Cornelius, E.B., Milliken, T.H., Mills, G.A., and Oblad, A.G., J. Phys. Chem., 59, 809 (1955).

28. Dalla Lana, I.G., Cho, B.K., and Liu, C.L., Paper Presented in CNGPA Research Seminar, Calgary, November, 1974.

29. Dalla Lana, I.G., McGregor, D.E., Liu, C.L., and Cormode, D.A., Paper 2-2, V European and II International Symp. on Chem. Reaction Eng., Amsterdam, May 2, (1972).

30. Davis, J.C., Chem. Eng., 79, 66 (1972).

31. deBoer, J.H., J. Catalysis, 1, 1 (1962).

32. deBoer, J.H., Fortuin, J.M.H., Lippens, B.C., and Meijs, W.H., J. Catalysis, 2, 1 (1963).

33. deRosset, A.J., Finstrom, C.G., and Adams, C.J., J. Catalysis, 1, 235 (1962).

34. Deo, A.V., Dalla Lana, I.G., and Habgood, H.W., J. Catalysis, 21, 270 (1971).

35. Eley, D.D., and Zammit, M.A., J. of Catalysis, 21, 366 (1971).

36. Field, G.W., Z. anorg. allgem. Chem., 70, 119, 225 (1921).

37. Figole, N.S. and Parera, J.M., J. of the Research Institute for Catalysis, Hokkaido University, 18, 3, 142, Dec. (1970).

38. Fink, P., Unpublished Result.

39. Flockhart, B.D., Uppal, S.S., Leith, I.R. and Pink, R.C., International Congr. Catalysis, 4th Moscow, Preprints of Papers No. 79 (1968).

40. Fogo, J.K., J. Phys. Chem. 65, 1919 (1961).

41. Froning, H.R., and Grekel, H., US Pat. 3154383 October 27, 1964.

42. Gamson, B.W., and Elkins, R.H., Chem. Eng. Prog. 49, 4, 203 (1953).

43. George, Z.M., J. Catalysis, 35, 218 (1974).

44. George, Z.M., J. Catalysis, 32, 261 (1974).

45. Glass, R.W., and Ross, R.A., Can. J. of Chem., 50, (16), 2537 (1972).

46. Glass, R.W., and Ross, R.A., J. Phys. Chem., 77, 2571 (1973).

47. Goar, B.G., Proceeding Gas Conditioning Conf., Univ. of Oklahoma 25, G1-28, (1975).

48. Goddin, C.S., Hunt, E.B., and Palm, J.W., Hydrocarbon Proc 10, 122 (1974).

49. Gomer, R., and Smith, C.S., "Structure and Properties of Solid Surfaces", Univ. of Chicago Press, Chicago, Ill., P147 (1953).

50. Graulier, M., and Papee, D., Energy Processing/Canada, 32-38, Mar.-Apr., 1974.

51. Gregg, S.J., "Surface Chemistry of Solids", Chapman and Hall, London, P37 (1961).

52. Gregg, S.J., and Sing, K., "Adsorption, Surface Area and Porosity", Academic Press, 1967, Chap. 3.

53. Griffith, R.H., Morcom, A.R., and Newling, W.B.S., Brit. Pat. 600118, March 31, 1948.

54. Haas, L.A., US Bureau of Mines Information Circular 8608, 1973.

55. Hammar, B.G., Doktorsowhandal, Chalmers Tek. Hogskola, No.14, 166 (1957).

56. Hansford , R.C., Advances in Catalysis, 4, 1, Academic Press (1952).

57. Hindin,S .G., and Weller, S.W., Advances in Catalysis, 9, 70, (1957).

58. Hirota, K., Imanaka, T., and Kobayashi, Y., Shokubai (Tokyo), 3, 2, 206 (1961).

59. Hudgins, R.R., Chem. Eng. Sci., 23 93 (1968)

60. Hyne, J.B., Natural Gas Processors Ass. 51st Convention Proc., New Orleans, 1972 pp 85-94.

61. Institut Francais du Petrole, des Carburants et. Lubrifiants US Pat. 3598, 529.

62. Jain, J.R., and Pillar, C.N., J. Catalysis, 9, 322 (1967).

63. Jones, W.J., and Ross, R.A., J. Chem. Soc. (A), 1021 (1967).

64. Karren, B.L., M. Sc. Thesis, Dept. of Chem. Eng., Univ. of Alberta, Edmonton, Alberta, Spring (1972).

65. Kerr, R.K., Paskall, H.G., and Ballash, N., Energy Processing/ Canada, 66-72, Sep.-Oct. 1976.

66. Kipling, J.J., and Peakall, D.B., J. Chem. Soc., 134 (1957).

67. Kittrell, J.R., Ph. D. Thesis, Univ. of Wisconsin, Madison, Wisconsin, (1966), Advan. Chem. Eng., 8, 97 (1970).

68. Knozinger, H., and Spannheiner, H., Ber. Bunsenges, Phys. Chem., 70, 575 (1966).

69. Kohl, A.L., and Riesenfeld, F.C., Chem. Eng., 66, 151, (1959).

70. Krylov, O.V., and Fokina, E.A., Probl. Kinetiki i Kataliza, Acad. Nauk, USSR, 8, 248 (1955).

71. Krylov, O.V., and Fokina, E.A., Intern. Congr. Catalysis, 4th Moscow, Preprints of Paper No. 64 (1968).

72. Landau, M., and Molyneux, A., I. Chem. Eng. Symp. Series No. 27 (1968).

73. Levenspiel, O., "Chemical Reaction Engineering", John Wiley, NY, Chap. 14 (1962).

74. Lippens, B.C., and deBoer, J., Acta. Crystallogr., 17, 1312 (1964).

75. Lippens, B.C., "Structure and Texture of Aluminas", Ph. D. Thesis, Delft Univ. of Technology, The Netherlands (1961).

76. Lippens, B.C., and Steggerda, J., "Physical and Chemical Aspects of Adsorbents and Catalyst", Edited Linsen, B.G., Academic Press (1970).

77. Little, L.H., "Infrared Spectra of Adsorbed Species", Academic Press Inc., (London) Ltd. (1966).

78. Liu, C.L., M. Sc. Thesis, Dept. of Chem. Eng., Univ. of Alberta, Edmonton, Alberta, Spring (1972).

79. Low, M.J.D., Goodsel, A.J., and Takezawa, N., Envir. Sci. Tech., 5 (12), 1191 (1971).

80. Marier, P., and Ingraham, T.R., Mines Branch Research Report R222, Canada Dept. of Energy, Mines and Resources, Ottawa, March, 1970.

81. Marier, P., and Ingraham, T.R., Mines Branch Information Circular IC263, Feb., 1971.

82. Marsh, J.D.F., and Newling, W.B.S., Brit. Pat. 867853, May 10, 1961.

83. McBride, B.J., Heimel, S., Ehlers, J.G., and Gordon, S., NASA SP-3001 (1963).

84. McGregor, D.E., Ph. D. Thesis, Dept. of Chem. Eng., Univ. of Alberta, Edmonton, Alberta, Fall (1971).

85. Mezaki, R., and Watson, C.C., Ind. Eng. Chem., Process Design and Develop., 5, 62 (1966).

86. Mezaki, R., and Kittrell, J.R., Can. J. Chem. Eng., 44 285 (1966).

87. Mills, G.A., and Hindin, S.G., J. Am. Chem. Soc. 72, 5549 (1950).

88. Misono, M., and Yoneda, Y., Dai 19-Nenkai Koenyoko - shu (Japanese) (1967).

89. Misono, M., and Yoneda, Y., Ann. Meeting Chem. Soc. Japan 19th Yokohama, Preprints of Papers 12A-123 (1966).

90. Moliere, K., Rathyl, W., and Strauski, I., Disc. Faraday Soc., 5 21 (1949).

91. Murthy, A.R., and Rao, S.B., Proc. Ind. Acad. Sci., 34A, 283 (1951).

92. Nicolescu, L.V., Nicolescu, A., Grina, M., Terleski-Baricevic, A., Dardan, M., Angelescu, E., and Ionescu, A., Intern. Congr. Catalysis, 4th Moscow, Preprints of Papers 78 (1968).

93. Noller, H., Hantsche, H., and Andreu, P., J. Catalysis, 4, 354 (1965).

94. Norman, W.S., Gas Conditioning Conf. March 8, 1976, Norman, Oklahoma.

95. Notari, B., La Chimica e L'Industria, 51, 11, 1200, Nov. (1969).

96. Ohki, K., Fujita, K.; Miyamura, A., and Ozaki, A., Shokubai (Tokyo), 7, 3, 309 (1965).

97. Ozawa, Sentaro and Ogino, Yoshisada, J. of Japanese Soc. of Chemistry, 1, 1 (1972).

98. Parkyns, N.D., and Patterson, B.C., Chem. Communication, 21, 530 (1965).

99. Parkyns, N.D., J. Chem. Soc. (A), 1910 (1967).

100. Parry, E. P., J. Catalysis, 2, 371 (1963).

101. Pearson, M.J., CNGPA Meeting, Calgary, Nov. 24, 1972.

102. Pearson, M.J., Hydrocarbon Proc., 81-85, 52, Feb. 1973.

103. Peri, J.B., Actas Congr., Intern. Catalysis, 2e, Paris, 1, 1333 (1960).

104. Peri, J.B., J. Phys. Chem., 69, 211 (1965).

105. Peri, J.B., J. Phys. Chem., 69, 220 (1965).

106. Peri, J.B., J. Phys. Chem., 69, 231 (1965).

107. Pfeiffer, J.B., Paper Presented at 167th ACS Meeting, LA, April, 1974.

108. Pilgrim, R.F., and Ingraham, T.R., US Dept. of Mines Information Circular IC 243 1973.

109. Pines, H., and Haag, W.D., J. Am. Chem. Soc., 82, 2471 (1960).

110. Pines, H., and Manassen, J., Advances in Catalysis, 16, 49, (1966)

111. Pines, H., and Pillai, C.N., J. Am. Chem. Soc., 83, 3270 (1961).

112. Rao, B.S., and Rao, M.R.A., Nature, 128, 413 (1931).

113. Rao, C.N.R., "Chemical Application of Infrared Spectroscopy", Academic Press, Chap. 11, (1963).

114. Rhea, K.H., and Basila, M.R., J. Catalysis, 10, 243, (1968).

115. Rondeau, R.E., J. of Chem. and Eng. Data., 11, 124, (1965).

116. Rosolovskaya, E.N., Shakhnovskaya, O.L., and Topchieva, K.V., Kinetika i Kataliz, 7, 750, (1966).

117. Ross, E.T., and Wilde, C.B., US Pat. 2534063 Dec. 12, 1950.

118. Ross, R.A., and Taylor, A.H., Proc. Brit. Ceram. Soc., 5, 167, (1965).

119. Rottig, W. and Hanisch, F., Ger. Pat. 1068228, Nov. 5, 1959.

120. Roux, A., Huang, A.A., Ma, Y.H., and Zwiehel, I., AIChE Symp. Series 69, (134), 46 (1973).

121. Saalfeld, H., and Mehrotra, B., Ber. dt. Keram., Ges., 42, 161 (1965).

122. Sabtier, P., and Maihe , A., Compt. Rend., 148, 890 (1919).

123. Sabtier , P., and Mailhe, A., Compt. Rend., 150, 1949 (1910).

124. Sabtier , P., and Reid, E.E., "Catalysis in Organic Chemistry", Princeton - Van Nostrand Co. NY (1922).

125. Satterfield, C.N., "Mass Transfer in Heterogeneous Catalysis", MIT Press (1970).

126. Schallis, A., US Pat. 2513524, July 4, 1950.

127. Schuit, G.C.A., and Gates, B.C., AIChE Journal, 19, 417, (1973).

128. Schwab, G.M., and Kral, H., Proc. Third Intern. Congr. Catalysis, Amsterdam, 1964, P.433, North Holland Publ., Amsterdam, No. 20 (1964).

129. Scott, J.A.N., Flockhart, B.D., and Pink, R.C., Proc. Chem. Soc., 139 (1964).

130. Singh, H., M. Sc. Thesis, Dept. of Chem. Eng., Univ. of Alberta, Edmonton, Alberta, Fall (1971).

131. Skoog, D.A., and Bartlett, J.K., Anal. Chem., 27, 369 (1955).

132. Slack, A.V., Int. J. Sulfur Chem., Part B, Vol. 7, No.1 (1972), 67-75.

133. Slager, T.L., and Amberg, C.H., Can. J. of Chemistry, 50, 3416 (1972).

134. Spillane, P.X., Brit. Pat. 642726, Sep. 13, 1950; US Pat. 2559325, July 3, 1951.

135. Tamele, M.W., Discussions Faraday Soc., 8, 270 (1950).

136. Tanabe, K., Nagata, A., and Takeshita, T., J. Res. Inst. Catalysis Hokkaido Univ., 15, 181 (1967).

137. Tanabe, K., "Solids Acids and Bases", Kodansha (Tokyo), Academic Press NY London 1970

138. Taylor, H.A., and Wesley, W.A., J. Phys. Chem., 31, 216 (1927).

139. Thaller, L.H., and Thodos, G., AIChE Journal, 6, 369 (1960).

140. Townsend, F.M., and Reid, L.S., Hydrocarbon Proc., 37, 263, (1958).

141. Udintseva, V.S., and Chufarov, G.I., J. Chem. Ind., (USSR), 17, 24 (1940).

142. Vecchioni, E., and Bertolini-Salimbeni, Ital. Pat. 483963, August 25, 1963.

143. Ward, D.M., and Shuttler, J.D., US Pat. 3186789 June 1, 1965.

144. Wayman, D.D., NBS Technical Note 270, US Government Printing Office (1968).

145. Weyl, W.A., Trans. N.Y. Acad. Sci., 12, 245 (1950)

146. Weyl, W.A., Mineral Industries Experiment Station Bulletin 57, State College, Pa., (1951).

147. Wiewiorowski, T.K., Chem. and Eng. News, 48 (18) 168 (1970).

148. Wiewiorowski, T.K., and Touro, F.J., J. of Phys. Chem., 70, 234 (1966).

149. Yamadaya, M., Shimomura, K., Konoshita, T., and Uchida, H., Shokubai (Tokyo), 7, 3, 313 (1965).

150. Zil'berman, J., Gen. Chem. (USSR), 10, 1257 (1940).

151. Zwietering, T.N., Chem. Eng. Sci., 11, 1, (1959).

NOMENCLATURE

The following list summarizes the nomenclature used in this thesis. Symbols and constants are also defined where they first occur. The special symbols separately used and defined in the Appendix are not included here.

English Letter Symbols

A_E	Specific external surface area of catalyst (cm^2)
A	Absorbance at wavelength
$\underline{a}_k$	Vector of unknown parameters corresponding to the k^{th} model
b_i	Arbitrary constant of i^{th} independent variable
C	Concentration (g-mol/l)
$\underline{C}_j$	Variance covariance matrix of the parameters in a kinetic model
d_p	Diameter of catalyst wafer (cm)
D	Diffusivity
D_{eff}	Effective diffusivity
E	Activation energy (K cal/g-mol)
E_n	Entropy
E_o	Apparent activation energy (K cal/g-mol)
E_T	True activation energy (K cal/g-mol)
ε_i	Error term in the i^{th} kinetic model

F, F_{AO}	Molal flow rate of the reactant (g-mol/h)
I	Intensity of the transmitted infrared beam
I_0	Intensity of the incident infrared beam
K_G	Gas diffusion ceofficient
K_i	Equilibrium constant for the reaction step i, or adsorption constant for ith species
k_i	Reaction rate constant for reaction step i
L_i	Total number of active sites of type i on the catalyst surface
ℓ	Length of the IR cell (cm)
M_i	Molecular weight of component i
m	The power factor for H_2S term in the rate equation
N	Total number of data point obtained
N_i	Diffusion flux of component i (g-mol/s cm^2)
n	The power factor for SO_2 term in the rate equation
P	Total pressure (atm)
P_i	Probability that the i^{th} model form is correct, or partial pressure of i^{th} component (mm Hg)
P_0	Partial pressure of reactant in the feed stream (mm Hg)
R	Ideal gas law constant
$-R$	Expected entropy change
r	Rate of reaction; g-mol of reactant converted per second per gm of catalyst
r_c	Ratio of volume over surface area of the catalyst (cm)
r_i	Rate of reaction for the reaction step i; g-mol of reactant converted per second per gm of catalyst

r_o	Initial rate of reaction; g-mol of reactant converted per second per gm of catalyst
$\hat{S}_k$	Minimum sum of error squared
T	Absolute temperature (°K)
w	Weight of catalyst (gm)
$\underline{X}_j$	Design matrix for j^{th} kinetic model
x	Independent variable for model discrimination
x_A	Fraction of reactant converted into product
y	Dependent variable for model discrimination

Greek Letter Symbols

ε	Extinction coefficient
σ^2	Error of variance of a single measurement
σ_j^2	The unbiased estimate of error variance
ϕ_i	Proposed i^{th} kinetic model
ϕ_L	Thiele diffusion modulus squared
θ	Porosity of catalyst
τ	Tortuosity factor of catalyst

APPENDIX

A. CALIBRATION OF GAS CHROMATOGRAPH

A sketch of the apparatus used for gas chromatographic calibration is shown in Figure A-1. The whole apparatus was made of glass and consisted of a calibration chamber, a storage chamber, a manifold and a vacuum system. The volume in the calibration chamber was calibrated by filling with various weighed amount of water. The size of both the calibration and storage chamber is about 1 litre.

To start a calibration, with reference to Figure A-1, both the calibration chamber and storage chamber were vented to atmosphere via stopcocks D, E, F and G while stopcock C was closed. At the same time, the mercury level in calibration chamber was dropped to the lowest point via stopcock H by venting the mercury reservoir No. 1 through stopcock A to the atmosphere. Then the calibration and storage chambers were evacuated by closing stopcocks D, B and H and opening stopcocks F and C. During the evacuation, a certain mercury level should be kept in both chambers. This could be done by opening slightly the stopcocks H and J and then closed again.

The system could be evacuated to below 10^{-5} mm Hg. A Pirani gauge not shown in Figure A-1 and situated between stopcock C and the vacuum system (similar to the one described in Chapter IV) was used to measure the vacuum in the system.

After the evacuation had been continued for more than 2 h, the system was ready for introduction of gases (H_2S or SO_2, depending on which was to be calibrated). To proceed, both chambers were isolated by closing stopcocks F, G, H and J. The desired gas supply line was connected to the ball joint on stopcock B and at that stage,

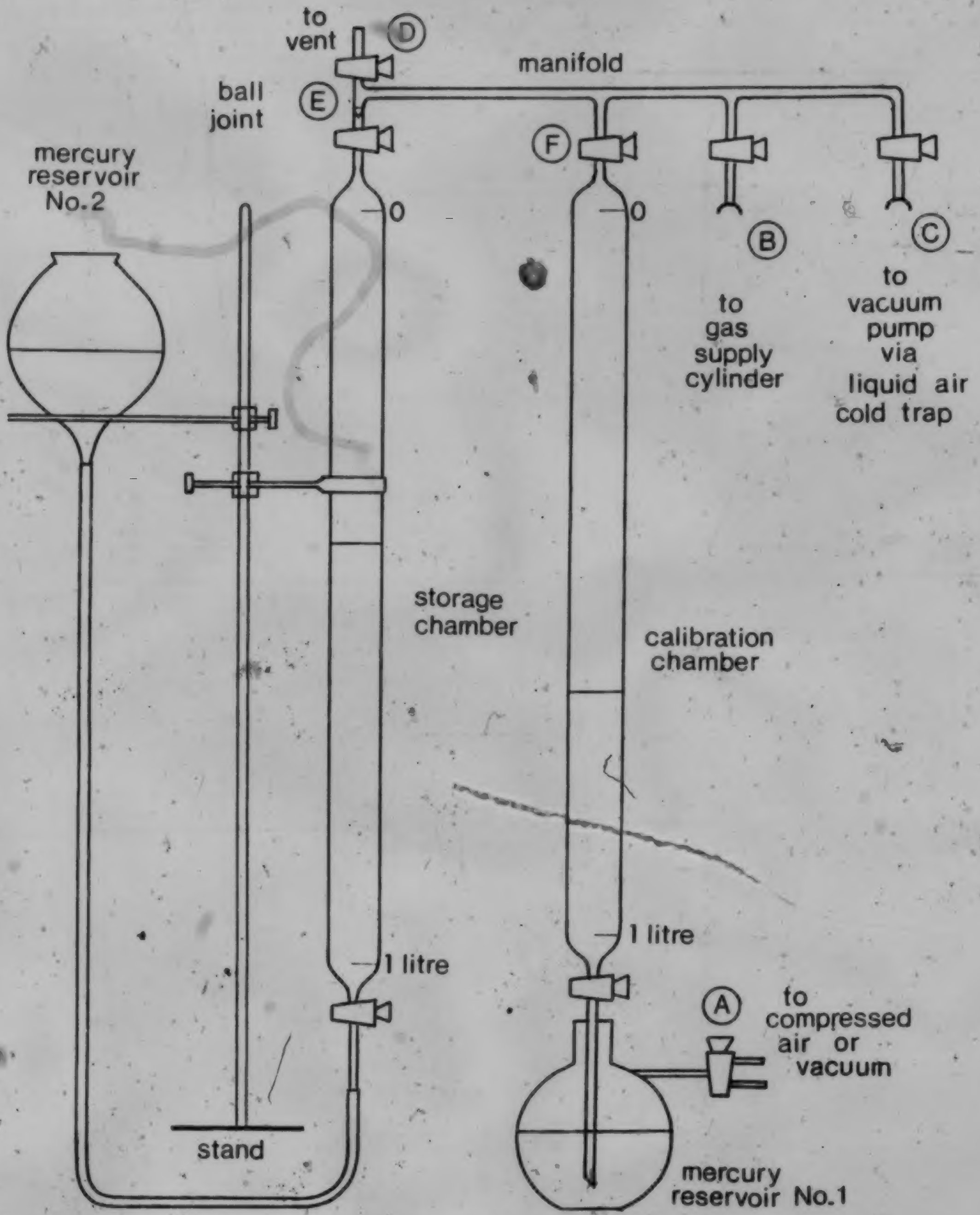
to vent
D
manifold
ball joint
E
F
mercury reservoir No.2
0
0
B
C
to gas supply cylinder
to vacuum pump via liquid air cold trap
storage chamber
calibration chamber
1 litre
1 litre
A
to compressed air or vacuum
stand
mercury reservoir No.1

Figure A-1. Apparatus for GC Calibration.

some air from the atmosphere still remained in the gas supply line. This could be eliminated by repeated purging and evacuation of the gas supply line and the manifold. The purging could be accomplished by turning on the regulator of the gas supply cylinder and opening stopcocks B and D while closing stopcock C. The evacuation was done by closing stopcock B and D while opening stopcock C. It has been found from this work that repeated purging and evacuation for a total of 15 min could almost completely reduce the air trapped in the system. Then the mercury level in the calibration chamber was raised to a point such that the void volume above the mercury level was about equal to the desired gas volume to be introduced. This was carried out by opening and closing stopcock H and by keeping mercury reservoir No. 1 vented through stopcock A to the atmosphere. To introduce the gas, stopcock B was opened for about 5 sec and then stopcock F was opened slowly. About 20 sec later, with the gas still flowing, stopcock D and F were opened to allow the pressure in the calibration chamber to drop to round atmospheric pressure. Then stopcocks D followed immediately by B and F were closed and the H_2S (or SO_2) gas supply could be shut off.

Next, the stopcock H was opened and the mercury reservoir No. 1 was vented to the atmosphere through stopcock A. As soon as the mercury level in the calibration chamber was stabilized, a cathetometer was used to measure the location of mercury levels in the calibration chamber (h_1 mm) and reservoir No. 1 (h_2 mm). The readings of atmospheric pressure ($P_o$mm Hg) and ambient temperature T_a°C) were also recorded. The void volume V_1c.c.) above the mercury in the calibration chamber could be read off the calibrated scale on the chamber wall. By using equation (A.1), the number of gram-moles of H_2S (or SO_2) introduced (N_1) could be calculated.

$$N_1 = \frac{V\ (Po - h_1 + h_2)}{RT_a} \quad 1 \qquad (A.1)$$

After all the required measurements and calculation had been completed, the gas supply line of H_2S (or SO_2) was removed from the ball joint on stopcock B and replaced by N_2 supply line. The whole procedure of purging and evacuating the gas supply line and manifold was repeated same as during the introduction of H_2S (or SO_2). When this was complete, stopcock C and D were closed and stopcock B was slowly opened. The manifold should be pressurized sufficiently above the atmospheric pressure before stopcock F was opened to allow the introduction of N_2 into the calibration chamber. In addition, stopcock H should be closed and the mercury reservoirs No. 1 vented to the atmosphere through stopcock A. After all these requirements had been checked, stopcock F was opened slowly and at the same time the mercury level drop was watched closely to make sure that it did not go below the lowest scale mark on the calibration chamber. When sufficient N_2 had been introduced, stopcock F was closely quickly, followed immediately by stopcock B. Then N_2 gas supply could be shut off and the mercury level in the calibration chamber allowed to stabilize. Similar measurements taken during the introduction of H_2S (or SO_2) were repeated. By using equation (A.2) the number of gram-moles of N_2 introduced could be calculated.

$$N_2 = \left[\frac{V(Po = h_1 + h_2)}{RT_a}\right]_2 \qquad (A.2)$$

By combining equation (A.1) and (A.2) the final molar ratio between H_2S (or SO_2) and N_2 in the calibration chamber could be calculated according to the following equation (A.3)

$$\frac{N_1}{N_2-N_1} = \frac{\left[\frac{V\ (Po - h_1 + h_2)}{RT_a}\right]_1}{\left[\frac{V\ (Po - h_1 + h_2)}{RT_a}\right]_2 - \left[\frac{V\ (Po - h_1 + h_2)}{RT_a}\right]_1} \qquad (A.3)$$

Where the subscribes of 1 and 2 below n as well as the square bracket indicate H_2S (or SO_2) and N_2 respectively.

At this stage, the gas sample in the calibration chamber might not be adequately mixed. To improve mixing, the manifold as well as the storage chamber was first evacuated by opening stopcock C and G. Then the stopcock C was closed and stopcock F was opened to allow part of the gas sample to flow into the storage chamber. The mileage was accomplished by raising the mercury levels in the two chambers to as high as possible or dropping to as low as possible, the raising and dropping could be carried out either simultaineously or alternately between the two chambers. The mercury level in the calibration chamber could be raised by applying compressed air to the mercury reservoir No. 1 through stopcock A and with stopcock H opened. It could be dropped by repeating the procedure, replacing compressed air with vacuum. On the other hand, the mercury level in storage chamber could be changed by moving the whole mercury reservoir No. 2 up and down with stopcock J opened. It was found in this work that adequate mixing could be achieved in 15 min by such method. Adequate mixing was defined as no change in the gas chromatographic analysis results between two samples taken from the same gas mixture but 24 h apart.

At the completion of mixing, the mercury level in the calibration chamber was raised to as high as possible but below stopcock F while that in the storage chamber to as low as possible but above stopcock J. This was to transfer the gas mixture from the calibration to storage chamber.

At this state, standard gas sample had been prepared and ready for gas chromatographic calibration. The whole storage chamber, stand and mercury reservoir No. 2 were detached from the system at ball joint E. The point of detachment was then reconnected to a similar ball joint at the sample injection point of the gas chromatograph. To allow the injection of gas samples into the gas chromatograph, the mercury level in the storage chamber was raised to build up the gas pressure and then stopcock G could be opened and closed for a short duration of time (about 1 sec) for every injection. The initial few injections were actually used to purge the line free of trapped air and therefore the corresponding analysis results should be discarded. As the analysis proceded, the gas pressure in the storage chamber dropped, resulting the progressly diminishing of sample sizes. This could be corrected as required by raising the mercury level in the storage chamber further. It was found in this work that the storage chamber was big enough for at least six analysis (excluding the initial few injections).

During calibration, the gas chromatograph was operated at the conditions outlined in Chapter V. For every analysis, the peak areas of the chromatograms were measured by a dish integrator. The peak area ratio between H_2S (or SO_2) and N_2 calculated from the measured results and since about six analysis of various sample sizes were obtained, an average area ratio was used. In this work, less than 0.2% variation in area ratio was produced by changing sample sizes.

A plot of average peak area ratio vs. molar ratio for H_2S/N_2 and SO_2/N_2 is shown in Figures A-2 and A-3 respectively. A good linear relation was obtained for both plots. Tables A-1 and A-2 indicate the results fitted by least square method for the same data shown in Figures A-2 and A-3. A computer program LEAST used for the data fitting process is listed in Appendix C.

TABLE A-1. Least Square Fitting of GC Calibration Data for H_2S

```
X STANDS FOR AREA RATIO OF H2S TO N2
Y STANDS FOR MOLE RATIO OF H2S TO N2 (X10)


THE COFFICIENTS OF THE POLYNOMIAL ARE$

     A0=     -0.01279

     A1=      0.24807



                    REGENERATED DATA

X MEASURED      Y OBSERVED      Y CALCULATED    PCT ERROR

    1.197          0.282           0.284           0.477

    1.676          0.400           0.402           0.593

    1.952          0.470           0.471           0.116

    2.260          0.558           0.547           1.818

    2.770          0.668           0.674           0.878


VARIANCE        =  0.000036

STANDARD DEVIATION V  0.006025

MAXIMUM PCT ERROR  =  1.818433
```

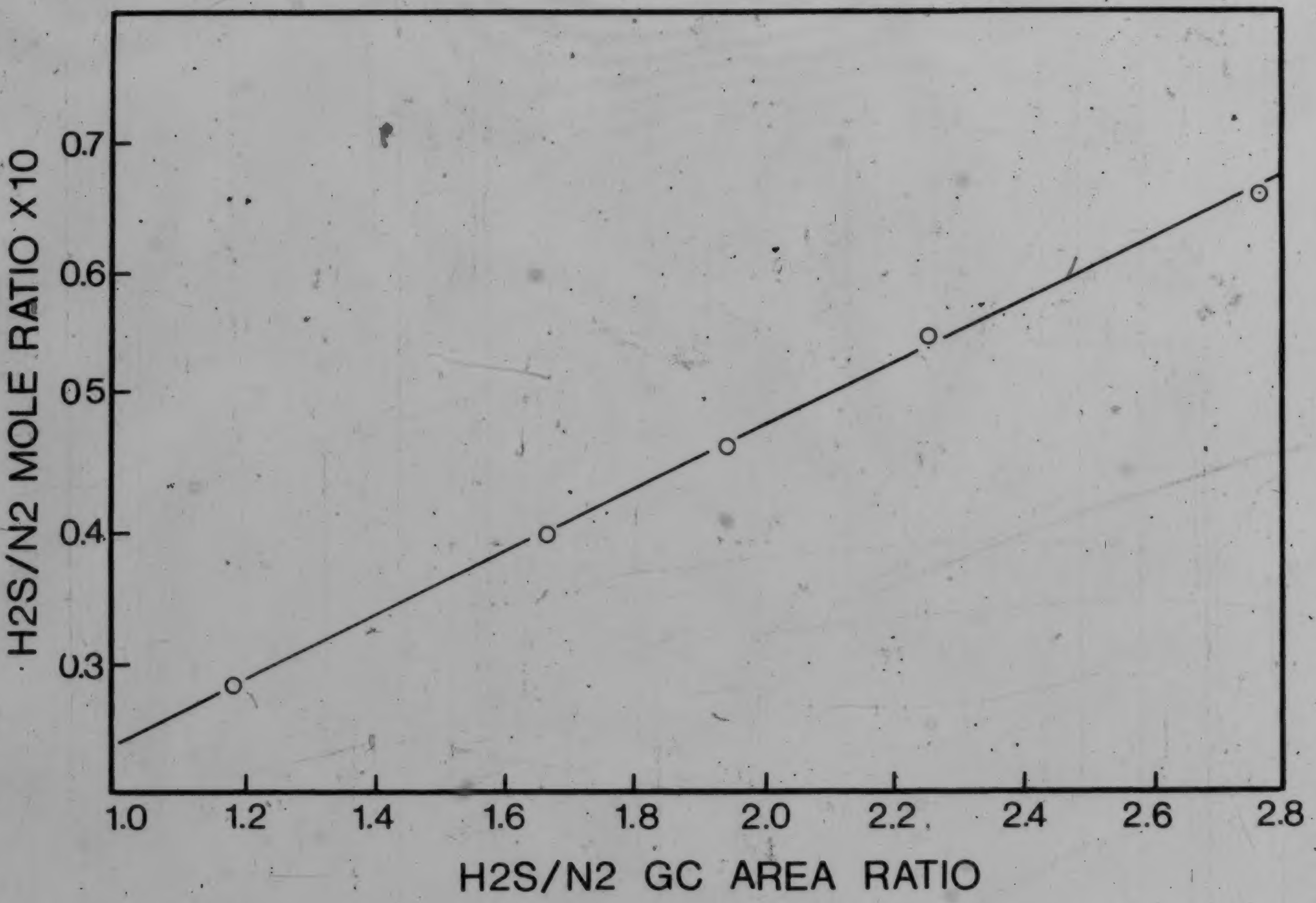

Figure A-2. GC Calibration Curve for H_2S.

TABLE A-2. Least Square Fitting of GC Calibration Data for SO_2

```
X STANDS FOR DISK INTEGRATOR AREA RATIO OF SO2 TO N2
Y STANDS FOR MOLAR RATIO OF SO2 TO N2 (X10)


THE COFFICIENTS OF THE POLYNOMIAL ARE$

     A0=      0.00959

     A1=      0.22709



                   REGENERATED DATA

X MEASURED      Y OBSERVED      Y CALCULATED    PCT ERROR

   0.573           0.142           0.139          2.111

   0.812           0.191           0.193          1.358

   1.635           0.384           0.380          0.961

   2.449           0.559           0.565          1.158

   2.500           0.579           0.577          0.303

   3.737           0.848           0.858          1.133

   4.084           0.947           0.937          1.079


VARIANCE        =   0.000045

STANDARD DEVIATION V  0.006729

MAXIMUM PCT ERROR  =  2.111648
```

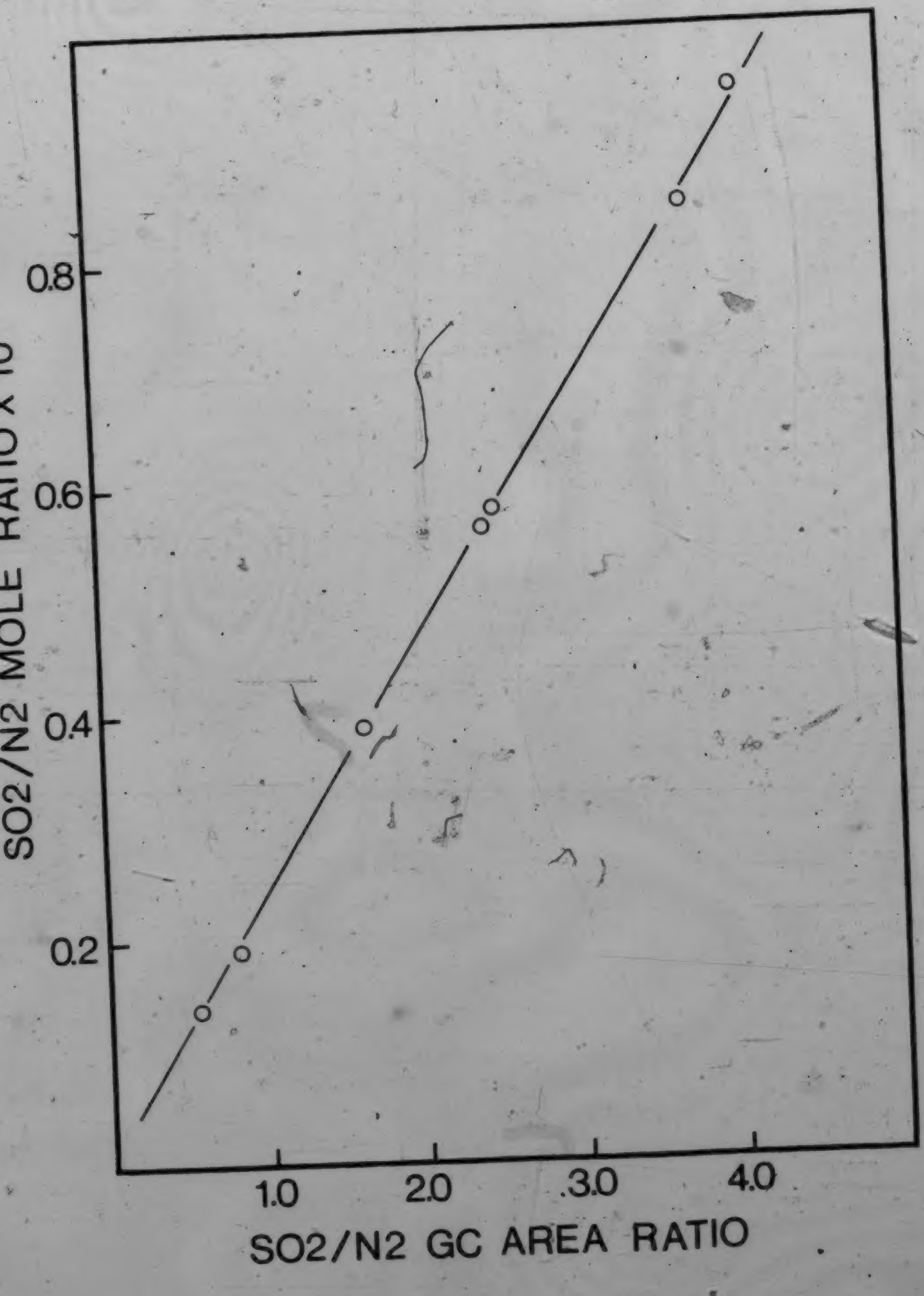

Figure A-3. GC Calibration Curve for SO_2.

B. COMPUTER PROGRAMS FOR MODEL DISCRIMINATION

The appendix contains the programs used in this thesis. The notation used in the following programs is described here.

A	Dispersion matrix $\underline{X}^t\underline{X}$
AO	Prior estimate of the dispersion matrix
B	Least squares estimate of the parameters (vector)
C	Variance-covariance matrix
D	Determinant, normalizing matrix
DSNM	A function subprogram to set up the design matrix
ER	Errors vector
FUCN	A fun-tion subprogram to compute the model predictions
INX	Mesh size in the design of experiments
IT	Reference index for the competing models
L,L1,L2	Expected likelihoods
LAM	A parameter in Marquardt's algorithm
M	Number of parameters in the given model
MUO	Prior estimate of the parameters (vector)
N	Number of data points
NM	Total number of competing models
PA,PW	Independent variables
R	Negative of the expected entropy change
SS	Minimum sum of errors squared

SETUP	A function subprogram to specify the prior parameter distribution for the given model
VAR	Error variance
Y	Vector of observations
YH	Expected value of the prediction from the entire methamodel

```
⍝   SAMPLE OUTPUT USING THE PROGRAMS OF APPENDIX B.
⍝   DEHYDRATION MODEL M3.SPECIFIED HERE BY LM=2.
      LM←2
⍝   SPECIFY THE PARAMETER PRIOR VARIANCE-COVARIANCE
⍝   MATRIX AND THE STARTING VALUE FOR THE PARAMETERS.
      A0←3 3⍴0
      B←.1 .01 .1
⍝   MARQURDT'S(1963) ALGORITHM IS USED TO COMPUTE THE
⍝   LEAST SQUARE ESTIMATE OF PARAMETERS AND VARIANCE-
⍝   COVARIANCE MATRIX IS COMPUTED AS DESCRIBED IN
⍝   CHAPTER TWO. PROGRAM 'HST' IS USED TO OBTAIN
⍝   THE MODEL LIKELIHOOD.CALL 'MGT' TO PERFORM THE
⍝   ABOVE CALCULATIONS. A SAMPLE OUTPUT IS:

      MGT
0.0798712325   0.01163917306  0.1354432714      PARAMETER VALUES AT
0.0848536293   0.01001486825  0.1888224163      VARIOUS ITERATIONS
0.09233897556  0.008185821263  0.2382591273     OF MARQUARDT'S ALG-
0.09519688775  0.007873153225  0.2560221165     ORITHM.
0.09543472473  0.007855672149  0.2574704119

PARAMETERS : 0.09543515955  0.007855869105  0.2574720037
95 PCNT LMT: 0.007987637281  0.001980287403  0.04827574289

VARIANCE : 4.125640078E¯5  STD DEV: 0.006423114 57
VAR-COVAR:
  1.595058733E¯5  ¯2.857511393E¯6   9.130670633E¯5
 ¯2.857511393E¯6   9.803845500E¯7  ¯2.152669197E¯5
  9.130670633E¯5  ¯2.152669197E¯5   5.826368378E¯4

MODEL LIKLIHD: 3.436255498E17
```

```
⍝         PROGRAM   'INV'

⍝    THIS PROGRAM COMPUTES THE INVERSE OF A NON-

⍝    SINGULAR MATRIX BY GAUSS-JORDON PIVOTING.


          ∇INV[⎕]∇
        ∇ Z←INV M;I;J;K;P
[1]     →3×⍳(2=⍴⍴M)∧=/⍴M
[2]     →0,⍴⎕←'NO INVERSE FOUND'
[3]     M←⍉(1 0 +⍴M)⍴(,⍉M),J←1<P←⍳I←1↑⍴M
[4]     M[K,1;]←M[1,K←K⍳⌈/K←|M[⍳I;1];]
[5]     P←1⌽P,0⍴P[K,1]←P[1,K]
[6]     M[;1+⍴J]←~J
[7]     →2×⍳1E¯30>|M[1;1]÷⌈/|,M
[8]     M←1⌽1⌽[1] M-(J×M[;1])∘.×M[1;]←M[1;]÷M[1;1]
[9]     →4×⍳0=I←I-1
[10]    Z←M[;⍋P]
        ∇


⍝         PROGRAM   'DET'

⍝    'DET' OBTAINS THE DETERMINANT OF A

⍝    SQUARE MATRIX BY CHIO'S METHOD.


          ∇DET[⎕]∇
        ∇ D←DET A;N;A
[1]     N←⍴A[1;]
[2]     I←0
[3]     D←1
[4]     →LAB×⍳N=1
[5]   LAL:I←I+1
[6]     D←D×A[I;I]
[7]     A[I;]←A[I;]÷A[I;I]
[8]     L←I
[9]   LAD:L←L+1
[10]    A[;L]←A[;L]-A[I;L]×A[;I]
[11]    →LAD×⍳L<N
[12]    →LAL×⍳I<N-1
[13]  LAB:D←D×A[N;N]
        ∇
```

```
⍝        PROGRAM  'HST'

⍝    THIS PROGRAM COMPUTES THE EXPECTED LIKELI-

⍝    HOODS FROM THE SUFFICIENT STATISTICS OF THE

⍝    DATA WHEN IMPROPER UNIFORM PRIORS ARE USED.


      ∇HST[⎕]∇
    ∇ HST;M;N
[1]   M←ρB
[2]   N←ρX[;1]
[3]   L←((2×○VAR)*(-N÷2))×(0.5*(M÷2))×(*(-SS÷(2×VAR)))
    ∇


⍝        PROGRAM  'HSS'

⍝    'HSS' COMPUTES THE EXPECTED LIKELIHOOD OF A GIVEN

⍝    MODEL FROM THE SUFFICIENT STATISTICS OF THE DATA

⍝    AS DEVELOPED IN CHAPTER 2 OF THIS THESIS. L1 USES

⍝    POSTERIOR DISTRIBUTION AND L2 USES THE PRIOR

⍝    DISTRIBUTION OF THE PARAMETERS.


      ∇HSS[⎕]∇
    ∇ HSS;AE;AA;AB;AC;L11;AD;DD;N
[1]   N←ρX[;1]
[2]   DD←DET(A0+A)
[3]   L11←((2×○VAR)*(-N÷2))×(*(-SS÷(2×VAR)))
[4]   AA←(A0+.×MU0)+A+.×B
[5]   AB←(A0+.×MU0)+2×A+.×B
[6]   AD←((⍉B)+.×A+.×B)+(⍉AA)+.×(INV A0+A)+.×AA
[7]   L1←(*-0.5×(AD-(⍉AB)+.×(INV A0+2×A)+.×AB))×L11
[8]   L1←(L1÷(DET(A0+A×2))*0.5)×DD*0.5
[9]   AE←((⍉B)+.×A+.×B)-(⍉AA)+.×(INV A0+A)+.×AA
[10]  AC←(AE+((⍉MU0)+.×A0+.×MU0))
[11]  L2←L11×((DET A0)*0.5)×(*¯0.5×AC)÷(DD*0.5)
    ∇
```

```
⍝     PROGRAM   'MGT'

⍝     THIS PROGRAM IS BASED ON MARQUARDT'S (128)

⍝     ALGORITHM FOR PARAMETER ESTIMATION FROM A

⍝ .   NON-LINEAR MODEL.


       ∇MGT[⎕]∇
      ∇ MGT
[1]     LAM←0.01
[2]     IT←0
[3]     I←(⍳M)∘.=⍳M
[4]    LBB:→⍳0
[5]     PHI←FUCN LM
[6]     X←DSMM LM
[7]     G←(⍉X)+.×(Y-PHI)
[8]     SS←(⍉(Y-PHI))+.×(Y-PHI)
[9]     A←((⍉X)+.×X)+A0
[10]    AA←A
[11]    D←I
[12]    IL←0
[13]   LAS:IL←IL+1
[14]    D[IL;IL]←A[IL;IL]*¯0.5
[15]    →LAS×⍳IL<M
[16]    A←D+.×A+.×D
[17]    D1←(D+.×(INV(A+LAM×I))+.×D)+.×G
[18]    D2←(D+.×(INV(A+(LAM÷NU)×I))+.×D)+.×G
[19]    B1←B+D1
[20]    B2←B+D2
[21]    BB←B
[22]    B←B1
[23]    PHI1←FUCN LM
[24]    B←B2
[25]    PHI2←FUCN LM
[26]    IT←IT+1
[27]    S1←(⍉(Y-PHI1))+.×(Y-PHI1)
[28]    S2←(⍉(Y-PHI2))+.×(Y-PHI2)
[29]    →THRE×⍳((|(+/(BB-B1)))<0.0001)
[30]    B←B1
[31]    B
[32]    →TWO×⍳S1>SS
[33]    →LBB
[34]   ONE:LAM←LAM÷NU
[35]    →LBB
[36]   TWO:LAM←LAM×NU
[37]    →LBB
[38]   THRE:→FOUR×⍳SS<S1
[39]    X←DSMM LM
[40]    VAR←S1÷N
[41]    CONTINUED ON NEXT PAGE
```

```
[41]  A←((⍉X)+.×X)+A0
[42]  C←VAR×(INV A)
[43]  →FIVE
[44] FOUR:B←BB
[45]  VAR←SS÷N
[46]  C←VAR×(INV AA)
[47] FIVE:'PARAMETERS : ';B
[48]  'VARIANCE : ';VAR
[49]  'VAR-COVAR: ';C


⍝          PROGRAM   'EXPD1'


⍝    'EXPD1' COMPUTES THE EXPECTED CHANGE IN

⍝    ENTROPY FOR A HYPOTHETICAL EXPERIMENT.


      ∇EXPD1[⎕]∇
     ∇ EXPD1;M;N;IT;I;NM
[1]    N←1
[2]    VARV←YHV←2⍴0
[3]    I←0
[4]    NM←2
[5]    INX←2
[6]    VAR←10*¯3
[7]    PA←PW←2
[8]   LAB:I←I+1
[9]    →LAT×⍳PW>40
[10]   →LAS×⍳PA>50
[11]   IT←0
[12]  LAC:IT←IT+1
[13]   A0←SETUP IT
[14]   YHV[IT]←B FUCN IT
[15]   PHI←YHV[IT]
[16]   X←B DSNM IT
[17]   VARV[IT]←X+.×(INV(A0))+.×(⍉X)×VAR
[18]   →LAC×⍳IT<NM
[19]   YH←+/P0×YHV
[20]   VARR←(+/(VARV×P0))+VAR
[21]   VTT←(⍟(VARR÷(VARV+VAR)))
[22]   R←0.5×((+/(P0×(VTT+(((YHV-YH)*2)÷VARR)))))
[23]   R;' PA,PW = ';PA;'  ';PW
[24]   PA←PA+INX
[25]   →LAB
[26]  LAS:PW←PW+INX
[27]   PA←0.2
[28]   →LAB
[29]  LAT:→⍳0
     ∇
```

```
⍝           PROGRAM    'FUCN'

⍝    THIS PROGRAM STORES THE FUNCTIONAL FORMS

⍝    FOR THE VARIOUS DEHYDRATION MODELS.

         ∇FUCN[⎕]∇
     ∇ PHI←B FUCN LM;LM;B
[1]     →TWO×⍳LM=2
[2]     →THRE×⍳LM=3
[3]     →FOUR×⍳LM=4
[4]     →FIVE×⍳LM=5
[5]     →SIX×⍳LM=6
[6]   ONE:PHI←B[1]×PA÷((1+(B[2]×PA)+(B[3]×PW)))
[7]    →TEN
[8]   TWO:PHI←B[1]×PA÷(((1+(B[2]×PA))×(1+B[3]×PW)))
[9]    →TEN
[10]  THRE:PHI←B[1]×PA÷(1+(B[2]×PA))
[11]   →TEN
[12]  FOUR:PHI←B[1]×PA÷((1+(B[2]×PW)+(B[3]×PA))*2)
[13]   →TEN
[14]  FIVE:PHI←B[1]×(*-B[2]÷(1.987×TMP))×PA÷((1+(B[3]×PW))*2)
[15]   →TEN
[16]  SIX:PHI←B[1]×PA÷(((1+B[2]×PA)+B[3]×PP)×(1+B[4]×PW))
[17]   →TEN
[18]  TEN:→⍳0
     ∇
```

```
⍝           PROGRAM    'FUCH'

⍝     THIS PROGRAM GENERATES THE MODEL PREDICTIONS

⍝     FOR THE DEHYDROGENATION OF 2-PROPANOL.


          ∇FUCH[⎕]∇
      ∇ PHI←B FUCH LM;LM;B
[1]     →TWO×⍳LM=2
[2]     →THRE×⍳LM=3
[3]     →FOUR×⍳LM=4
[4]     →FIVE×⍳LM=5
[5]     →SIX×⍳LM=6
[6]     →SEVEN×⍳LM=7
[7]   ONE:PHI←B[1]×PA÷((PH2*0.5)+(B[2]×PA)+B[3]×PH2)
[8]     →TEN
[9]   TWO:PHI←B[1]×(PA÷PH2*0.5)÷((1+B[2]×PH2*0.5)×(1+B[3]×PA÷PH2*0.5))
[10]    →TEN
[11]  THRE:PHI←B[1]×(PA÷PH2*0.5)÷((1+B[2]×PH2*0.5)×(1+B[3]×PA÷PH2*0.5))
[12]    →TEN
[13]  FOUR:PHI←B[1]×PA÷((PH2*0.5)+(B[2]×PA)+B[3]×PH2)
[14]    →TEN
[15]  FIVE:PHI←B[1]×(PA÷PH2*0.5)÷(1+(B[2]÷PH2*0.5)+(B[3]×PA÷PH2*0.5)+(B[4]×PA))
[16]    →TEN
[17]  SIX:PHI←B[1]×PA÷((B[4]×PA÷PH2*0.5)+(1+B[2]×PA÷PH2*0.5)×(1+B[3]×PH2*0.5))
[18]    →TEN
[19]  SEVEN:PHI←B[1]×(PA÷PH2*0.5)÷(((1+B[2]×PH2*0.5)×(1+(B[3]×PA)+(B[4]×PA÷PH2*0.5)))+B[5])
[20]  TEN:→⍳0
      ∇
```

```
        ⍝           PROGRAM   'DSHM'

        ⍝    DSHM COMPUTES THE DESIGN MATRIX X FOR THE

        ⍝    VARIOUS DEHYDRATION MODELS.


          ∇DSHM[⎕]∇
        ∇ X←B DSHM LM;LM;B
  [1]     X←(ιN)∘.=ιM
  [2]     →TWO×ιLM=2
  [3]     →THRE×ιLM=3
  [4]     →FOUR×ιLM=4
  [5]     →FIVE×ιLM=5
  [6]     →SIX×ιLM=6
  [7]   ONE:X[;1]←PHI÷B[1]
  [8]     X[;2]←-PHI×PA÷(1+(PA×B[2])+(PW×B[3]))
  [9]     X[;3]←X[;2]×PW÷PA
  [10]    →TEN
  [11]  TWO:X[;1]←PHI÷B[1]
  [12]    X[;2]←-PHI×PA÷(1+B[2]×PA)
  [13]    X[;3]←-PHI×PW÷(1+B[3]×PW)
  [14]    →TEN
  [15]  THRE:X[;1]←PHI÷B[1]
  [16]    X[;2]←-PHI×PA÷(1+(B[2]×PA))
  [17]    →TEN
  [18]  FOUR:X[;1]←PHI÷B[1]
  [19]    DHM←1+(B[2]×PW)+(B[3]×PA)
  [20]    X[;2]←-2×PHI×PW÷DHM
  [21]    X[;3]←-2×PHI×PA÷DHM
  [22]    →TEN
  [23]  FIVE:X[;1]←PHI÷B[1]
  [24]    X[;2]←-PHI÷(1.987×TMP)
  [25]    X[;3]←-2×PHI×PW÷(1+(B[3]×PW))
  [26]    →TEN
  [27]  SIX:X[;1]←PHI÷B[1]
  [28]    DHM←((1+(B[2]×PA)+B[3]×PP)×(1+B[4]×PW))
  [29]    X[;2]←-PHI×PA×(1+B[4]×PW)÷DHM
  [30]    X[;3]←-PHI×PP×(1+B[4]×PW)÷DHM
  [31]    X[;4]←-PHI×PW×(1+(B[2]×PA)+B[3]×PP)÷DHM
  [32]    →TEN
  [33]  TEN:→ι0
        ∇
```

```
⍝            PROGRAM   'DSNM'

⍝    'DSNM' COMPUTES THE DESIGN MATRIX FOR THE

⍝     DEHYDROGENATION MODELING.

    ∇DSNM[⎕]∇
      ∇ X←B DSNM LM;LM;B;DNM
[1]     X←(⍳N)∘.=⍳M
[2]     →TWO×⍳LM=2
[3]     →THRE×⍳LM=3
[4]     →FOUR×⍳LM=4
[5]     →FIVE×⍳LM=5
[6]     →SIX×⍳LM=6
[7]     →SEVEN×⍳LM=7
[8]   ONE:X[;1]←PHI÷B[1]
[9]     DNM←(PH2*0.5)+(B[2]×PA)+(B[3]×PH2)
[10]    X[;2]←-PHI×PA÷DNM
[11]    X[;3]←-PHI×PH2÷DNM
[12]    →TEN
[13]  TWO:X[;1]←PHI÷B[1]
[14]    X[;2]←-PHI×(PH2*0.5)÷(1+B[2]×PH2*0.5)
[15]    X[;3]←-PHI×(PA÷PH2*0.5)÷(1+B[3]×PA÷PH2*0.5)
[16]    →TEN
[17]  THRE:X[;1]←PHI÷B[1]
[18]    X[;2]←-PHI×(PH2*0.5)÷(1+B[2]×PH2*0.5)
[19]    X[;3]←-PHI×(PA÷PH2*0.5)÷(1+B[3]×PA÷PH2*0.5)
[20]    →TEN
[21]  FOUR:X[;1]←PHI÷B[1]
[22]    DNM←(PH2*0.5)+(B[2]×PA)+(B[3]×PH2)
[23]    X[;2]←-PHI×PA÷DNM
[24]    X[;3]←-PHI×PH2÷DNM
[25]    →TEN
[26]  FIVE:X[;1]←PHI÷B[1]
[27]    DNM←1+(B[2]÷PH2*0.5)+(B[3]×PA÷PH2*0.5)+(B[4]×PA)
[28]    X[;2]←-PHI×(÷PH2*0.5)÷DNM
[29]    X[;3]←-PHI×(PA÷PH2*0.5)÷DNM
[30]    X[;4]←-PHI×PA÷DNM
[31]    →TEN
[32]  SIX:X[;1]←PHI÷B[1]
[33]    DNM←((1+B[2]×PA÷PH2*0.5)×(1+B[3]×PH2*0.5))+(B[4]×PA÷PH2*0.5)
[34]    X[;2]←-PHI×(PA÷PH2*0.5)×(1+B[3]×PH2*0.5)÷DNM
[35]    X[;3]←-PHI×(PH2*0.5)×(1+B[2]×PA÷PH2*0.5)÷DNM
[36]    X[;4]←-PHI×(PA÷PH2*0.5)÷DNM
[37]    →TEN
[38]  SEVEN:X[;1]←PHI÷B[1]
[39]    DNM←B[1]×(PA÷PH2*0.5)÷PHI
[40]    X[;2]←-PHI×(PH2*0.5)×(1+(B[3]×PA)+(B[4]×PA÷PH2*0.5))÷DNM
[41]    X[;3]←-PHI×PA×(1+B[2]×PH2*0.5)÷DNM
[42]    X[;4]←-PHI×(PA÷PH2*0.5)×(1+B[2]×PH2*0.5)÷DNM
[43]    X[;5]←-PHI÷DNM
[44]    →TEN
[45]  TEN:→⍳0
      ∇
```

C. CALIBRATION OF LIQUID SYRINGE FEEDER

The syringe feeder used for introducing liquid through the Sage syringe pump into the reaction system was calibrated by filling with distilled water at room temperature at 24°C. The distilled water was first de-aerated by repeated thawing and unthawing in a vacuum system. The amount of water filled into the syringe was measured by weighing the water at 24°C. During calibration, the water ejected through the syringe needle was collected in a 25 ml pycnometer submerged in an ice-water bath to prevent the loss of water due to evaporation. The quantity of water collected in the pycnometer was measured by weighing. The duration of each calibration was one hour. Each piston speed was calibrated four times in such a way that the whole range of piston travel (about 12 cm) was covered. The repeatability of the results showed that the speed was reproducible within ± 0.1% with respect to the position of the syringe position. The average values of the four runs for each speed is used to obtain calibration curves. For the speed range of 1/1000X, six data points (average values) were collected and of 1/100X, five were obtained. These two sets of data were fitted by the least squares method and the results are shown in Tables C-1 and C-2 for each speed range. The computer programs, LEAST, of the least squares method are also listed.

TABLE C-1. Least Square Fitting of Calibration Data for the Syringe Feeder at Low Speed Range

```
X=    OF (1/1000X) ON THE CONTROL DIAL OF THE FEEDER
Y= FEED RATE- CC PER HOUR AT 24 DEG.


THE COEFFICIENTS OF THE POLYNOMIAL, Y=A0+A1*X+A2*X**2,
     A0 =    -0.00690
     A1 =     0.05274
     A2 =    -0.00000


                      REGENERATED DATA
X MEASURED      Y OBSERVED     Y CALCULATED      PCT ERROR
  10.0000         0.5211          0.5197          0.2554
  20.0000         1.0433          1.0449          0.1564
  30.0000         1.5666          1.5685          0.1264
  40.0000         2.0935          2.0907          0.1329
  60.0000         3.1300          3.1304          0.0120
  80.0000         4.1640          4.1641          0.0029

VARIANCE                = 0.000003
STANDARD DEVIATION      = 0.001803
MAXIMUM PCT ERROR       = 0.255461
```

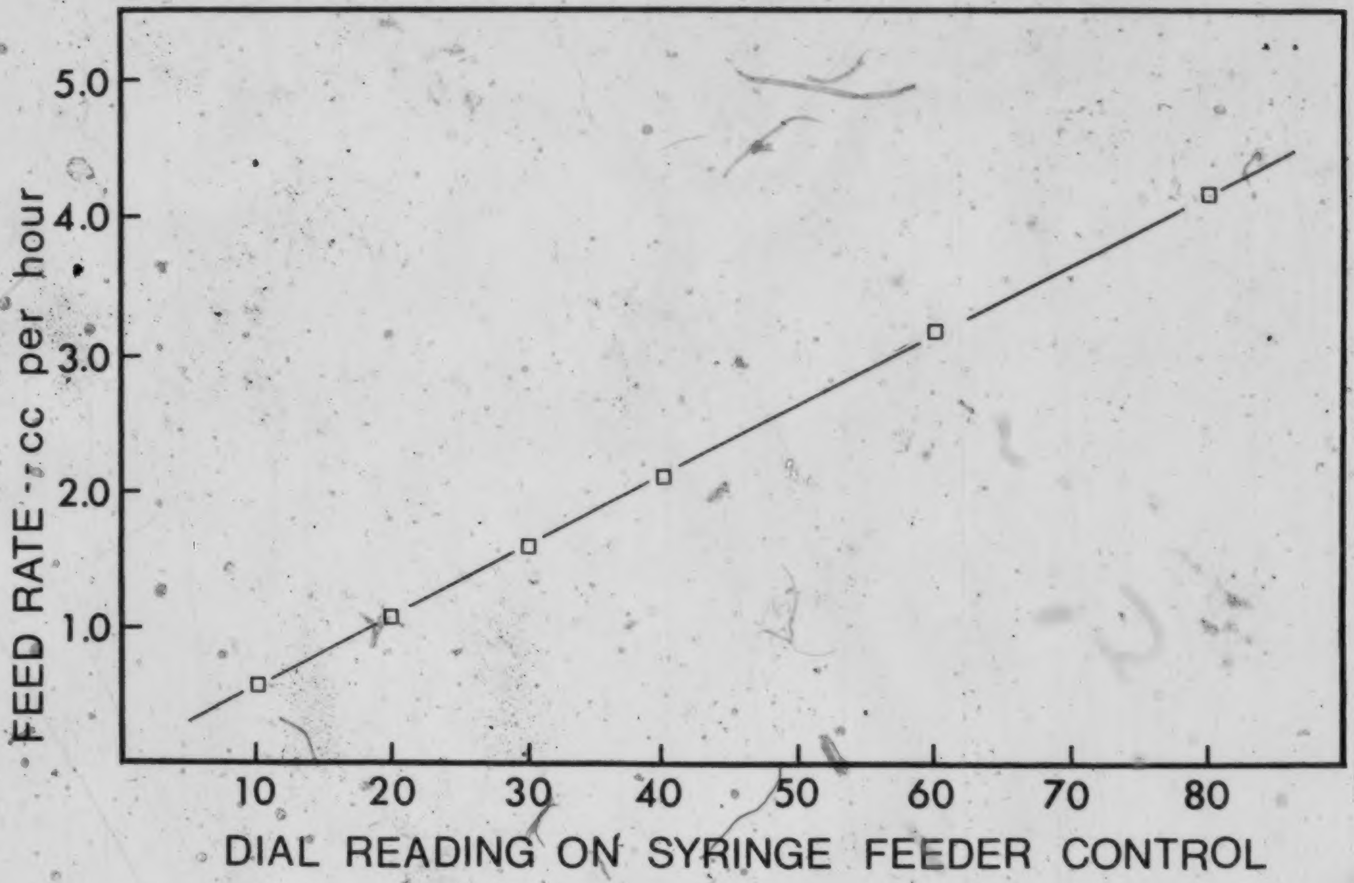

Figure C-1. Calibration Curve for Syringe Feeder at Low Speed Range.

TABLE C-2. Least Square Fitting of Calibration Data for the Syringe Feeder at High Speed Range

```
   X=   OF (1/100X) ON THE CONTROL DIAL OF THE FEEDER

   Y= FEED RATE- CC PER HOUR AT 24 DEG.


THE COEFFICIENTS OF THE POLYNOMIAL, Y = A0 + A1 * X,

     A0 =    -0.03847
     A1 =     0.52202


                 REGENERATED DATA

X MEASURED     Y OBSERVED    Y CALCULATED     PCT ERROR

   10.000          5.211           5.181         0.561

   20.000         10.439          10.402         0.360

   30.000         15.575          15.622         0.304

   40.000         20.765          20.842         0.372

   60.000         37.341          31.283         0.184


VARIANCE              = 0.003467

STANDARD DEVIATION = 0.058884

MAXIMUM PCT ERROR   = 0.561762
```

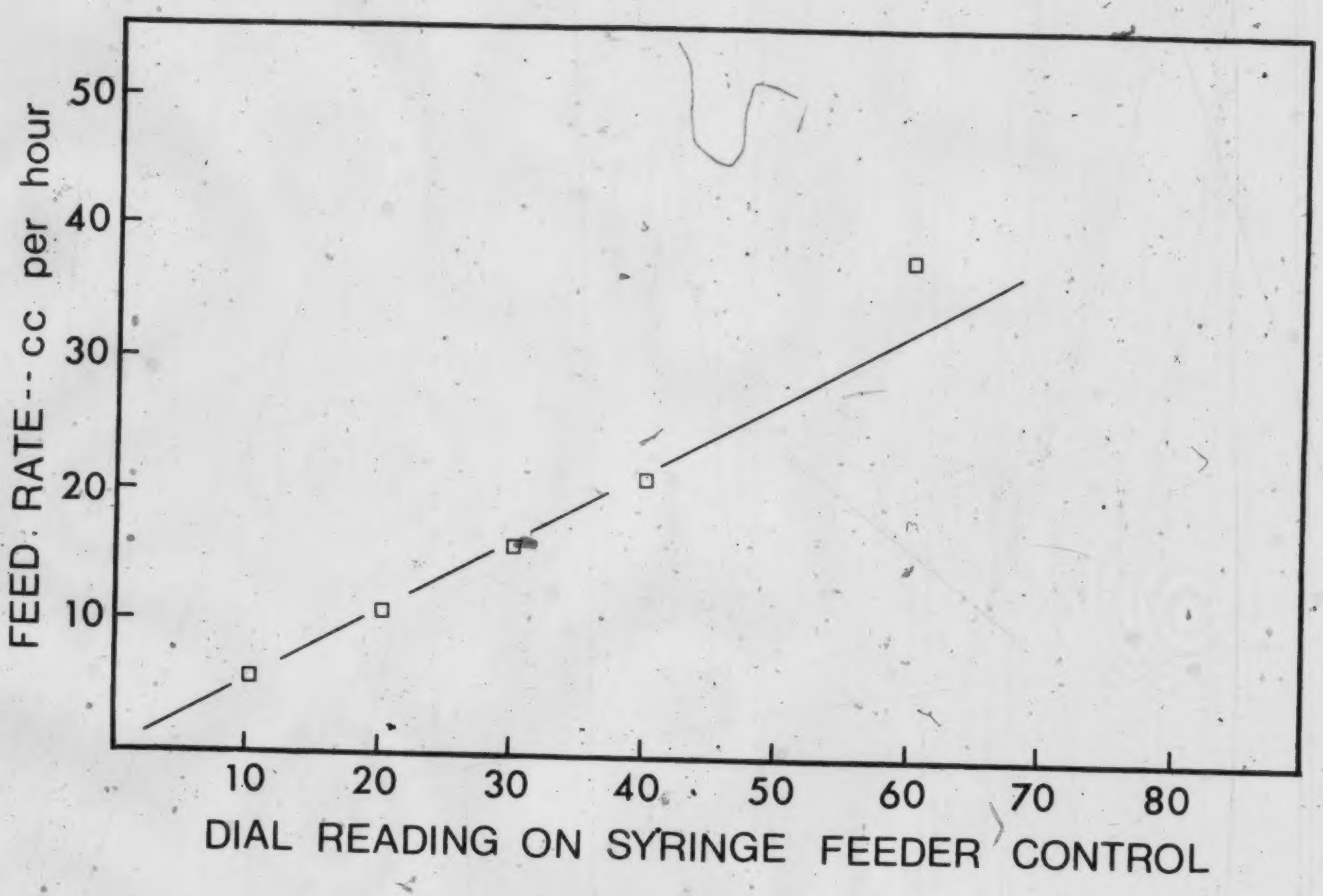

Figure C-2. Calibration Curve for Syringe Feeder at High Speed Range.

```
   C     MAINLINE LEAST

C     MAINLINE LEAST

C     ****************************************************
C     *                                                  *
C     *              MAINLINE LEAST                      *
C     *                                                  *
C     * THIS PROGRAM WAS WRITTEN FOR FITTING A MAXIMUM OF *
C     * 50 DATA POINTS TO POWER SERIES TYPE POLYNOMIALS OF *
C     * ANY ORDER UP TO A MAXIMUM OF FOURTH DEGREE.      *
C     *   INPUT DATA                                     *
C     *      NCASE  - NUMBER OF SETS OF DATA             *
C     *      NCOPY  - NUMBER OF COPIES OF OUTPUT DESIRED *
C     *      N      - NUMBER OF DATA POINTS              *
C     *      M      - DEGREE OF POLYNOMIAL               *
C     *      NTL    - NUMBER OF CARDS FOR TITLE          *
C     *      NPAGE  - PAGE NUMBER OF OUTPUT              *
C     *      NPLT   - DATA REGENERATION FLAG             *
C     *               ...0-REGENERATE GIVEN DATA ONLY    *
C     *               ...1-REGENERATE GIVEN DATA PLUS 20 *
C     *                    INTERMEDIATE POINTS           *
C     *      DES(K) - ALPHANUMERIC DESCRIPTION OF THE TITLE *
C     *      XNAME  - ALPHANUMERIC DESCRIPTION OFX       *
C     *      YNAME  - ALPHANUMERIC DESCRIPTION OF Y      *
C     *      X(I)   - INDEPENDENT VARIABLE               *
C     *      Y(I)   - DEPENDENT VARIABLE                 *
C     *                                                  *
C     ****************************************************

      DIMENSION X(50),Y(50),A(50,5),P(20,20),V(20),Z(20),
     1DES(10,15),SNAM(5),XNAME(100),YNAME(100)
      DATA SNAM/'A0 =','A1 =','A2 =','A3 =','A4 ='/
      READ(5,1) NCASE,NCOPY
      DO 9 NC=1,NCASE
      READ(5,1) N,M,NTL,NPAGE,NPLT
    1 FORMAT(5I5)
      DO 11 NT=1,NTL
   11 READ(5,12) (DES(NT,K),K=1,15)
   12 FORMAT(15A4)
      READ (5,20) (XNAME(I),I=1,15)
   20 FORMAT (15A4)
      READ (5,21) (YNAME(J),J=1,15)
   21 FORMAT (15A4)
   13 FORMAT(10X,15A4/)
      MM=M+1
      DO 2 I=1,N
    2 READ(5,3) X(I),Y(I)
    3 FORMAT(2F10.5)
      DO 4 I=1,N
      DO 4 J=1,MM
    4 A(I,J)=X(I)**(J-1)
```

```
     C    MAINLINE LEAST    ...(CONT'D)
   DO 5 I=1,MM
   DO 5 J=1,MM
   P(I,J)=0.
   DO 5 K=1,N
 5 P(I,J)=P(I,J)+A(K,I)*A(K,J)
   DO 6 I=1,MM
   V(I)=0.
   DO 6 J=1,N
 6 V(I)=V(I)+Y(J)*A(J,I)
   CALL GAUSS(P,V,MM,Z)
   DO 16 ICOP=1,NCOPY
   WRITE(6,10) NPAGE
10 FORMAT('1',///,66X,'A-',I2,/)
   DO 17 I=1,NTL
17 WRITE(6,13)(DES(I,K),K=1,15)
   WRITE (6,30) (XNAME(I),I=1,15)
30 FORMAT (///,12X,15A4)
   WRITE (6,31) (YNAME(J),J=1,15)
31 FORMAT (12X,15A4)
   WRITE(6,8)
 8 FORMAT( ///,10X,'THE COEFFICIENTS OF THE POLYNOMIAL '
  1,'AREA'/)
   DO 15 I=1,MM
15 WRITE(6,7) SNAM(I),Z(I)
 7 FORMAT(15X,A4,F11.5/)
16 CALL REGEN(X,Y,Z,MM,N)
   IF(NPLT) 9,9,14
14 CALL POLYT (X,Z,N,MM)
 9 CONTINUE
   CALL EXIT
   END
```

```
C     SUBROUTINE POLYT

C     SUBROUTINE POLYT
C
C     *******************************************************
C     *                                                     *
C     *               SUBROUTINE POLYT                      *
C     *                                                     *
C     * POLYT SUPPLIES REGENERATED DATA AT POINTS INTER-    *
C     * MEDIATE TO THE GIVEN DATA.                          *
C     *                                                     *
C     *******************************************************
      SUBROUTINE POLYT(X,Z,N,MM)
      DIMENSION X(50),Z(20)
      WRITE(6,1)
    1 FORMAT(///,32X,'PLOT TEST DATA'//25X'X CALCULATED',4X
     1,'Y CALCULATED'/)
      XMAX=0.
      XMIN=99999.
      DO 2 I=1,N
      IF(XMAX-X(I)) 3,3,4
    3 XMAX=X(I)
    4 IF(X(I)-XMIN) 5,5,2
    5 XMIN=X(I)
    2 CONTINUE
      DELX=(XMAX-XMIN)/20.
      XY=XMIN
      DO 6 I=1,20
      CAL=0.
      DO15 J=1,MM
   15 CAL=CAL+Z(J)*XY**(J-1)
      WRITE(6,7) XY,CAL
    7 FORMAT(24X,2(F10.3,5X))
    6 XY=XY+DELX
      RETURN
      END
```

C * SUBROUTINE REGEN

```
C     SUBROUTINE REGEN
C
C     ************************************************************
C     *                                                          *
C     *                  SUBROUTINE REGEN                        *
C     *                                                          *
C     * THIS SUBROUTINE REGENERATES THE GIVEN DATA AND           *
C     * CALCULATES THE VARIANCE AND STANDARD DEVIATION OF        *
C     * THE FIT.                                                 *
C     *                                                          *
C     ************************************************************
C
      SUBROUTINE REGEN(X,Y,Z,MM,N)
      DIMENSION X(50),Y(50),Z(20)
      WRITE(6,1)
    1 FORMAT(///,29X,'REGENERATED DATA'//10X,'X MEASURED',5X
     1,'Y OBSERVED',5X,'Y CALCULATED',3X,'PCT ERROR',/)
      VAR=0.
      HI=0.
      DO 2 I=1,N
      CAL=0.
      DO 3 J=1,MM
    3 CAL=CAL+Z(J)*X(I)**(J-1)
      CAT=ABS(Y(I)-CAL)
      PCE=CAT/Y(I)*100.
      VAR=VAR+CAT**2
      IF(HI-PCE)4,4,2
    4 HI=PCE
    2 WRITE(6,5) X(I),Y(I),CAL,PCE
    5 FORMAT( 9X,4(F10.3,5X)/)
      VAR=VAR/(N-1)
      DEV=VAR**0.5
      WRITE(6,6) VAR,DEV,HI
    6 FORMAT(//,10X'VARIANCE           =',F10.6//10X,
     1'STANDARD DEVIATION =',F10.6//10X,
     2'MAXIMUM PCT ERROR  =',F10.6)
      RETURN
      END
      C     SUBROUTINE GAUSS
C     SUBROUTINE GAUSS
C     ******************************************************
C     *                                                    *
C     *                SUBROUTINE GAUSS                    *
C     *                                                    *
C     * THE FUNCTION OF THIS SUBROUTINE IS TO SOLVE THE    *
C     * SET OF EQUATIONS A*X=B USING GAUSSIAN ELIMINATION  *
C     * AND BACK SUBSTITUTION ROTATING ABOUT THE ELEMENT   *
C     * OF MAXIMUM MODULUS.                                *
C     *                                                    *
C     ******************************************************
      SUBROUTINE GAUSS (A,R,N,X)
      DIMENSION A(20,20),R(20),X(20)
      M=N-1
      DO 11 J=1,M
      S=0.
      DO 12 I=J,N
      U= ABS(A(I,J))
      IF(U-S) 12,12,112
  112 S=U
      L=I
   12 CONTINUE
      IF(L-J) 119,19,119
  119 DO 14 I=J,N
      S=A(L,I)
      A(L,I)=A(J,I)
   14 A(J,I)=S
      S=R(L)
      R(L)=R(J)
      R(J)=S
   19 IF( ABS(A(J,J))-1.E-30) 115,115,15
  115 WRITE(6,3)
      GO TO 500
   15 MM=J+1
      DO 11 I=MM,N
      IF( ABS(A(I,J))-1.E-30) 11,111,111
  111 S=A(J,J)/A(I,J)
      A(I,J)=0.0
      DO 16 K=MM,N
   16 A(I,K)=A(J,K)-S*A(I,K)
      R(I)=R(J)-S*R(I)
   11 CONTINUE
      DO 17 K=1,N
      I=N+1-K
      S=0.0
      IF(I-N) 117,17,117
  117 MM=I+1
      DO 18 J=MM,N
```

```
        C     SUBROUTINE GAUSS   ...(CONT'D)
 18 S=S+A(I,J)*X(J)
 17 X(I)=(R(I)-S)/A(I,I)
500 RETURN
  3 FORMAT (1H ,'MATRIX SINGULAR')
    END
```

D. INFRARED SPECTROSCOPIC CALIBRATION OF SO_2

The infrared cell which was used for infrared spectroscopic calibration of SO_2 is shown in Figure 4-1. The length of this infrared cell was the same as that of the infrared-cell-reactor mentioned in Section 5.1.3. The whole apparatus set up for the calibration is indicated in Figure D-1. It is essentially a vacuum rack equipped with SO_2 gas reservoir, manometer, Pirani vacuum gauge and facilities to allow introduction and evacuation of gases from the infrared cell.

Before a calibration was started, the whole vacuum rack and the infrared cell were thoroughly evacuated. When the Pirani gauge indicated a pressure lower than 10^{-5} mm Hg, the stopcock used to isolate the system from the cold trap and vacuum pump was closed. Next, the stopcock on the SO_2 gas reservoir was slowly opened, thus introducing the gas into the system. The reading indicated by the manometer was closely watched while introducing the SO_2 gas. The stopcock on the SO_2 gas had been introduced. The system was allowed to sit for 3 h before the exact pressure reading was taken. The duration of 3 h was considered sufficient because it was found that an equilibrium pressure could be reached in 2 h. A cathetometer was employed to measure the mercury levels in the manometer and the observed pressure recorded. The temperature in the infrared cell was maintained at 200°C during the whole process of the introduction of SO_2 gas.

The infrared cell containing a desired pressure of SO_2 was removed from the vacuum rack to the Perkin-Elmer 621 infrared

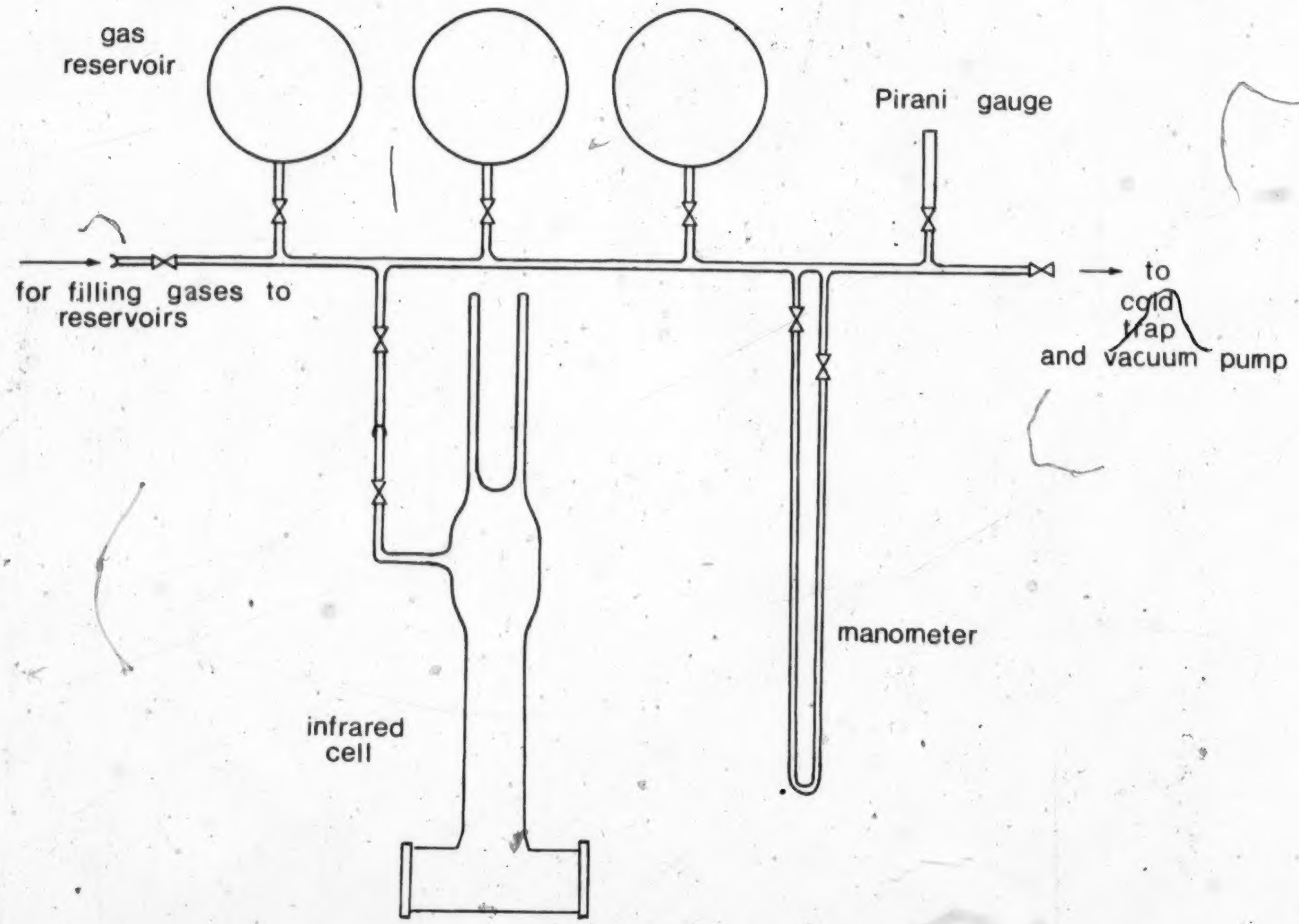
gas
reservoir
Pirani gauge
for filling gases to
reservoirs
to
cold
trap
and vacuum pump
manometer
infrared
cell

Figure D-1. Apparatus for IR Calibration of SO_2.

spectrophotometer. With air in the reference beam, the infrared cell was placed in the sample beam of the infrared spectrophotometer. An infrared absorbance chart paper was placed on the recording drum and then the frequency of the infrared spectrophotometer was set at 4000 cm^{-1}. Depending on the transparency of the infrared cell windows, the absorbance indicated on the recorder at this instance could be from 0.01 to 0.07. The desired starting absorbance (i.e. at 4000 cm^{-1}) could be changed by adjusting the attenuator opening on reference beam side of the infrared spectrophotometer. Before a scan was started, the selection knob was set at "PROGRAM", suppression knob at 4.8 and amplifier gain 6.0. The scanning speed was set at 1/32. A complete scan from 4000 cm^{-1} to 200 cm^{-1} was carried out. During the entire scan, the temperature in the infrared cell was kept at 200°C.

After a complete scan, the magnitudes (in terms of absorbance) of all the infrared bands recorded were measured. Two more complete scans using different starting absorbances at 4000 cm^{-1} were then performed and the magnitudes of the three spectra were calculated. Figure D-2 to D-9 indicate the plots of the magnitudes of the various infrared spectra recorded vs. the corresponding known SO_2 pressures in the infrared cell. The least square fitted results for these data are shown in Tables D-2 to D-9.

TABLE D-1. Least Square Fitting of IR Calibration of SO_2 at 1369 cm^{-1}

```
X STANDS FOR RECORDER MEASURED PEAK HEIGHT (ABSORBANCE)
Y STANDS FOR MEASURED PRESSURE (CM HG)


THE COFFICIENTS OF THE POLYNOMIAL ARE$

    A0=      0.02235

    A1=      1.89959


                   REGENERATED DATA

X MEASURED      Y OBSERVED      Y CALCULATED    PCT ERROR
   0.054          0.123           0.125           1.295
   0.120          0.252           0.251           0.222
   0.211          0.431           0.423           1.975
   0.369          0.718           0.724           0.924
   0.638          1.230           1.234           0.291
   1.082          2.081           2.078           0.131

VARIANCE        =  0.000028
STANDARD DEVIATION V  0.005291
MAXIMUM PCT ERROR  =  1.975665
```

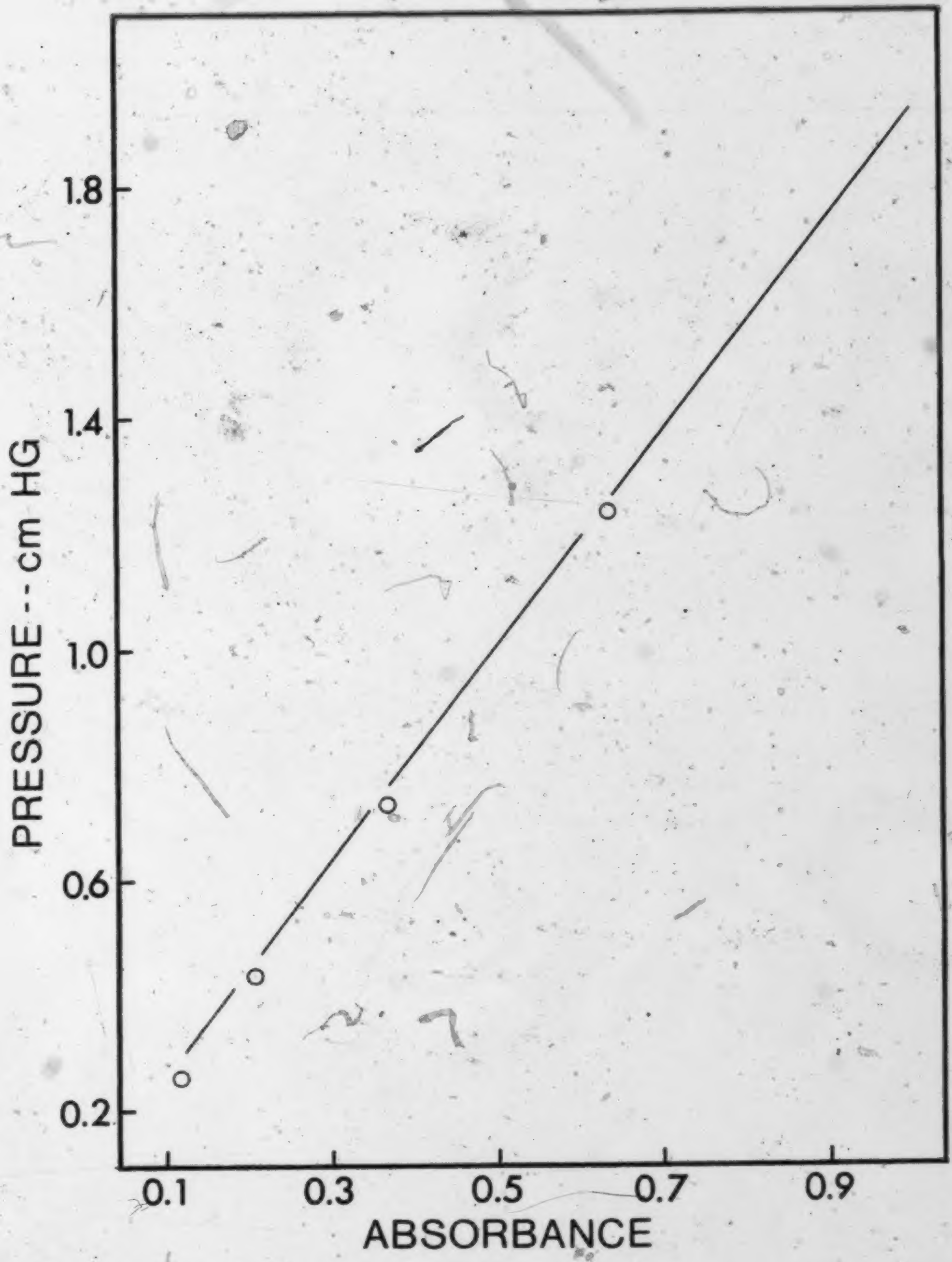

Figure D-2. IR Calibration Curve for SO_2 at 1369 cm^{-1} using Beer's Law.

TABLE D-2. Least Square Fitting of IR Calibration of SO_2 at 1357.8 cm^{-1}

```
X STANDS FOR MEASURED PEAK HEIGHT FROM RECORDER (ABSORBANCE)
Y STANDS FOR MEASURED SO2 PRESSURE   (CM HG)


THE COFFICIENTS OF THE POLYNOMIAL ARES

      A0=      0.00361

      A1=      1.70324


                     REGENERATED DATA

X MEASURED      Y OBSERVED       Y CALCULATED     PCT ERROR

   0.069           0.123            0.122           1.407

   0.147           0.252            0.253           0.708

   0.248           0.431            0.426           1.316

   0.425           0.718            0.727           1.321

   0.718           1.230            1.227           0.312


VARIANCE          =  0.000035

STANDARD DEVIATION V  0.005987

MAXIMUM PCT ERROR  =  1.407143
```

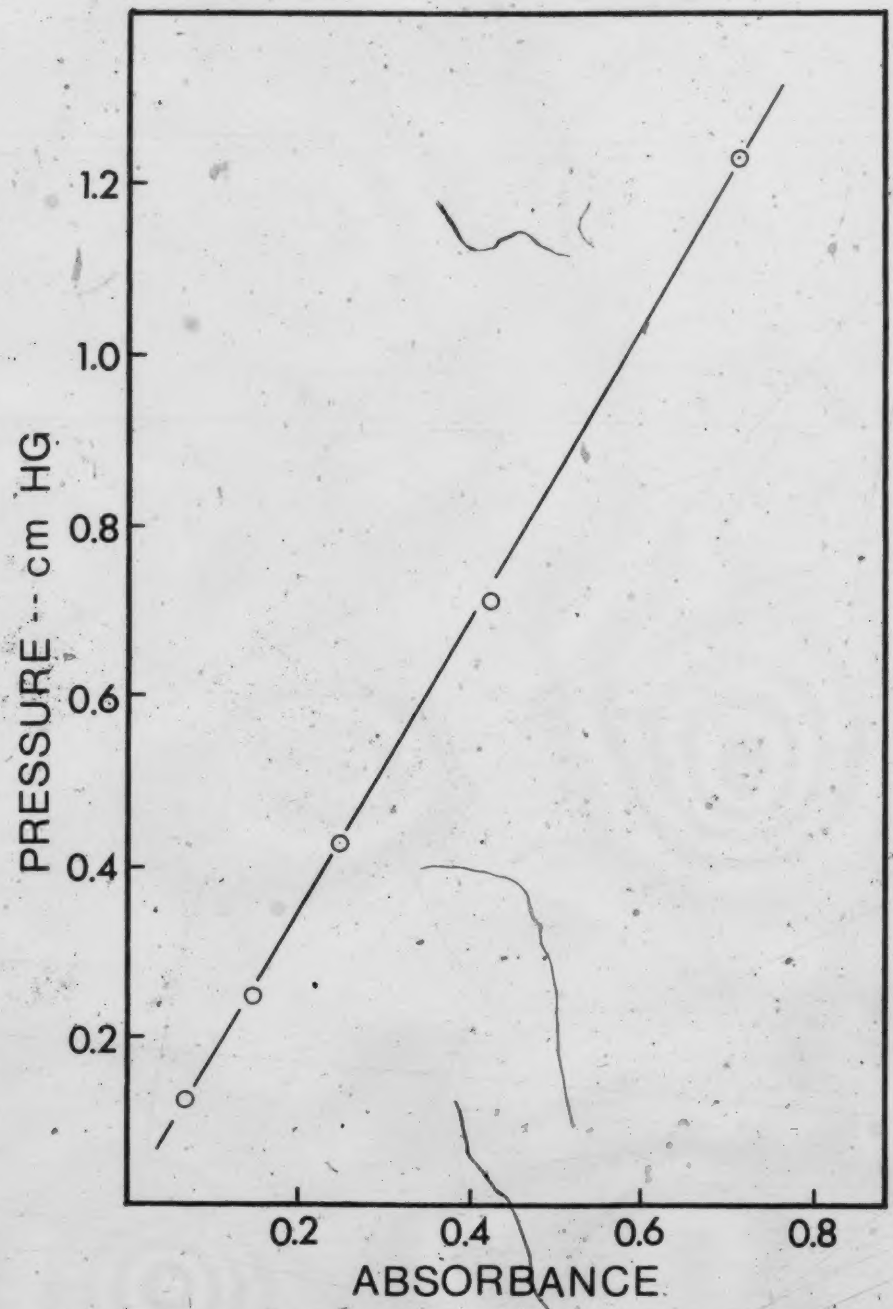

Figure D-3. IR Calibration Curve for SO_2 at 1357.8 cm^{-1} using Beer's Law.

TABLE D-3. Least Square Fitting of IR Calibration of SO_2 at 1339 cm^{-1}

```
X STANDS FOR MEASURED PEAK HEIGHT FROM RECORDER (ABSORBANCE).
Y STANDS FOR MEASURED SO2 PRESSURE   (CM HG)


THE COFFICIENTS OF THE POLYNOMIAL ARE$

     A0=      0.00502

     A1=      2.38502



                       REGENERATED DATA

X MEASURED      Y OBSERVED      Y CALCULATED    PCT ERROR

    0.050          0.123           0.124           0.497

    0.101          0.252           0.248           1.641

    0.180          0.431           0.434           0.609

    0.300          0.718           0.720           0.352

    0.513          1.230           1.229           0.133


VARIANCE          =  0.000008

STANDARD DEVIATION V  0.002896

MAXIMUM PCT ERROR  =  1.641148
```

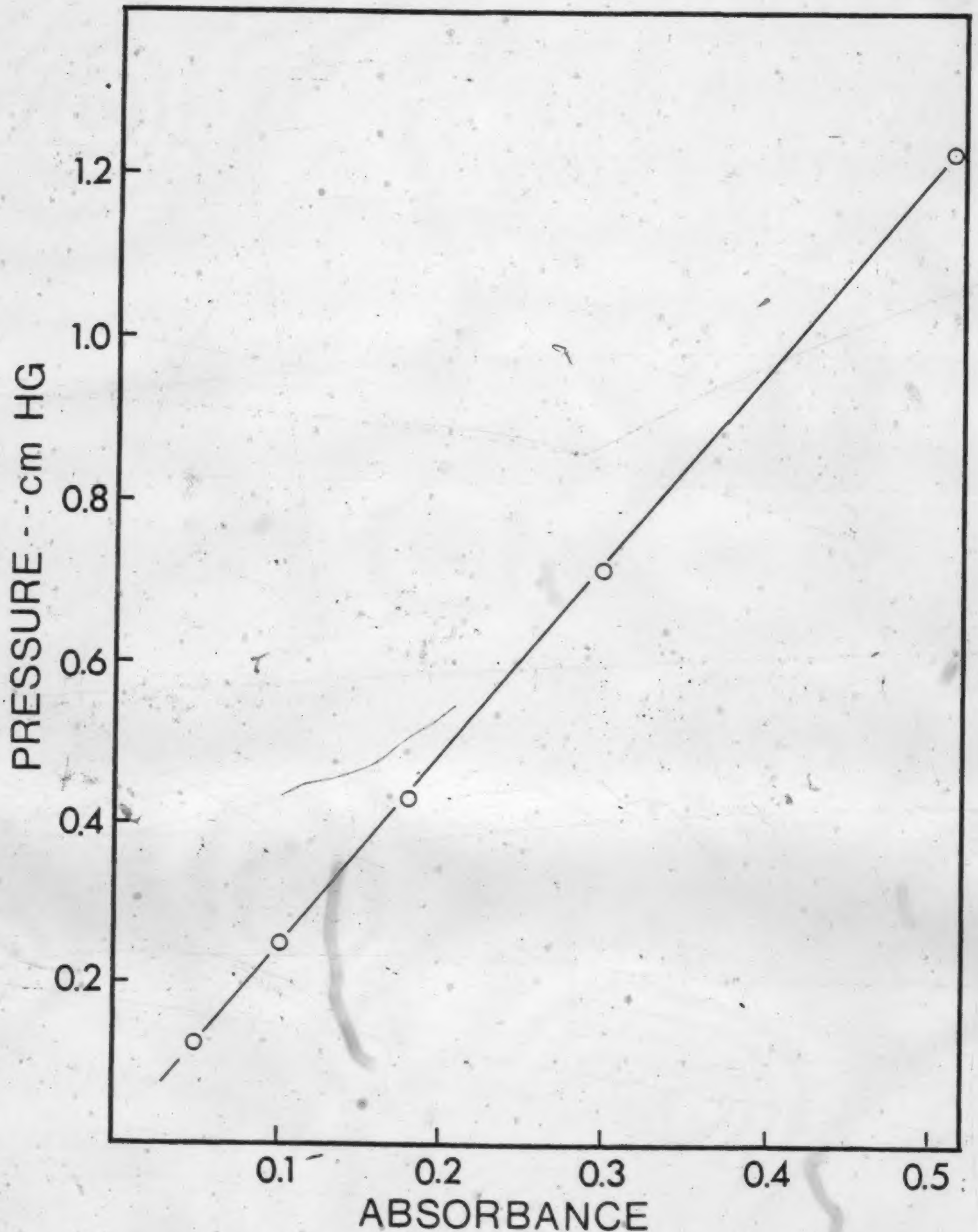

Figure D-4. IR Calibration Curve for SO_2 at 1339 cm^{-1} using Beer's Law.

TABLE D-4. Least Square Fitting of IR Calibration of SO_2 at 2500 cm^{-1}

```
X STANDS FOR RECORDER MEASURED PEAK HEIGHT (ABSORBANCE)
Y STANDS FOR MEASURED PRESSURE (CM HG)


THE COFFICIENTS OF THE POLYNOMIAL ARE$

     A0=       0.18446

     A1=     73.69729


                          REGENERATED DATA

X MEASURED        Y OBSERVED       Y CALCULATED    PCT ERROR

     0.033             2.650            2.623           0.987

     0.047             3.659            3.648           0.294

     0.068             5.227            5.195           0.595

     0.093             6.958            7.038           1.154

     0.121             9.040            9.101           0.683

     0.168            12.514           12.565           0.412

     0.229            17.233           17.061           0.997

     0.346            25.670           25.683           0.053

     0.446            33.021           33.053           0.098


VARIANCE        =  0.005685

STANDARD DEVIATION V  0.075401

MAXIMUM PCT ERROR  =  1.154195
```

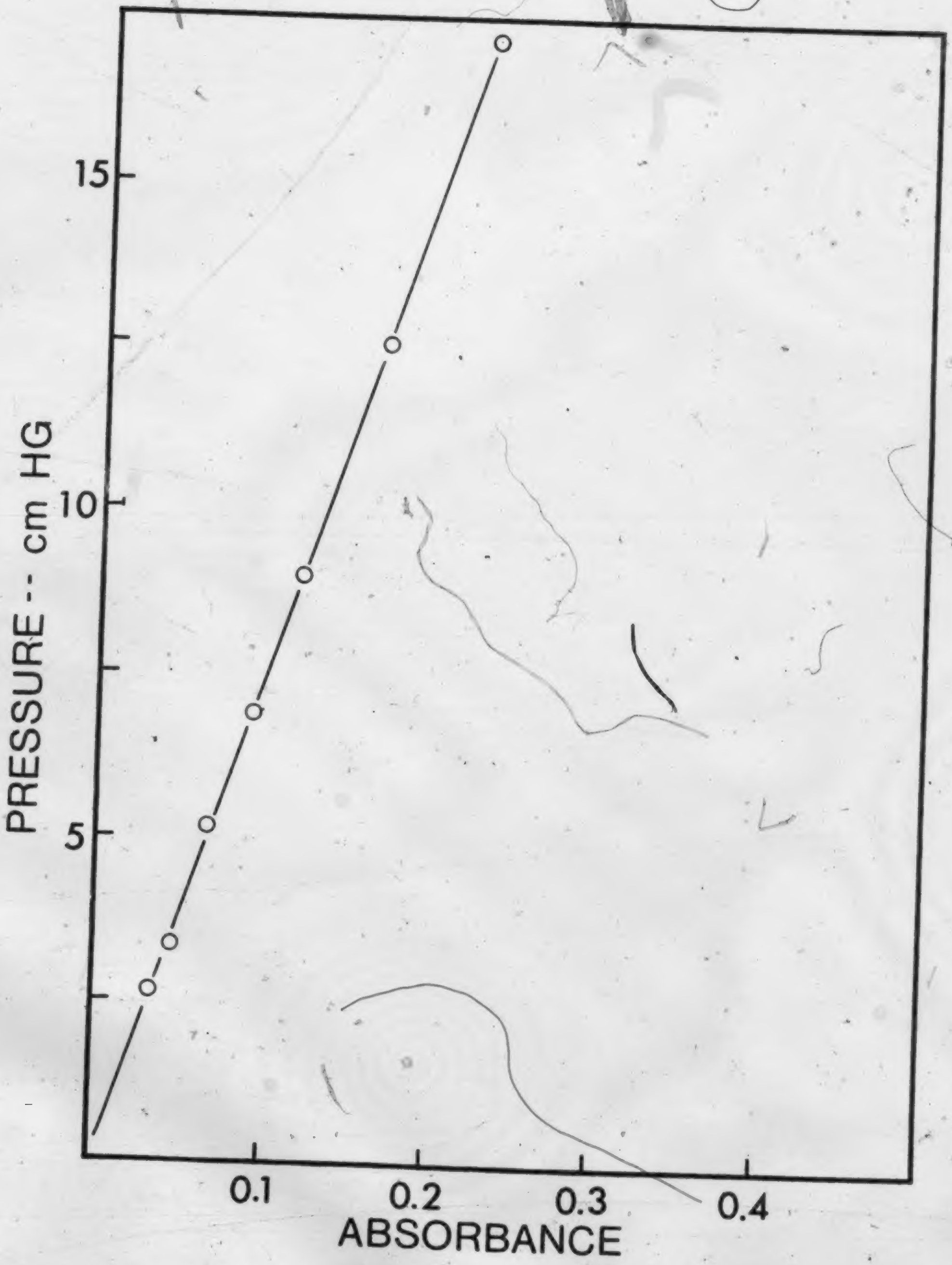

Figure D-5. IR Calibration Curve for SO_2 at 2500 cm^{-1} using Beer's Law.

TABLE D-5. Least Square Fitting of IR Calibration of SO_2 at 2506 cm^{-1}

```
X STANDS FOR RECORDER MEASURED PEAK HEIGHT (ABSORBANCE)
Y STANDS FOR MEASURED PRESSURE (CM HG)


THE COFFICIENTS OF THE POLYNOMIAL ARE$

      A0=       0.14848

      A1=     63.41037



                      REGENERATED DATA

X MEASURED        Y OBSERVED        Y CALCULATED      PCT ERROR

     0.106             6.958             6.914           0.627

     0.139             9.040             8.962           0.856

     0.178            11.356            11.435           0.700

     0.195            12.514            12.513           0.003

     0.271            17.233            17.332           0.578

     0.331            21.101            21.137           0.172

     0.401            25.670            25.576           0.366


VARIANCE           =  0.005719

STANDARD DEVIATION V   0.075627

MAXIMUM PCT ERROR   =  0.856977
```

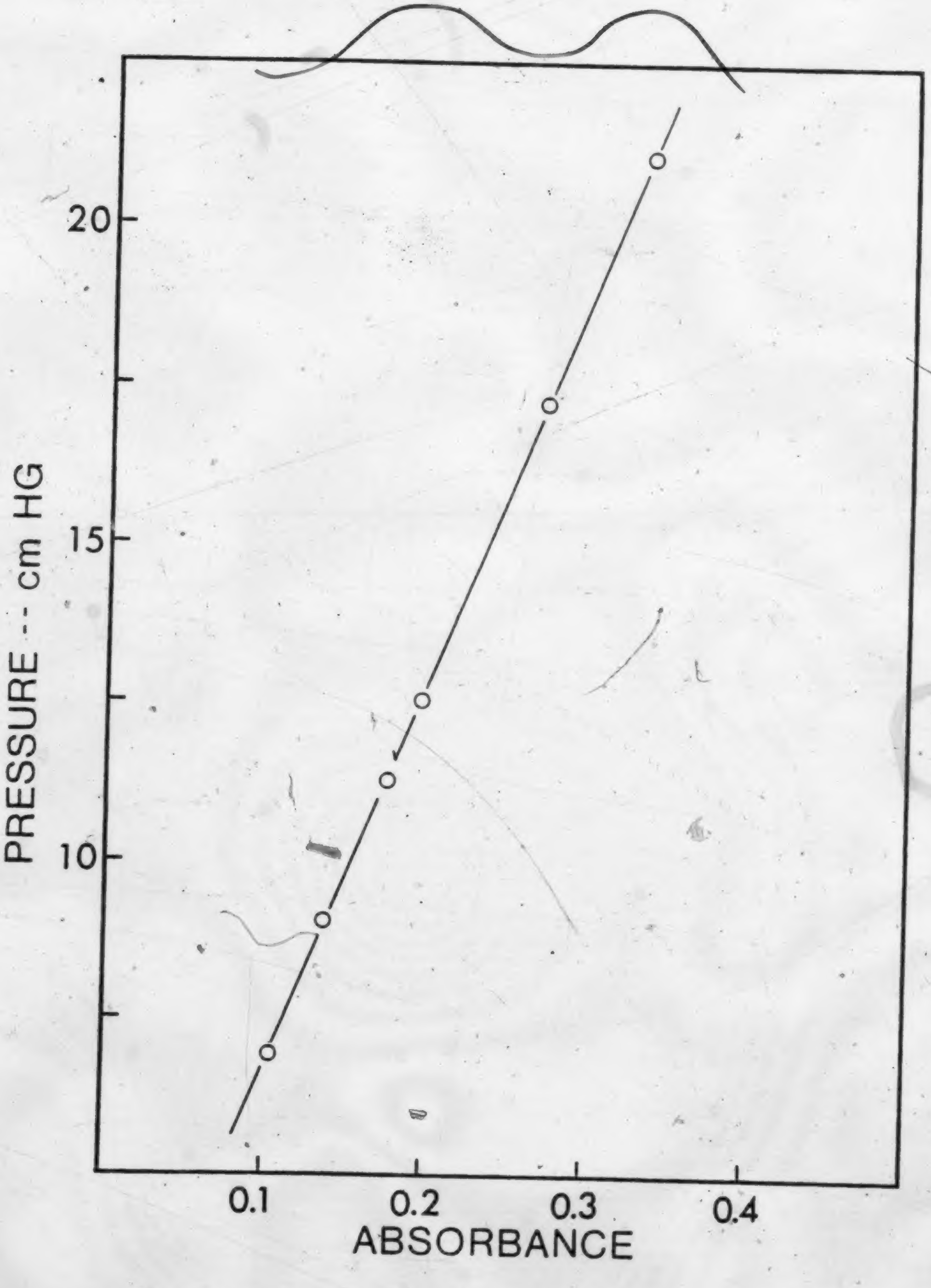

Figure D-6. IR Calibration Curve for SO_2 at 2506 cm^{-1} using Beer's Law.

TABLE D-6. Least Square Fitting of IR Calibration of SO_2 at 2485 cm^{-1}

```
X STANDS FOR RECORDER MEASURED PEAK HEIGHT (ABSORBANCE)
Y STANDS FOR MEASURED PRESSURE (CM HG)


THE COFFICIENTS OF THE POLYNOMIAL ARES

      A0=      0.05961

      A1=     91.56909



                        REGENERATED DATA
X MEASURED          Y OBSERVED        Y CALCULATED     PCT ERROR
    0.028             2.650              2.623            0.997
    0.040             3.659              3.722            1.732
    0.057             5.227              5.288            1.171
    0.075             6.958              6.927            0.441
    0.098             9.040              9.042            0.028
    0.136            12.514             12.513            0.007
    0.159            14.579             14.619            0.275
    0.186            17.233             17.091            0.821
    0.279            25.670             25.607            0.243
    0.361            33.021             33.116            0.287

VARIANCE         =  0.004889

STANDARD DEVIATION V  0.069926

MAXIMUM PCT ERROR  =  1.732226
```

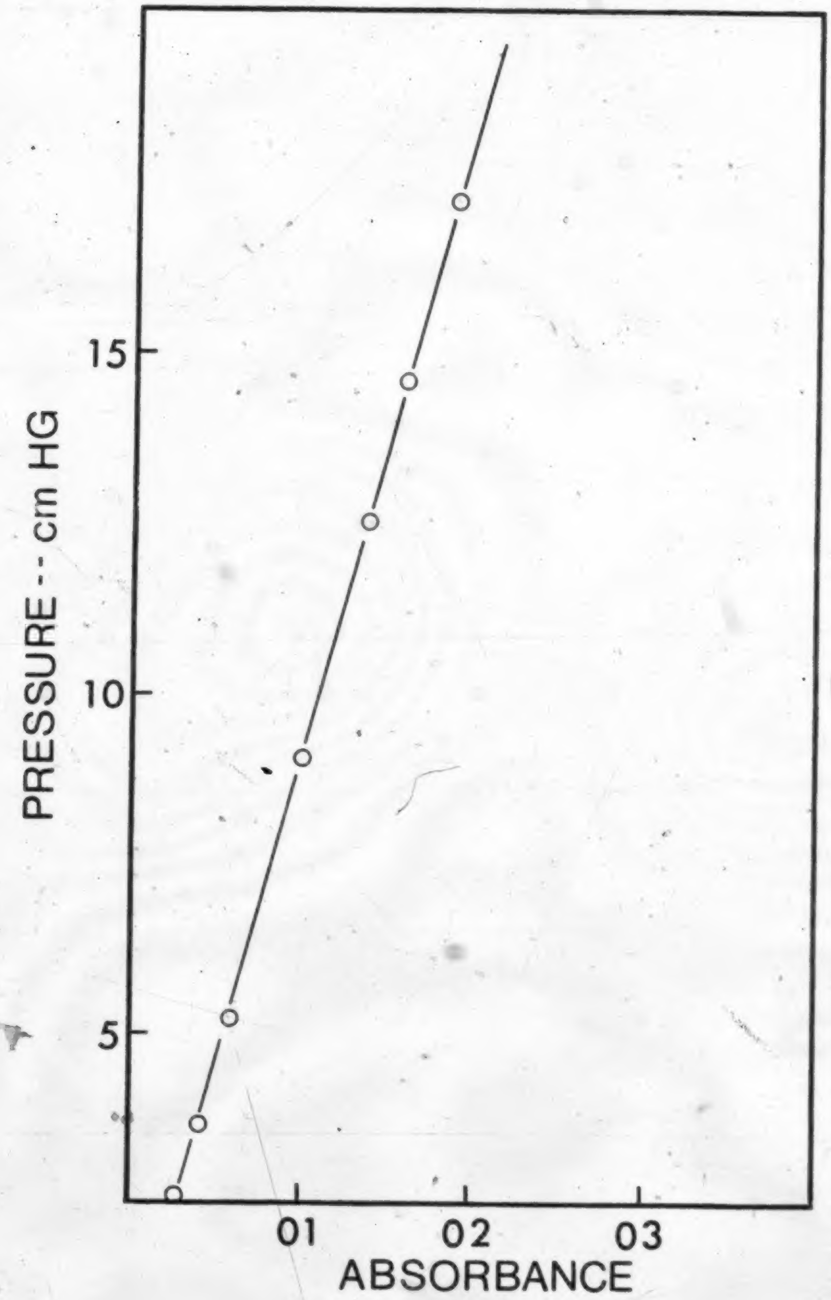

Figure D-7. IR Calibration Curve for SO_2 at $2485\ cm^{-1}$ using Beer's Law.

TABLE D-7. Least Square Fitting of IR Calibration of SO_2 at 1162 cm^{-1}

```
X STANDS FOR RECORDER MEASURED PEAK HEIGHT (ABSORBANCE)
Y STANDS FOR MEASURED PRESSURE (CM HG)


THE COFFICIENTS OF THE POLYNOMIAL ARE$

      A0=      -0.06971

      A1=      17.62653


                       REGENERATED DATA
X MEASURED        Y OBSERVED      Y CALCULATED    PCT ERROR
     0.075            1.231           1.255           2.014
     0.124            2.081           2.115           1.680
     0.154            2.650           2.644           0.197
     0.214            3.659           3.702           1.184
     0.295            5.227           5.130           1.853
     0.398            6.958           6.945           0.177
     0.517            9.040           9.043           0.035
     0.712           12.514          12.480           0.268
     0.984           17.233          17.274           0.242


VARIANCE        =   0.002021

STANDARD DEVIATION V  0.044963

MAXIMUM PCT ERROR  =  2.014337
```

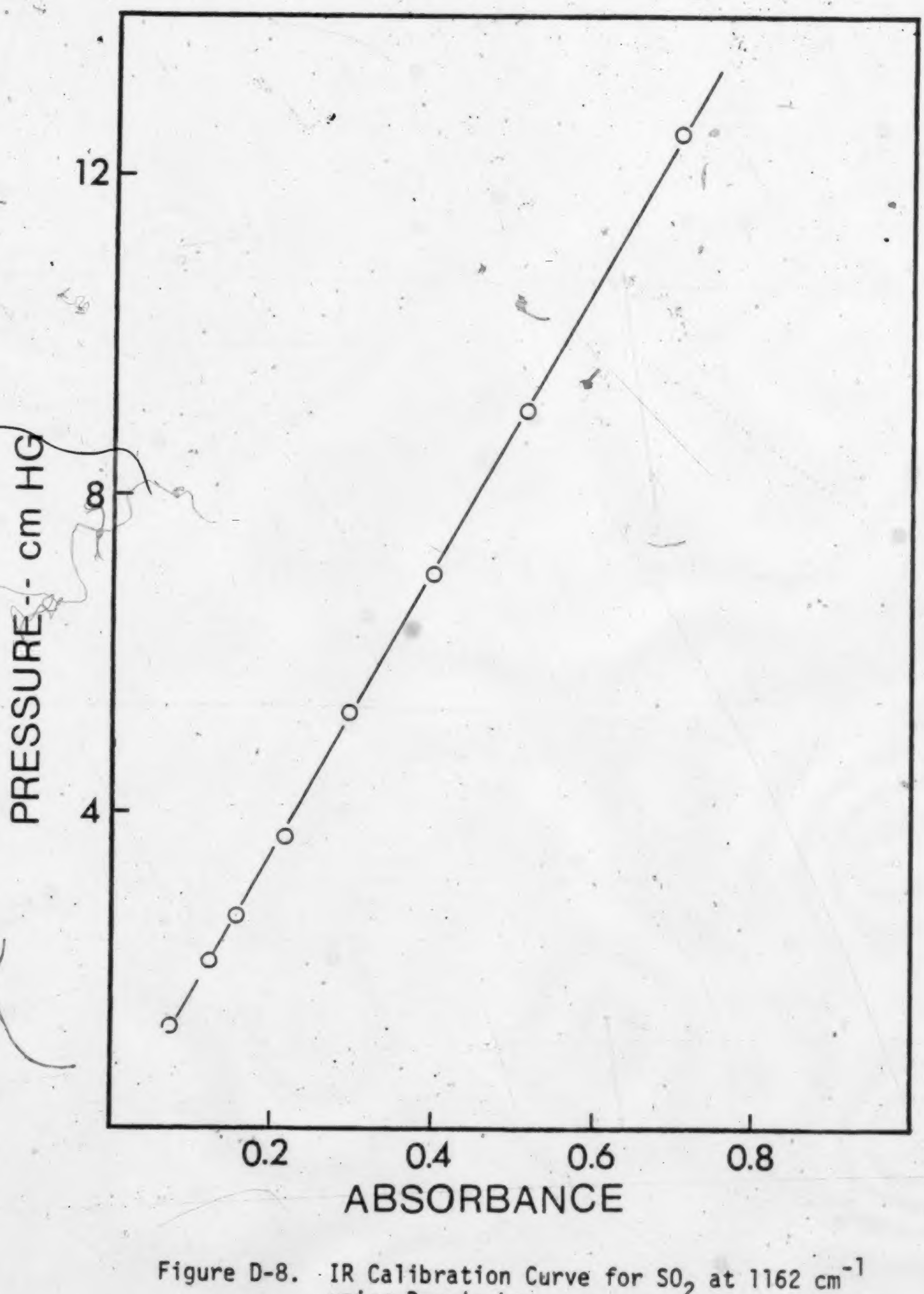

Figure D-8. IR Calibration Curve for SO_2 at 1162 cm^{-1} using Beer's Law.

TABLE D-8. Least Square Fitting of IR Calibration of SO_2 at 1132 cm^{-1}

```
X STANDS FOR RECORDER MEASURED PEAK HEIGHT (ABSORBANCE)
Y STANDS FOR MEASURED PRESSURE (CM HG)


THE COFFICIENTS OF THE POLYNOMIAL ARE$

     A0=      -0.03229

     A1=      19.53224


                        REGENERATED DATA
X MEASURED        Y OBSERVED        Y CALCULATED      PCT ERROR
    0.065            1.231             1.241            0.828
    0.109            2.081             2.096            0.755
    0.139            2.650             2.682            1.233
    0.189            3.659             3.659            0.008
    0.266            5.227             5.163            1.219
    0.357            6.958             6.940            0.248
    0.463            9.040             9.011            0.319
    0.586           11.356            11.413            0.507
    0.642           12.514            12.507            0.052

VARIANCE          =  0.001246

STANDARD DEVIATION V  0.035307

MAXIMUM PCT ERROR  =  1.233335
```

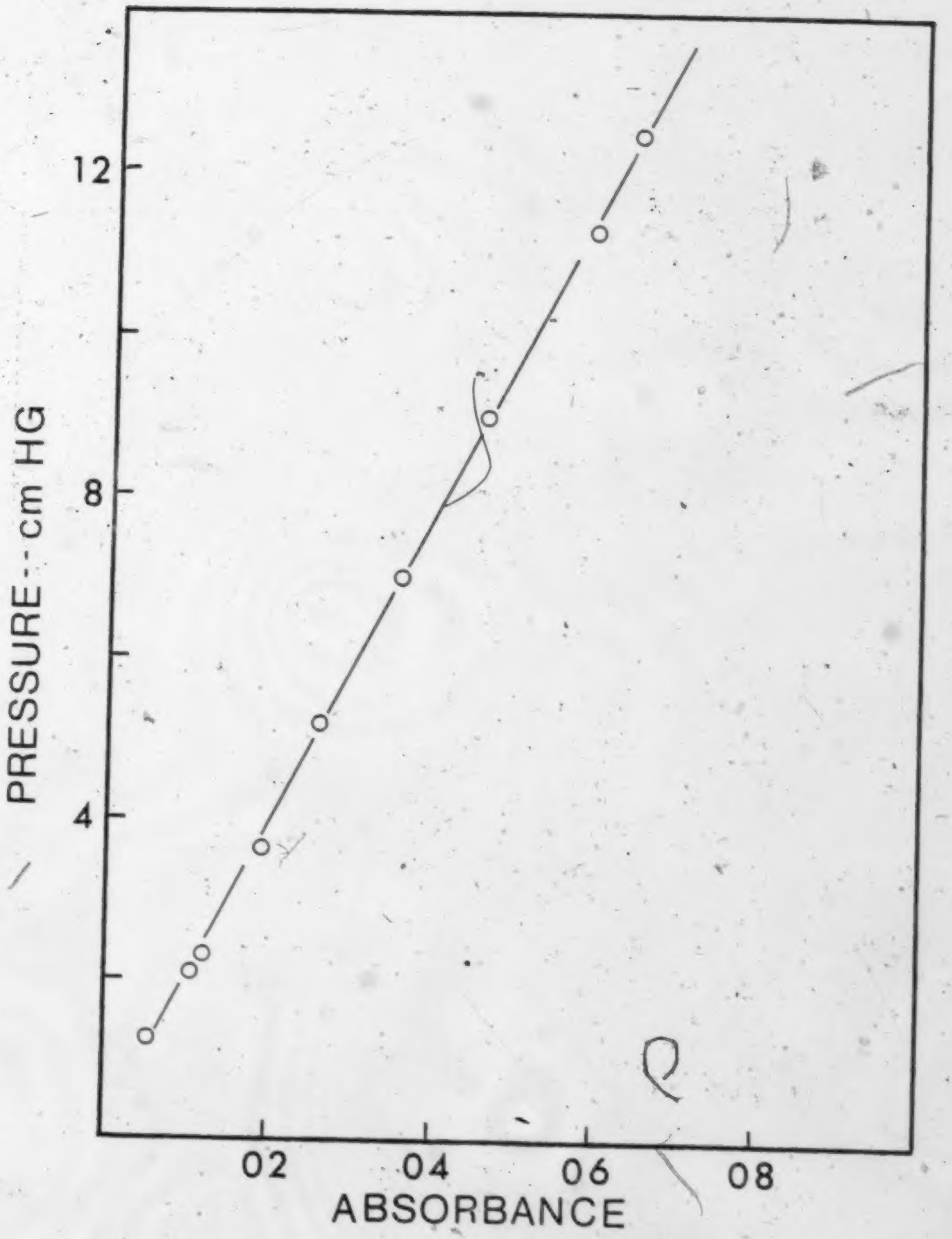

Figure D-9. IR Calibration Curve for SO_2 at 1132 cm^{-1} using Beer's Law.

E. CALIBRATION OF SULFUR FEED SYSTEM

It was not practical to use the syringe mentioned in Appendix C for introducing sulfur into the feed system of the reactor. The reasons are two fold. First it is difficult to heat and operate the syringe at temperatures above the sulfur dew point. Second, it would be almost impossible to separate the piston from the cylinder if the syringe containing sulfur is allowed to cool to room temperature. Moreover, introducing sulfur into the syringe and accurate recording of sulfur fed would be quite complicated. As a result, other means of introducing sulfur into the feed system of the reactor was necessary.

In the present work, a method that involved the bubbling of an inert carrier gas (N_2) into a reservoir of molten sulfur and hence carrying the sulfur vapor into the feed system of the reactor was employed. By maintaining the molten sulfur reservoir at different temperatures, various amounts of sulfur could be introduced.

A schematic sketch of the apparatus used for such service together with its calibration equipment is shown in Figure E-1. All material of fabrication except that of the flasks and burette were of 316 stainless steel. All lines before the cold traps as well as the sulfur reservoir were wound with nichrome heating wire. The distance from the tip of the tube below valve A to the molten sulfur level was kept constant. Cold trap A was used before calibration started and cold trap B was employed to trap sulfur during calibration. The sulfur reservoir temperature was measured by a thermocouple. The soap bubble meter was used to measure the flow rate of inert gas.

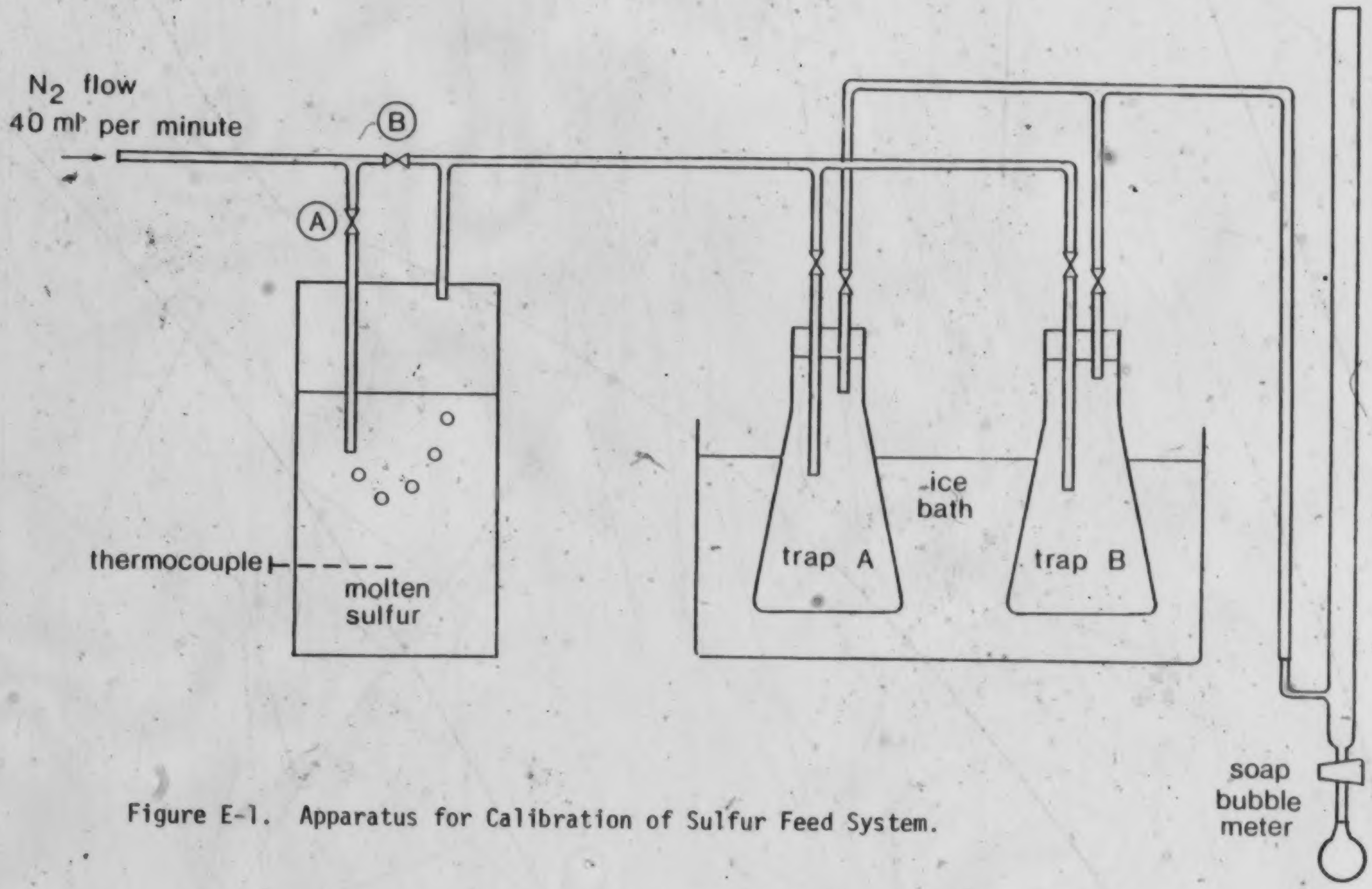
N_2 flow
40 ml per minute
B
A
thermocouple
molten sulfur
ice bath
trap A
trap B
soap bubble meter

Figure E-1. Apparatus for Calibration of Sulfur Feed System.

Before a calibration started, cold trap B was dried and weighed and the ice bath was empty. To start a calibration, the apparatus was set up as shown in Figure E-1. Valve A was closed while valve B was opened to allow inert gas to by-pass the sulfur reservoir. The inert gas was allowed to purge trap B thoroughly free of water and air. While doing so, the inert gas flow rate was adjusted to 40 ml/min. After 1 h of purging, the two valves on trap B were closed while those on trap A were opened, thus diverting the inert gas flow. The power supply to the sulfur reservoir and all nichrome wires were turned on. When the sulfur reservoir temperature reached 200°C, valve B was closed while valve A was opened to allow inert gas to bubble into molten sulfur and then into cold trap A. This bubbling was continued for 1/2 h and then if the inert gas flow rate remained unchanged, the gases exit from the sulfur reservoir was diverted from cold trap A to cold trap B. As soon as the valves on cold trap B were opened, time count was started. One hour later, the flow was diverted from cold trap B back to A again. The cold trap B containing sulfur was removed and weighed and the increase in weight represented the amount of sulfur trapped.

Similar runs were repeated at various sulfur reservoir temperatures (250°C, 300°C and 350°C). The calibrated results are summarized in Table E-1 and plotted in Figure E-2. Since only one flow rate of inert gas was employed in the whole calibration process, the same 40 ml/min inert gas flow through the sulfur reservoir also used for feeding sulfur into the system during the experimental runs of the present work.

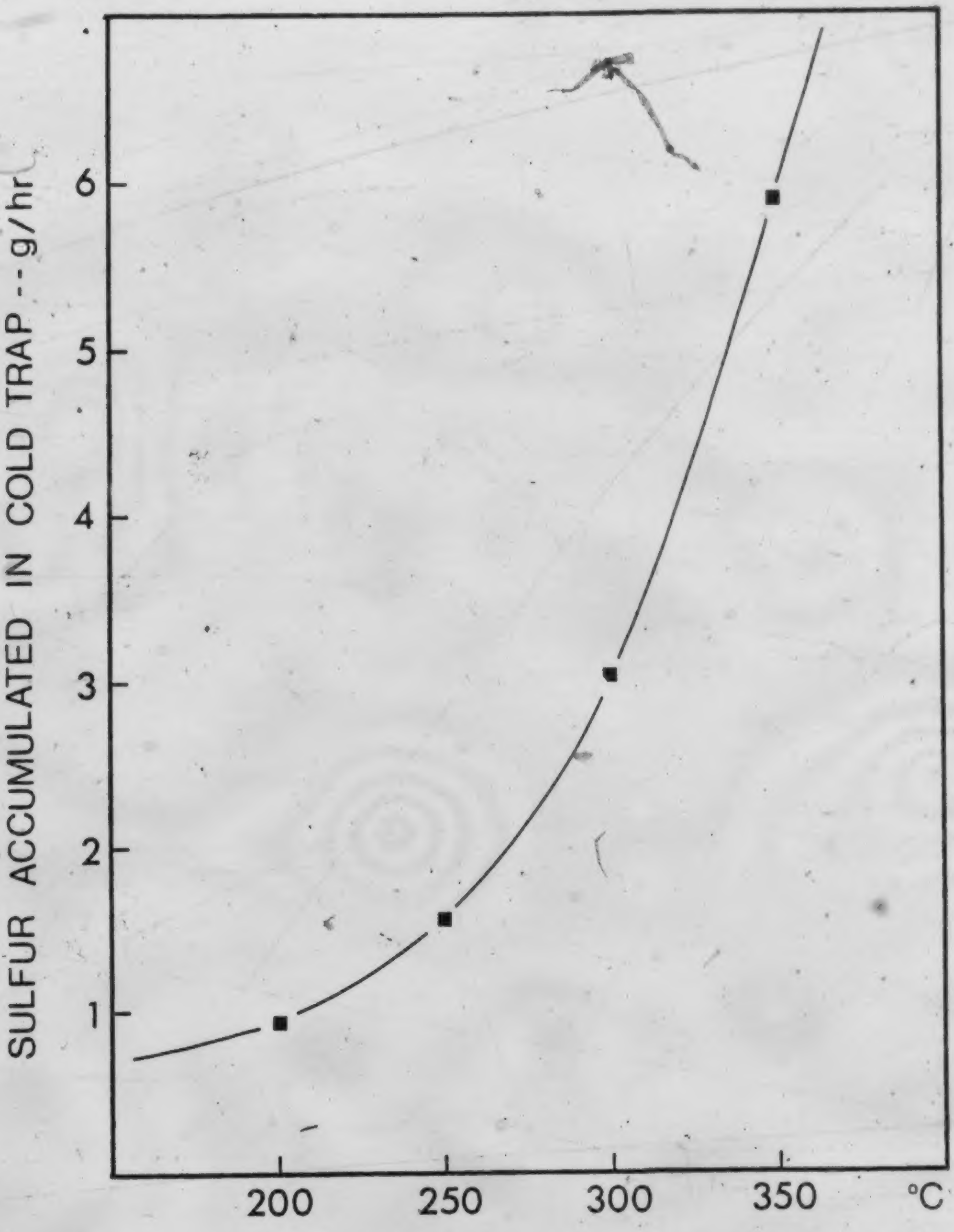

Figure E-2. Calibration Curve for Sulfur Feed System.

Table E-1

Calibrated Results for Sulfur Feed System

(with 40 ml/min N_2 through sulfur reservoir)

Temperature (°C)	Amount of Sulfur Accumulated (gm/hr)
200	0.9121
250°C	1.5430
300°C	3.0157
350°C	5.8437

F. MASS TRANSFER LIMITATIONS

F.1 Film Diffusion

The theoretical calculation for examining film-diffusion limitation is shown below:

If $N_i = K_G P_i$ is much larger than the reaction rate then film-diffusion is not the limitation

where K_G can be calculated by

$$K_G = \frac{j_D \, G_m}{P} \, N_{Sc}^{2/3} \qquad \text{(F.1)}$$

j_D can be found from the plot of j_D versus N_{Re} [125]

The kinetic run T6CC5 was chosen for examination of film-diffusion limitation because it has high r_{H_2S}/P_{H_2S} value and low P_{H_2S} value and the numbers used for such calculation are shown in Table F-1.

Table F-1

Results for Theoretical Estimation of Mass Transfer Coefficient

d_p (cm) - particle diameter	2.54
G_m (g-mol/s cm^2)	0.0067
N_{Re} - Reynolds number	183.2
N_{Sc} - Schmidt number	1.252
j_D	0.137
P (atm) - total pressure	1.0
P_{H_2S} (mm Hg)	10.07

Using the data in Table F-1 and equation (F.1), the value of K_G was calculated to be 0.00082 g-mol/s cm^2 atm. This value is rather high for the type of system under investigation. A more realistic value should be about half i.e. 0.0004 g-mol/s cm^2 atm. With this value, then,

$$N_i = K_G P_i = 0.0004 \times 10.07/760$$
$$= 5.3 \times 10^{-6} \text{ g-mol/s cm}^2$$

The values of the reaction rate and the external surface area of the catalyst are 2.4648 x 10^{-5} g-mol/g s and 10.22 cm^2/g. Therefore,

$$r_{H_2S}/A_E = \frac{2.4648 \times 10^{-5}}{10.22} \times 0.1036$$
$$= 0.25 \times 10^{-6} \text{ g-mol/s cm}^2$$

where 0.1036 is the weight of the catalyst in gram.

The above results show that the possible diffusion flux is about 21 times as rapid as the flux required to sustain the surface reaction, and hence the kinetic run T6CC5 was probably not film-diffusion controlled. Since the reaction conditions of run T6CC5 had the highest chance of film-diffusion rate controlled, the problem of film-diffusion limitation could probably be theoretically ignored in the present work.

F.2 Pore Diffusion

F.2.1 Pore Diffusion Limitation in McGregor's Work

McGregor [84] used the following Hudgin's criterion [59] to investigate the significance of pore diffusion in his study of the kinetics of Claus reaction

$$\text{If} \quad \frac{L_r^2}{D_{eff}} < \frac{1}{r'_{(C_o)}} \quad \text{, then pore diffusion is insignificant.} \qquad (F.2)$$

$$\text{where} \quad \cancel{r'}_{(C_o)} = \frac{(\rho_p)(k_1)(\text{Exp } F^1)(RT_a)(P_A)^{m+n-1}}{(3600)\ (2^n)} \qquad (F.3)$$

The data used and the results calculated by McGregor are summarized in the first column of Table F-2. McGregor omitted the porosity (θ) and tortuosity (τ) factors in his calculation of effective diffusivity D_{eff}. According to Hudgin's criterion, the pore diffusion limitation was theoretically significant in his work. McGregor's calculations were repeated in the present work using the values of porosity and tortuosity factors of an γ-alumina catalyst [125] with pore radius of 96 Å (closest to that used in the present work), but different results were obtained as exhibited in the second column of Table F-2. According to the results obtained here, the pore diffusion limitation should actually be theoretically insignificant in McGregor's work. However, without the true values of porosity and tortuosity factors for McGregor's catalyst, it would be difficult to conclude whether pore-diffusion limitation was significant in McGregor's work. An increase in the value of tortuosity and/or a decrease in the value of porosity can easily change the results listed in Table F-2.

TABLE F-2

Results of McGregor's Theoretical Pore Diffusion Limitations Calculation

		McGregor's work	This Work
e	Å	84	84
p	g-catalyst/cm^3	2.55	2.55
k_1	$\frac{(\text{g-mol } H_2S)(\text{mm Hg})^{m-n}}{(\text{h})\ (\text{g-catalyst})}$	2.198	1.128*
L_r	cm	0.0255	0.0255
m		0.963	0.828*
n		0.359	0.467
Exp F1		exp (-7589/ 1.98x533)	exp (-7440/ 1.98x533)*
R	$\frac{(\text{mm Hg})(\text{cm}^3)}{(\text{g-mol})(°\text{K})}$	82.057 x 760	82.057 x 760
T_a	K	533	533
r (Co)	sec^{-1}	92.0	44.86*
1/r (Co)	sec	0.011	0.0223*
D_{eff}	cm^2/sec	0.032	0.031
$L_r^2\ /D_{eff}$	sec	0.203	0.0213
θ			0.812**
τ_m			0.850**

Where * represents the values calculated by using rate equation developed from McGregor's rate data by Dalla Lana et al. [29]

** represents values obtained from the alumina (pore radius 96Å) in Table 1.9 [125]

The value of D_{eff} in Table F-2 was calculated from equation (F.4)

$$D_{eff} = 9700\ r_e\ \frac{Ta}{M} \qquad (F.4)$$

The pore diameter of 84Å and molecular weight of 34 were used for the above equation.

F.2.2 Pore Diffusion Limitations in the Present Work

After examining McGregor's work, kinetic data with the highest possibliity of pore diffusion rate-controlled in the present work were used to investigate the theoretical significance of pore diffusion. Two methods were used for such investigation. The first is according to Hudgin's criterion and is the same as that used by McGregor. The second is to examine whether concentration gradient existed within the alumina catalyst wafer by estimating the effectiveness factor; η (the ratio of the actual rate to the rate which would be observed in the absence of diffusion limitations), as reported by Satterfield [125] and used by Chuang [23].

F. 2.2.1 Pore Diffusion Limitation According Hudgin's Method

The data and results of the three kinetic runs in this work to determining the theoretical pore diffusion limitation are summarized in Table F-3. According to Hudgin's criterion, pore diffusion was not significant in all three runs. The values of porosity and tortuosity used in Table F-3 are different from those in Table F-2. According to the list by Satterfield [125] the smallest porosity and largest tortuosity for catalysts with pore radius larger than 60 Å are 0.52 and 3.8 respectively. Even with these values, the calculated $1/r_{(Co)}$ will still be larger than Lr^2/D_{eff}. Therefore according to Hudgin's criterion, pore diffusion limitation is theoretically insignificant in the three kinetic runs of this work.

TABLE F-3

Results of Theoretical Pore Diffusion

Limitations Calculated by Hudgin's Method

	Run No.		
	T4CA4	T5CG1	T6CC3
d_e	84	84	84
ρ_p	2.55	2.25	2.27
k_1 Exp F1	2.56×10^{-7}	3.62×10^{-7}	4.86×10^{-7}
T_a	535	571	596
L_r	0.00900	0.00876	0.00826
m	1	1	1
n	0.5	0.5	0.5
R	82.057 x 760	82.057 x 760	82.057 x 760
θ	0.5	0.5	0.5
τ_m	1.4	1.4	1.4
$r'(Co)$	55.6	100.6	94
$1/r'_{(Co)}$	0.018	0.0099	0.0106
D_{eff}	0.0100	0.0104	0.0106
L_r^2/D_{eff}	0.008	0.0078	0.0076

F.2.2.2 Pore Diffusion Limitations by Estimation of Effectiveness Factor Method

The detail description on the method of estimating effectiveness factor for the determination of theoretical pore diffusion limitations has been reported by Satterfield [125] and an example for such calculation has been given by Chuang [23]. Therefore these will not be repeated here. Briefly, the following parameter values are required:

$$D_A = 9700 \cdot \gamma_e \cdot (T_a/M)^{1/2} \qquad (F.5)$$

$$\Phi_L = \frac{Lc^2}{D_A} \; (-r_A)/C_A \qquad (F.5)$$

$$K = [K_A - D_A \; {}_i(K_i \, \upsilon_i/D_i)]/w \qquad (F.6)$$

and

$$w = 1 + {}_i \, K_i \; (P_i + (P_A \, \upsilon_i \, D_A/D_i)] \qquad (f.7)$$

The terms within the expression for D_A, Φ_L, K and w are defined as follows:

D_A = effective diffusivity of reactant based on Knudson diffusion within the pores, cm^2/sec

γ_e = pore radius, cm

T_a = absolute temperature, °K

M = molecular weight

Φ_L = Thiele diffusion modulus squared

$-r_A$ = the observed reaction rate, g-mole/sec. c.c. of catalyst

L_c = ratio of the catalyst volume to outside surface area through which reactant has access, cm

K, w = parameters used to evaluate η

i = subscript for species other than reactant A

υ = stoichiometric coefficient

C_A = concentration of the reactant, g-mole/c.c.

By using the data from kinetic run T6CC5, the calculation results are shown below:

$$D_{eff} = 9700 \times 84 \times 10^{-8} \times \left(\frac{596}{34}\right)^{1/2} \times \frac{0.5}{1.4} = 0.01134$$

$$L_c = \frac{2.54^2}{4} \times 0.00826 \quad \left(\frac{2.54^2}{2} + 2.54 \times 0.00826\right)$$

$$= 0.00413$$

$$= \frac{0.00413}{0.0315} \left(\frac{1.2363 \times 10^{-5}}{10.07}\right) \times 760 \times 82.06 \times 596$$

$$= 0.025$$

Using the above results and from figure 4.3 and 4.4 in Satterfield, the effectiveness factor approaches unity even for the extremely high adsorption component (and even the highest tortuosity and lowest porosity for catalysts with pore size larger than 60 Å listed by Satterfield were used) and this means that the pore diffusion limitation is theoretically insignificant.

According to the results obtained from the calculations by using Hudgin's and the effectiveness factor method, it could be assumed that pore-diffusion limitation was theoretically insignificant in this work because the runs chosen for the calculation had highest possibility of pore-diffusion rate-controlled.

G. PUMP PERFORMANCE AND CHARACTERISTIC CHECK

The performance and characteristic of the recirculation pump were evaluated by using a set-up shown in Figure G.1. The pump was tested under two modes; namely open flow mode and recycle flow mode. Under each mode, a stop watch was used to measure the time elapsed for a flow of 2 cubic feet through the dry test meter. The choice of 2 cubic feet was arbitrary and was only based on convenience so that excessive time was not required for each measurement yet long enough to provide reasonable accuracy. The pressure difference across the recirculation pump was measured by mercury manometer. For the sake of simplicity throughout the test, only atmospheric air and not the gaseous mixture employed in the present research was used. The readings on the pump speed control dial were used to represent the reciprocating speeds of the pump piston. No attempt was made to count the actual number of reciprocation per unit time for each dial setting.

The performance data is tabulated in Table G-1 and the curves are depicted in Figure G-2. The flow rate under recycle flow mode was always lower than that under open flow mode. The pressure on the pump discharge was not varied since it was felt that the reactor recycle loop including the catalyst bed would offer less resistance to flow than the dry test meter used in this experiment. The pump was then allowed to run for more than 12 hours continuously and the performance test repeated. It was found that the repeatability was better than 98%.

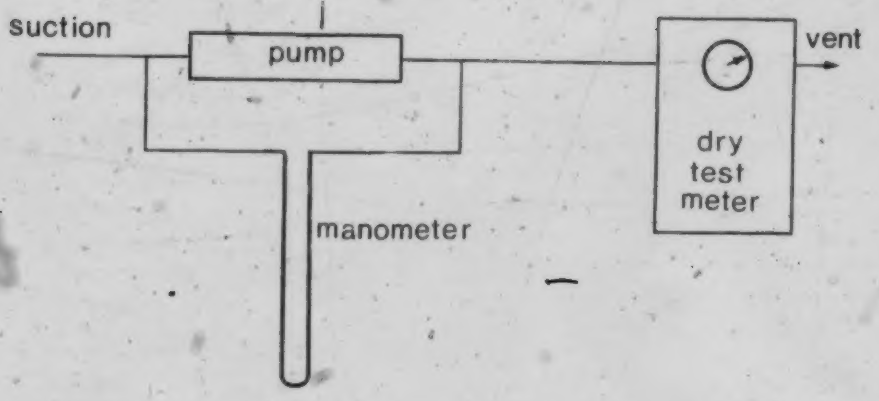
suction
pump
vent
dry
test
meter
manometer

open flow mode

recycle mode

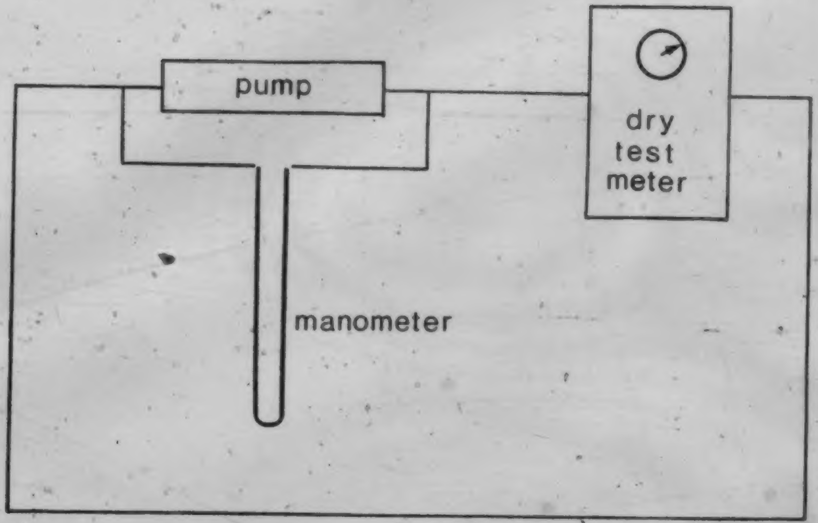
pump
dry
test
meter
manometer

Figure G-1. Apparatus for testing Pump Performance.

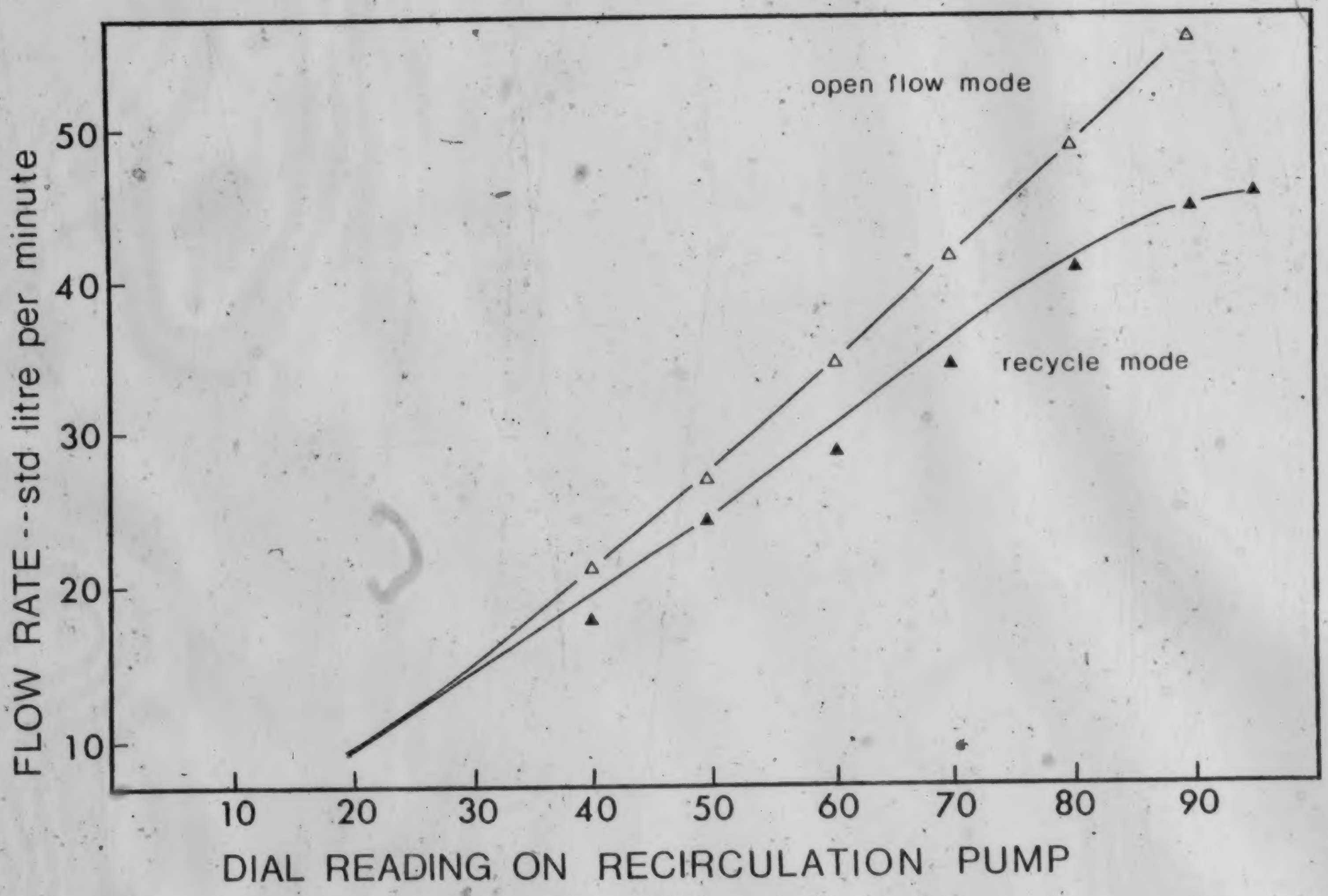

Figure G-2. Performance Curves for Recirculation Pump.

Table G.1

Performance Data for Recirculation Pump

Dial Reading	Open Flow Mode			Recycle Flow Mode		
	Time	Head	Flow Rate	Time	Head	Flow Rate
40	2.703	1.3	21.0	3.710	1.5	17.9
50	2.109	1.7	26.9	2.354	1.7	24.1
60	1.645	2.3	34.5	1.984	2.0	28.6
70	1.381	3.0	41.1	1.664	2.4	34.1
80	1.175	3.9	48.3	1.404	2.9	40.4
90	1.022	5.1	55.5	1.275	3.4	44.5
95				1.258		45.1

Atmospheric Pressure	702 millimeters of mercury
Atmospheric Temperature	22.0 degrees Centigrade

Time - number of minutes elapsed for the flow of two cubic feet of air through the dry test meter

Head - static pressure difference across the recirculation pump in centimeters of mercury at the entrance of the dry test meter

Flow Rate - standard litres per minute

H. SAMPLE DERIVATIONS OF RATE EQUATIONS

H.1 Reaction Mechanism Involving Dissociation of Adsorbed H_2S into Hydroxyl Groups

(1) $2H_2S + 2\# \rightleftharpoons 2H_2S.\#$

(2) $SO_2 + \# \rightleftharpoons SO_2.\#$

(3) $SO_2.\# + 2\# \rightleftharpoons S.\# + 2O.\#$

(4) $H_2S.\# + 2O.\# \rightleftharpoons S.\# + 2HO.\#$

(5) $H_2S.\# + 2HO.\# \rightleftharpoons S.\# + 2H_2O.\#$

(6) $2H_2O.\# \rightleftharpoons 2H_2O + 2\#$

(7) $3S.\# \rightleftharpoons 3/x\ S_x + 3\#$

where notations are identical to those given in Section 6.8.2. Assume surface reaction step (4) to be rate determining, then $-r_{H_2S} = r_4 - r_{-4}$ where subscripts refer to the reaction step numbers in the above reaction scheme with the negative sign on the subscript numbers to indicate the reverse reaction term. The other reaction steps are assumed to be in equilibrium and thus

$$K_1 = C_{H_2S.\#} / P_{H_2S}C_\# \tag{H.1}$$

$$K_2 = C_{SO_2.\#} / P_{SO_2}C_\# \tag{H.2}$$

$$K_3 = C_{S.\#}C^2_{O.\#} / C_{SO_2.\#}C^2_\# \tag{H.3}$$

$$K_5 = C_{S.\#}C^2_{H_2O.\#} / C_{H_2S.\#}C^2_{OH.\#} \tag{H.4}$$

$$K_6 = P_{H_2O}C_\# / C_{H_2O.\#} \tag{H.6}$$

$$K_7 = P_{S_x}^{1/x}\, C_\# \,/\, C_{S.\#} \qquad \text{(H.7)}$$

Now the total number of active sites # are assumed to be constant L Therefore

$$L = C_\# + C_{H_2S.\#} + C_{SO_2.\#} + C_{O.\#} + C_{OH.\#} + C_{S.\#} + C_{H_2O.\#} \qquad \text{(H.8)}$$

Substitute equations (H.1) to (H.7) into (H.8)

$$\begin{aligned} C_\# &= L/(1 + K_1P_{H_2S} + K_2P_{SO_2} + K_3K_2K_7\, P_{SO_2}^{1/2}/P_{S_x}^{1/2x} \\ &\quad + P_{S_x}^{1/2x}\, P_{H_2O}/K_6P_{H_2S}^{1/2}\; K_5K_1K_7 + P_{S_x}^{1/x}/K_7 + P_{H_2O}/K_6\,) \\ &= L/(1 + b_1P_{H_2S} + b_2P_{SO_2} + b_3P_{H_2O} + b_4P_{S_x}^{1/x} + b_5P_{SO_2}^{1/2}/P_{Sx}^{1/x} \\ &\quad + b_6P_{S_x}^{1/2x}P_{H_2O}/\, P_{H_2S}^{1/2}\,) \\ &= L/Y \end{aligned} \qquad \text{(H.9)}$$

The rate equation can be written as

$$\begin{aligned} -\, r_{H_2S} = -2r_{SO_2} &= r_4 - r_{-4} \\ &= k_4C_{H_2S.\#}C_{O.\#}^2 \;-\; k_{-4}C_{S.\#}C_{OH.\#}^2 \end{aligned}$$

$$= k_4L^3K_1P_{H_2S}K_2K_3P_{SO_2} \;/\; K_7P_{S_x}^{1/x}Y^3$$

$$- k_{-4}L^3P_{S_x}^{2/x}\;P_{H_2O}^2 \;/\; K_1K_6^2K_7^2\;P_{H_2S}Y^3$$

$$= b_{10}\,P_{H_2S}P_{SO_2} \;/\; P_{S_x}^{1/x}\;Y^3 \;-\; b_{-10}P_{S_x}^{2/x}\;P_{H_2O}^2\;/P_{H_2S}Y^3$$

Since the reverse reaction was negligible in the present research, the rate expression becomes

$$-r_{H_2S} \;=\; -2r_{SO_2} = b_{10}P_{H_2S}P_{SO_2} \;/\; P_{S_x}^{1/x}\;Y^3 \qquad (H.10)$$

which is the model HS4 in Table 6-7.

H.2 Reaction Mechanism Involving Adsorbed H_2S Reacting with Surface "Oxygen" and Hydroxyl Groups

(1) $2H_2S + 2\# \rightleftarrows 2H_2S.\#$

(2) $SO_2 + \# \rightleftarrows SO_2.\#$

(3) $SO_2.\# + 2\# \rightleftarrows S.\# + 2O.\#$

(4) $H_2S.\# + 2HO.\# \rightleftarrows 2H_2O.\# + S.\#$

(5) $H_2S.\# + O.\# \rightleftarrows H_2O.\# + S.\#$

(6) $H_2O.\# + O.\# \rightleftarrows 2HO.\#$

(7) $2H_2O.\# \rightleftarrows 2H_2O + 2\#$

(8) $3S.\# \rightleftarrows 3\# + 3/x\ S_x$

Again the notations are identical to those given in Section 6.8.2. Assume surface reaction step (5) to be rate determining, the rate expression can be written as

$$\begin{aligned} -r_{H_2S} &= -2r_{SO_2} \\ &= k_5 C_{H_2S.\#} C_{O.\#} - k_{-5} C_{H_2O.\#} C_{S.\#} \end{aligned} \qquad (H.11)$$

Thoe other steps are assumed to be in equilibrium and can be expressed in terms of equilibrium constants.

$$K_1 = C_{H_2S.\#} / P_{H_2S} C_{\#} \qquad (H.12)$$

$$K_2 = C_{SO_2.\#} / P_{SO_2} C_{\#} \qquad (H.13)$$

$$K_3 = C_{S.\#} C^2_{O.\#} / C_{SO_2.\#} C^2_{\#} \qquad (H.14)$$

$$K_4 = C^2_{H_2O.\#} C_{S.\#} / C_{H_2S.\#} C^2_{OH.\#} \qquad (H.15)$$

$$K_6 = C^2_{OH.\#} / C_{H_2O.\#} C_{O.\#} \qquad (H.16)$$

$$K_7 = P_{H_2O} C_{\#} / C_{H_2O.\#} \qquad (H.17)$$

$$K_8 = P^{1/x}_{S_x} C_{\#} / C_{S.\#} \qquad (H.18)$$

Thoe total number of active sites # are assumed to be constant L. Therefore

$$L = C_{\#} + C_{H_2S.\#} + C_{SO_2.\#} + C_{S\#} + C_{H_2O.\#} + C_{O.\#} + C_{OH.\#} \qquad (H.19)$$

Substitute equations (H.12) to (H.18) into (H.19)

$$C_{\#} = 1 / (1 + K_1 P_{H_2S} + K_2 P_{SO_2} + P_{H_2O}/K_7 + P_{S_x}^{1/x}/K_8$$
$$+ \quad K_2 K_3 K_7 \; P_{SO_2}^{1/2}/P_{S_x}^{1/2x} \; + P_{H_2O} P_{S_x}^{1/2x}/ \; K_7 \; K_4 K_1 K_8 P_{H_2S}^{1/2})$$
$$= L/Y \qquad (H.20)$$

Substitute equations (H.12) to (H.20) into equation (H.11), the rate expression becomes

$$-r_{H_2S} = -2r_{SO_2}$$
$$= k_5 C_{H_2S.\#} C_{O.\#} - k_{-5} C_{H_2O.\#} C_{S.\#}$$
$$= k_5 K_1 \; K_2 K_3 K_7 \; L^2 P_{H_2S} \; P_{SO_2}^{1/2}/ \; P_{S_x}^{1/2x} Y^2 \; - k_{-5} P_{H_2O} P_{S_x}^{1/x} / K_7 K_8 \; Y^2$$
$$= b_{11} P_{H_2S} P_{SO_2}^{1/2} \; / \; P_{S_x}^{1/2x} Y^2 - b_{-11} P_{H_2O} P_{S_x}^{1/x} \; / \; K_7 K_8 Y^2$$

Since the reverse reaction was found to be negligible, the final rate expression can be written as

$$-r_{H_2S} = -2r_{SO_2}$$
$$= b_{11} P_{H_2S} P_{SO_2}^{1/2} \; / \; P_{S_x}^{1/2x} \; Y^2$$

which is the model DOH5 in Table 6-8

TABLE H-1

CORRELATION RESULTS FOR MODEL DOH5' AGAINST VARIOUS ISOTHERMAL RATE DATA

Temperature (°C)	b_1	b_2	b_3	b_4	b_5	Variance
200.0	2.074×10^{-8}	9.011×10^{-6}	8.816×10^{-6}	3.563×10^{-3}	-2.134×10^{-1}	1.353×10^{-15}
	$\pm 1.669 \times 10^{-8}$	$\pm 1.003 \times 10^{-6}$	$\pm 5.093 \times 10^{-6}$	$\pm 2.967 \times 10^{-4}$	$\pm 1.014 \times 10^{-1}$	
212.3	6.503×10^{-8}	4.868×10^{-6}	5.780×10^{-7}	6.645×10^{-3}	-1.428×10^{-2}	2.999×10^{-19}
	$\pm 3.896 \times 10^{-10}$	$\pm 5.205 \times 10^{-6}$	$\pm 4.062 \times 10^{-6}$	$\pm 2.182 \times 10^{-5}$	$\pm 2.807 \times 10^{-3}$	
235.2	8.939×10^{-8}	-2.240×10^{-6}	4.000×10^{-5}	4.990×10^{-3}	-4.179×10^{-3}	2.077×10^{-17}
	$\pm 3.446 \times 10^{-9}$	$\pm 3.409 \times 10^{-5}$	$\pm 3.198 \times 10^{-5}$	$\pm 1.087 \times 10^{-4}$	$\pm 1.732 \times 10^{-2}$	
261.5	1.353×10^{-7}	-2.349×10^{-5}	8.492×10^{-6}	1.790×10^{-3}	-1.757×10^{-1}	4.589×10^{-15}
	$\pm 4.849 \times 10^{-9}$	$\pm 5.482 \times 10^{-5}$	$\pm 9.038 \times 10^{-5}$	$\pm 3.339 \times 10^{-5}$	$\pm 1.267 \times 10^{-2}$	
2.98.2	1.317×10^{-7}	-7.954×10^{-7}	-2.525×10^{-7}	5.657×10^{-3}	-1.543×10^{-2}	1.232×10^{-18}
	$\pm 3.145 \times 10^{-10}$	$\pm 4.372 \times 10^{-6}$	$\pm 3.469 \times 10^{-6}$	$\pm 7.641 \times 10^{-6}$	$\pm 1.055 \times 10^{-3}$	

TABLE H-1 (Continued)

Temperature (°C)	b_1	b_2	b_3	b_4	b_5	Variance
323.0	2.709×10^{-7}	4.959×10^{-7}	2.368×10^{-6}	4.420×10^{-3}	-1.612×10^{-2}	1.363×10^{-18}
	$\pm 6.442 \times 10^{-10}$	$\pm 3.56 \times 10^{-6}$	$\pm 4.267 \times 10^{-6}$	$\pm 5.712 \times 10^{-6}$	$\pm 9.914 \times 10^{-4}$	

TABLE H-2

CORRELATION RESULTS FOR MODEL DS06' AGAINST VARIOUS ISOTHERMAL RATE DATA

Temperature (°C)	b_1	b_2	b_3	b_4	b_5	Variance
200.0	2.054×10^{-8} $\pm 1.083 \times 10^{-8}$	8.998×10^{-4} $\pm 1.123 \times 10^{-3}$	3.734×10^{-4} $\pm 5.969 \times 10^{-4}$	2.986×10^{-3} $\pm 7.107 \times 10^{-4}$	-2.748×10^{-1} $\pm 1.454 \times 10^{-1}$	4.106×10^{-15}
212.3	6.306×10^{-8} $\pm 3.385 \times 10^{-9}$	1.485×10^{-5} $\pm 3.101 \times 10^{-5}$	1.047×10^{-5} $\pm 2.425 \times 10^{-5}$	4.193×10^{-3} $\pm 8.674 \times 10^{-5}$	-1.754×10^{-2} $\pm 1.671 \times 10^{-2}$	2.624×10^{-17}
235.2	9.145×10^{-8} $\pm 4.025 \times 10^{-9}$	-3.919×10^{-6} $\pm 2.604 \times 10^{-5}$	2.350×10^{-5} $\pm 2.438 \times 10^{-5}$	3.194×10^{-3} $\pm 5.662 \times 10^{-5}$	5.585×10^{-3} $\pm 1.331 \times 10^{-2}$	2.850×10^{-17}
261.5	1.357×10^{-7} $\pm 5.188 \times 10^{-9}$	-1.748×10^{-5} $\pm 3.927 \times 10^{-5}$	4.477×10^{-6} $\pm 6.440 \times 10^{-5}$	1.241×10^{-3} $\pm 2.066 \times 10^{-5}$	-1.202×10^{-1} $\pm 9.689 \times 10^{-3}$	4.663×10^{-15}
298.2	1.317×10^{-7} $\pm 3.145 \times 10^{-10}$	5.581×10^{-6} $\pm 1.119 \times 10^{-4}$	4.145×10^{-6} $\pm 8.641 \times 10^{-5}$	1.018×10^{-2} $\pm 1.229 \times 10^{-3}$	-1.609×10^{-2} $\pm 2.279 \times 10^{-3}$	1.934×10^{-16}

TABLE H-2 (Continued)

Temperature (^{o} C)	b_1	b_2	b_3	b_4	b_5	Variance
323.0	2.737×10^{-7}	4.268×10^{-6}	1.529×10^{-5}	2.846×10^{-3}	-6.961×10^{-3}	1.576×10^{-16}
	$\pm 6.856 \times 10^{-9}$	$\pm 2.504 \times 10^{-5}$	$\pm 2.984 \times 10^{-5}$	$\pm 2.741 \times 10^{-5}$	$\pm 7.035 \times 10^{-3}$	

TABLE H-3

CORRELATION RESULTS FOR MODEL DSOH6' AGAINST VARIOUS ISOTHERMAL RATE DATA

Temperature (^{o} C)	b_1	b_2	b_3	b_4	b_5	Variance
200.0	4.334×10^{-8} $\pm 3.020 \times 10^{-8}$	1.921×10^{-3} $\pm 1.904 \times 10^{-3}$	7.756×10^{-4} $\pm 1.062 \times 10^{-3}$	6.072×10^{-3} $\pm 2.443 \times 10^{-3}$	-1.088×10^{-1} $\pm 3.466 \times 10^{-1}$	3.854×10^{-15}
212.3	3.005×10^{-7} $\pm 3.677 \times 10^{-8}$	-4.993×10^{-6} $\pm 1.072 \times 10^{-4}$	1.167×10^{-5} $\pm 8.28] \times 10^{-5}$	1.494×10^{-2} $\pm 9.518 \times 10^{-4}$	1.109 $\pm 1.260 \times 10^{-1}$	2.473×10^{-17}
235.2	3.119×10^{-7} $\pm 1.677 \times 10^{-7}$	8.033×10^{-5} $\pm 3.153 \times 10^{-4}$	-8.331×10^{-5} $\pm 2.944 \times 10^{-4}$	4.821×10^{-3} $\pm 9.808 \times 10^{-4}$	5.382×10^{-1} $\pm 2.579 \times 10^{-1}$	1.718×10^{-15}
261.5	3.406×10^{-7} $\pm 2.095 \times 10^{-8}$	-2.470×10^{-5} $\pm 9.352 \times 10^{-5}$	8.383×10^{-6} $\pm 1.551 \times 10^{-4}$	3.099×10^{-3} $\pm 8.467 \times 10^{-5}$	3.096×10^{-1} $\pm 3.657 \times 10^{-2}$	4.656×10^{-15}
298.2	6.188×10^{-7} $\pm 8.542 \times 10^{-8}$	6.841×10^{-5} $\pm 2.461 \times 10^{-4}$	3.592×10^{-5} $\pm 1.946 \times 10^{-4}$	1.251×10^{-2} $\pm 9.091 \times 10^{-4}$	1.125 $\pm 1.397 \times 10^{-1}$	7.827×10^{-16}

TABLE H-3 (Continued)

Temperature (° C)	b_1	b_2	b_3	b_4	b_5	Variance
323.0	1.131×10^{-6}	-1.348×10^{-6}	1.118×10^{-5}	9.534×10^{-3}	1.003	6.706×10^{-16}
	$\pm 1.301 \times 10^{-7}$	$\pm 1.708 \times 10^{-4}$	$\pm 2.054 \times 10^{-4}$	$\pm 5.666 \times 10^{-4}$	$\pm 1.065 \times 10_{-1}$	

I. DATA REDUCTION

The ideal gas law is inherent in the data reduction calculation procedure and the validity of its use has been verified by McGregor [84] whose experimental conditions were similar to those in the present work. The kinetic run No. T1CA1 (Table I-2) was chosen to demonstrate how the rate data was obtained by the data reduction procedure. The measured data of this kinetic run is summarized as follows

GC Area Ratio

$A_{H_2S}/A_{N_2} = 0.99$

$A_{SO_2}/A_{N_2} = 0.80$

IR Absorbance of SO_2 at 1357.8 cm^{-1}

$A_\lambda = 0.683$

Room Temperature = 22° C
Reactor Temperature = 200° C
Atmospheric Pressure = 703 mm Hg
Reactor Pressure = 806 mm Hg
Nitrogen Flow Rate = 99.38 ml/min
Catalyst Weight = 0.1036 g
Conversion of SO_2. = 17.64 %
Molecular volume of N_2 at standard condition = 22.4 l/g-mol

By applying the GC calibration results in Appendix A to the measured GC area ratio, the following molar ratio's are obtained

$$M_{H_2S}/M_{N_2} = 0.0221 \qquad (I.1)$$

$$M_{SO_2}/M_{N_2} = 0.0190 \qquad (I.2)$$

By applying IR calibration result to the measured absorbance with with temperature correction

$$P_{SO_2} \text{ in feed} = 11.64 \times \frac{273 + 200}{373} = 14.76 \text{ mm Hg.}$$

$$P_{N_2} \text{ in feed} = \frac{14.76}{0.019} = 776.8 \text{ mm Hg.}$$

$$P_{H_2S} \text{ in feed} = 776.8 \times 0.0221 = 17.13$$

$$P_{SO_2} \text{ in reactor} = 14.76\ (1 - 0.1764) = 12.16 \text{ mm Hg.}$$

$$P_{H_2S} \text{ in reactor} = 17.13 - 2(14.76 \times 0.1764) = 11.92 \text{ mm Hg.}$$

$$P_{H_2O} \text{ in reactor} = 2 \times 14.76 \times 0.1764 = 5.21 \text{ mm Hg.}$$

By assuming equilibrium distribution among various sulfur species

$$P_{S_x} \text{ calculated} = 0.99 \text{ mm Hg.}$$

$$P_{N_2} = P_{Reactor} - P_{H_2S} - P_{SO_2} - P_{H_2O} - P_{S_x} = 775.7 \text{ mm Hg.}$$

Moles of various component in feed.

$$M_{N_2} = 99.38 \times \frac{703}{760} \times \frac{273.16}{295.16} \times \frac{}{22400}$$

$$= 3.7978 \times 10^{-3} \text{ g-mol/min}$$

$$M_{H_2S} = 3.7978 \times 0.0221 = 8.397 \times 10^{-5} \text{ g-mol/min.}$$

$$M_{SO_2} = 3.7978 \times 0.019 = 7.238 \times 10^{-5} \text{ g-mol/min.}$$

Reaction rate of SO_2

$$-r_{SO_2} = \frac{7.238 \times 10^{-5} \times 0.1764}{0.1036 \times 60}$$

$$= 0.2054 \times 10^{-5} \text{ g-mol/g-catalyst sec.}$$

Other kinetic data obtained by same method of calculation are summarized in Tables I-1 and I-2.

TABLE I-1 SUMMARY OF RAW RATE DATA

Run No.	Room Temp. (°C)	Atm Press (mm HG)	M_{H_2S} / M_{N_2}	M_{SO_2} / M_{N_2}	M_{N_2}	M_{H_2S}	M_{SO_2}	M_{H_2O}	P_{N_2}	P_{H_2S}	P_{SO_2}	P_{H_2O}	Total P
T1CA1	22.0	703	0.0221	0.0190	379.78	8.397	7.238	Nil	776.8	17.13	14.76	Nil	808.7
T1CA2	22.0	703	0.0386	0.0345	365.89	14.132	12.637	Nil	749.4	28.94	25.88	Nil	804.2
T1CA3	22.0	703	0.0502	0.0406	379.94	19.076	15.418	Nil	747.1	37.51	30.34	Nil	815.0
T1CB1	22.0	698	0.0743	0.0568	390.79	29.023	22.208	Nil	715.8	53.18	40.66	Nil	809.6
T1CB2	22.0	698	0.0240	0.0280	409.16	9.810	11.441	Nil	768.0	18.43	21.50	Nil	807.9
T1CB3	22.0	698	0.0270	0.0380	400.95	10.819	15.227	Nil	761.0	20.54	28.90	Nil	810.4
T1CB4	22.0	698	0.0308	0.0491	389.21	11.972	19.116	Nil	747.5	23.00	36.70	Nil	807.2
T1CB5	22.0	698	0.0438	0.0215	398.44	17.434	8.556	Nil	765.6	33.54	16.46	Nil	815.6
T1CC1	22.0	700	0.0546	0.0354	381.56	20.828	13.523	Nil	740.0	40.40	26.22	Nil	806.6
T1CC2	22.0	700	0.0599	0.0574	365.13	21.858	20.950	Nil	725.5	43.46	41.64	Nil	810.6
T1CC3	22.0	700	0.0614	0.0260	384.09	23.594	9.981	Nil	743.0	45.66	19.32	Nil	808.0
T1CC4	22.0	700	0.0631	0.0373	375.03	23.659	13.988	Nil	737.1	46.43	27.49	Nil	811.0
T1CC5	22.0	700	0.0745	0.0464	357.89	26.661	16.597	Nil	719.0	53.57	33.36	Nil	806.0
T1CD1	22.0	701	0.0760	0.0588	364.06	27.661	21.402	Nil	716.2	54.43	42.11	Nil	812.7
T1CD2	22.0	701	0.0362	0.0355	399.71	14.484	14.207	14.185	731.3	26.47	25.96	25.92	809.6
T1CD3	22.0	701	0.0518	0.0240	349.56	18.109	8.393	11.506	731.0	37.87	17.55	24.06	810.5
T1CD4	22.0	701	0.0639	0.0255	368.76	23.553	9.397	10.721	723.6	46.26	18.45	21.05	809.4
T1CE1	22.0	700	0.0314	0.0320	389.31	12.242	12.457	15.245	730.3	22.93	23.37	28.60	805.2

TABLE I-1 (continued)

Run No.	Room Temp. (°C)	Atm Press (mm HG)	$\frac{M_{H_2S}}{M_{N_2}}$	$\frac{M_{SO_2}}{M_{N_2}}$	M_{N_2}	M_{H_2S}	M_{SO_2}	M_{H_2O}	P_{N_2}	P_{H_2S}	P_{SO_2}	P_{H_2O}	Total P
T1CE2	22.0	700	0.0520	0.0445	410.28	21.325	18.264	28.104	722.7	37.57	32.16	20.90	813.3
T2CA1	21.0	700	0.0274	0.0210	278.03	7.624	5.842	Nil	771.0	21.13	16.19	Nil	808.3
T2CA2	21.0	700	0.0371	0.0218	420.13	15.573	9.173	Nil	760.3	28.20	16.58	Nil	805.1
T2CA3	21.0	700	0.0470	0.0208	501.40	23.625	10.409	Nil	754.0	35.46	15.63	Nil	805.1
T2CB1	22.0	704	0.0343	0.0285	450.84	15.445	12.829	Nil	764.1	26.17	21.74	Nil	812.1
T2CB2	22.0	704	0.0359	0.0411	538.65	19.338	22.142	Nil	750.4	26.81	30.77	Nil	808.0
T2CB3	22.0	704	0.0469	0.0405	709.82	33.281	28.720	Nil	745.9	34.97	30.18	Nil	811.0
T2CB4	22.0	704	0.0350	0.0220	362.71	12.678	7.995	9.329	746.4	26.10	16.42	19.16	808.1
T2CC1	22.0	701	0.0484	0.0222	477.45	23.087	10.608	11.095	736.5	35.62	16.35	17.10	805.6
T2CC2	22.0	701	0.0303	0.0292	451.55	13.692	13.177	10.584	743.7	22.54	21.70	17.43	805.4
T2CD1	22.0	697	0.0349	0.0409	497.75	17.373	20.378	11.252	735.9	25.66	30.10	16.63	808.3
T2CD2	22.0	697	0.0461	0.0402	640.10	29.508	25.721	14.915	726.0	33.45	29.11	16.88	805.4
T2CD3	22.0	697	0.0552	0.0257	533.07	29.408	13.702	Nil	753.9	41.53	19.37	Nil	814.8
T2CD4	22.0	697	0.0539	0.0399	572.13	30.860	22.852	24.532	717.9	38.55	28.57	30.67	815.7
T2CE1	22.0	695	0.0667	0.0302	630.44	42.023	19.025	Nil	742.9	49.55	22.42	Nil	814.9
T2CE2	22.0	695	0.0670	0.0331	513.79	34.412	17.030	21.157	709.4	47.48	23.48	29.17	809.5
T2CE3	22.0	695	0.0709	0.0463	811.87	57.528	37.614	Nil	724.7	51.18	33.46	Nil	809.3

TABLE I-1 (continued)

Run NO.	Room Temp. (°C)	Atm Press (mm HG)	M_{H_2S}/M_{N_2}	M_{SO_2}/M_{N_2}	M_{N_2}	M_{H_2S}	M_{SO_2}	M_{H_2O}	P_{N_2}	P_{H_2S}	P_{SO_2}	P_{H_2O}	Total P
T2CE4	22.0	695	0.0703	0.0512	687.77	48.363	35.211	21.866	707.1	49.71	36.20	22.48	815.5
T2CF1	22.0	702	0.0357	0.0509	422.34	15.104	21.533	Nil	741.7	26.47	37.70	Nil	805.9
T2CF2	22.0	702	0.0352	0.0486	361.13	12.713	17.560	12.752	720.8	25.34	34.99	25.41	806.5
T3CA1	22.0	699	0.0223	0.0167	327.53	7.319	5.458	Nil	784.2	17.46	13.04	Nil	814.7
T3CA2	22.0	699	0.0362	0.0305	707.67	25.611	21.631	Nil	756.1	27.36	23.07	Nil	806.5
T3CB1	22.0	706	0.0580	0.0470	836.17	48.536	39.305	Nil	737.5	42.78	34.66	Nil	814.9
T3CB2	22.0	706	0.0247	0.0294	333.65	8.235	9.830	Nil	763.3	18.85	22.44	Nil	804.6
T3CC1	21.0	701	0.0345	0.0187	377.88	13.043	7.095	Nil	773.5	26.66	14.46	Nil	814.6
T3CC2	21.0	701	0.0271	0.0458	368.72	10.009	16.881	Nil	754.4	20.46	34.55	Nil	809.4
T3CC3	21.0	701	0.0376	0.0441	580.18	21.861	25.627	Nil	752.6	28.30	33.19	Nil	814.1
T3CC4	21.0	701	0.0524	0.0198	626.27	32.839	12.423	Nil	761.1	39.83	15.07	Nil	816.0
T3CC5	21.0	701	0.0546	0.0333	841.77	45.979	28.050	Nil	742.6	40.51	24.71	Nil	807.8
T3CD1	22.0	697	0.0371	0.0306	545.08	20.235	16.676	38.711	717.0	26.60	21.94	50.93	816.5
T3CD2	22.0	697	0.0405	0.0222	289.47	11.737	6.434	17.378	718.5	29.10	15.95	43.08	806.6
T3CD3	22.0	697	0.0524	0.0203	505.46	26.467	10.265	30.944	710.4	37.10	14.42	43.47	805.4
T3CD4	22.0	697	0.0540	0.0342	688.75	37.167	23.600	46.019	700.9	37.81	23.97	46.74	809.4

TABLE I-1 (continued)

Run NO.	Room Temp. (°C)	Atm Press (mm HG)	M_{H_2S}/M_{N_2}	M_{SO_2}/M_{N_2}	M_{N_2}	M_{H_2S}	M_{SO_2}	M_{H_2O}	P_{N_2}	P_{H_2S}	P_{SO_2}	P_{H_2O}	Total
T3CE1	22.0	705	0.0518	0.0465	770.37	39.878	35.822	55.012	696.0	36.02	32.35	49.68	814.0
T3CF1	22.0	704	0.0251	0.0282	331.20	8.312	9.354	18.685	731.6	18.36	20.63	41.21	811.8
T3CF2	22.0	704	0.0300	0.0452	316.91	9.497	14.342	18.882	713.5	21.33	32.19	42.38	809.4
T4CA1	22.0	703	0.0218	0.0307	612.02	13.343	18.785	Nil	772.6	16.85	23.72	Nil	813.2
T4CA2	22.0	703	0.0214	0.0175	466.55	10.017	8.204	Nil	777.1	16.62	13.6	Nil	807.3
T4CA3	22.0	703	0.0512	0.0393	618.02	31.679	24.310	Nil	745.3	38.13	29.29	Nil	812.7
T4CA4	22.0	703	0.0801	0.0610	999.35	80.080	61.000	Nil	708.5	56.78	43.19	Nil	808.5
T4CA5	22.0	703	0.0324	0.0159	813.65	26.350	13.000	Nil	777.6	25.10	12.38	Nil	815.1
T4CA6	22.0	703	0.0215	0.0177	348.15	7.483	6.162	24.553	724.5	15.57	12.79	50.35	803.2
T4CB1	21.0	700	0.0398	0.0311	515.15	20.500	16.022	37.644	704.9	27.97	21.86	51.36	806.1
T4CB2	21.0	700	0.0178	0.0372	723.61	12.884	26.923	50.011	722.9	12.84	26.83	49.84	812.4
T4CC1	22.0	699	0.0396	0.0178	1065.16	42.015	18.961	115.357	695.0	27.41	12.39	75.38	815.2
T4CC2	22.0	699	0.0255	0.0503	788.34	20.114	39.705	Nil	751.7	19.16	37.81	Nil	808.7
T4CD1	22.0	696	0.0600	0.0203	1150.90	69.060	23.438	Nil	750.0	45.02	15.21	Nil	810.2
T4CD2	22.0	696	0.0238	0.0533	583.68	13.875	31.130	49.18	702.3	16.70	37.43	59.13	815.6
T4CD3	22.0	696	0.0210	0.0620	1034.76	64.118	21.721	114.472	681.1	42.21	14.29	75.31	812.8

TABLE I-1 (continued)

Run NO.	Room Temp. (°C)	Atm Press (mm HG)	$\frac{M_{H_2S}}{M_{N_2}}$	$\frac{M_{SO_2}}{M_{N_2}}$	M_{N_2}	M_{H_2S}	M_{SO_2}	M_{H_2O}	P_{N_2}	P_{H_2S}	P_{SO_2}	P_{H_2O}	Total P
T4CD4	22.0	696	0.0636	0.0589	1184.66	75.014	69.794	89.730	679.0	43.16	39.98	51.40	813.5
T5CA1	22.0	701	0.0168	0.0150	391.49	6.572	5.901	Nil	782.7	13.12	11.74	Nil	807.6
T5CA2	22.0	701	0.0225	0.0251	410.19	9.225	10.328	Nil	769.3	17.29	19.31	Nil	805.9
T5CA3	22.0	701	0.0195	0.0170	427.41	8.360	7.289	Nil	780.5	15.22	13.27	Nil	809.0
T5CA4	22.0	701	0.0177	0.0195	618.01	10.920	12.100	Nil	778.9	13.70	15.19	Nil	807.8
T5CB1	22.0	698	0.0227	0.0620	744.09	16.918	46.138	Nil	748.9	16.98	46.37	Nil	812.3
T5CB2	22.0	698	0.0267	0.0632	458.05	12.234	28.950	52.324	666.7	17.76	42.14	77.62	804.2
T5CB3	22.0	698	0.0268	0.0300	578.21	15.482	17.389	Nil	769.0	20.55	23.07	Nil	812.6
T5CB4	22.0	698	0.0314	0.0215	322.62	10.120	6.964	Nil	769.7	24.05	16.55	Nil	810.3
T5CC1	21.0	696	0.0326	0.0350	483.72	15.768	16.943	Nil	755.4	24.59	26.44	Nil	806.4
T5CC2	21.0	696	0.0331	0.0610	680.43	22.495	41.513	Nil	739.3	24.27	45.10	Nil	808.7
T5CC3	21.0	696	0.0400	0.0229	349.98	13.988	8.020	Nil	768.1	30.70	17.59	Nil	816.4
T5CD1	22.0	704	0.0411	0.0454	567.02	23.289	25.743	Nil	748.0	30.73	33.96	Nil	812.7
T5CD2	22.0	704	0.0484	0.0532	470.40	22.779	25.065	Nil	739.5	35.78	39.34	Nil	814.6
T5CD3	22.0	704	0.0487	0.0408	406.24	19.790	16.570	Nil	746.3	36.35	30.45	Nil	813.1
T5CE1	22.0	706	0.0523	0.0338	306.59	16.049	10.360	14.512	721.1	37.72	24.38	34.15	817.4

TABLE I-1 (Continued)

Run NO.	Room Temp. (°C)	Atm Press (mm HG)	$\frac{M_{H_2S}}{M_{N_2}}$	$\frac{M_{SO_2}}{M_{N_2}}$	M_{N_2}	M_{H_2S}	M_{SO_2}	M_{H_2O}	P_{N_2}	P_{H_2S}	P_{SO_2}	P_{H_2O}	Total P
T5CF1	22.0	705	0.0332	0.0478	1075.85	35.711	51.426	Nil	750.1	24.87	35.82	Nil	810.8
T5CF2	22.0	705	0.0335	0.0612	1278.61	42.882	78.251	Nil	742.3	24.83	45.35	Nil	812.5
T5CG1	22.0	702	0.0590	0.0580	968.79	57.403	56.190	Nil	730.4	43.24	42.34	Nil	815.98
T5CG2	22.0	702	0.0503	0.0521	508.99	25.578	26.551	Nil	737.0	37.07	38.40	Nil	812.5
T5CG3	22.0	702	0.0455	0.0341	464.98	21.164	15.851	Nil	755.0	34.37	25.74	Nil	815.1
T5CG4	22.0	702	0.0512	0.0602	832.82	42.620	50.126	Nil	733.6	37.55	44.15	Nil	815.3
T5CG5	22.0	702	0.0538	0.0362	563.55	30.329	20.427	Nil	746.7	40.15	27.03	Nil	813.9
T5CG6	22.0	702	0.0633	0.0565	558.80	35.389	31.571	Nil	728.1	46.09	41.14	Nil	815.3
T5CH1	22.0	697	0.0593	0.0566	597.56	35.466	33.852	65.793	660.4	39.16	37.38	72.65	809.6
T5CH2	22.0	697	0.0588	0.0348	428.87	25.236	14.947	43.000	678.7	39.90	23.62	67.95	810.2
T5CH3	22.0	697	0.0547	0.0384	971.45	50.191	35.230	Nil	748.0	40.91	28.72	Nil	817.6
T5CH4	22.0	697	0.0507	0.0286	1050.52	53.201	30.045	Nil	759.2	38.46	21.71	Nil	819.4
T5CH5	22.0	697	0.0461	0.0201	1149.75	53.101	23.110	Nil	768.0	35.44	15.40	Nil	818.8
T5CH6	22.0	697	0.0731	0.0567	802.56	58.647	45.492	34.282	692.2	50.43	39.12	29.48	811.2
T5CH7	22.0	697	0.0721	0.0296	472.62	34.080	13.991	20.165	709.4	51.00	20.94	30.18	811.5
T5CI1	22.0	700	0.0731	0.0429	640.31	46.800	27.458	27.668	701.9	51.30	30.10	30.33	813.6
T5CI2	22.0	700	0.0780	0.0298	544.80	42.476	16.241	46.506	685.9	53.45	20.44	58.53	818.3

TABLE I-1 (continued)

Run NO.	Room Temp. (°C)	Atm Press (mm HG)	$\frac{M_{H_2S}}{M_{N_2}}$	$\frac{M_{SO_2}}{M_{N_2}}$	M_{N_2}	M_{H_2S}	M_{SO_2}	M_{H_2O}	P_{N_2}	P_{H_2S}	P_{SO_2}	P_{H_2O}	Total P
T5CI3	22.0	700	0.0637	0.0271	1273.41	34.510	81.116	Nil	748.0	47.64	20.26	Nil	815.9
T5CI4	22.0	700	0.0842	0.0318	608.38	51.203	19.375	89.4[illegible]	645.0	54.11	20.51	94.71	814.3
T5CI5	22.0	700	0.0800	0.0324	1256.27	100.65	40.703	Nil	740.3	59.18	23.99	Nil	823.5
T5CI6	22.0	700	0.1125	0.0404	1253.12	141.2	50.626	Nil	720.6	81.09	29.11	Nil	830.8
T6CA1	22.0	698	0.0392	0.0225	377.05	14.771	8.469	Nil	769.4	30.10	17.28	Nil	816.8
T6CA2	22.0	698	0.0261	0.0247	571.10	14.901	14.108	Nil	766.4	20.00	18.93	Nil	805.3
T6CA3	22.0	698	0.0454	0.0203	1271.92	57.753	25.820	Nil	769.0	35.04	15.61	Nil	819.7
T6CB1	22.0	695	0.0285	0.0382	738.85	20.071	28.228	Nil	758.6	21.59	28.94	Nil	809.1
T6CB2	22.0	695	0.0232	0.0172	634.47	14.708	10.900	Nil	776.5	18.00	13.34	Nil	807.8
T6CB3	22.0	695	0.0244	0.0178	432.96	10.576	7.730	30.266	734.5	17.91	13.11	51.33	816.9
T6CB4	22.0	695	0.0262	0.0374	623.21	16.344	23.308	42.031	715.0	18.72	26.74	48.22	808.7
T6CB5	22.0	695	0.0464	0.0195	789.28	36.615	15.421	49.062	720.5	33.37	14.05	44.70	812.6
T6CC1	22.0	701	0.0497	0.0369	1216.90	60.362	44.904	Nil	746.2	37.05	27.57	Nil	810.8
T6CC2	22.0	701	0.0478	0.0377	945.38	45.219	35.641	60.637	704.8	33.66	26.55	45.17	810.2
T6CC3	22.0	701	0.0689	0.0481	1271.93	87.608	61.180	Nil	745.1	51.35	35.85	Nil	832.3
T6CC4	22.0	701	0.0683	0.0456	1024.76	69.729	46.770	54.707	710.1	48.50	32.41	37.91	828.9

TABLE I-1 (continued)

Run NO.	Room Temp. (°C)	Atm Press (mm HG)	$\frac{M_{H_2S}}{M_{N_2}}$	$\frac{M_{SO_2}}{M_{N_2}}$	M_{N_2}	M_{H_2S}	M_{SO_2}	M_{H_2O}	P_{N_2}	P_{H_2S}	P_{SO_2}	P_{H_2O}	Total P
T6CC5	22.0	701	0.0313	0.0458	788.31	24.717	36.109	Nil	748.5	23.43	34.26	Nil	806.2
T6CC6	22.0	701	0.0346	0.0498	671.15	23.258	33.404	29.720	714.1	24.68	35.54	31.62	805.9

TABLE I-2 SUMMARY OF KINETIC DATA

Run No.	Reaction Temp. (°C)	Reaction Press (mm HG)	Cat. Wt. (g)	N_2Flow Rate x 10^3 $(\frac{g\text{-mol}}{min})$	RXN Rate x 10^5 $(\frac{g\text{-mol } SO_2}{g.\ s})$	Conversion(%) H_2S	Conversion(%) SO_2	Reactor Partial Pressures (mmHG) N_2	Reactor Partial Pressures (mmHG) H_2S	Reactor Partial Pressures (mmHG) SO_2	Reactor Partial Pressures (mmHG) H_2O	Reactor Partial Pressures (mmHG) S_x
T1CA1	200.0	806.0	0.1036	3.7978	0.2054	30.41	17.64	775.7	11.92	12.16	5.21	0.99
T1CA2	200.0	800.0	0.1036	3.6589	0.4056	35.68	19.95	748.4	18.62	20.72	10.33	1.97
T1CA3	200.0	809.0	0.1036	3.7994	0.5484	35.74	22.11	745.3	24.11	23.62	13.41	2.55
T1CB1	200.0	802.0	0.1133	3.9079	0.8131	38.09	24.89	714.5	32.90	30.54	20.24	3.85
T1CB2	200.0	804.0	0.1133	4.0916	0.2516	34.87	14.95	766.1	12.01	18.29	6.43	1.22
T1CB3	200.0	806.0	0.1133	4.0095	0.3062	38.48	13.67	759.0	12.63	24.95	7.90	1.50
T1CB4	200.0	802.0	0.1133	3.8921	0.3650	41.45	12.98	745.3	13.46	31.94	9.53	1.81
T1CB5	200.0	810.0	0.1133	3.9844	0.3816	29.76	30.32	763.1	23.55	11.47	9.98	1.90
T1CC1	200.0	800.0	0.1156	3.8156	0.5309	35.36	27.23	737.8	26.11	19.08	14.28	2.72
T1CC2	200.0	803.0	0.1156	3.6513	0.6569	41.69	21.74	723.5	25.33	32.59	18.11	3.45
T1CC3	200.0	802.0	0.1156	3.8409	0.5196	30.55	36.11	741.3	31.72	12.34	13.95	2.66
T1CC4	200.0	804.0	0.1156	3.7503	0.6046	35.45	29.98	735.1	30.01	19.25	16.48	3.14
T1CC5	200.0	798.0	0.1156	3.5789	0.7236	37.65	30.24	717.3	33.40	23.27	20.17	3.84
T1CD1	200.0	804.0	0.1161	3.6406	0.8025	40.42	26.12	714.3	32.43	31.11	22.00	4.19
T1CD2	200.0	804.0	0.1161	3.9971	0.3410	32.80	16.72	728.4	17.79	21.62	34.50	1.65
T1CD3	200.0	805.0	0.1161	3.4956	0.3811	29.32	31.63	729.0	26.77	12.00	35.16	2.11

TABLE I-2 (Continued)

Run No.	Reaction Temp. (°C)	Reaction Press (mm HG)	Cat. Wt. (g)	N_2 Flow Rate x 10^3 $(\frac{g\text{-mol}}{min})$	RXN Rate x 10^5 $(\frac{g\text{-mol } SO_2}{g \cdot s})$	Conversion(%) H_2S	Conversion(%) SO_2	Reactor Partial Pressures (mm HG) N_2	Reactor Partial Pressures (mm HG) H_2S	Reactor Partial Pressures (mm HG) SO_2	Reactor Partial Pressures (mm HG) H_2O	Reactor Partial Pressures (mm HG) S_x
T1CD4	200.0	803.0	0.1161	3.6876	0.4732	27.99	35.08	720.3	33.31	11.98	34.97	2.46
T1CE1	200.0	801.0	0.1170	3.8931	0.2818	32.32	15.88	728.4	15.54	19.66	36.01	1.41
T1CE2	200.0	807.0	0.1170	4.1028	0.5193	34.19	19.96	720.4	24.71	25.74	33.73	2.44
T2CA1	212.3	804.0	0.1150	2.7803	0.2369	42.88	27.98	769.5	12.07	11.66	9.06	1.74
T2CA2	212.3	800.0	0.1150	4.2013	0.3725	33.01	28.02	758.1	18.85	11.93	9.29	1.79
T2CA3	212.3	801.0	0.1150	5.0140	0.4749	27.74	31.48	752.9	25.63	10.71	9.84	1.89
T2CB1	212.3	807.0	0.1125	4.5084	0.4018	35.12	21.14	762.0	16.94	17.10	9.17	1.76
T2CB2	212.3	803.0	0.1125	5.3865	0.5055	35.29	15.41	748.3	17.38	26.02	9.48	1.82
T2CB3	212.3	806.0	0.1125	7.0982	0.7063	28.65	16.60	744.0	24.95	25.17	10.02	1.93
T2CB4	212.3	804.0	0.1125	3.6271	0.2929	31.19	24.73	745.0	17.91	12.36	27.18	1.56
T2CC1	212.3	802.0	0.1241	4.7745	0.4130	26.64	28.99	735.9	26.11	11.61	26.55	1.82
T2CC2	212.3	800.0	0.1241	4.5155	0.3058	33.26	17.28	740.6	15.05	17.95	24.93	1.44
T2CD1	212.3	803.0	0.1143	4.9975	0.4166	32.89	14.02	733.2	17.22	25.88	25.06	1.62
T2CD2	212.3	801.0	0.1143	6.4010	0.5727	26.62	15.27	724.3	24.53	24.66	25.77	1.71
T2CD3	212.3	809.0	0.1143	5.3307	0.6012	28.04	30.09	751.8	29.85	13,51	11.63	2.24
T2CD4	212.3	810.0	0.1143	5.7213	0.5618	24.97	16.86	715.2	28.93	23.75	40.31	1.85

TABLE I-2 (continued)

Run No.	Reaction Temp. (°C)	Reaction Press (mm HG)	Cat. Wt. (g)	N_2 Flow Rate x 10^3 $(\frac{g\text{-mol}}{min})$	RXN Rate x 10^5 $(\frac{g\text{-mol } SO_2}{g.\ s})$	Conversion(%) H_2S	Conversion(%) SO_2	Reactor Partial Pressures (mm HG) N_2	Reactor Partial Pressures (mm HG) H_2S	Reactor Partial Pressures (mm HG) SO_2	Reactor Partial Pressures (mm HG) H_2O	Reactor Partial Pressures (mm HG) S_x
T2CE1	212.3	809.0	0.1019	6.3044	0.8296	24.14	26.66	740.8	37.55	16.44	11.95	2.30
T2CE2	212.3	805.0	0.1019	5.1379	0.6270	22.28	22.51	708.2	36.88	18.19	39.74	2.03
T2CE3	212.3	803.0	0.1019	8.1187	1.1117	23.63	18.07	722.1	39.07	27.41	12.09	2.33
T2CE4	212.3	809.0	0.1019	6.8777	0.8990	22.73	15.61	704.1	38.41	30.55	33.78	2.17
T2CF1	212.3	800.0	0.1213	4.2234	0.4574	44.08	15.46	739.4	14.79	31.87	11.66	2.24
T2CF2	212.3	802.0	0.1213	3.6113	0.3484	39.89	14.44	719.4	15.22	29.93	35.51	1.94
T3CA1	235.2	810.0	0.1188	3.2753	0.2392	46.59	31.24	782.0	9.33	8.96	8.14	1.57
T3CA2	235.2	802.0	0.1188	7.0767	0.6376	35.49	21.01	754.6	17.61	18.22	9.69	1.87
T3CB1	235.2	805.0	0.0978	8.3617	1.3048	31.55	19.48	735.0	29.28	27.91	13.50	2.61
T3CB2	235.2	800.0	0.0978	3.3365	0.3441	49.04	20.54	761.6	9.58	17.83	9.22	1.78
T3CC1	235.2	808.0	0.1112	3.7788	0.3988	40.80	37.50	770.3	15.74	9.04	10.85	2.09
T3CC2	235.2	804.0	0.1112	3.6872	0.4142	55.22	16.37	752.5	9.17	28.89	11.31	2.18
T3CC3	235.2	809.0	0.1112	5.8018	0.7033	42.93	18.31	751.3	16.15	27.11	12.15	2.34
T3CC4	235.2	811.0	0.1112	6.2627	0.7191	29.22	38.62	759.7	28.19	9.25	11.64	2.25
T3CC5	235.2	803.0	0.1112	8.4177	1.0275	29.82	24.44	741.5	28.43	18.67	12.08	2.33
T3CD1	235.2	812.0	0.0966	5.4508	0.5202	29.80	18.08	714.6	18.68	17.97	58.86	1.53

TABLE I-2 (continued)

Run No.	Reaction		Cat. Wt. (g)	N_2 Flow Rate x 10^3 $(\frac{\text{g-mol}}{\text{min}})$	RXN Rate x 10^5 $(\frac{\text{g-mol } SO_2}{\text{g. s}})$	Conversion(%)		Reactor Partial Pressures (mmHG)				
	Temp. (°C)	Press (mm HG)				H_2S	SO_2	N_2	H_2S	SO_2	H_2O	S_x
T3CD2	235.2	802.0	0.0966	2.8947	0.3881	38.33	34.96	717.3	17.94	10.37	54.23	2.15
T3CD3	235.2	800.0	0.0966	5.0546	0.5813	25.46	32.82	708.0	27.64	9.66	52.91	1.82
T3CD4	235.2	805.0	0.0966	6.8875	0.8189	25.54	20.11	699.5	28.11	19.15	56.38	1.86
T3CE1	235.2	809.0	0.0939	7.7037	0.7954	22.47	12.51	693.5	27.92	28.30	57.77	1.56
T3CF1	235.2	808.0	0.1011	3.3120	0.2927	42.72	18.98	728.2	10.50	16.71	51.04	1.51
T3CF2	235.2	804.0	0.1011	3.1691	0.3828	48.90	16.19	711.3	10.89	26.98	52.80	2.01
T4CA1	261.5	809.0	0.1076	6.1202	0.4833	46.77	16.61	770.8	8.97	19.78	7.88	1.54
T4CA2	261.5	801.0	0.1076	4.6655	0.3496	45.06	27.50	773.1	9.12	9.86	7.48	1.46
T4CA3	261.5	807.0	0.1076	6.1802	1.0555	43.02	28.03	744.6	21.75	21.08	16.42	8.20
T4CA4	261.5	802.0	0.1076	9.7851	2.2230	35.62	23.21	707.8	36.19	33.15	20.02	3.91
T4CA5	261.5	810.0	0.1076	8.1365	0.6214	30.45	30.86	774.9	17.45	8.56	7.64	1.49
T4CA6	261.5	801.0	0.1076	3.4815	0.2281	38.84	23.61	723.9	9.51	9.77	56.39	1.18
T4CB1	261.5	801.0	0.1102	5.1515	0.5387	34.75	22.23	702.8	18.25	17.00	61.08	1.90
T4CB2	261.5	809.0	0.1102	7.2361	0.3339	34.27	8.20	720.0	8.44	24.62	54.24	0.86
T4CC1	261.5	807.0	0.0962	10.6516	0.5702	15.69	17.41	693.2	23.11	10.22	79.68	0.84
T4CC2	261.5	807.0	0.0962	7.8834	0.7560	43.39	10.99	750.6	10.84	33.65	8.31	1.62

TABLE I-2 (continued)

Run No.	Reaction Temp. (°C)	Reaction Press (mm HG)	Cat. Wt. (g)	N_2 Flow Rate x 10^3 $(\frac{\text{g-mol}}{\text{min}})$	RXN Rate x 10^5 $(\frac{\text{g-mol } SO_2}{\text{g. s}})$	Conversion(%) H_2S	Conversion(%) SO_2	Reactor Partial Pressures (mm HG) N_2	Reactor Partial Pressures (mm HG) H_2S	Reactor Partial Pressures (mm HG) SO_2	Reactor Partial Pressures (mm HG) H_2O	Reactor Partial Pressures (mm HG) S_x
T4CD1	261.5	804.0	0.0983	11.5090	1.3319	22.75	33.66	749.4	34.78	10.09	10.24	2.00
T4CD2	261.5	813.0	0.0983	5.8368	0.4365	37.11	8.27	701.7	10.49	34.33	65.32	1.21
T4CD3	261.5	806.0	0.0983	10.3476	0.8648	15.91	23.48	676.4	35.41	10.92	82.01	1.31
T4CD4	261.5	808.0	0.0983	11.8466	1.4709	23.13	12.43	676.2	33.18	35.01	61.33	1.94
T5CA1	298.2	801.0	0.1054	3.9149	0.3002	57.77	32.17	778.5	5.52	7.96	7.55	1.49
T5CA2	298.2	800.0	0.1054	4.1019	0.4565	62.59	27.95	766.7	6.45	13.91	10.79	2.13
T5CA3	298.2	804.0	0.1054	4.2741	0.3761	56.90	32.63	778.1	6.56	8.94	8.66	1.71
T5CA4	298.2	802.0	0.1054	6.1801	0.4418	51.17	23.08	775.2	6.89	11.68	7.01	1.38
T5CB1	298.2	808.0	0.1049	7.4409	0.8005	59.56	10.92	747.7	6.87	41.30	10.12	2.00
T5CB2	298.2	800.0	0.1049	4.5805	0.5883	60.53	12.79	665.8	7.01	36.66	88.37	2.12
T5CB3	298.2	807.0	0.1049	5.7821	0.6976	56.72	25.25	766.9	8.89	17.24	11.65	2.30
T5CB4	298.2	802.0	0.1049	3.2262	0.5029	62.55	45.45	766.0	9.00	9.02	15.03	2.96
T5CC1	298.2	801.0	0.1149	4.8372	0.7238	63.29	29.45	754.7	9.03	18.65	15.57	3.07
T5CC2	298.2	802.0	0.1149	6.8043	1.0267	62.93	17.05	737.2	9.00	37.41	15.38	3.04
T5CC3	298.2	810.0	0.1149	3.4998	0.6216	61.27	53.43	767.4	11.88	8.19	18.79	3.70

TABLE I-2 (continued)

Run No.	Reaction Temp. (°C)	Reaction Press (mm HG)	Cat. Wt. (g)	N_2 Flow Rate x 10^3 $(\frac{g\text{-mol}}{min})$	RXN Rate x 10^5 $(\frac{g\text{-mol } SO_2}{g. s})$	Conversion(%)		Reactor Partial Pressures (mm HG)				
						H_2S	SO_2	N_2	H_2S	SO_2	H_2O	S_x
T5CD1	298.2	805.0	0.1103	5.6702	1.0779	61.26	27.71	746.0	11.90	24.55	18.82	3.71
T5CD2	298.2	806.0	0.1103	4.7040	1.1374	66.09	30.03	738.1	12.12	27.52	23.62	4.65
T5CD3	298.2	804.0	0.1103	4.0624	0.9750	65.21	38.94	744.4	12.65	18.59	23.71	4.68
T5CE1	298.2	808.0	0.1303	3.0659	0.6793	66.18	51.26	719.3	12.77	11.88	59.14	4.93
T5CF1	298.2	806.0	0.0977	10.7585	1.3975	45.88	15.93	748.8	13.46	30.11	11.41	2.25
T5CF2	298.2	806.0	0.0977	12.7861	1.6379	44.78	12.26	739.4	13.71	39.79	11.12	1.99
T5CG1	298.2	806.0	0.1007	9.6879	2.2906	48.22	24.63	726.7	22.39	31.91	20.85	4.11
T5CG2	298.2	805.0	0.1007	5.0899	1.3113	61.95	29.84	736.1	14.08	26.94	22.92	5.00
T5CG3	298.2	807.0	0.1007	4.6498	1.0253	58.54	39.08	753.0	14.25	15.68	20.12	3.96
T5CG4	298.2	807.0	0.1007	8.3282	1.8725	53.09	22.57	731.4	17.61	34.18	19.93	3.93
T5CG5	298.2	807.0	0.1007	5.6355	1.3493	53.76	39.91	745.6	18.55	16.24	21.57	5.06
T5CG6	298.2	805.0	0.1007	5.5880	1.7343	59.22	33.19	726.0	18.80	27.48	27.30	5.39
T5CH1	298.2	803.0	0.1018	5.9756	1.4316	49.31	25.83	659.7	19.85	27.72	91.95	3.81
T5CH2	298.2	803.0	0.1018	4.2887	1.0288	49.80	42.04	677.7	20.02	13.69	87.71	3.92
T5CH3	298.2	807.0	0.1018	9.1745	1.8209	44.32	31.57	743.9	22.78	19.65	18.13	2.57

TABLE I-2 (continued)

Run No.	Reaction Temp. (°C)	Reaction Press (mm HG)	Cat. Wt. (g)	N_2 Flow Rate x 10^3 $(\frac{g\text{-mol}}{min})$	RXN Rate x 10^5 $(\frac{g\text{-mol } SO_2}{g.s})$	Conversion(%) H_2S	Conversion(%) SO_2	Reactor Partial Pressures (mm HG) N_2	H_2S	SO_2	H_2O	S_x
T5CH4	298.2	811.0	0.1018	10.5052	1.6813	38.61	34.18	755.0	23.61	14.29	14.85	2.93
T5CH5	298.2	812.0	0.1018	11.4975	1.3946	32.03	36.86	764.4	24.09	9.72	11.35	2.24
T5CH6	298.2	802.0	0.1018	8.0256	2.2329	46.51	29.98	690.1	26.98	27.39	52.94	4.63
T5CH7	298.2	802.0	0.1018	4.7262	1.2962	46.46	56.58	707.1	27.30	9.09	53.87	4.68
T5CI1	298.2	805.0	0.0983	6.4031	1.8421	46.48	39.51	700.6	27.44	18.20	54.11	4.69
T5CI2	298.2	809.0	0.0983	5.4480	1.4357	39.87	52.10	683.1	32.12	9.79	79.83	4.20
T5CI3	298.2	808.0	0.0983	12.7341	2.1240	30.86	36.30	745.6	32.94	12.90	14.70	2.90
T5CI4	298.2	807.0	0.0983	6.0838	1.4893	34.31	45.29	643.3	35.57	11.22	113.29	3.67
T5CI5	298.2	814.0	0.0983	12.5627	2.6887	31.51	38.96	737.9	40.53	14.62	18.65	3.68
T5CI6	298.2	820.0	0.0983	12.5312	3.7070	30.98	43.17	717.1	55.97	16.54	25.12	4.96
T6CA1	323.0	810.0	0.0957	3.7750	0.7688	59.77	52.06	768.0	12.10	8.28	17.98	3.64
T6CA2	323.0	801.0	0.0957	5.7110	0.7438	57.31	30.25	765.5	8.53	13.20	11.45	2.32
T6CA3	323.0	813.0	0.0957	12.7192	1.7164	34.13	38.17	766.3	23.08	9.65	11.95	2.42
T6CB1	323.0	804.0	0.0941	7.3885	1.0588	56.74	21.17	757.1	9.34	22.81	12.25	2.48
T6CB2	323.0	804.0	0.0941	6.3447	0.6570	50.44	34.00	775.4	8.91	8.80	9.07	1.84

TABLE I-2 (continued)

Run No.	Reaction Temp. (°C)	Reaction Press (mm HG)	Cat. Wt. (g)	N_2 Flow Rate x 10^3 $(\frac{\text{g-mol}}{\text{min}})$	RXN Rate x 10^5 $(\frac{\text{g-mol } SO_2}{\text{g. s}})$	Conversion(%) H_2S	Conversion(%) SO_2	Reactor Partial Pressures (mm HG) N_2	Reactor Partial Pressures (mm HG) H_2S	Reactor Partial Pressures (mm HG) SO_2	Reactor Partial Pressures (mm HG) H_2O	Reactor Partial Pressures (mm HG) S_x
T6CB3	323.0	812.0	0.0941	4.3296	0.4553	48.61	33.17	732.3	9.19	8.76	60.02	1.76
T6CB4	323.0	804.0	0.0941	6.2321	0.7331	50.65	17.75	713.2	9.24	21.98	57.71	1.92
T6CB5	323.0	807.0	0.0941	7.8928	1.0905	33.63	39.90	718.3	22.13	8.44	55.91	2.27
T6CC1	323.0	802.0	0.0950	12.1690	2.1995	41.54	27.92	742.0	21.66	19.87	15.39	3.12
T6CC2	323.0	803.0	0.0950	9.4538	1.5307	38.59	24.48	701.5	20.67	20.05	58.16	2.63
T6CC3	323.0	823.5	0.0950	12.7193	3.2853	42.75	30.63	742.8	29.40	24.87	21.94	4.44
T6CC4	323.0	820.9	0.0950	10.2476	2.4821	40.58	30.25	708.1	28.72	22.60	57.52	3.97
T6CC5	323.0	801.0	0.0950	7.8831	1.2363	57.02	19.51	747.3	10.07	27.56	13.36	2.70
T6CC6	323.0	801.0	0.0950	6.7115	1.1050	54.16	18.85	713.1	11.33	28.81	45.01	2.71